UNIVERSITY OF OKLAHOMA

GRADUATE COLLEGE

INTEGRATED RESERVOIR CHARACTERIZATION AND GEOLOGICAL UPSCALING FOR RESERVOIR FLOW SIMULATIONS OF THE SYCAMORE/MERAMEC AND HUNTON PLAYS IN OKLAHOMA

A DISSERTATION

SUBMITTED TO THE GRADUATE FACULTY

in partial fulfillment of the requirements for the

Degree of

DOCTOR OF PHILOSOPHY

By

BENMADI MILAD
Norman, Oklahoma
2019

INTEGRATED RESERVOIR CHARACTERIZATION AND GEOLOGICAL UPSCALING FOR RESERVOIR FLOW SIMULATIONS OF THE SYCAMORE/MERAMEC AND HUNTON PLAYS IN OKLAHOMA

A DISSERTATION APPROVED FOR THE
CONOCOPHILLIPS SCHOOL OF GEOLOGY AND GEOPHYSICS

BY

Dr. Roger M. Slatt, Chair

Dr. Kurt J. Marfurt

Dr. Brett Carpenter

Dr. Fuge Zou

Dr. Mashhad Fahes

To my father, sisters, brothers, and late mother.

Acknowledgements

This document is the result of several years of research which could not have been possible without the continuous financial and technical support of my generous advisor, Dr. Roger Slatt. I would like to express my sincere gratitude to Dr. Slatt for his continuous support of my Ph.D. study and research. In addition, Dr. Slatt plays a major role in the story of changing my career from Engineering to Geology. He brought geology to life for me. He made me study rocks not only at the labs but also in the field by applying his saying, "A bad day in the field is better than a good day in the office." I am very grateful that he inspired me to learn geology while also applying my engineering background. If not for Dr. Slatt, none of this would have been possible and I would not be half the geologist I am today.

I would like to express my appreciation to my dissertation committee members, Dr. Kurt Marfurt, Dr. Mashhad Fahs, Dr. Brett Carpenter, and Dr. Fuge Zou for their insight into my research and for their time dedicated to reviewing this document. My special thanks goes out to Dr. Kurt Marfurt and Dr. Mashhad Fahs for their professional feedback on this project. I also wish to acknowledge Dr. Fuge Zou for his insight on the Sycamore project. Special thanks and honor to the late Dr. Tom Ronald for his friendship and support.

Sincere thanks to the industry consortium for its continued funding to the Institute of Reservoir Characterization (IRC) at the University of Oklahoma. This research would not be possible without the data support of Pathfinder LLC, in particular, Luis Castillo and the late Jerry Wilson. I am also grateful to AASPI consortium, Schlumberger, CGG, and EasyCore Company for providing the software that made this work possible.

Special acknowledgment to the University of Oklahoma and the ConocoPhillips School of Geology and Geophysics (CPSGG) for providing the academic infrastructure and resources.

Special thanks to the CPSGG staff for various support: Robert Turner for helping with lab work; Ginny Gandy's assistance in renting vehicles for field trips; Rebecca Fay for helping me with the Graduate College requirements and deadlines; and Ginger Leivas and Leah Moser for helping me process financial reports.

I would like to thank the Institute for Reservoir Characterization at the University of Oklahoma for their positive contributions and suggestions. In particular, I would like to thank Dr. Sayantan Ghosh for his contribution to fracture study; Henry Galvis Portilla and Caleb P. Bontempi for helping me with the field work; Jing Zhang and Ifunanya "Naya" Ekwunife for assisting with XRF measurements; Daniela Becerra Rondon for geomechanic discussions; Emilio Torres for his geochemistry guidance; Dalila Jesus for helping with SEM imaging studies; David Duarte and Austin McGlannan for excellent discussions about the Sycamore project. Many thanks to Julian Chenin for his support.

Thank you to my colleagues Hanna Morgan for helping with field work; Gerhard "Gerry" Heij for his assistance with the SEM analysis; and Alali Abdulmohsen for guiding me through data conditioning and seismic inversion. My gratitude to Mr. Herman Burrough for helping find outcrop locations, and Mahmoud Mohamed Aljabri, Redouane Laaroussi, and Eyad Aljishi for assisting in the field work. Especial thanks to Mr. Mohamed Suliman for helping me with running the flow simulation.

I would be remiss if I did not also thank my friend Salem Naeeri and his wife, Amira Elasfer, for their incredible support and guidance, as well as their children Mahmoud, Munder, and Yazan for bringing me joy whenever I see them – they are like my second family.

Finally, I would like to thank my parents and siblings for their continuous encouragement and support throughout my education. My infinite gratitude is to my late mother, Mabrouka

Mohamed, and my father, Muftah Lahwaj. Yet again, immeasurable love and gratitude to my mother, who is a big part of my academic and life successes. May Allah protect her, bless her and grant her paradise.

I am immensely grateful to CPSGG and everyone who has taken a chance on me, shaped me, and poured into my development as a geoscientist. You have inspired me more than you will ever know.

Table of Contents

List of Tables

List of Figures

Abstract

This study fully integrates multidisciplinary, multi-scalar subsurface and surface data for successful exploration and development programs in a fractured rock reservoir. Unconventional Sycamore/Meramec and conventional Hunton Carbonate plays in Oklahoma are the focus of this study. The following questions are addressed in this thesis: 1) what factors control natural fracture distributions, parameters, and their effect on fluid flow?, 2) what are the effects of geological upscaling on fluid flow simulations? and 3) what is the lithology and depositional environment of the Mississippian Sycamore/Meramec strata in the South Central Oklahoma Oil Province (SCOOP) area?

Hydrocarbon production in naturally fractured reservoirs vary because some areas are more prone to fracturing than others. Also, some fracture parameters are more important than others. To address these issues, multiscale data was used to build a realistic fracture model for fluid flow simulations. As a result, a generic fracture model was developed to predict the lithology and structure of the rocks as two main factors controlling fracture distributions. Grain supported rock and/or curvature were found to be more prone to fracturing than mud supported rock and/or negative curvature. Also, fracture length was found to have a greater influence on production response than aperture. The implication of these findings helps optimize landing well locations.

The upscaling process of geologic models can lead to losing fine-scale geological features, resulting in errors in production and reservoir performance predictions. To overcome this issue, the upscaling workflow was validated with history matching to find the optimal level of upscaling (OLU). OLU preserves the geological features and balance between simulation accuracy and simulation run time. As a result, horizontal upscaling larger than 100x150 ft results in increasing hydrocarbon production prediction errors. Logarithmic equations for

different levels of upscaling were developed to define the production accuracy. Also, power law and lognormal relationships among grid cell size, computational simulation running time, and the number of processes were obtained. The implication of these findings can help predict the error in production if excessive upscaling is required. This workflow might be applied to other reservoirs to find optimal levels of upscaling.

Additionally, many operators in the oil industry have been actively exploring the Mississippian Sycamore/Meramec strata in southern Oklahoma. The optimum drilling locations are not well known because the depositional environment, lithology, and reservoir quality, are still not well understood. To shed light on these issues, comprehensive quantitive and qualitative field, lab, and machine learning studies were conducted on two outcrops and a subsurface well. The lithofacies from the outcrop and subsurface are identified, outcrop-to-subsurface correlation were determined, and the depositional environment was interpreted. Sediment gravity flows was interpreted as the process of transport and deposition. I suggest that the bioturbated shale and/or the sandy siltstone of the Sycamore rock types can be potential target zones due to their reservoir quality, lithology, bed continuity, and brittleness. The implication of this specific study can be of direct benefit to the exploration and development programs of many companies in the Ardmore Basin of South Central Oklahoma.

Chapter 1: Introduction

This dissertation integrates multi-scalar data from the fields of geology, geophysics, and petroleum engineering (**Figure 1.1**) for the characterization and development of static and dynamic reservoir models for application to the Sycamore/Meramec and Hunton Plays in Oklahoma. This dissertation is divided into four main chapters. The focus of **Chapter 2** and **Chapter 3** is on multiscale, natural fracture characterization of the Hunton Group. The emphasis of **Chapter 3** is the stratigraphic natural fracture variations in the Hunton Group in Oklahoma. **Chapter 4** focuses on the 3D fine scale geocellular models, optimized upscaling, and 3D reservoir simulation models. **Chapter 5** focuses on the lithology, stratigraphy, and the depositional environment of the Mississippian Sycamore/Meramec strata in the SCOOP area, located in the Arbuckle Mountains.

Chapter 2 includes data collections of natural fractures in the Hunton Group from cores and outcrops to build fracture models using real data, which can be used for reservoir performance prediction. Measurements include fracture intensity, orientation, aperture, and spacing. These are necessary in order to understand the natural fracture distributions and to build 3D fracture intensity and discrete fracture network (DFN) models (discussed in **Chapters 3 and 4**). This chapter also includes discussion of rock properties (porosity, permeability, and hardness), and fractures aided by karsting.

Chapter 3 investigates the impact of lithological variations and structural changes on natural fracture distributions. I studied natural fractures at different scales using borehole images, three outcrops (two horizontally bedded outcrops and one folded and exposed as an anticline top), and seismic data. Detailed discussions on fracture intensity at different curvatures for different lithology types are is also present in this chapter.

Chapter 4 expounds on the effects of upscaling geological models for reservoir fluid flow simulations using Hunton Group data. Multiscale natural fracture data in **Chapter 2 and 3** were used to build a realistic discrete fracture network (DFN) model. Additionally, seismic data was utilized to build fine scale—high heterogeneity—geological models. Fine scale geological models were upscaled vertically and laterally to find the optimal level of upscaling that matches the well production data.

Chapter 5 presents the lithology, depositional environment, and stratigraphy of the Mississippian Sycamore in the SCOOP area. Qualitative and quantitative techniques of field, lab, and machine learning studies were conducted using outcrops and subsurface well log data.

The main aims of this dissertation are to: a) present natural fracture attributes at different scales (i.e., thin sections, core, borehole image logs, outcrops, and seismic), b) predict the impact of lithofacies changes and structural effects on fracture distributions to optimize drilling location and orientation by building a generalized fracture model for the Hunton Group carbonate, c) examine the effect of varying fracture aperture and length on hydrocarbon production, d) develop a workflow to construct high-resolution 3D geologic models incorporating geological and geophysical multiscale data into an optimized 3D reservoir simulation model, e) find the optimal level of upscaling at which significant geological and petrophysical properties can be retained in the reservoir simulation model, f) conduct production simulation on multiple vertically and aerially upscaled grid cell sizes to assess production accuracy, g) determine relationships among the computational time for different upscaled (coarser) reservoir models for a different number of parallel processes, h) determine optimal numbers of clusters for electrofacies and chemofacies by applying semi-supervised machine learning techniques of K-means, SOM, PCA, and elbow method, i) understand the Mississippian Sycamore depositional environment,

lithology, and its significance to geological assessments for optimal drilling locations, j) utilize outcrop studies for subsurface correlation, yielding enhanced subsurface interpretation, and k) develop criteria for predicting rock properties from wireline logs.

In a nutshell, these studies engage multiscale data integration within disciplines of geology, geophysics, and petroleum engineering, using field, lab, and modeling studies as well as statistical and machine learning techniques. This dissertation presents an example for successful integrated studies for geological and fluid flow assessments to optimize drilling locations, development, and reservoir management programs.

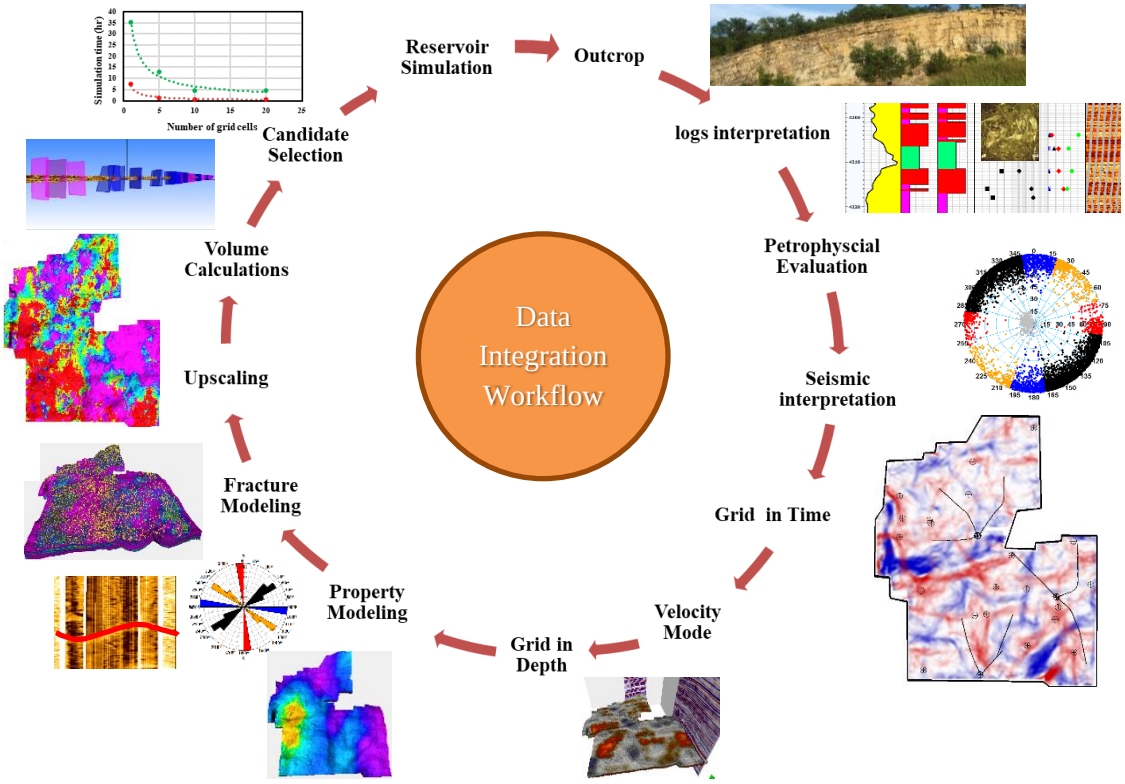

Figure 1.1. The integrated outcrop- to- simulation approach to build a detailed geological model. (Modified after Schlumberger, 2012).

References

Schlumberger, 2012: The American Oil & Gas Reporter.

Chapter 2: Comparison of rock and natural fracture attributes in karsted and non-karsted Hunton Group: Ada and Fittstown area, Oklahoma

Published as:

Milad, B., S. Ghosh, and R. M. Slatt, 2018, Comparison of rock and natural fracture attributes in karsted and non-karsted Hunton Group Limestone: Ada and Fittstown area, Oklahoma: Shale Shaker, v. **69**, no. 2, p. 70–86.

Abstract

The Hunton Group carbonate often exhibit highly variable porosity and lithology resulting in unpredictable production. Apart from depositional circumstances, the variable rock and petrophysical properties may arise from diagenetic and structural phenomena related to karsting and resulting collapse breccia. To investigate this effect, two horizontally bedded outcrops of the non-brecciated Chimneyhill subgroup in Southern Oklahoma were studied for natural fracture orientation, aperture, and spacing. In the outcrops, three to four stratabound macrofracture (opening displacement > 0.05 mm) sets, i.e., N-S (175^{o} azimuth), E-W (95^{o} azimuth), NW-SE (300-320^{o} azimuth), and NE-SW (40-70^{o} azimuth), were identified. Fracture aperture and spacing generally exhibit a characteristic, exponential or lognormal, distribution. We also described a partly-brecciated core of the Chimneyhill Subgroup of the Hunton Group from Pottawatomie County in Oklahoma. The core was used for petrographic analysis and measurement of fracture aperture, intensity, porosity, and permeability in both the upper brecciated and lower non-brecciated portions. In the core, fractures occur strictly in the brecciated zones. The brecciated zones show high rebound-hardness values. These zones also have relatively high permeability and porosity values compared to the non-brecciated portions. Fracture intensity is higher in the

brecciated part of the core compared to that in the outcrop. The average fracture aperture in the brecciated part of the core is lower compared to that in the outcrops. Highlighting these differences may help understand differences in the hydrocarbon production from the Hunton Group carbonate contingent upon data availability.

Introduction

Fractures can provide permeability which contributes to hydrocarbon production (e.g., Nelson, 2001). Understanding natural fracture distributions, networks, and their orientations can be critical for successful exploration and production (Hanks et al., 1997; Bratton et al., 2006). The origin of natural fractures in carbonate reservoirs can be controlled by different processes, such as karstification of subaerial unconformity and brecciation (Missman and Jameson, 1991; Friedman, 1995; Luo and Machel, 1995; Machel et al., 2012), structural effects including fold geometry (Smith, 1951; Narr, 1991; Garfield et al., 1992; Barbier et al., 2012), and faulting (Smith, 1951; Thomas, 1986; Hanks et al., 1997; Antonellini and Mollema, 2000; Kim et al., 2004).

The Hunton Group is considered a prolific oil and gas producing reservoir in the U.S. Midcontinent (Gaswirth and Higley, 2014). The cumulative oil produced, is 290 MMBO and the cumulative gas production is 5 TCFG (IHS Energy, 2010), with unproduced 9 MMBO and 38 BCFG of oil and gas respectively (Gaswirth and Higley, 2013). Fractures in the Hunton Group are considered one of the key components that enhance hydrocarbon production (Al-Shaieb et al., 1993). Previously, authors described the effect of curvature on fracture abundance in the Hunton Group using seismic and borehole image data (Staples et al., 2010; Staples, 2011); they found that the most positive curvature (folded area) correlated to high fracture abundance. However, there is a dearth of literature addressing fractures in the Hunton Group from outcrop and core studies. Studying both core and outcrop are important for a better understanding of reservoir properties

(Brito et al., 2017). Since the fractures in the Hunton Group carbonates are poorly understood, this study is focused on parameterization of its fractures (mainly joints).

Specifically, this study was undertaken to 1) compare the fracture apertures and intensities from core and outcrops, 2) determine fracture spacing from outcrops, 3) explain the occurrence of three to four major fracture sets observed in outcrops, and 4) provide detailed fracture field data to be used to build a realistic fracture model as discussed in the next chapters.

Geological setting

The Hunton Group carbonates were deposited through the Late Ordovician-Silurian-Early Devonian Time in many areas in the Oklahoma and Texas Panhandles, including the southwestern part of the Cherokee platform and in the Anadarko, Arkoma, and Ardmore basins (**Figure 2.1A**). The depositional environment of the Hunton Group was associated with a shallow-warm water carbonate ramp of a gently sloping surface with less than 1 degree dip (Amsden, 1975; Stanley and Rottmann, 2001). The Hunton Group is a sequence of limestone, dolomite and interbedded calcareous shale (**Figure 2.1B**) deposited through upper subtidal, intertidal, and supratidal depositional environments (Fritz and Medlock, 1994) with intra-Hunton unconformities due to a time-stratigraphic gap (Al-Shaieb et al., 2002). The Hunton facies are shallowing-upward cycles, comprising a series of progradational and aggradational parasequences that occurred on the Hunton ramp (Fritz and Medlock, 1994). The Hunton facies experienced a wide range of diagenetic changes during the Silurian-Devonian Periods (Johnson et al., 2000), and the facies changes were related to subtidal, intertidal, and supratidal areas (Fritz and Medlock, 1994).

Stratigraphically, the Hunton Group carbonates in Oklahoma are conformably underlain by the Ordovician Sylvan shale and unconformably overlain by the Late Devonian-Mississippian Woodford Shale, or locally by the Middle to Late Devonian Misener Sandstone (Amsden, 1975).

The oldest Hunton subunit is the lowermost Ordovician Keel Formation. The Keel Formation is part of the Chimneyhill subgroup, which also contains the Silurian Cochrane and Clarita Formations; they are dolomitic limestones and dolomites. The clay-rich and silty limestones and dolomites of the Silurian Henryhouse Formation and the Devonian Bois d'Arc limestone (Haragan equivalent) overlay the skeletal limestones and dolomites of the Chimneyhill (**Figure 2.1B**). The Henryhouse strata are described as dolomitized intertidal facies (Al-Shaieb and Puckette, 2000) and are overlain by the Devonian Frisco limestone in central and southern Oklahoma where it is preserved. The Frisco Formation comprises packstones and grainstones with allochem components, including brachiopods, corals, and pelmatozoans (Morgan and Schneider, 1981).

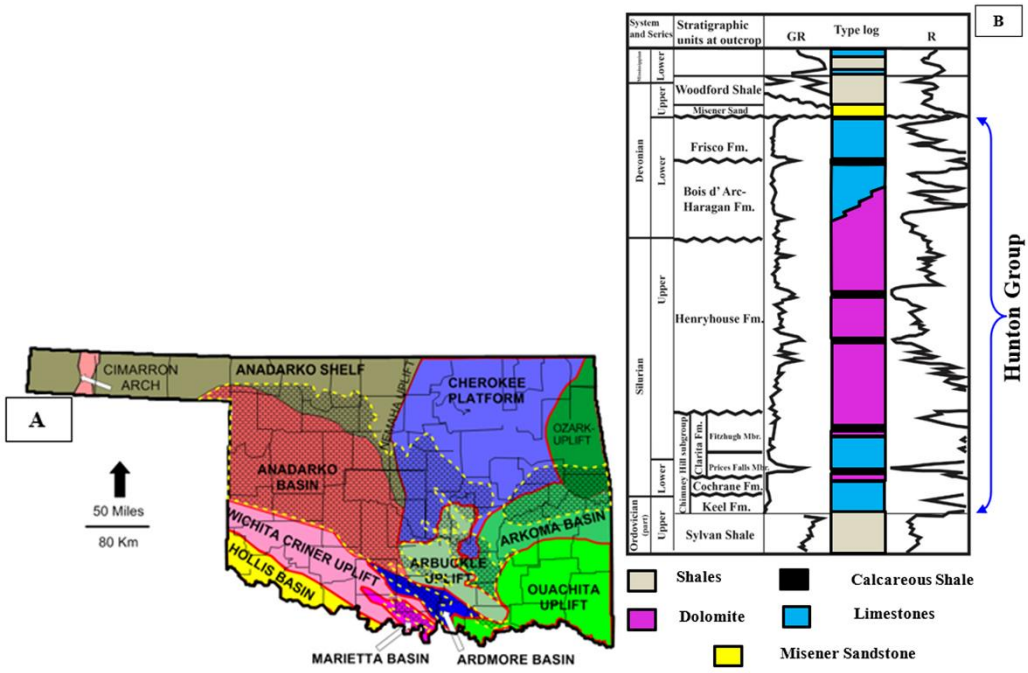

Figure 2.1. Oklahoma geological provinces and the stratigraphic column of the Hunton Group. A) Map of Oklahoma showing geologic provinces and the Hunton Group distribution (Northcutt, 2002). Yellow dashed lines show the boundaries of the Hunton Group. B) Hunton Group stratigraphic column in central Oklahoma with gamma ray (GR) and resistivity (GR) type logs (modified from Fritz and Medlock 1994). The Misener Sandstone (overlying Hunton) was added to this stratigraphic column as it was observed in a core and subsurface logs in the Cherokee Platform (Milad, 2017).

Paleokarst features that are present in Hunton subsurface rocks include breccias, vugs, and

molds, solution-enlarged fractures and channels, infill sediment, and possible cavern porosity (Johnson et al., 2000; Milad and Slatt 2017). The brecciation is related to karst processes which occurred during extensive periods of subaerial exposure during sea level lowstands, when the ramp/platform was subaerially exposed. Different chemical processes led to karsting, including dissolution, remobilization, and precipitation of calcium carbonate (Moore and Wade, 2013). Karstification in the Hunton can increase the local permeability. Vugs and enlarged fractures filled with calcite may occlude the porosity as a result of diagenesis (Rechlin, 2005). Three types of karstification features are common in the Hunton Group, i.e., mosaic, collapse, and crackle breccias (Matthews, 1992). Stylolites are observed in the Hunton core, which provides evidence of pressure solution due to compaction.

Data collection (study areas)

Figure 2.2 shows the locations of the outcrops and core. The core data was collected from a 4-in diameter butt and a slab core from the Robertson A#1 Well in Pottawatomie County (Sec.6, T 9N, R 3E) (**Figure 2.2B**). To compare the core data, two outcrops (mentioned earlier) with gentle slopes of less than 10 degrees comprising the Chimneyhill Subgroup of the Hunton Group carbonates were studied (**Figures 2.2B and 2.2C**). The first outcrop is located in the Fittstown City on OK-99 road cut (34.565669, -96.634459). The second outcrop is located in Ada City (34.701979, -96.701826). Both outcrops are located in Pontotoc County and are separated by 13.5 miles (**Figure 2.2B**). I studied the fracture orientations, aperture, spacing, and intensity for the major fracture set at each outcrop.

Ada and Fittstown outcrops are located in the Lawrence Uplift to the east of the Arbuckle Mountains and west of the Arkoma Basin (**Figure 2.2C**). They are bounded by two faults, to the north by the Ahloso Fault and to the south by the Stonewall Fault.

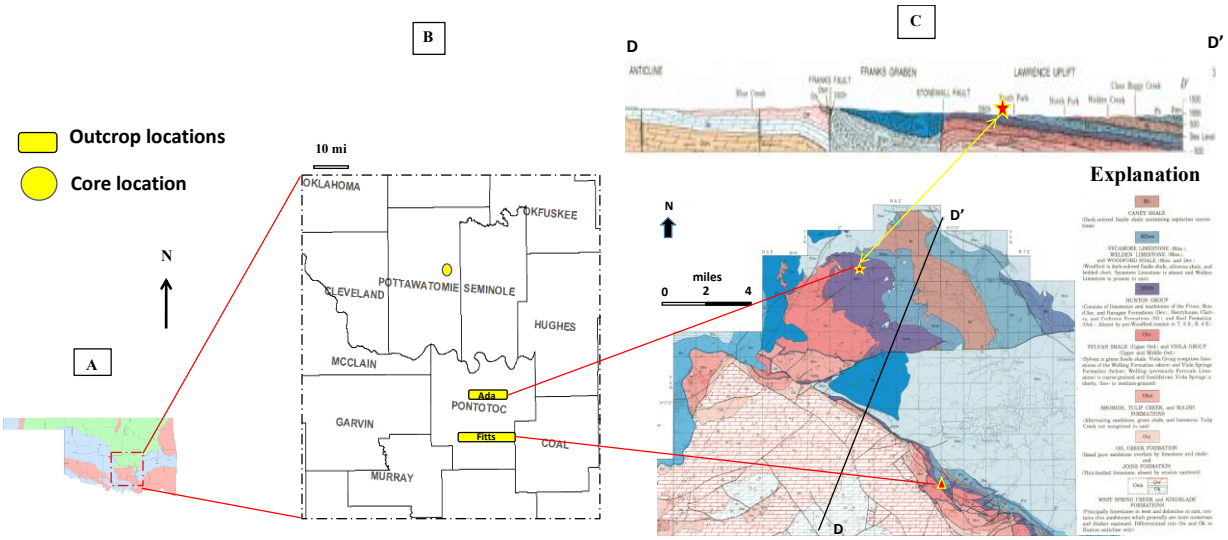

Figure 2.2. Locations of studied areas. A) Regional map of Oklahoma. B) The location of the core is the circled area. The upper rectangle shape in Pontotoc County is the Ada outcrop, and the lower one is the Fittstown outcrop. C) The structural cross section of the Arbuckle Mountains in Oklahoma showing the locations of the Fittstown and Ada outcrops (modified from Ham and McKinley, 1954). Fittstown outcrop (triangle shape) is located in a faulted area while the Ada outcrop (star shape) is located on the flank of a monocline.

Methodology

Core facies

Facies were classified based on gamma ray measurements, visual descriptions using a hand lens, and petrographic analysis of 24 thin sections throughout the cored stratigraphic section. Thin sections were stained using Alizarin Red-S to distinguish calcite and potassium ferricyanide stain from ferroan and nonferroan varieties of calcite and dolomite. Also, thin sections were impregnated with color-dyed epoxy to easily recognize the porosity under the microscope. The core facies were classified based on the abundance of fossils, structures, bioturbation percentage, fracture intensity, and lamination intensity. Thin sections were examined under a microscope using plane-polarized light, cross-polarized light, and reflected light to identify the minerals, allochems, fractures, porosity, and diagenesis effect.

Core fractures

The first step was to identify types of fractures/joints and stylolites present at both micro- (under a microscope) and macro-scales. The core was not oriented; therefore, it was pointless to measure the fracture strikes but possibly to measure the dips if core was vertical. The upper 15 ft. of the Hunton core is brecciated due to karstification and is broken into several parts. Therefore, fracture abundance using a scan line could not be measured. However, the fracture intensity was measured using the area method (described below) on a planar face every 6 inches (on average) along the core length.

We quantified the core fracture data manually at the core site and using Image J^{TM} software. More than 200 fractures were counted and apertures measured. High-resolution photographs of the core in the top view perpendicular to the core face were taken. The core pictures resolution was enhanced by changing the color saturation. Then, photographs were imported into Image J^{TM} software, scales were noted, and specific areas were selected to conduct thresholding using Image J^{TM} software. Subsequently, the number of fracture traces and their dimensions were obtained using the software. The fracture aperture and fracture traces lengths were quantified. The fracture intensities were calculated per unit area (Fracture intensity = [total visible fracture length in the core]/area of core face).

The only shortcoming of using the Image J^{TM} software is that the fracture aperture measurements were exaggerated compared to the manual fracture aperture measurements using a comparator and a hand lens. Therefore, an empirical relationship based on best curve fitting was developed to be used for correcting the fracture aperture measured from the software. Manually measured fracture apertures were plotted against the digitized fracture apertures from Image J^{TM} software for comparison. The equation is: Core aperture =0.0217*(digitized aperture) $^{\wedge 0.4273}$

Core porosity, permeability, and hardness

The porosity and permeability measurements of the 12 core samples were performed. A rebound hammer^{TM} was used to measure the core hardness for the entire Roberston# A1 core. The Leeb hardness (LH) value is the ratio of rebound velocity (Vr) to the impact velocity (Vi) (Leeb, 1979). A piece of the core was selected and fixed on a bench press to prevent the movement of the core. The test was conducted on a flat core surface. At least, five continuous impacts were shot on a set location on the sample to obtain a repeatable rebound value (Poole and Farmer, 1980). The average value of the five impacts at each point was used as the representative hardness for those points.

Outcrop Fracture intensity

The scanline method was used for the outcrop studies to measure fracture intensity, aperture, and spacing. (e.g., Marrett, 1996; Marrett et al., 1999; Micarelli et al., 2006; Ortega et al., 2006; Ghosh et al., 2018). **Figure 2.3** shows an example of fracture length, height, and spacing. Measurements were made along 1D scanlines oriented at high angles to fracture strikes (plan view) for each fracture set (e.g., **Figures 2.4A** and **2.4C**). Measurements include fracture aperture, spacing, and intensity in bed-perpendicular fractures for each visible fracture set. Measuring the fracture length and height are problematic in truncated outcrops (Micarelli et al., 2006; Ortega et al., 2006, Ghosh, 2017) and therefore not reported. **Figures 2.4A** and **2.4B** show the truncated fracture heights and lengths. Fracture apertures were measured using a comparator and hand lens (e.g., Ortega et al., 2006). Fracture spacing was measured using a tape oriented perpendicular to fracture strikes (**Figure 2.3 and 2.4C**). Fracture spacings were measured in both cross-section and top (plan) views. I measured the bed and fracture orientations at the two outcrops. Rose diagrams

of bed and fracture strike and dip were generated using Techlog™ software for individual fracture sets in the outcrop (shown in the result section).

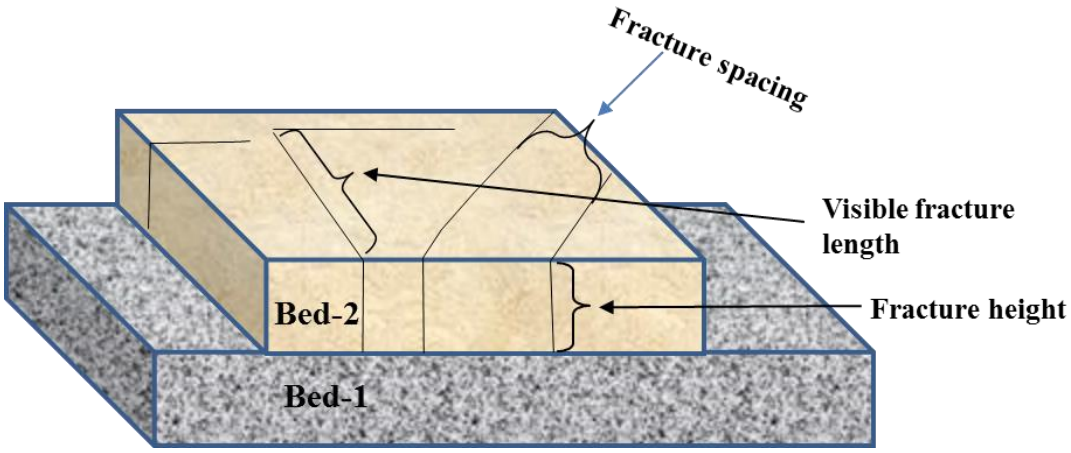

Figure 2.3. Three-dimensional cartoon showing the fracture spacing, length, and height.

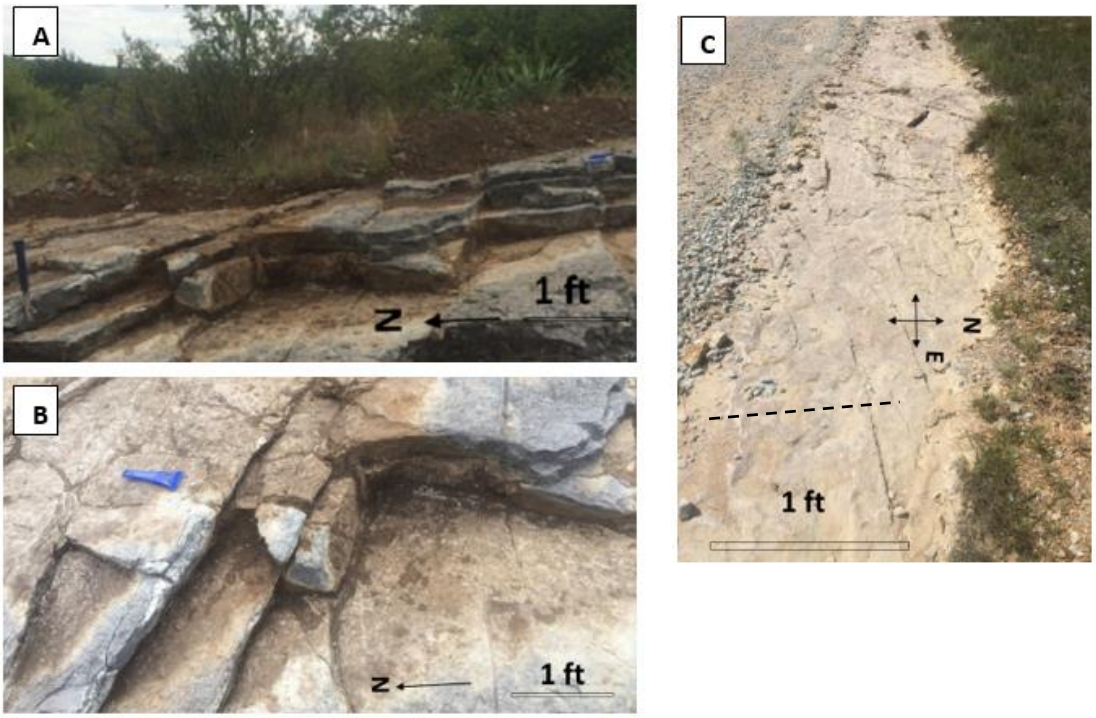

Figure 2.4. Outcrop samples. A) A sample of the Fittstown outcrop showing the truncated fracture height traces (scanline shown in dashed line). B, C) Top surface photograph of the Ada outcrop next to a paved road. Dashed line in C is an example of a scanline for fracture spacing and aperture measurements.

Fracture-size distributions

Cumulative-fracture frequency plots were used to characterize the fracture-size distribution (e.g., Marrett, 1996; Ortega et al., 2006; Hooker et al. 2013). Cumulative frequencies of aperture or spacing in the y-axes (i.e., number of apertures or spacing per scanline length) with the aperture or spacing in x-axes were plotted on a log-log scale. The size-distribution types, such as normal, lognormal, exponential, or power law were fitted to the data. The best fit was judged by comparing the best curve fitting distribution type and the lowest χ_2-error curve fit value (Hooker et al., 2012; Hooker et al., 2013).

Results

Core descriptions

Robertson A#1 core mainly consists of five lithologies: dolomitized wackestone, wackestone, crystalline carbonate, packstone in the lower section of the Chimneyhill Subgroup of the Hunton Group, and siliceous black Woodford Shale (**Figure 2.5**). The lower 15 ft of the Hunton core is not karstified. The lower stratigraphic section of the core started with more bioturbation and fewer laminations. Stratigraphically higher sections of the core have gradually less bioturbation and more laminations. This section is composed of traces of pyrite, crinoids, vertical and horizontal burrows, and wavy laminations (**Figure 2.5**). The middle section (18 ft) of the core is extensively brecciated, so it was difficult to distinguish between bioturbation and laminations due to karstification effects (**Figure 2.5**). Stylolites are predominant and visible in the lower 3 ft of this karstified section and in thin sections. Many of the styolites are filled with dark organic matter and/or clay (**Figure 2.5**). The overlying 12 ft of this section is highly karsted and brecciated, creating many horizontal and vertical fractures, followed by the Hunton-Woodford contact. The contact consists of two inches of fine calcareous crystalline carbonate, an erosional unconformity

surface between the Hunton Group and the overlying Woodford Shale, and 3 inches of mixed siltstone and 2 inches of sandstone and siltstone. The upper section (15 ft) of the core is siliceous Woodford Shale and has high organic matter with pyrite (**Figure 2.6**).

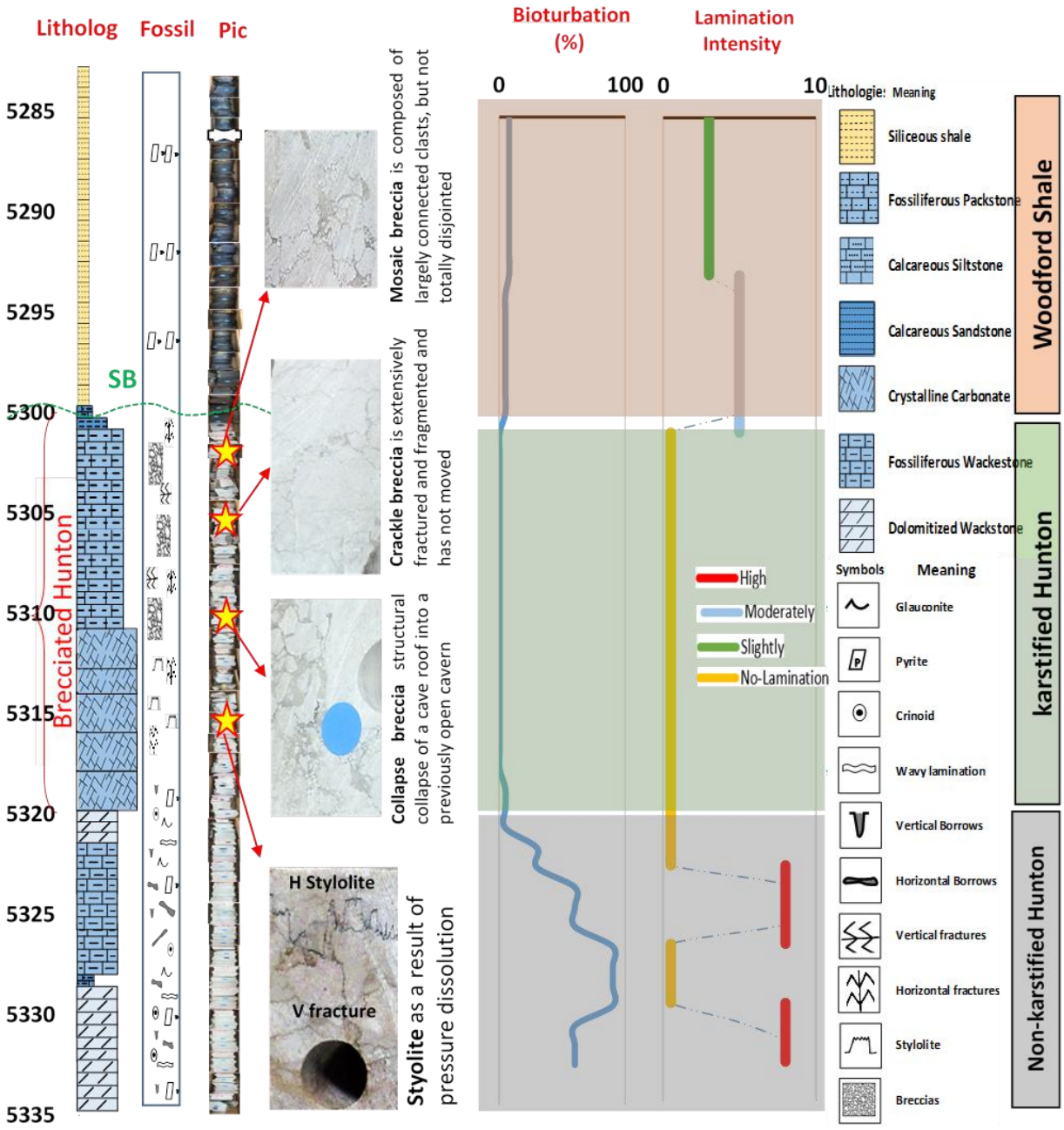

Figure 2.5. Robertson A#1 cored well showing profiles of lithology, fossils and structure, core photograph, karst features, interpreted bioturbation percentage, and the lamination intensity present in the core. Symbols of lithologies, structures, and fossils are presented to the left column with different code features. This core consists of five lithologies which comprise the Chimneyhill Subgroup, the Hunton-Woodford contact, and part of the Woodford Shale. From bottom to the top: dolomitized wackstone (5335-5328 ft), wackstone (5328-5320 ft), crystalline carbonate (5310-5320 ft), packstone (5300-5310 ft) and the Woodford Shale (5285-5300 ft). The lower 15 ft of the Hunton core throughout this stratigraphic section is not karstified.

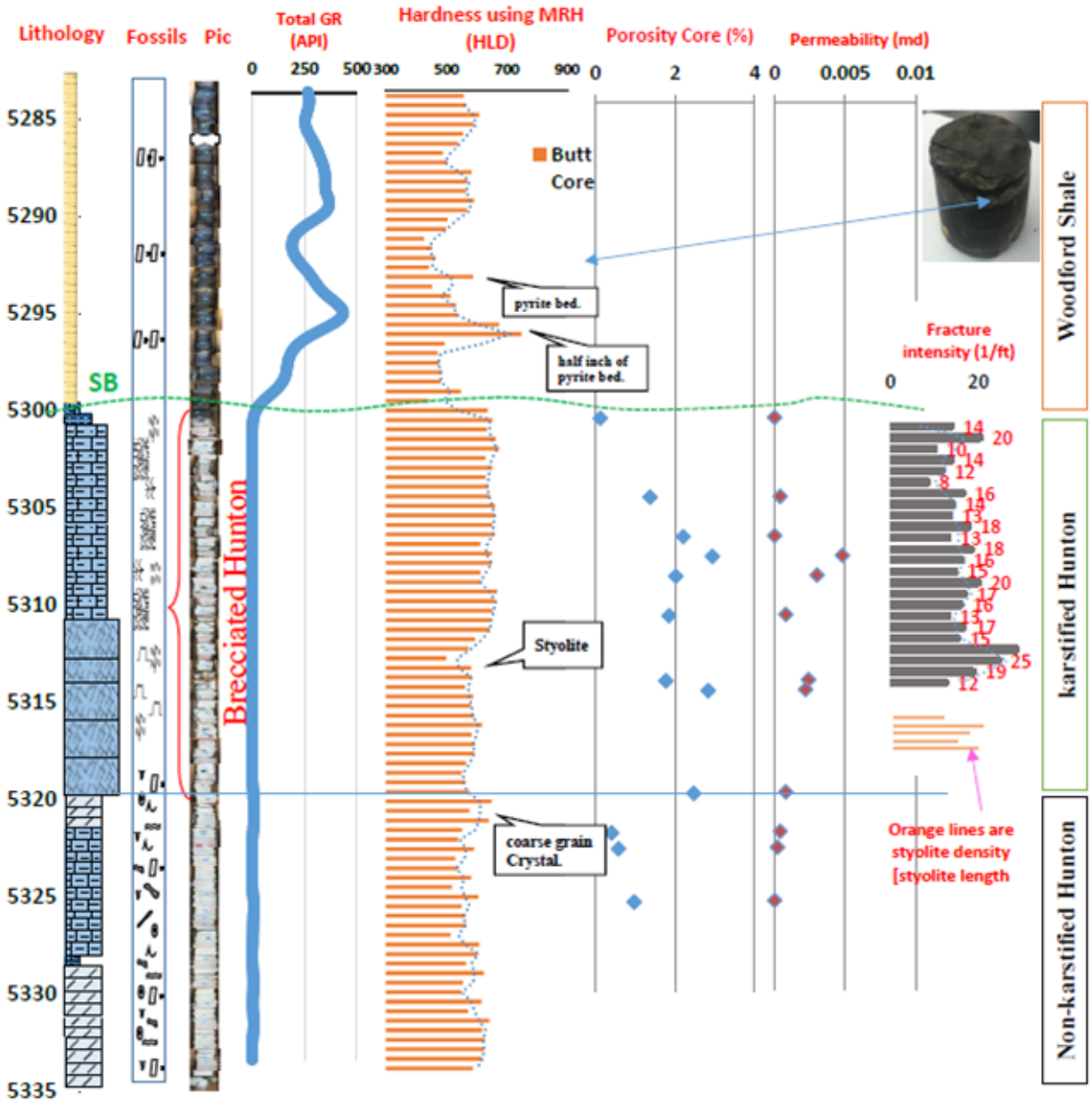

Figure 2.6. Core analysis for Robertson A#1 well including lithology profile, fossil distribution, core photograph, core gamma ray, core hardness measurements, core porosity, core permeability, natural fracture intensities. This core is divided into three sections, non-karstified Hunton, karstified Hunton, and Woodford Shale. Fractures occur only in the brecciated zones. The fractured zone records the highest hardness measurements (brittle rock). The brecciated section has enhanced porosity and permeability. In the Woodford section, there is a consistent positive relation between GR and hardness measurements which is unusual and probably due to pyrite presence at the high GR intervals (Milad and Slatt, 2017).

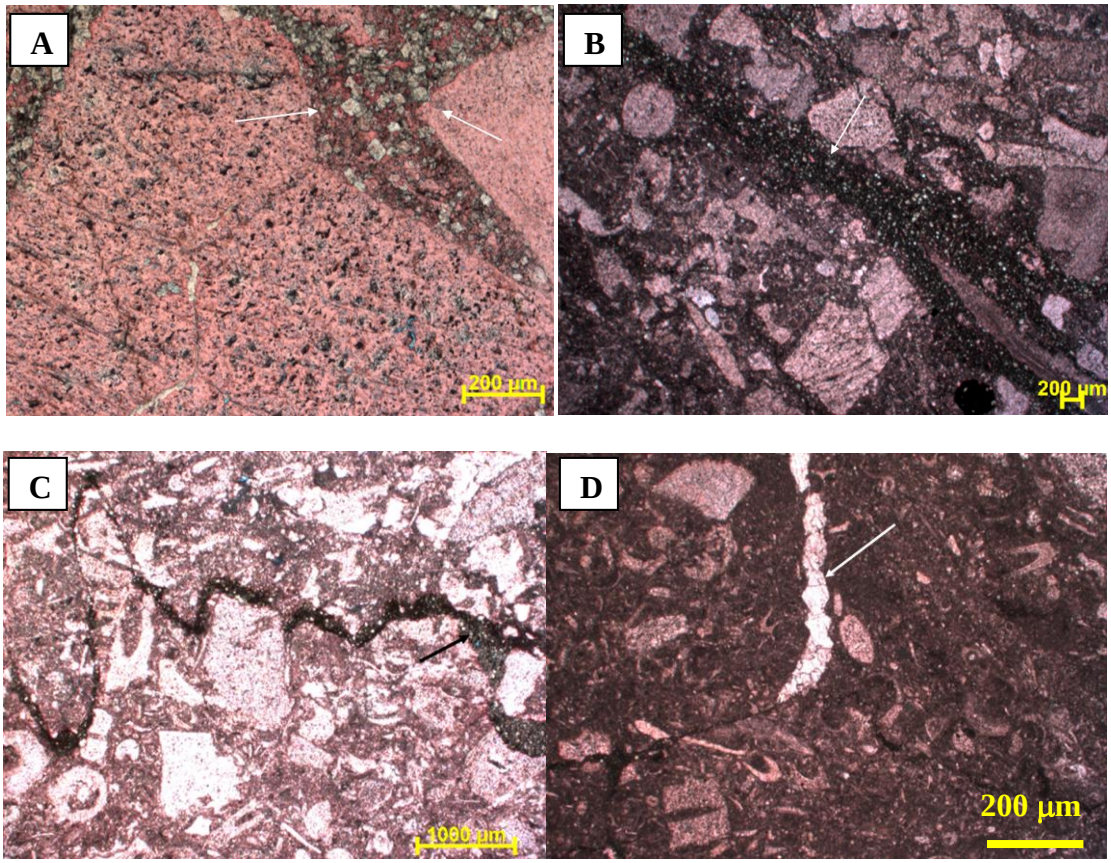

Figure 2.7. Thin sections acquired from Robertson A#1 cored well of the Chimneyhill Subgroup of Hunton Group. The labels from A to D are in the chronological order of the core stratigraphic section from deep (Figure A at depth 5330 ft) to shallow (Figure D at depth 5303.4 ft). A) Plane-polarized light thin-section showing calcite in pink color and dolomite rhombs in golden gray (5330 ft). B) Burrows filled with mud and exposed to dolomitization (5325.5 ft). C) Plane-polarized light sample showing dolomite mineral precipitated over a stylolite which is filled with organic matter (5305 ft). D) Closed vertical fracture filled with calcite. Fossil offset along a stylolite is indicated by the lower arrow (5303.4 ft).

Core fractures

Fractures exist only in the brecciated section of the Hunton core due to karstification (**Figure 2.6**). The majority of the fractures are filled with calcite cement, organic material clay minerals, or dolomite (**Figures 2.7A to D**).

The fracture aperture was measured only on sealed fractures. They range from 0.05 to 0.33 mm. A high abundance of fractures has apertures ranging from 0.1 to 0.15 mm (**Figure 2.8**). The fracture intensity ranges from 8 to 30 fractures/ft (26.2 to 98.4 fractures/m) taken every 6 inches

(on average) along the core length.

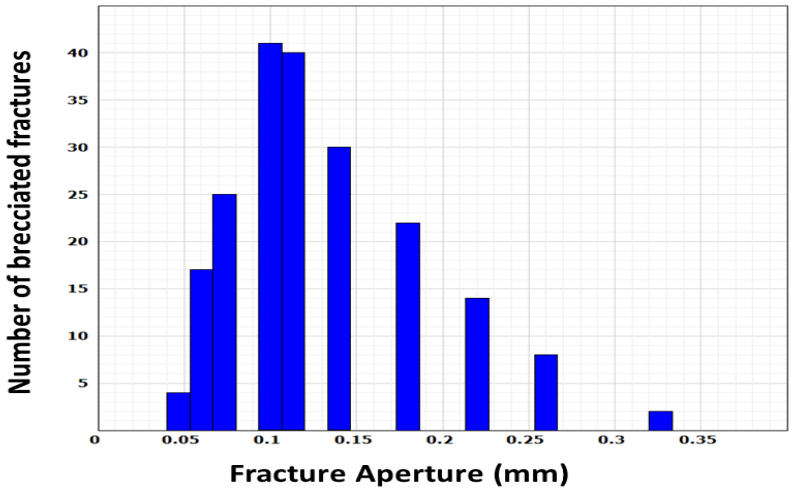

Figure 2.8. Histogram of fractures' aperture-size distributions and their abundance in the Chimneyhill core. Kinematic apertures are narrow, ranging from 0.05 to 0.33 mm. Peaks in the histogram range between 0.1 and 0.15 mm. Fractures are from the brecciated zone.

Porosity, permeability, and hardness from core

Porosity and permeability measurements showed porosity ranging from 0.13 % to 2.94% and permeability ranging between 0 and 0.0048 md in the karstified interval (**Figure 2.7**). The lowest hardness values range from 100 to 150 HLD (HLD: Hardness Leeb Device), in the Woodford Shale. The pyrite-rich beds in the Woodford Shale record high hardness measurements (800 HLD) (**Figure 2.6**) (depth 5300 ft). In the Hunton Group, the highest hardness (~700 HLD on average) occurs in the karstified section of the Chimenyhill Subgroup core. In the lower 12 ft of the unbrecciated Hunton, hardness values recorded were in the 200 to 350 HLD range. The higher hardness measurements correspond to areas with higher fracture abundance (karsted zone).

Outcrops fracture orientations

In the Fittstown outcrop, three sets of steeply dipping fractures (>80 degrees), striking north-south (N-S), east-west (E-W) and northwest-southeast (NW-SE), were documented (**Figure 2.9A**) from 16 measurements in the outcrop site. In the Ada outcrop, four fracture sets were

apparent; three of them have similar orientations as in the Fittstown outcrop with an extra steeply dipping fracture set striking northeast-southwest (NE-SW) (**Figure 2.9C**). In the Ada outcrop, the NE-SW fracture set is the most predominant set followed by the NW-SE set. The east-west fracture set is predominant in the Fittstown outcrop followed by a N-S set. All of the four sets of fractures dip more than 80 degrees, and the beds strike 285 degrees with gentle dips of less than 10 degrees (**Figure 2.9B**) in both outcrop locations.

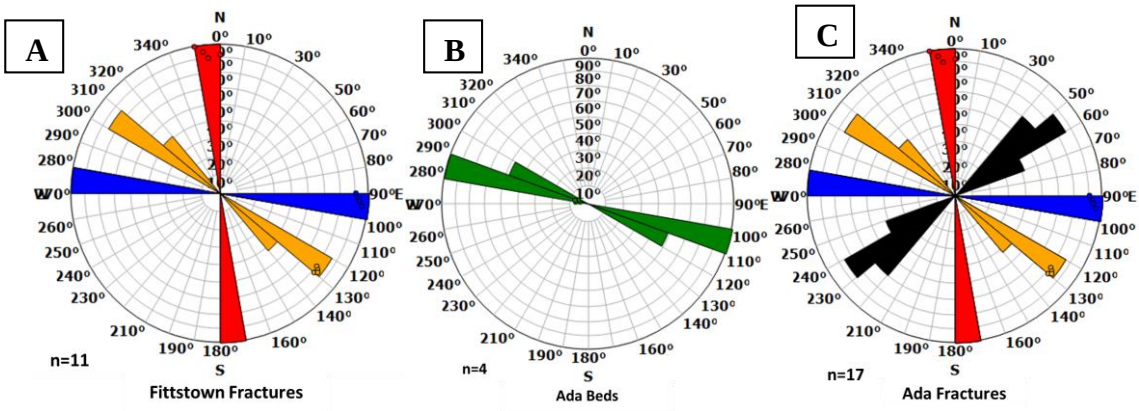

Figure 2.9. Outcrop and bed orientations. A) Rose diagram showing three sets of fractures at the Fittstown outcrop. B) Bed orientations at the Ada outcrop. C) Orientations of four fracture sets at the Ada outcrop. Color codes correspond to fracture sets. Blue color corresponds to the E-W set, red color corresponds to N-S set, orange color corresponds to NW-SE set, black color corresponds to NE-SW set, and green color corresponds to bed orientation.

Fracture-size distributions (histograms)

Fractures studied from the outcrops have different ranges of kinematic aperture and spacing for each fracture set (**Figure 2.10**). **Figures 2.10A** and **2.10B** show histograms of aperture and spacing. The apertures range from 0.11 to 2.3 mm with an average of 0.265 and standard deviation of 0.213 including all sets. Spacing ranges from 0.04 to 2.5 m with an average of 0.43 m and standard deviation of 0.41 m including all sets.

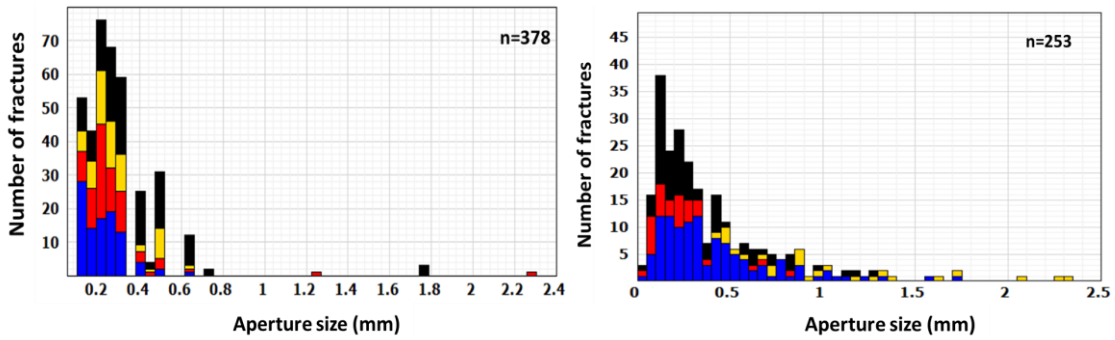

Figure 2.10. Histograms of fractures aperture-size distributions in the two studied outcrops. The legend is color coded by a fracture set orientation as is shown in rose diagrams (Figures 9A, 9B, and 9C). A) Histogram of kinematic aperture and relative fracture abundance for the four fracture orientations. B) Number of fractures vs. fracture spacing. The orange set has higher spacing compared to the other sets.

Fracture-size distributions (cumulative-frequency plots)

Figure 2.11 shows log-log plots of the cumulative frequency distribution of macrofracture dataset from two outcrops of each fracture set. Most aperture (**Figures 2.11A-2.11D**) and spacing (**Figures 2.11E-2.11H**) distributions fit the exponential and lognormal (both characteristic) distribution. Only one aperture dataset (N-S) shows a power law (**Figure 2.11B**) best fit.

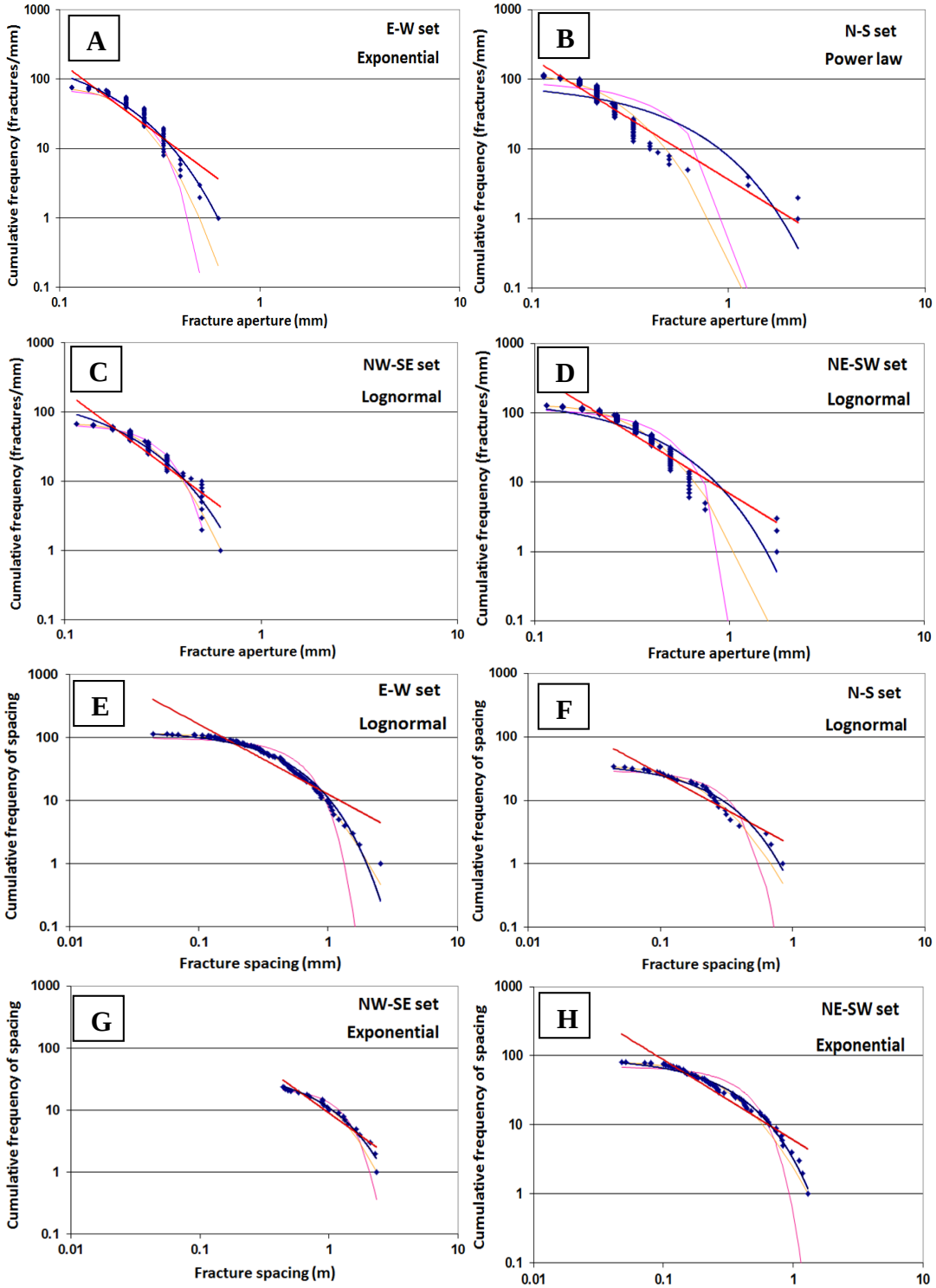

Figure 2.11. Log-log cumulative fracture-size distributions for four fracture sets for two Chimneyhill Group outcrops in Fittstown and Ada, with the best curve fitting distribution type for four fracture sets (Set 1 to Set 4). Figures A to D are the best fits for fracture aperture data for all fracture sets (Set 1 to Set 4). Plots E to H are the best fits for fracture spacing data.

Discussion

Core porosity and permeability

The karst in the Hunton Group developed during the Silurian-Devonian Period (Johnson et al., 2000) and indicates when the Hunton Group was subaerially exposed. These karsted fractures may play a major role in the hydrocarbon productivity similar to the karst-related fracturing in the Lisburne field, Alaska, as the permeability increases due to the fractures (Missman and Jameson, 1991; Jameson, 1994) and in the Barnett shale, in which fractures are water filled. The measured porosity and permeability results support the fact that the matrix porosity and permeability increase in the brecciated areas. In the core, the porosity increases from a minimum of 0.5 to maximum of 3 %, and permeability increases from a minimum of 0.0004 to maximum of 0.005 md from the non-karsted (non-brecciated) to the karsted (brecciated) areas in the lower Roberston# A1 core (**Figure 2.5**), respectively. Similar observations regarding porosity and permeability increase due to karstification were made earlier (Rechlin, 2005) in the Hunton Group (Esteban, 1991; Wright, 1991; Loucks, 1999).

Outcrop fractures

Several studies showed that the local structural position can affect the fracture orientations such as proximity to a fold and faulted area (Hanks et al., 1997; Nelson, 2001; Watkins et al., 2015). The structural cross section (**Figure 2.2C**) shows that the Fittstown outcrop is in a faulted area, while the Ada outcrop is located on the flank of a monocline (Ham and McKinley, 1954). The fault, anticline axis, and bed strike in the Ada and Fittstwon outcrop are similar, i.e., NW-SE (300-320^{o} azimuth). The fracture sets present in the two outcrops are similar. Three fracture sets, i.e., N-S, E-W, and NW-SE in the Fittstown outcrop, and one extra NE-SW set in the Ada outcrop were observed. The NW-SE striking fractures (also similar to the local fault strikes (N60^{o}W) bisect

the N-S and the E-W striking fractures in both outcrops. The NW-SE Set, striking parallel to the fold strike may be fold related. The fold-oblique sets striking N-S and E-W and may be related to folding as well. Similar fracture patterns (two oblique sets and a bisector) have been reported in the Teton Anticline carbonate rocks in Montana (Ghosh and Mitra, 2009).

On the other hand, the exact orientation of the N-S and E-W fracture sets at both the outcrops, and their obliqueness to the fold orientation indicates that they might not be related to the structural deformation related to the folding and faulting but might originate at a different time under the influence of overpressure. Tan et al. (2014) and Ghosh (2017) mentioned that joints could form without significant structural bending with the main cause being fluid overpressure. The NE-SW set (Ada outcrop) may be related to the local deformation near the Ada outcrop area or may be present at the Fittstown outcrop but were not visible on the exposed beds. Consistent crosscutting relations between the fracture sets were not observed at any of the outcrops.

Core to outcrop comparison

The origin of the observed fractures in the core and outcrop are different. The fractures in the core are caused by the paleocave collapse and brecciation, which are common in carbonate environments (e.g., Moore and Wade, 2013). However, as mentioned earlier, the fractures in the Fittstown and Ada outcrops may be fold or fluid overpressure related. In the core, the brecciated zone has significantly high fracture intensity ranging from 8 to 29 fractures/ft (average: 14.7 fractures/ft), compared to the outcrop fracture intensity of 0.3-8 fractures/ft (average: 2.1 fractures/ft) (**Figures 2.12A and 2.12B**). Also, the fracture apertures in the core range from 0.05 to 0.33 mm (**Figure 2.8**) and apertures from outcrops range from 0.11 to 2.3 mm (**Figure 2.10A**). These results indicate that the karstification process may lead to narrower apertures and higher intensities compared to the outcrops where the fractures originated under consistent stress fields

over longer duration.

These results can aid in predicting certain attributes of subsurface fractures. If the karstification features can be predicted from seismic mapping, a lower average aperture, and a higher average permeability might be expected. The permeability is most likely isotropic due to random fracture orientations related to karsting. On the other hand, in the absence of karstification and presence of natural fractures, higher permeability anisotropy might be expected.

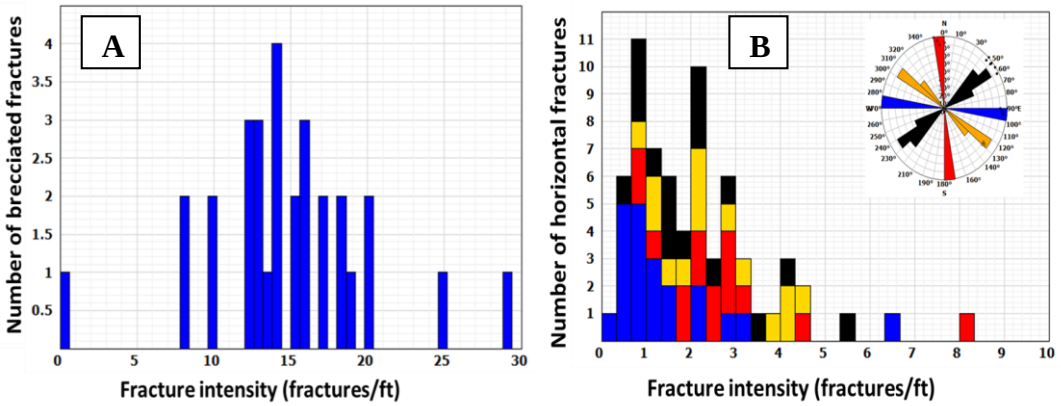

Figure 2.12. Comparison between core and outcrop fracture intensity. Y-axis is the number of fractures, and x-axis shows the fracture intensity. A) Fracture intensity from the Fittstown and Ada outcrops range from 0 to 8 fractures per unit length with an average of 2.1 fractures/ft (6.9 fractures/m) and standard deviation of 2.2. B) Fracture intensity from the core ranges from 8-29 fractures per ft. with an average of 14.7 fractures/ft (48.2 fractures/m) and standard deviation of 5.3, indicating a much higher core fracture intensity compared to the outcrop.

Fracture size and spacing from outcrops

The aperture sizes from the outcrops mainly follow the exponential and lognormal characteristic distributions, possibly due to height growth constraints offered by layering. The characteristic fracture spacing or regularity in spacing indicates fracture growth under consistent stress shadows. The outcrop size and spacing statistical size analysis can be used to build a realistic discrete fracture model (for hydraulic fracturing or reservoir simulation) given the fracture heights and lengths can be accurately constrained.

Conclusions

Understanding natural fracture distributions, networks, and their orientations are vital because natural fractures are recognized as one of the important factors in successful exploration and development of hydrocarbon reservoirs. Following are the conclusions from this study:

1) Core fractures are related to the karstification processes, while the fractures in the outcrops are related to structural deformation and, possible overpressure. Compared to the outcrops, the fracture intensities are higher, and apertures are lower in the core. The karstification process may have enhanced the porosity and permeability in the studied core, and related cementation could have provided extra hardness.

2) Four fracture sets are observed in the flank of the monoclional structure. Two primary sets are parallel (NW-SE) and perpendicular (NE-SW) to the axis of the fold. The two other sets, i.e., E-W and N-S sets, are oblique to the fold direction. These four fracture sets could have originated either due to structural folding or due to abnormally high fluid pressure.

3) Mostly characteristic (exponential or lognormal) kinematic aperture size and spacing distributions were observed indicating the influence of bedding on sizes of the fractures and their stress shadows.

4) All fracture data obtained in this study are used to build a realistic discrete fracture network model in the subsequent chapters.

Acknowledgments

We thank the Woodford Consortium at the University of Oklahoma for research funding. We would also like to thank Herman Burrough for helping us find good spots for measuring fracture attributes. Also, we would like to thank Dr. Tom Rowland for various technical help. Thanks to

Dr. John Hooker for providing the methodology for calculating the cumulative-frequency distribution.

References

Al-Shaieb, Z., G. Beardall, P. Medlock, K. Lippert, F. Matthews, and F. Manni, 1993, Overview of Hunton facies and reservoirs in the Anadarko Basin: Hunton Group core workshop and field trip: Oklahoma Geological Survey Special Publication, p. 93-4.

Al-Shaieb, Z., and J. Puckette, 2000, Sequence stratigraphy of Hunton Group ramp facies, Arbuckle Mountains and Anadarko Basin, Oklahoma: Platform Carbonates in the southern Midcontinent. 1996 symposium, Oklahoma Geological Survey Circular, p. 131-137.

Al-Shaieb, Z., J. Puckette, and A. Close, 2002, Seal characterization and fluid-inclusion stratigraphy of the Anadarko basin: Revisiting old and assessing new petroleum plays in the southern Midcontinent, Oklahoma Geological Survey Circular, v. 107, p. 153-161.

Amsden, T.W., 1975, Hunton Group, Late Ordovician, Silurian, and Early Devonian in the Anadarko Basin of Oklahoma, v. 121, Oklahoma Geological Survey, University of Oklahoma.

Antonellini, M., and P.N. Mollema, 2000, A natural analog for a fractured and faulted reservoir in dolomite: Triassic Sella Group, northern Italy: AAPG bulletin, v. 84, p. 314-344.

Brito, R., R.M. Slatt, H. Galvis, D. Becerra, S. Ghosh, 2017, Importance of Outcrop Characterization of Unconventional Shale Resources. AAPG Search and Discovery.

Barbier, M., Y. Hamon, J.P. Callot, M. Floquet, and J.M. Daniel, 2012, Sedimentary and diagenetic controls on the multiscale fracturing pattern of a carbonate reservoir: The Madison Formation (Sheep Mountain, Wyoming, USA): Marine and Petroleum Geology, v. 29, p. 50-67.

Bratton, T., D.V. Canh, N. Van Que, N.V. Duc, P. Gillespie, D. Hunt, B. Li, R. Marcinew, S. Ray, and B. Montaron, 2006, The nature of naturally fractured reservoirs: Oilfield Review, v. 18, p. 4-23.

Esteban, M., 1991, Palaeokarst: practical applications: Palaeokarsts and Palaeokarstic Reservoirs, v. 152, p. 89-119.

Friedman, G.M., 1995, Unconformities and porosity development in carbonate strata: Ideas from a Hedberg conference: Discussion: AAPG Bulletin, v. 79, p. 1183-1184.

Fritz, R.D., and P.L. Medlock, 1994, Sequence stratigraphy of the Hunton Group as defined by core, outcrop, and log data: Bulletin Houston Geological Society, p. 29-58.

Garfield, T.R., N.F. Hurley, and D.A. Budd, 1992, Little Sand Draw Field, Big Horn Basin, Wyoming: A Hybrid Dual-Porosity and Single-Porosity Reservoir in the Phosphoria Formation (1): AAPG Bulletin, v. 76, p. 371-391.

Gaswirth, S.B., and D.K. Higley, 2013, Petroleum system analysis of the Hunton Group in West Edmond field, Oklahoma: AAPG bulletin, v. 97, p. 1163-1179.

Gaswirth, S.B., and D.K. Higley, 2014, Petroleum systems and assessment of undiscovered oil and gas in the Anadarko Basin Province, Colorado, Kansas, Oklahoma, and Texas: USGS Province 58, US Geological Survey.

Ghosh, S.G., 2017, Integrated studies on Woodford Shale natural fracture attributes, origin, and their relation to hydraulic fracturing. Ph.D. Dissertation, University of Oklahoma, Norman, OK. https://doi.org/10.13140/rg.2.2.15739.82722

Ghosh, S.G., J.N. Hooker, C.P. Bontempi, and R.M. Slatt, 2018, High-resolution stratigraphic characterization of natural fracture attributes in the Woodford Shale, Arbuckle Wilderness and US-77D Outcrops, Murray County, Oklahoma.

Ghosh, K., and S. Mitra, 2009, Structural controls of fracture orientations, intensity, and connectivity, Teton anticline, Sawtooth Range, Montana: AAPG bulletin, v. 93, p. 995-1014.

Ham, W.E., and M.E. McKinley, 1954, Geologic map and sections of the Arbuckle Mountains, Oklahoma: Oklahoma Geological Survey Map A-2, p. scale 1:72,00.

Hanks, C.L., J. Lorenz, L. Teufel, and A. P. Krumhardt, 1997, Lithologic and structural controls on natural fracture distribution and behavior within the Lisburne Group, northeastern Brooks Range and North Slope subsurface, Alaska: AAPG bulletin, v. 81, p. 1700-1720.

Hooker, J.N., L.A. Gomez, S.E. Laubach, J.F.W. Gale, and R. Marrett, 2012, Effects of diagenesis (cement precipitation) during fracture opening on fracture aperture-size scaling in carbonate rocks: Geological Society, London, Special Publications, v. 370, p. 187-206.

Hooker, J.N., S.E. Laubach, and R. Marrett, 2013, Fracture-aperture size—frequency, spatial distribution, and growth processes in strata-bounded and non-strata-bounded fractures, Cambrian Mesón Group, NW Argentina: Journal of Structural Geology, v. 54, p. 54-71.

Jameson, J., 1994, Models of porosity formation and their impact on reservoir description, Lisburne field, Prudhoe Bay, Alaska: AAPG Bulletin, v. 78, no. 11, p. 1651-1678

Kim, Y.S., D.C. Peacock, and D.J. Sanderson, 2004, Fault damage zones: Journal of structural geology, v. 26, p. 503-517.

Leeb, D., 1979, Dynamic hardness testing of metallic materials: NDT International, **12**, 274–278, doi: 10.1016/ 0308-9126(79)90087-7.

Loucks, R.G., 1999, Paleocave carbonate reservoirs: origins, burial-depth modifications, spatial complexity, and reservoir implications: AAPG bulletin, v. 83, p. 1795-1834.

Luo, P., and H.G. Machel, 1995, Pore size and pore throat types in a heterogeneous dolostone reservoir, Devonian Grosmont Formation, Western Canada sedimentary basin: AAPG bulletin, v. 79, p. 1698-1719.

Machel, H.G., M.L. Borrero, E. Dembicki, H. Huebscher, L. Ping, and Y. Zhao, 2012, The Grosmont: a complex dolomitized, fractured and karstified heavy oil reservoir in a Devonian carbonate-evaporite platform: GeoConvention-2012: Vision.

Marrett, R., 1996, Aggregate properties of fracture populations: Journal of Structural Geology, v. 18, p. 169-178.

Marrett, R., O.J. Ortega, and C.M. Kelsey, 1999, Extent of power-law scaling for natural fractures in rock: Geology, v. 27, p. 799-802.

Matthews, F.D., 1992, Paleokarstic features and reservoir characteristics of the Hunton Group in the Anadarko basin: Oklahoma: Unpublished masters thesis, Oklahoma State University, Stillwater, OK.

Micarelli, L., I. Moretti, M. Jaubert, and H. Moulouel, 2006, Fracture analysis in the south-western Corinth rift (Greece) and implications on fault hydraulic behavior: Tectonophysics, v. 426, p. 31-59.

Milad, B., 2017, The Effect of Karsting on Natural Fracture, Hardness, and Brittleness of the Hunton Limestone and Paleo-Deposition of the Woodford Shale: A Study Using 3-D Seismic, Outcrop, Well Log, and Core Data. AAPG 2017 Southwest Section Annual Convention, Midland, Texas, Search and Discovery Article #51417. https://doi.org/10.13140/rg.2.2.25647.23205

Milad, B., and R.M. Slatt. 2017, Integrated 3-D Seismic, Outcrop, and Core Data for Characterization of Natural Fractures of the Hunton Limestone and the Woodford Shale in Central Oklahoma. AAPG 2017 Annual Convention and Exhibition, Houston, Texas, United States, Search and Discovery Article #51382. https://doi.org/10.13140/rg.2.2.24808.37121

Missman, R.A., and J. Jameson, 1991, An evolving description of a fractured carbonate reservoir: the Lisburne field, Prudhoe Bay, Alaska: International Arctic Technology Conference.

Moore, C.H., and W.J. Wade, 2013, Carbonate Reservoirs: Chapter 8. Meteoric Diagenetic Environment, v. 67, Elsevier Inc. Chapters.

Morgan, W.A., and R.E. Schneider, 1981, Subtle Porosity and Traps Within Frisco Formation (Devonian, Hunton Group): Geologic-Seismic Waveform Approach, Example from West El Reno Field, Canadian County, Oklahoma: Abstract: AAPG Bulletin, v. 65, p. 960-961.

Narr, W., 1991, Fracture density in the deep subsurface: techniques with application to point Arguello oil field (1): AAPG bulletin, v. 75, p. 1300-1323.

Nelson, R., 2001, Geologic analysis of naturally fractured reservoirs, Gulf Professional Publishing.

Northcutt, R.A., 2002, History of Hunton oil and gas exploration and development in Oklahoma: Shale Shaker.

Ortega, O. J., R.A. Marrett, and S. E. Laubach, 2006, A scale-independent approach to fracture intensity and average spacing measurement: AAPG bulletin, v. 90, p. 193-208.

Poole, R.W., and I.W. Farmer, 1980, Consistency and repeatability of Schmidt hammer rebound data during field testing: International Journal of Rock Mechanics and Mining Sciences & Geomechanics Abstracts, p. 167-171.

Rechlin, K.J., 2005, Reservoir Quality of the Frisco Formation, Hunton Group, Seminole County, Oklahoma,(Part 2, Conclusion): Shale Shaker, p. 15-24.

Smith, J., 1951, The Cretaceous Limestone Producing Areas of the Mara and Maracaibo District–Venezuela, Geology: 3rd World Petroleum Congress.

Stanley, T.M., and K. Rottmann, 2001, Stratigraphy and facies relationships of the Hunton Group, Northern Arbuckle Mountains and Lawrence Uplift, Oklahoma, v. 33, Oklahoma Geological Survey, University of Oklahoma.

Staples, E., K. Marfurt, and Z. Reches, 2010, Preliminary Analysis of the Fractured Hunton Limestone, Oklahoma.

Staples, E.R., 2011, Subsurface and Experimental Analyses of Fractures and Curvature, University of Oklahoma.

Thomas, E., 1986, Understanding fractured oil-reservoirs: Oil & Gas Journal, v. 84, p. 75-79.

Watkins, H., R.W. Butler, C.E. Bond, and D. Healy, 2015, Influence of structural position on fracture networks in the Torridon Group, Achnashellach fold and thrust belt, NW Scotland: Journal of Structural Geology, v. 74, p. 64-80.

Wright, V., 1991, Palaeokarst: types, recognition, controls and associations: Palaeokarsts and Palaeokarstic Reservoirs, Reading: PRIS Occassional Publication Series, v. 2, p. 56-88.

Chapter 3: Impact of lithofacies variations and structural changes on natural fracture distributions

Published as:

Milad, B., and R. Slatt, 2018, Impact of lithofacies variations and structural changes on natural fracture distributions: Interpretation, v. **6**, no. 4, p. T873–T887, doi:10.1190/INT-2017-0138.1.

Abstract

Understanding and predicting the impact of lithofacies changes and structural effects on fracture distributions is vitally important to optimize a drilling location and well trajectory. To evaluate and model fracture intensity of the Late Ordovician-Silurian-Early Devonian Hunton Group carbonates in Oklahoma, natural fractures were studied at different scales using borehole images, three outcrops (two horizontally bedded and one anticline), and seismic data. Natural fractures identified from eight horizontal well borehole images include conductive (open), partially open, mineralized (closed), and drilling induced fractures. Four fracture sets were identified from both borehole images and from the two horizontally bedded outcrops. A 3D fracture intensity model was populated from the fracture intensity borehole logs, and compared to a 3D lithofacies model. Principal component analysis (PCA) from lithology logs produced input to a self-organizing map (SOM) to classify and cluster electrofacies. Thin sections and borehole images corroborated the electrofacies around the wellbores, while 3D seismic data were used as constraints to build a 3D lithofacies model. A 3D lithofacies model resulted from the extrapolation of the lithofacies from the well scale to the regional seismic scale.

In this study area, lithofacies and structure are interrelated and control fracture distributions. Lithofacies is the primary control while structure is the secondary control. Three

lithofacies (wackestone, mudstone, and mud-dominated wackestone) were identified. A positive relationship between the fracture intensity and presence of wackestone was observed at both well locations and in the mapped subsurface area. The other two lithofacies do not exhibit high fracture abundance. Structural effects influence fracture distributions near faults and positive curvature areas in the subsurface measured on the 3D seismic data. Curvature measures how bent a curve is at a particular point on a 2D or 3D surface.

For the Hunton Anticline outcrop exposure, there was a positive linear relationship between fracture intensity and changes in curvature for the mudstone and mud-dominated wackestone, and an exponential relationship for the wackestone textures. The integration of lithology and structure from multidisciplinary, multi-scalar data, (i.e., outcrops, image logs, and 3D seismic) helps identify and predict the fractured zones in the Hunton carbonates and can be used for horizontal well planning as well as stimulation programs. More importantly, this study proposes a generic model to predict the variability of fractures at different scales of curvatures combined with lithology changes and can be used for other carbonate reservoirs.

Introduction

Understanding the key factors that control fracture distribution is vital for new drilling, hydraulic fracture treatments, and wellbore development stages to ultimately increase the hydrocarbon production of a reservoir (Meissner and Thomasson, 1999; Wennberg et al., 2006). Some studies have shown that spatial variations of fractures in carbonate reservoirs can be controlled by different processes, such as lithology changes (Hanks et al., 1997; Ericsson et al., 1998; Di Cuia et al., 2004; Wennberg et al., 2006; Sonntag et al., 2014), structural effects including fold geometry (Smith, 1951; Narr, 1991; Garfield et al., 1992; Ghosh and Mitra, 2009; Staples et al., 2010; Staples, 2011; Barbier et al., 2012; Watkins et al., 2015), and faulting (Smith, 1951,

Thomas, 1986; Hanks et al., 1997; Antonellini and Mollema, 2000; Kim et al., 2004). However, no previous study predicted the change of fracture intensity with respect to the change of both lithofacies and curvature and which one most influences the fracture changes. By investigating the relationship between the fracture distributions and the lithofacies and structural effects, we identified potential drilling sites in new areas with more fractures. To address this issue, surface and subsurface studies can improve the understanding and prediction of fracture distributions in areas that vary in lithofacies, curvature, or a combination of both lithofacies and curvature variation. Multi-scale data used in this study included eight borehole images, 28 well log suites, three outcrops, and a 3D seismic volume for the Hunton reservoir.

The purpose of this study was to: 1) develop a 3D fracture intensity model for successful exploration and future production of the Chimneyhill subgroup of the Hunton Group carbonate reservoir in the subsurface study area; and 2) predict the change of fracture intensity with changing curvature and lithology in the subsurface using the proposed generic model. The methodology of integrating lithology and structure from multidisciplinary, multi-scalar surface and subsurface data allowed us to propose a generalized schematic model (**Figure 3.1**) to predict the variability of fractures at different scales of curvatures combined with lithology changes of a carbonate reservoir, which ultimately can improve placing a horizontal well in areas with more fractures.

In this study, we begin with an overview of the geological setting, study areas, and the methodology. We analyzed the fractures and lithofacies using surface and subsurface data. From the surface data, we measured the fractures at different curvature scales from the two horizontally bedded outcrops (Ada and Fittstown outcrops), and from a deformed bedded exposure (Hunton Anticline) with curvature changes to test the variability of fractures for the lithofacies found in the subsurface. From the subsurface data, we examined the relationship between the structural effects

and the fracture distributions using most positive and negative curvatures seismic attributes. Afterwards, we determined and populated the lithofacies at well locations and in the seismic area, aiming to examine the relationship between the lithofacies type and fracture abundances. This paper concludes with results, discussion, and summary of findings of this study.

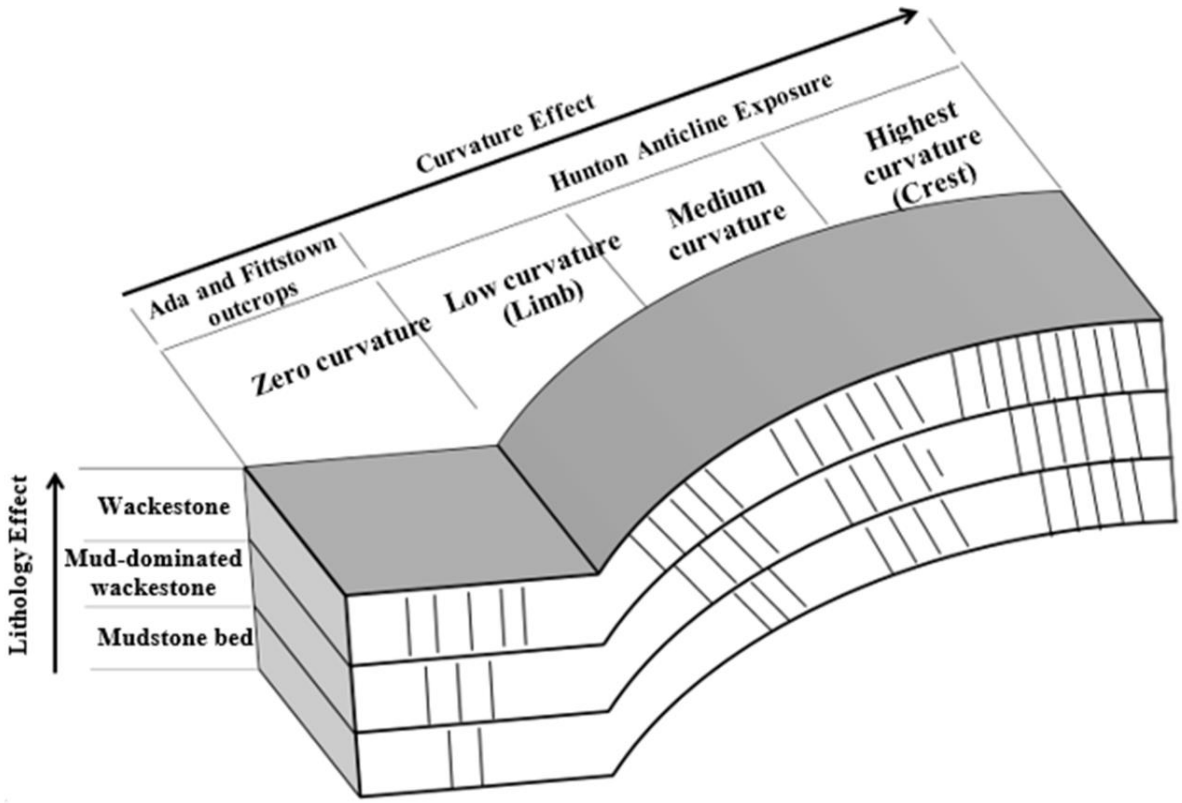

Fracture Intensity (No. of frac/ft^2)				
Lithofacies effect		Curvature effect		
		Low Curvature	Medium Curvature	High Curvature
	Wackestone	1.191	1.358	2.594
	Mud-dominated wackestone	0.791	0.95	1.337
	Mudstone	0.726	0.885	1.278

Figure 3.1. Schematic model showing the hypothesized fracture intensity in a carbonate formation as a function of curvature and lithology. The model was generated based on fracture analyses from three lithologies (mudstone, mud-dominated wackestone, and wackestone) at outcrops with different scales of curvatures as shown in the associated table. Bed thicknesses are considered the same because there is no effect of bed thickness on fracture intensity in the Hunton Group as seen in Woodford shale. The Ada and Fittstown outcrops are located in areas of zero to very low curvatures, and the Hunton Anticline is located in areas of low, medium, and very high curvatures. The black lines in the front view show the fracture distributions at each lithology at different curvature scales. The effect of lithology on fracture frequency increases upward and the effect of curvature on fractures increase towards the right. Wackestone is more prone to fracturing than mudstone, and areas of curvature are more fracture-prone than non-distorted areas. Wells should target wackestone at highest curvature to increase the amount of intersected fractures.

Field and geologic setting

The Hunton Group carbonates were deposited during the Late Ordovician-Silurian-Early Devonian time in many areas in the Oklahoma and Texas Panhandles, including the southwestern part of the Cherokee platform and in the Anadarko, Arkoma, and Ardmore basins of Oklahoma (**Figure 3.2A**). The Hunton Group is associated with a shallow-warm water carbonate ramp of a gently sloping surface with less than 1^{o} dip (Amsden, 1975; Stanley and Rottmann, 2001). The Hunton Group is a sequence of limestone, dolomite, and interbedded calcareous shale (**Figure 3.2B**) deposited through upper subtidal, intertidal, and supratidal depositional environments (Fritz and Medlock, 1994) with intra-Hunton unconformities or time-stratigraphic gaps (Amsden, 1975; Al-Shaieb and Puckette, 2000). The Hunton facies are characterized by shallowing upward cycles, comprising a series of progradational and aggradational parasequences (Fritz and Medlock, 1994). The Hunton facies had a wide range of diagenetic changes during the Silurian-Devonian Periods (Johnson et al., 2000).

The Hunton play is characterized by a combination of structural and stratigraphic traps. Most of the structural traps are present in the Arkoma Basin, the Ardmore Basin, the deep Anadarko Basin, and the southwestern part of the Cherokee platform (**Figure 3.2A**). The presence of structural traps appears on the Anadarko shelf and on the central part of the Cherokee platform (Northcutt, 2002). Common stratigraphic traps in the Hunton are formed by unconformity truncations either within the Hunton or by the pre-Woodford unconformity wherein the overlying Woodford Shale provides the source rock, traps, and seal.

The Hunton Group is a prolific oil and gas producing reservoir in the Midcontinent (Gaswirth and Higley, 2014). The cumulative oil production is 290 MMBO and the cumulative gas production is 5 TCFG (IHS Energy, 2010), with unproduced 9 MMBO and 38 BCF of oil and

gas respectively (Gaswirth and Higley, 2013). Fractures in the Hunton Group are considered one of the key components to enhance the hydrocarbon production (Al-Shaieb et al., 1993).

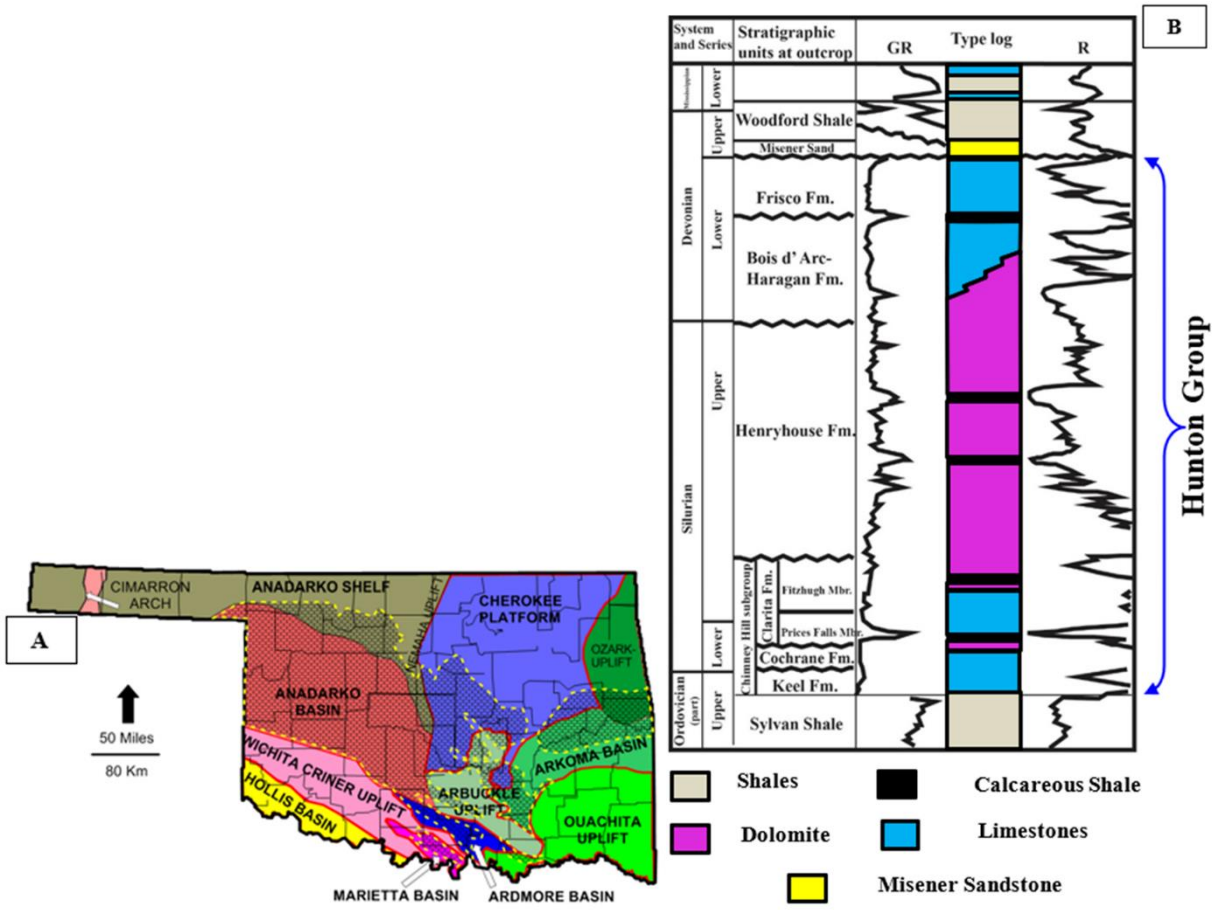

Figure 3.2. Oklahoma geological provinces and the stratigraphic column of the Hunton Group. A) Map of Oklahoma showing geologic provinces and the Hunton Group distribution (Northcutt, 2002). Yellow dashed lines show the boundaries of the Hunton Group. B) Hunton Group stratigraphic column in central Oklahoma with gamma ray (GR) and deep resistivity (RT90) type logs (Fritz and Medlock, 1994). The Misener Sandstone was added to this stratigraphic column as it was observed in a core and subsurface logs in the Cherokee Platform.

Studied areas

To utilize outcrop fracture data for the subsurface reservoir of the Chimneyhill subgroup, two horizontally bedded outcrops (Ada and Fittstown) with slopes of less than 10^{o} were selected to match the subsurface slope (average >10^{o}). Both outcrops are located in Pontotoc County and

are separated by 13.5 miles (**Figure 3.3**). We studied the fracture orientations for the major fracture set at each outcrop to be compared to the borehole fracture orientations. In addition, we selected the Hunton Anticline exposure because it incorporates both the structural geology of an anticline with curvature changes and the lithofacies found at other sites (mudstone, mud-dominated wackestone, and wackestone).

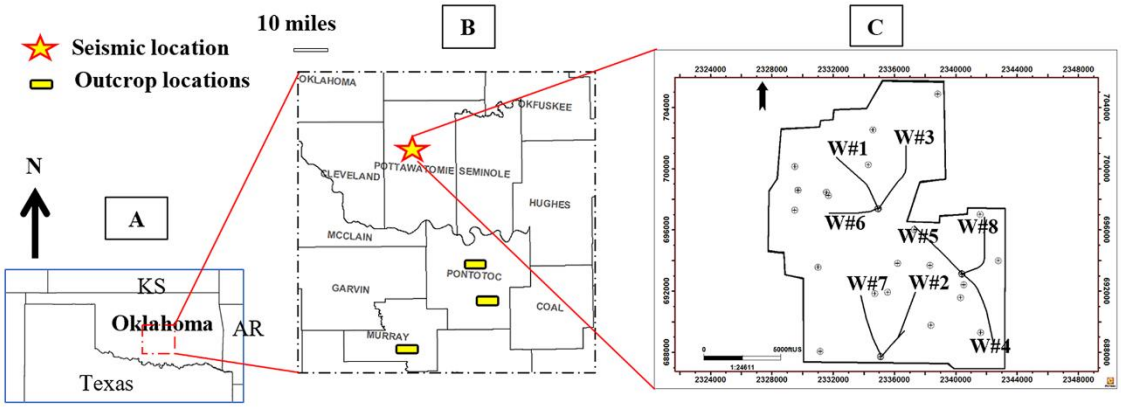

Figure 3.3. Locations of studied areas. A) Regional map of Oklahoma with adjacent states. B) Locations of data showing in Pottawatomie, Pontotoc, and Murray counties. The location of the 3D seismic volume is in the star, and the locations of the outcrop are in the rectangles. The upper rectangle symbol in Pontotoc county is the Ada outcrop, and the lower one is the Fittstown outcrop. The lowermost rectangle in Murray county is the Hunton Anticline Quarry C) Zoomed section of the star symbol from Figure 3B shows the locations of subsurface wells within the 3D seismic polygon. Black curves show the path of deviated and horizontal wells and the circles show the locations of vertical wells.

Natural fracture analysis

Outcrops

We measured the bed and fracture orientations at the two horizontally bedded outcrops. Rose diagrams of bed and fracture strike and dip were generated using Techlog© commercial software for individual fracture sets in the outcrop. To study the effect of both structure and lithofacies, we measured the fracture intensity for each of the three lithofacies types that we observed in the subsurface from the Hunton Anticline exposure (**Figure 3.4**). The lithofacies of

the Hunton Anticline were identified by Stanley (2013) as the lowermost part of the Hunton exposure where mudstone with higher amounts of argillaceous material is overlain by strata with less argillaceous material and presence of fossils (mud-dominated wackestone). The amount of fossils and the presence of skeletal wackestone texture increases in the uppermost section of the exposure (Stanley, 2013). We also selected five specific areas (marked with star symbols in **Figure 3.4**) for each lithofacies type at different curvatures along the exposure wall of the Hunton Anticline to incorporate and predict the effect of both structure and lithology on fracture distributions.

The curvature of the Hunton Anticline was calculated at each deformed area of the selected star symbol windows (**Figure 3.4**) by measuring the inverse of the radius of a circle tangent to a curve (K=1/R) (Chopra and Marfurt, 2010). This was accomplished by fitting the circle tangent to a surface in orthogonal planes of each selected windows of the Hunton Anticline. Then the fractures were mapped at the curvature locations for the three lithofacies and the fracture intensities were calculated at each deformed area for each lithofacies type by dividing total measured fracture length in each polygon by the polygon area with an average area of 10 ft by 5 ft. We selected a total of fifteen polygons away from faults in the quarry to avoid the bias in the fracture intensity measurements. Fracture intensity versus curvatures were plotted for each lithofacies types in the results section.

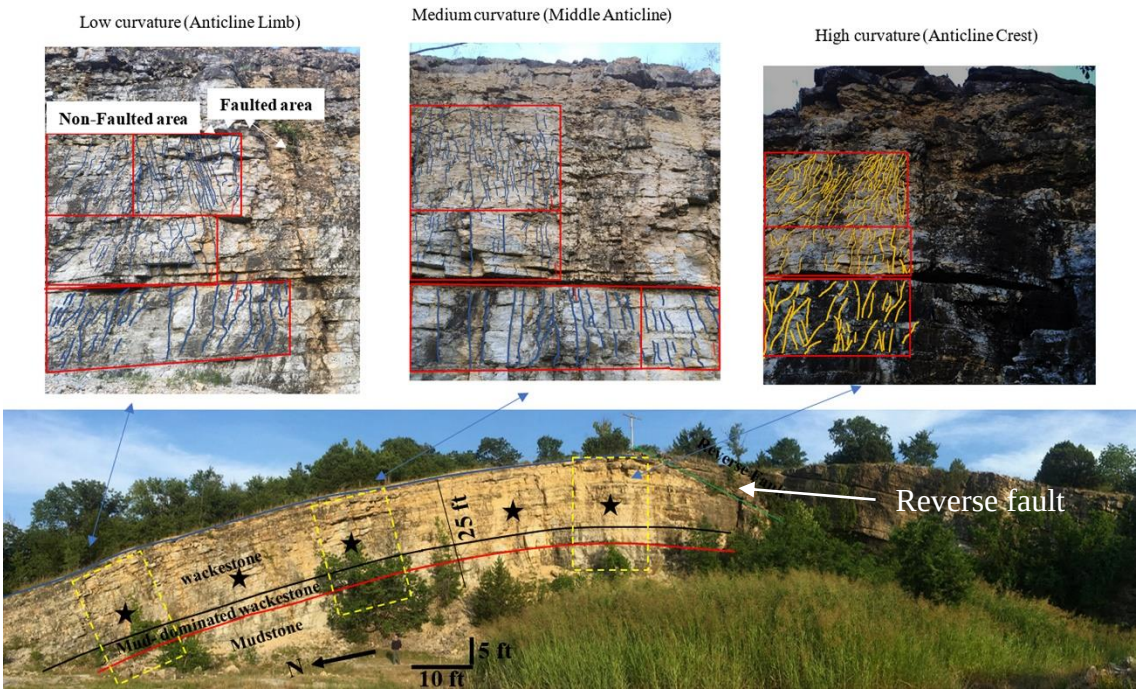

Figure 3.4. Hunton anticline quarry in Murray County, Oklahoma. Mudstone is at the base of the quarry wall, mud-dominated wackestone is in the middle and wackestone is in the upper section of this photo (Stanley, 2013). Black stars show the selected locations to measure fracture intensity. The zoomed three photos were selected three examples out of five locations to conduct the fracture analyses at three curvature locations of the quarry wall. The yellow dashed boxes are the zoomed photos. Reverse fault is indicated by the white arrow.

Borehole images

Microresistivity image logs from eight horizontal wells were loaded, processed, quality checked, and oriented in Techlog© commercial software. The fractures were classified based on the visibility and continuity around the wellbore since fracture features were not equally visible. The structural and fracture types were identified and picked manually from the image logs. These features included bed boundaries, breakouts, faults, microfaults, induced fractures, open fractures (conductive), partially open fractures, and closed/mineralized fractures.

1D and 3D fracture intensity

Fracture intensity was calculated along the borehole from image logs. Fracture intensity (P10) is a measure of the number of fracture intersections per length interval of the well bore

(Dershowitz and Herda, 1992; Aliverti et al., 2003). In our case, fracture intensity (P10) determined the number of fractures per one-foot interval at the borehole image well locations. Since we have four fracture sets from both outcrops and borehole images **(Figure 3.9A**) [N-S (340-10^{o}), E-W (81-110^{o}), NW-SE (111-160^{o}), and NE-SW (11-80^{o})], both the fracture intensity for a single fracture set, and for the total population of fracture sets was calculated. The correct calculations of the fracture intensity occur when the number of fractures are counted perpendicular to the scan line (borehole). However, since some of the wells are deviated and horizontal and the fractures intersect differently along the well bore depending on the orientation of the scan line of the borehole trajectory, the fracture intensity calculations can be biased. To overcome this sampling bias, Terzaghi's corrections were performed to obtain a corrected P10 (P10c) (number of fractures/window length) for individual fracture sets and total fracture populations (Terzaghi, 1965). We corrected the intensity log for the angle of the borehole to the fractures by measuring the window length perpendicular to the principle fracture direction. This allowed the generation of fracture intensity logs of borehole images to become less biased. The fracture intensity log is a virtual log connected to the fracture observations from image logs so that the fracture data provided are used as a starting point for fracture distribution for a 3D fracture model using Petrel© software. One output fracture intensity log for each of the four sets was generated.

The sequential Gaussian simulation (SGS) geostatistical method was used to interpolate the fracture intensity (P10c) logs at the well locations throughout the subsurface rocks of the upper, middle and lower Chimneyhill subgroup. The main steps of the fracture intensity modeling are as follows:

- Generate the intensity logs for all boreholes

- Upscale the intensity logs to the geocellular grid
- Perform vertical variogram from the upscaled logs
- Perform horizontal variogram upon acoustic impedance seismic inversion volume (explained in detail in lithofacies section).

The first step of the 3D fracture intensity modeling was generated from the fracture intensity logs at the boreholes. The intensity logs were upscaled, using an arithmetic averaging method, into equivalent cell values of the geocellular grids. There are a number of different existing methods that can be used to populate the fracture intensity (e.g., Kriging or sequential Gaussian simulation (SGS)). The difference between Kriging and SGSIM is that Kriging is an estimation to generate one model given one variogram. However, SGSIM is a simulation given multiple variograms (Gringarten and Deutsch, 1999; Al-Mudhafar, 2017). The Kriging method provides a best estimate of a reservoir property at well locations but it also smooths the values away from the borehole significantly as it reduces the variance of the data (Wang and Carr, 2013; Rogers et al., 2015) .Therefore, the Kriging method does not preserve the heterogeneity properly. Hence, we used a sequential Gaussian simulation (SGS) method because it is more geologically realistic and better preserves the variance of the data of fracture intensity (Rogers et al., 2015). In this case, all cells intersected by the boreholes and their neighbors had average values of fracture intensity (P10c). Having transformed the intensity logs into the intersected grid cells, these data at cells were used as an input for the vertical variogram parameters including vertical range. The horizontal variogram parameters, including minor and major ranges were used from the acoustic impedance variance maps. Acoustic impedance is a multiplication of density and P and S wave velocity logs. A simultaneous inversion model interpolates the values of the logs throughout the

seismic volume using Hampson-Russell© Software. Models of P and S impedance were generated using well logs and Hunton horizons (detailed discussion in the lithofacies section). Seismic inversion steps are available in **Appendix A**.

Borehole Image Fracture Intensity and Seismic Curvatures

Once the fracture intensity was calculated along the wellbores, most positive curvature and most negative curvature attributes were generated for the seismic survey of seven square miles. These seismic attributes were converted from the time to the depth domain. Afterwards, the most positive curvature and negative curvature values were extracted along the wellbores and plotted against the borehole image fracture intensity to examine the effect of seismic curvature changes and the fracture intensity. In this case, fracture intensity can be compared from outcrops and seismic data.

Lithofacies determination

To examine the subsurface relationship between the fracture intensity maps and lithofacies variations, lithofacies were identified at well locations and populated for the subsurface area. Lithofacies of the Chimneyhill subgroup of the Hunton Group carbonates were identified by integrating mineralogy, core porosity, core permeability, thin sections analyses, borehole images, and the unsupervised clustering analysis of K-means and self-organizing map (SOM) outputs based on well log data. At two wells with core data, we first classified the well log data into electrofacies types using statistical approaches. A combination of principal components analysis (PCA), optimal number of clustering, self-organizing map (SOM) and K-means were used to characterize and identify electrofacies types. These statistical methods were coded in R© programming language.

PCA finds the variables (well logs) that best account for the variability in the data set to be used as an input for the clustering by reducing the data dimensionality. Well logs including gamma ray (GR), photoelectric (PE), density (RHOB), neutron (NPHI), deep resistivity (RT90), and acoustic (DT) were examined for their variances. GR, PE and RHOB represent the first, second, and third components with the highest variability to be used as primary input to classify different clusters of facies. The components of these three logs counted for more than 95% of the variance in the dataset (**Table 3.1**). Next, the identified well log variables from PCA were used to determine the optimal number of clusters (electrofacies in groups).

Table 3.1. Standard deviations for each log based on PCA result.

Summary (PCA)	GR	PE	RHOB
Importance of components	PC1	PC2	PC3
Standard deviation	17.041	4.914	0.185
Proportion of Variance	0.923	0.076	0.0001
Cumulative Proportion	0.923	0.999	1

Identifying the number of clusters was required prior to applying SOM and K-means clustering techniques in this study. An arbitrary number of clusters can lead to redundant numbers of facies. For the purpose of accuracy, an elbow method (Ketchen and Shook, 1996) was used to determine the optimal number of clusters, which was determined by plotting variance of the sum of the square within clusters (SSW) and the sum of the square between clusters (SSB) versus the number of clusters. An optimal number of clusters occurs when there are small variances within each cluster (SSW) and large variances between clusters (SSB) of three clusters. The aim of using SOM and K-means unsupervised clustering analysis was to classify a well log data set into groups on the basis of a measure of similarity within a group and dissimilarity between groups. SOM and K-means used the identified well log data set from PCA to classify the log traces over a geologic

interval into groups (Coléou, Poupon, and Azbel 2003, Al-Mudhafar and Bondarenko 2015). These groups have internally similar rock properties (homogenous) and externally different rock properties (heterogenous). The purpose of using these two methods (K-means and SOM) was to compare the results of these two techniques using the same electrofacies output for the same log variables input.

Once the electrofacies classifications were identified at the two cored wells, a comparison was done with the core analyses including thin sections analyses, mineralogy, core porosity, core permeability, and borehole images. Twenty thin sections were taken from sidewall cores from two wells drilled through the upper, middle and lower Chimneyhill subgroup of the Hunton Group. Analyses of thin sections, mineralogy, and borehole characteristics allowed us to interpret electrofacies code numbers (e.g., electrofacies codes 1, 2, and 3). These electrofacies codes were correlated to a particular Dunham (1962) classification of carbonate rock and texture types from the well log response to provide a geologically meaningful Chimneyhill reservoir description. The three lithofacies identified are wackestone, mudstone, and mud-dominated wackestone. Lithofacies logs were generated on 28 wells to be used to build a 3D lithofacies model.

3D Lithofacies modeling

The purpose of building a 3D lithofacies model was to examine the relationship between the fracture intensity and lithofacies maps on an area of seven square miles. To establish a quantitative spatial correlation for the electrofacies, integration of lithofacies logs and seismic data (Xu et al., 1992; Pyrcz and Deutsch, 2014) were applied. In addition, the sequential indicator simulation (SIS) algorithm was recommended by Deutsch (2006) to be used for the diagenetically altered environment (e.g., Hunton Group) because it preserved the lithofacies heterogeneity of a reservoir. We considered the 3D acoustic impedance volume generated from seismic data to infer

reliable measurements of azimuthal direction, minor and major horizontal ranges of the horizontal variogram parameters. These parameters were used as input for the SIS algorithm (Xu et al., 1992; Pyrcz and Deutsch, 2014). The preferential direction of maximum continuity is N15E and minimum continuity (minor) direction is perpendicular to the maximum direction (S75E) (**Figure 3.5**). The estimated major range was 25,283 ft and the minor range was 13,545 ft with anisotropy ratio of 1.87 for each facies for each zone of the upper, middle, and lower Chimneyhill subgroup. **Figure 3.5d** shows the semivariogram for the upper, middle, and lower Chimneyhill subgroup.

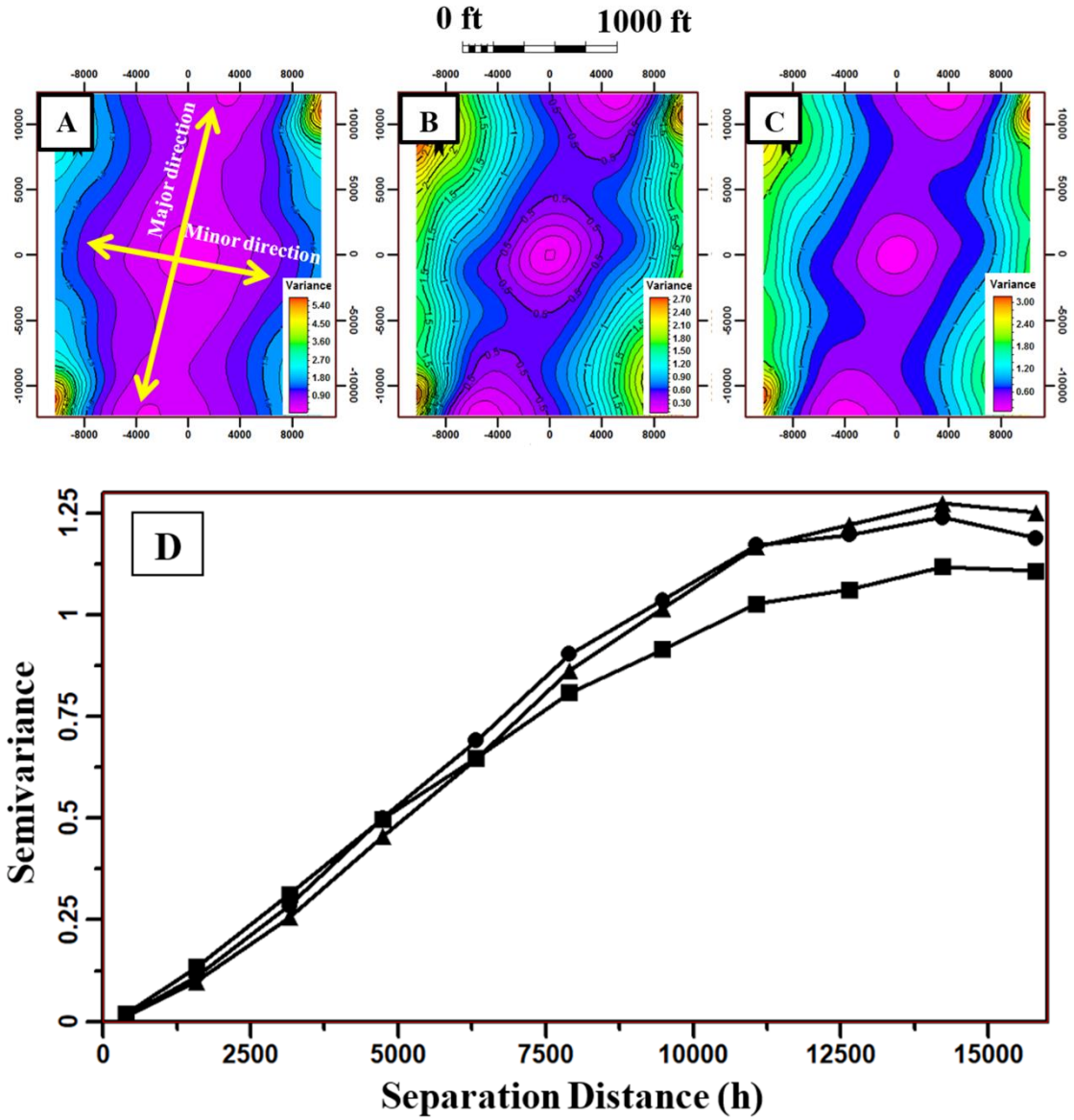

Figure 3.5. Horizontal variogram variance map generated from the acoustic inversion. A) Variogram variance map for the upper Chimneyhill subgroup. B) Variogram variance map for the middle Chimneyhill subgroup. C) Variogram variance map for the lower Chimneyhill subgroup. D) Three curves of the horizontal variogram maps (A, B, and C) from the seismic acoustic impedance for the upper, middle, and lower Chimneyhill subgrop. Square symbol curve represents the variogram curve for the upper Hunton, triangle symbol is for the middle Hunton, and the circle symbol is for the lower Hunton Group. The three maps show that the preferential direction of maximum continuity is N15E and minimum continuity (minor) direction is perpendicular to the maximum direction (S75E).

Results

Fractures from outcrops

Four fracture sets were documented within the Chimneyhill subgroup: N-S (340-10^{o}), E-W (81-110^{o}), NW-SE (111-160^{o}), and NE-SW (11-80^{o}). In the Fittstown outcrop, the N-S, E-W, and NW-SE sets dip about 80^{o}. In the Ada outcrop, all four sets were present and also dip about 80^{o}. In the Ada outcrop, the NE-SW fracture set is the predominant set followed by the NW-SE set. In the Fittstown outcrop, the E-W fracture set is the predominant set followed by the N-S (Milad et al., 2018). All of the four sets of fractures dip more than 80^{o}, and the beds strike 285^{o}with gentle dips of less than 10^{o}in both outcrop locations. Thus, the four observed fracture sets in these outcrops helped to cluster similar sets for the fractures that were interpreted from the subsurface borehole images.

Figure 3.6 shows the fracture intensities from the Hunton Anticline. Fracture intensity increased with curvature with all lithofacies. Correlations show a positive linear relationship between fracture intensity and changes in curvature for the mudstone and mud-dominated wackestone, and an exponential relationship for the wackestone textures (**Figure 3.6**).

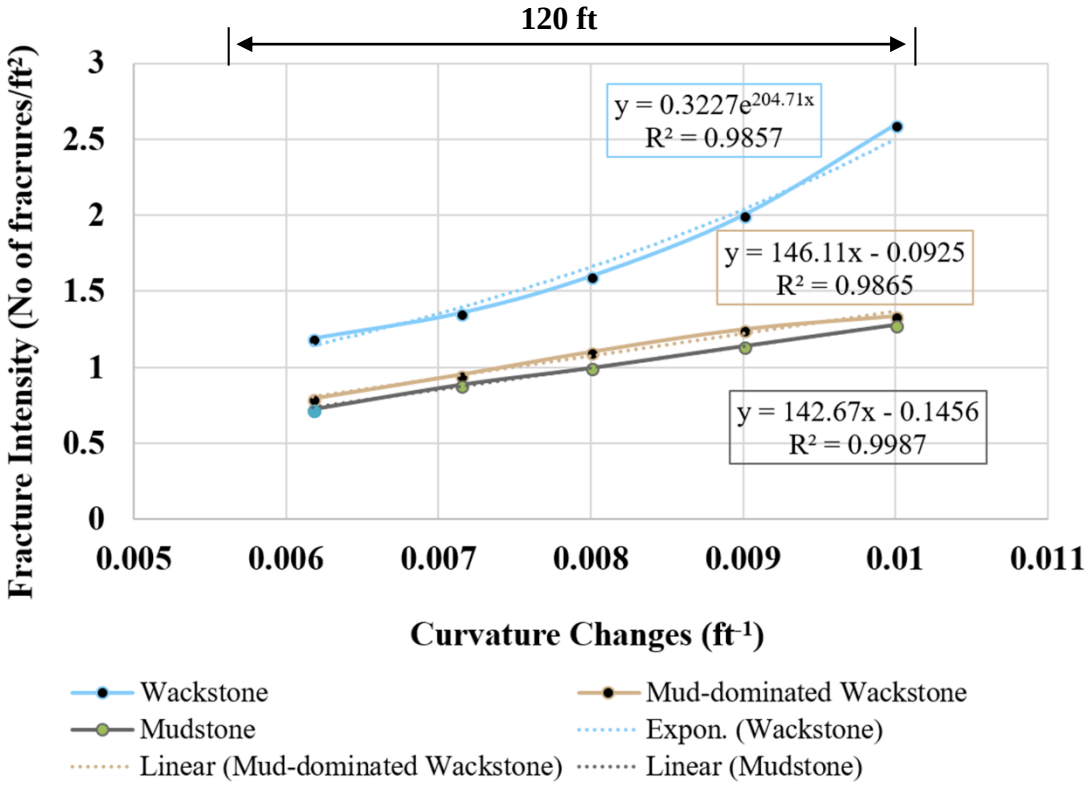

Figure 3.6. Fracture intensity versus curvature for mudstone, mud-dominated wackestone, and wackestone lithofacies at the Hunton Anticline Quarry. Solid lines represent the data points and the dashed lines show the best curve fitting for the data points. As curvature increases, the fracture intensity increases for those three lithofacies types based on five location measurements at the Quarry wall shown in Figure 4. However, the wackestone has higher fracture intensity at different curvatures, compared to the mudstone and mud-dominated wackestone.

Fractures from borehole images

Bed boundary features in the studied area were characterized by low dip angles of less than 10^{o}in the horizontal wells, whereas the fracture planes had high dip angles of more than 70^{o}. The natural fractures are transverse; meaning the fractures cut the horizontal well almost perpendicularly at angles of more than 70^{o} (**Figure 3.7**). Fracture orientations from the borehole images were clustered in similar orientations to those observed in the two horizontally bedded (Fittstown and Ada) outcrops (**Figure 3.8 A**). Four fracture sets, set-1: E-W (81-110^{o}), set-2: N-S (340-10^{o}), set-3: NW-SE (111-160^{o}), and set-4: NE-SW (11-80^{o}), were identified from both

borehole images and the two horizontally bedded outcrops (**Figure 3.8**). The NE-SW fracture set is the dominant set identified with the most fractures. The dip of fractures is very steep to the axis of the borehole image (**Figure 3.7**). In all four sets of fractures, dip angles vary between 70 and 90°, so the fractures are essentially vertical (**Figure 3.8 B**). The bed boundary has a low dip angle between 10 and 20°.

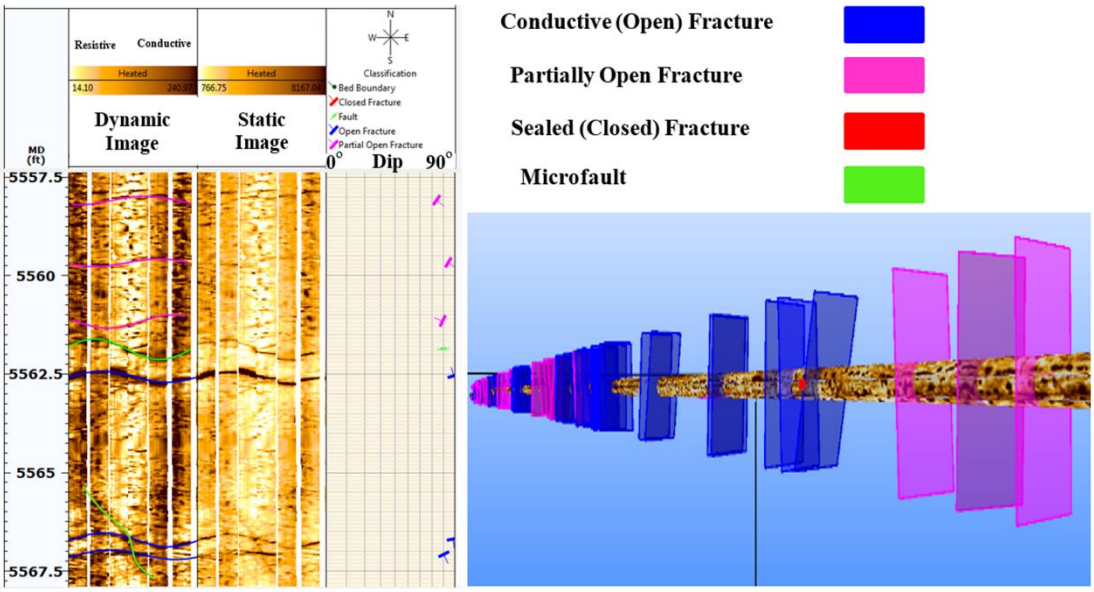

Figure 3.7. Fracture classification on borehole image. The figure on the left shows the picked fractures on the dynamic image track 1. Track 2 is the static image, and track 3 shows the dips of the picked fractures. The figure on the right shows the image of a horizontal well with the cross-cutting fracture planes along the well. Different colors of fracture planes correspond to a specific fracture type: conductive fractures (blue), partial conductive fractures (magenta), healed fractures (red), and fault (green).

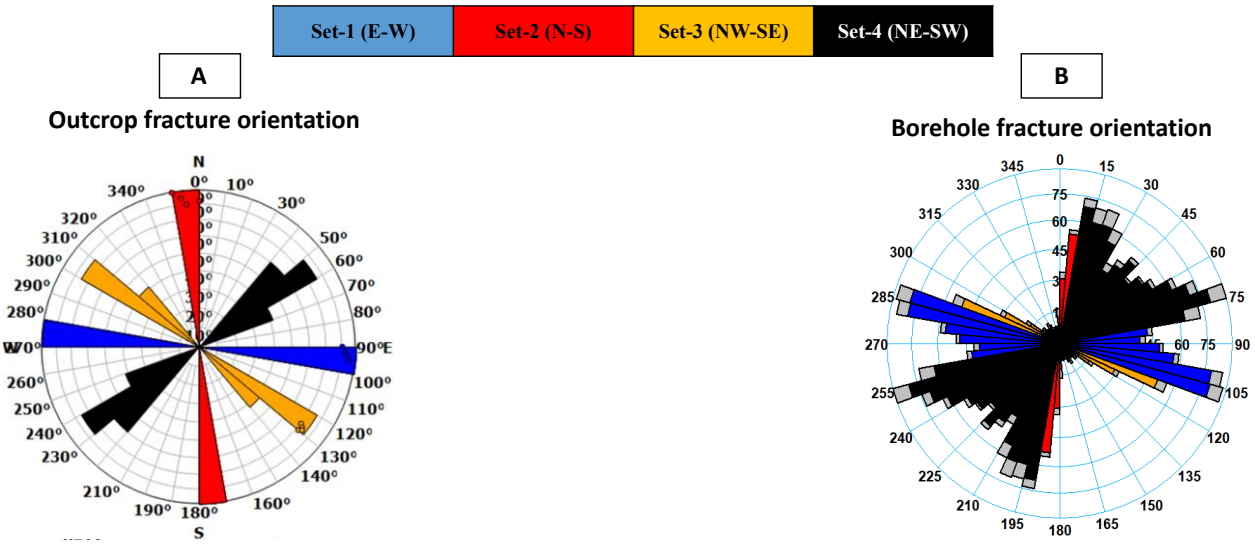

Figure 3.8. Four sets of fracture orientations. The different colors correspond to different fracture sets: blue corresponds to E-W set-1, red corresponds to N-S set-2, orange corresponds to NW-SE set-3, and black corresponds to NE-SW fracture set. A) The rose diagram on the left shows fracture strikes from the Ada and Fittstown outcrops. B) The rose diagram on the right shows fracture strikes for the fracture sets from eight borehole images; these fractures are steeply dipping (>70º). Out of the four E-W and NE-SW fracture sets are most likely to be active currently because of their 20º-40º angles with SHmax. Fractures that are oriented with low angles to the maximum horizontal stress (SHmax) are more likely to slip. In Oklahoma, max stress slightly varies from one basin to another, but in general, the maximum stress is E-W and NE-SW. Hence, E-W and NE-SW fracture set are most likely active and will slip.

Lithofacies

In **Figure 3.9**, the three electrofacies outputs from K-means and SOM (tracks 2&3) were correlated with the features and results of the core porosity and permeability (tracks 4&5), mineralogy (track 6), borehole image (track 7), and thin section analyses through the Chimneyhill subgroup reservoir zones. Borehole image (track 7) displays different colors; dark colors correspond to higher conductivity and lighter colors correspond to higher resistivity (less conductivity). Mudstone is usually more conductive (dark colors) while wackestone is less conductive (lighter colors). The three different intervals can be distinguished from the borehole image (track 7). The lower 25 ft interval (4210- 4235 ft) of lower Chimneyhill subgroup has a low

to medium conductivity. The examined thin sections from this interval were interpreted as wackestone from Dunham's classification. The middle 15 ft interval (4195-4210 ft) has low resistivity (dark color) and more conductivity suggesting the presence of conductive fluids (i.e formation water or fresh water mud). The examined thin sections from this interval were interpreted as mudstone based on Dunham's classification. The upper 15 ft interval (1480-4195ft) is less conductive (lighter color) of wackestone interbedded with the dark colored mudstone. The examined thin sections from this interval correspond to wackestone with lime-mud. The three electrofacies outputs of K-means and SOM techniques (tracks 2 &3) (**Figure 3.9**) yielded three very similar electrofacies outputs and they matched the integration of the petrographic, petrophysical analysis, and borehole visual identification results. Therefore, we can easily now relate the code number of K-means and SOM to the actual geological facies interpretations. Code 2 of both K-means and SOM represents mud dominated and code 1, and code 3 represent more calcite. Therefore, electrofacies 1 and 3 show substantial proportions of wackestone and mud-dominated wackestone respectively while electrofacies 2 substantially corresponds to mudstone.

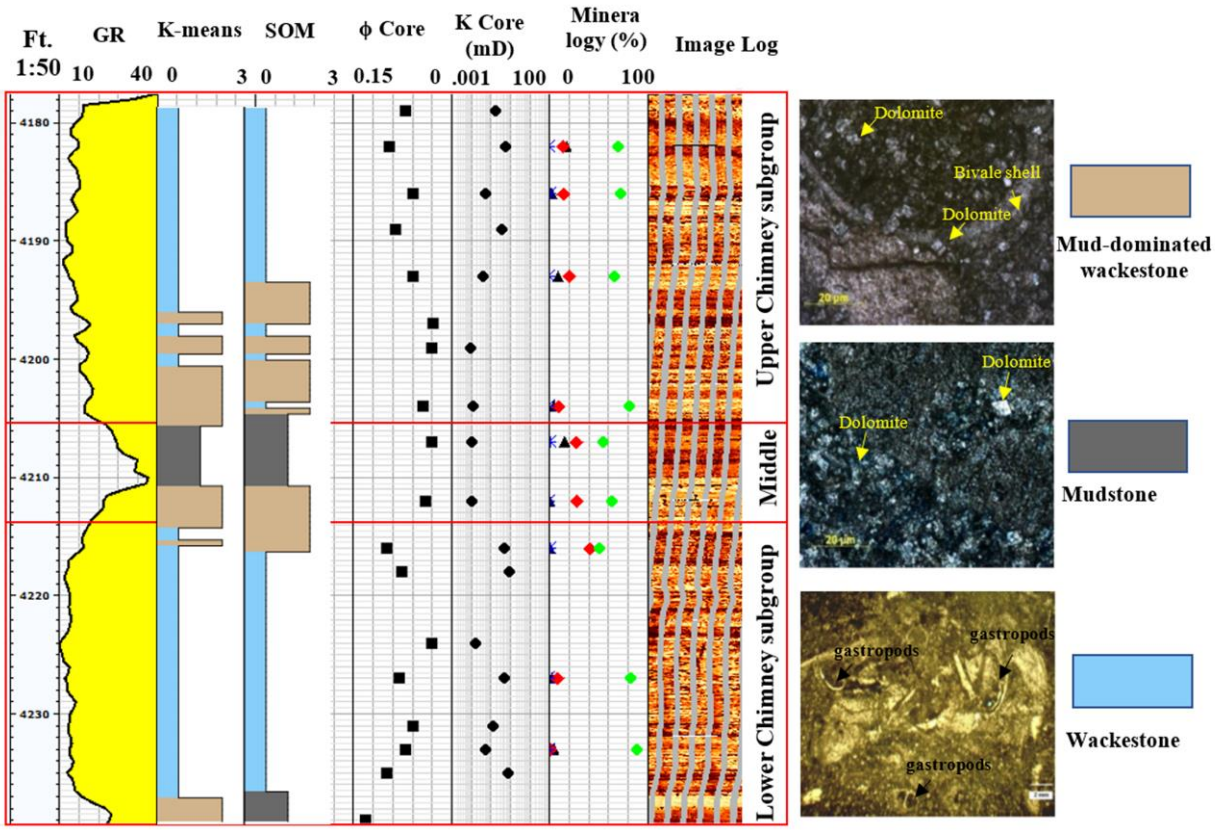

Figure 3.9. Lithofacies classification in well #1 using well logs, borehole image, and thin sections. Track 1 represents GR log and tracks 2 and 3 show the three electrofacies outputs from K-means and SOM. Track 5 & 6 show core porosity and permeability. Track 6 shows mineralogy results in percentage. A circle (green) corresponds to calcite, a diamond (red) represents dolomite, a triangle corresponds to clay (black), and a star (blue) corresponds to quartz percentage. Track 7 shows borehole image; dark colors correspond to higher conductivity and lighter colors correspond to higher resistivity (less conductivity). Mud is usually more conductive. The three electrofacies colors of K-means and SOM correspond to specific lithofacies based on thin section analyses: tan represents mud-dominated wackestone, dark gray represents mudstone, and light blue represents wackestone.

Fracture intensity: 1D and 3D

Lithofacies and fracture intensity were calculated locally at well locations and spatially of the Chimneyhill subgroup in the subsurface. We divided the lithofacies into wackestone, mudstone, and mud-dominated wackestone. These three lithofacies occurred at each vertical and horizontal well and the fracture intensity varied in these wells. The relationship between the

distribution of fracture abundance and the lithofacies variations were examined at 1D and 3D scales.

For the 1D scale, fracture occurrences were compared to discrete lithofacies logs at each well to examine the relationship between lithofacies and fracture occurrence within the Chimneyhill. The fracture intensity of each lithofacies in each well was calculated and plotted in a histogram column chart as shown in **Figure 3.10**. For example, in well 1, 2.2 fractures per one foot (frac/ft) occurred in wackestone, 1.6 frac/ft occurred in the mud-dominated wackestone, and only 0.3 frac/ft occurred in the mudstone lithofacies. The mean statistical analysis of the fracture intensity from eight wells for every lithofacies was determined and we found that wackestone was 2.3 frac/ft, mudstone was 0.76 frac/ft, and mud dominated wackestone was 0.9 frac/ft. These results show that fractures are two and half times more common in wackestone (close to grain supported) lithofacies than in mudstone matrix-supported lithofacies.

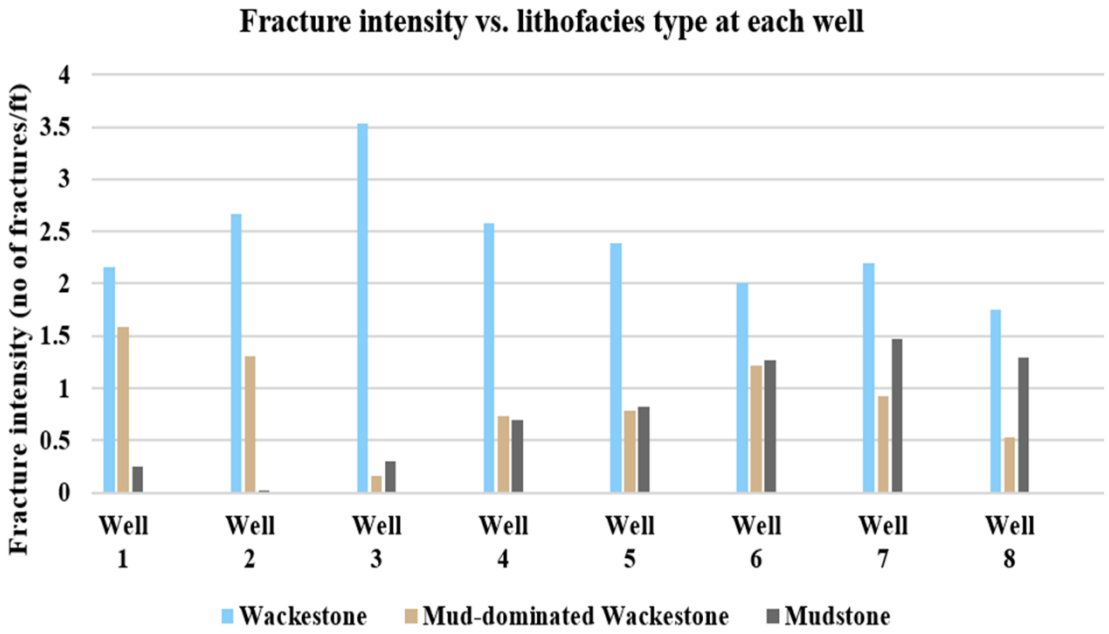

Figure 3.10. Histogram column chart of fracture intensity for each lithofacies. Mean fracture intensity (frac/ft) from these wells for the lithofacies include wackestone=2.3, mudstone=0.76, and mud-dominated wackestone=0.9. These results show that fractures are two and half times more common in wackestone (>10% of grain-supported textures) lithofacies than in mudstone matrix-supported lithofacies.

For the 3D scale, fractures were populated in the subsurface studied area. Fracture intensity and lithofacies maps of the upper, middle, and lower Chimneyhill subgroup are shown in **Figures 3.11** and **3.12**. For the wackestone-dominated lower Chimneyhill, (**Figure 3.11 C**), the fracture intensity was relatively high (**Figure 3.12 C**) whereas the mudstone-dominated middle Chimneyhill (**Figure 3.11 B**) had low fracture intensity (**Figure 3.12 B**). In the upper Chimneyhill, which is a mix of both mudstone and wackestone (**Figure 3.11 A**), the fracture intensity is variable (**Figure 3.12 A**). The fracture intensity maps suggest that within the wackestone lithofacies, the fracture intensity is very high (up to 2.25 frac/ft) with an average of more than 0.7 frac/ft. Conversely, in mudstone areas, the fracture intensity is very low (<0.1 frac/ft) with an average of 0.15 frac/ft. In areas of mixed mudstone and wackestone lithofacies (mud-dominated wackestone

lithofacies), the fracture intensity varies with an average of about 0.25 frac/ft (**Figures 3.11 A** & **3.12 A**).

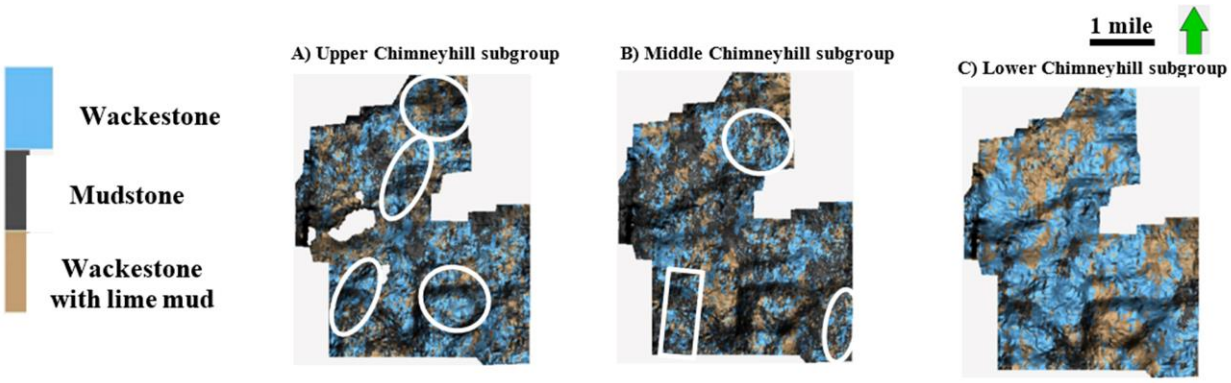

Figure 3.11. Lithofacies maps of the Chimneyhill subgroup for the upper, middle, and lower Chimneyhill subgroup. White circle, ellipse, and square shapes highlight lithofacies areas that are associated with higher fracture intensity in Figure 3.12.

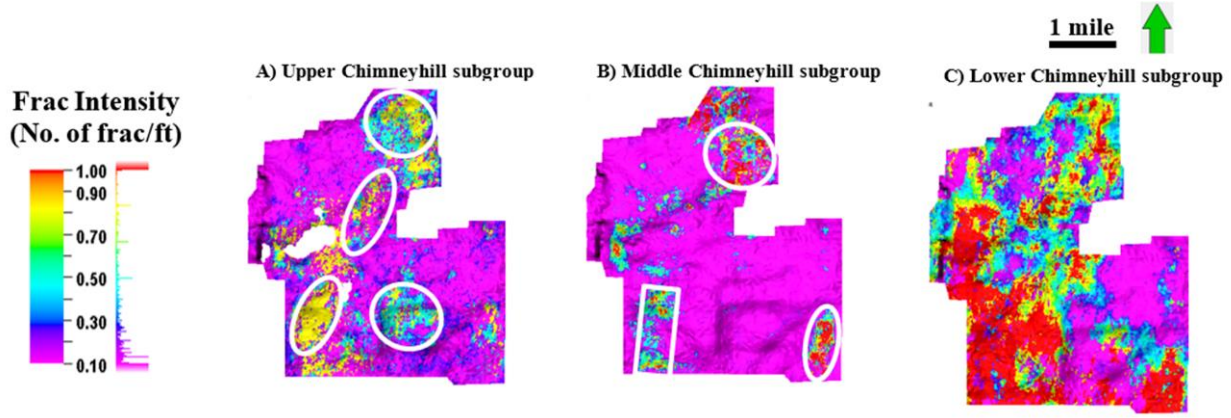

Figure 3.12. Fracture intensity maps of the upper, middle, and lower Chimneyhill subgroup. In the upper Chimneyhill subgroup reservoir, which contains both mudstone and wackestone (Figure 3.11 A), the fracture intensity of the upper Chimneyhill subgroup is variable as shown in the circles and ellipses. The changes of fracture intensity depend on the abundance of wackestone lithofacies type as higher fracture intensity is associated in areas of wackestone. In the middle Chimneyhill subgroup reservoir, which is dominated by mudstone, the fracture intensity is relatively very low (with an average of <0.1 frac/ft). However, fracture intensity in the lower Chimneyhill is relatively high (with an average of <0.25 frac/ft) as a result of the presence of wackestone lithofacies.

Influence of faulting and curvature on fracture distribution

Both structural effects and lithofacies changes can be principal components that control fracture distribution. A major control on fracture distributions in this study is related to the wackestone lithofacies where the greatest fracture intensity occurred (**Figure 3.10**).

Comparison among well locations, faults, and curvature attributes was done by overlaying the well trajectories with the fracture intensity displayed on a *k1*-curvature (structural highs), and *k2*- curvature (structural lows) horizon slice of the Chimneyhill subgroup of the Hunton (**Figure 3.13**). Results show that the most fracture intensity in each well is associated with the most positive curvature area (**Figure 3.13 A**). **Figure 3.13 D** shows least fracture intensity in most negative curvature area from the seismic data while fracture intensity increases proportionally with an increase of the curvature value. Hence, the most positive curvature is a major contributor to fracture intensity prediction.

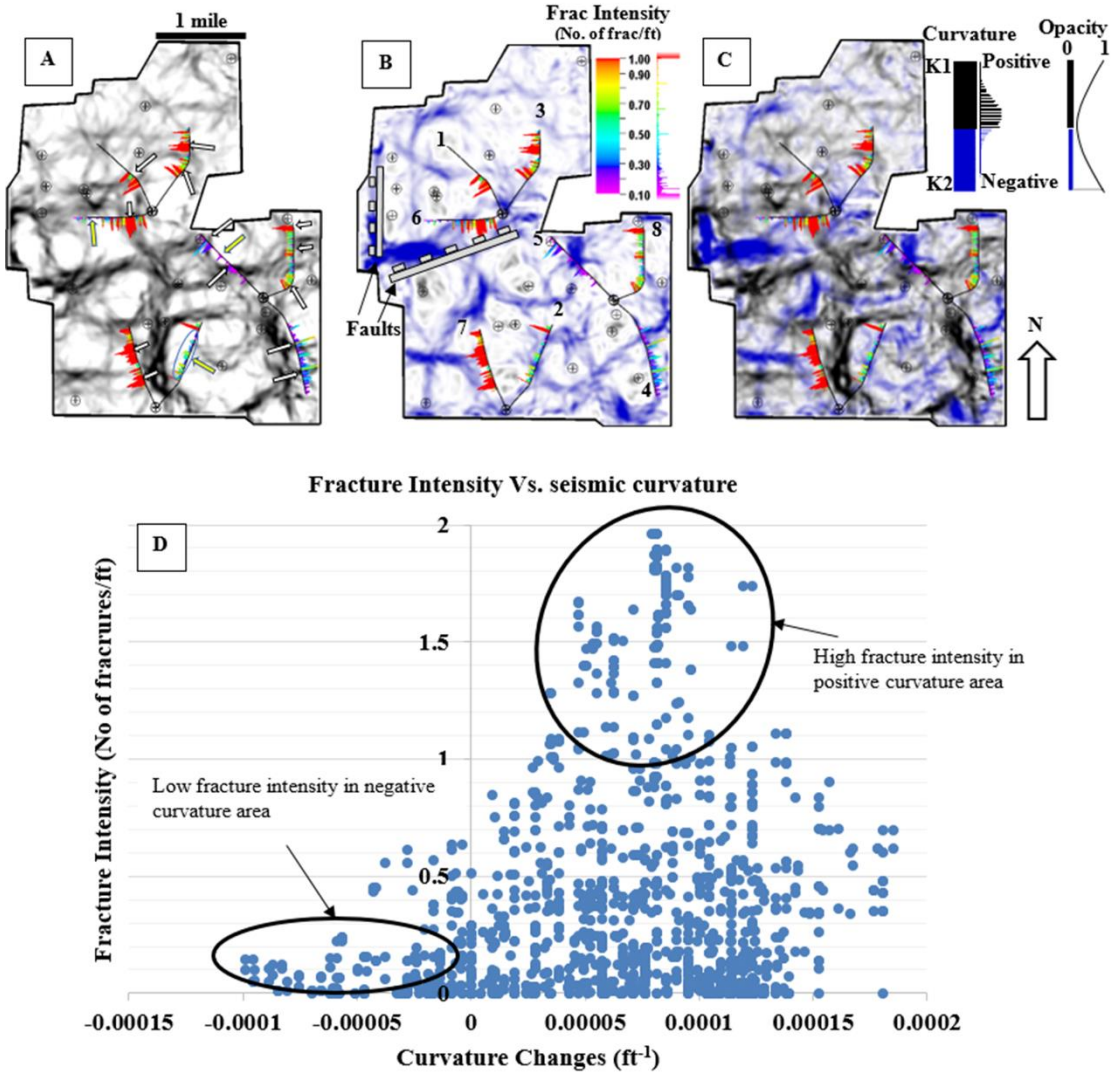

Figure 3.13. Structural seismic attributes of the Chimneyhill subgroup slices and fracture intensity versus seismic curvature crossplot. Black circles show the location of vertical wells and black curves show the trajectory of deviated and horizontal wells. Black corresponds to most positive curvatures (*k1*), and blue corresponds to most negative curvatures (*k2*). Borehole image fracture intensities are displayed on the structural seismic attributes (in pictures A, B, and C). Two white lines show the locations of the normal faults in picture B. A) most positive curvature seismic attribute in black colors shows the structural high (e.g., anticline). White arrows in picture A indicate areas of most positive curvature and higher fracture intensity while yellow arrows indicate areas of most negative curvature and lower fracture intensity B) most negative curvature seismic attribute in blue colors shows structural low (e.g., syncline). C) Co-render of most-positive and most-negative curvature attributes. Most positive curvatures and negative curvatures color bar used in attribute blending. D) Crossplot of fracture intensity from borehole images versus seismic curvatures. Fracture intensity increases as curvature increases. Fracture orientations were corrected so that boreholes image orientation are perpendicular to fractures.

Discussion

The Chimneyhill subgroup carbonate was used to understand and predict fracture distributions in areas with different lithofacies and curvature at different scales including borehole images, two outcrops, one exposed anticline, and seismic data. From surface and subsurface data, the lithofacies and structural effects on fracture distributions are examined in 1D and 3D views. Both lithofacies and structure are interrelated such that they control fracture distributions in this study. Lithofacies is the primary control of the fracture distribution and the structure seems to be the secondary control based on the outcrop and seismic studies.

As seen in the surface data (two outcrops and one anticline exposure), the fracture distributions in the three lithofacies types have been affected by the curvature changes. As the curvature increases, the fracture intensity increases (**Figure 3.6**). However, the wackestone has the highest fracture intensity at different curvature locations compared to the mud-dominated wackestone and mudstone (**Figure 3.6**). In the wackestone lithofacies, the fracture intensity increases by 54% from 1.2 fractures per ft^2 at low curvature to 2.6 fractures per ft^2 at high curvature followed by the mud-dominated wackestone, and wackestone (**Figure 3.6**). Hence the lithofacies types are considered the primary component affecting the fracture changes followed by the curvature changes during tectonism.

As seen in the subsurface data, a major factor that affects fracture distributions is also related to rocks that have more than 10% grains (wackestone in the Dunham classification). On the 1D scale, fracture distributions vary with the three lithofacies. Wackestone has the most fractures compared to the mudstone and mud-dominated wackestone (**Figure 3.10**). The influence of the mudstone is probably minimal since mud-supported textures are not considered to be

representative of higher fracture intensity. The mud-dominated wackestone appears to have random fracture distributions. 56.9% of the fractures in these wells occur in wackestone, 20.4% occur in mudstone, and 22.4% occur in mud-dominated wackestone (**Figure 3.10**). These results show that fractures are two-and-a-half times more common in wackestone (close to grain supported) lithofacies than in mudstone matrix-supported lithofacies. Similar results were found by Ericsson et al. (1998), Wennberg et al. (2006), and Sonntag et al. (2014) where more fractures occurred in grain-supported than mud-supported textures. However, no previous studies have identified correlations to predict the change of fracture intensity in wackestone, mudstone, and mud-dominated wackestone with changing curvature.

On the 3D scale (subsurface data), higher fracture intensity occurred in areas dominated by wackestone lithofacies. Fracture intensity maps (**Figures 3.11** & **3.12**) suggest that in wackestones, the fracture intensity is very high, up to 2.25 frac/ft, with an average of 0.7 frac/ft. Conversely, in mudstone dominated areas, the fracture intensity is very low: <0.1 frac/ft with an average of 0.15 frac/ft. For mixed mud and wackestone lithofacies, the fracture intensity varies with an average of 0.25 frac/ft (**Figures 3.11** & **3.12**). The texture is shown to be more important for the fracture intensity since less mud-supported textures (wackestone) have higher fracture intensities than more mud-supported textures (mudstone) (**Figure**s **3.11** & **3.12**). A similar relationship between texture classifications and fracture intensity was reported from Cretaceous platform carbonates in the Central Apennines of Italy (Di Cuia et al., 2004), in the Carboniferous Lisbourne Group carbonates of Alaska (Hanks et al., 1997), and in the late Cretaceous Ilam Carbonate Formation of the Arabian Gulf Fateh Field (Ericsson et al., 1998), where >62 % of the fractures occurred in grain-supported textures based on image log and core fracture data. Also, results were observed by Ericsson et al.

(1998) where 82% of the fractures occurred in areas of either grain-supported rocks or high structural curvatures.

The relationship between the amount of mud-supported texture and fracture intensity in a carbonate environment can be related to the rock strength. Higher fracture intensities occur for more brittle and stronger rock (Ericsson et al. (1998) and Nelson (2001). Wackestone is more brittle than mudstone rocks in the Chimneyhill subgroup. Results of a rebound hammer™ study on Roberson# A1 Hunton core which is seven miles to the west of the borehole image wells shows that higher Leeb hardness (LH) measurements (average of 630 LH) occur in the wackestone compared to mudstone lithofacies (average 580 LH) (**Figure 3.14**). The differences of the hardness measurements seem to be statistically significant.

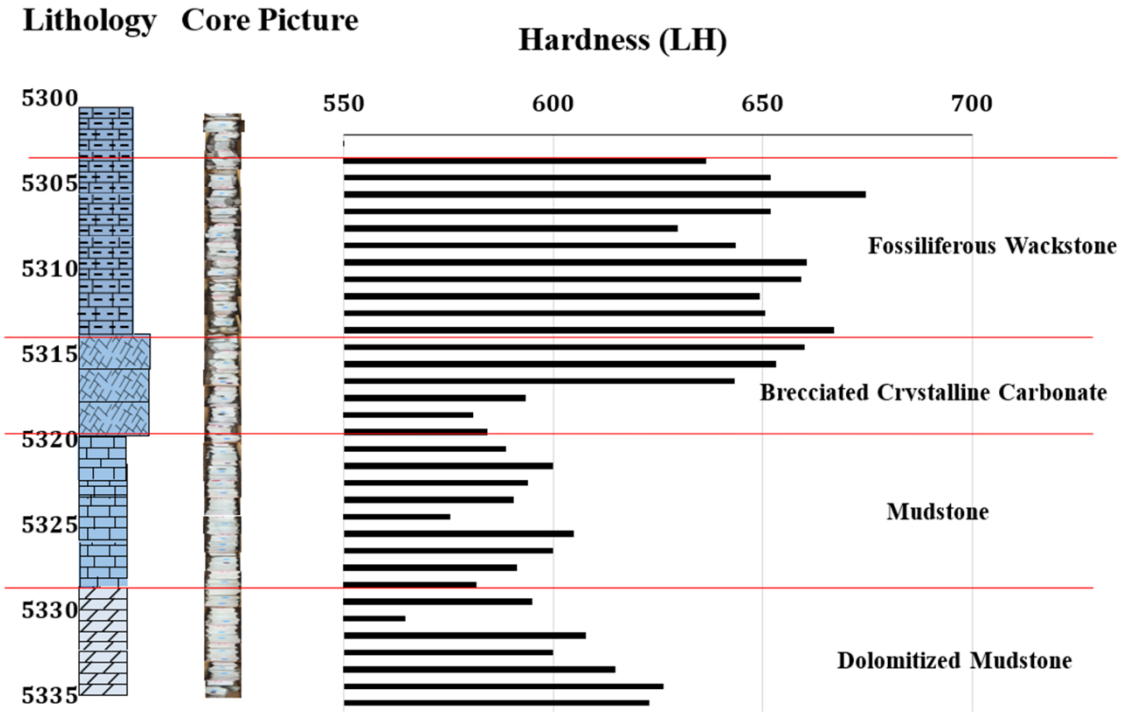

Figure 3.14. Core analysis for Robertson A#1 well (located ~7 miles to the west of the study area) including lithology profile, core photograph, and core hardness measurements using rebound hammer™. This core is located seven miles to the west of the borehole image wells (Figure 3) in Pottawatomie county. The rock hardness for the fossiliferous wackestone is higher than the rock strength of mudstone. The average value of hardness measurements for fossiliferous wackestone stratigraphic interval (5314 to 5300 ft) is 650 LH. The average value of the hardness measurement for mudstone (5329 to 5320ft) is 580 LH. Hence, the wackestone lithofacies in this study is considered a brittle rock compared to the mudstone.

Structure is another crucial factor for fracture distributions. Curvature areas are other principal factors that can be used to predict the fracture distributions. Wells 6, 7, and 8 (**Figure 3.10**) have relatively higher fracture intensity (≤1.4 frac/ft) in mudstone areas compared to the other wells which have >2.4 frac/ft in wackestone. Values of 1.2, 1.4, and 1.3 frac/ft occurred in the mudstone areas for wells 6,7, and 8, respectively (**Figure 3.10**). Results show that the trajectory of well #6 is located in a nearby fault zone and wells #7 and 8 are on structural highs (anticlines) of higher most positive curvature compared to the rest of the wells (**Figure 3.13**). Therefore, the increased fracture percentage of these wells in the mudstone area appear to be influenced by their

proximity to faults and most positive curvature areas. Additionally, borehole image fracture intensity versus seismic curvature attributes (positive and negative) shows a positive relationship between the fracture intensity and curvature (**Figure 3.13 D**). Fracture intensity increases with the increase of the curvature. In addition, the structural effect on fracture distribution was examined experimentally using clay models (Busetti 2009, Staples 2011). The clay model experiments showed a linear relationship between fracture intensity and curvature.

The two positive linear correlations (**Figure 3.6**) for the mud-dominated wackestone and mudstone, and the exponential relationship (**Figure 3.6**) for the wackestone can be used to predict the change of the fracture intensity in subsurface carbonate reservoirs. The fracture intensity model presented here has a number of advantages over 1D fracture modeling in that it is better able to capture the reservoir scale heterogeneity and distribution of the fractures. Most importantly, 3D fracture intensity modeling provides a clear view of how to drill and simulate new areas by identifying areas with high and low fracture intensity as well as the more brittle areas. The proposed schematic model (**Figure 3.1**) was developed based on the surface and subsurface data and can be used for picking fractured areas to land horizontal wells for carbonate reservoirs. The limitation of the proposed model is that the lithofacies types found in the surface and subsurface sites are limited to the mudstone, mud-dominated wackestone, and wackestone. However, we expect that the higher grain-supported rocks (packstone and grainstone) would provide strata of high fracture frequency.

Implications for stimulation program

By understanding fracture characteristics of different Hunton lithofacies types at the reservoir scale, hydraulic fracture treatments can be optimally designed to stimulate each reservoir accordingly. Lateral wellbores can be designed to penetrate through wackestone and stimulate each

reservoir differently in order to optimize production. If a wellbore intersects multiple wackestone lithofacies perpendicular to the dominant NE-striking fracture set, hydraulic fractures have the potential to travel long distances along the natural fracture network, resulting in more efficient drainage of the NE-trending wackestone facies. In addition, NW-propagating hydraulic fractures have the potential to reactivate the NE-striking fracture set and potentially other sets (N-S, and E-W), providing better connectivity between the natural fracture system and increased drainage of the reservoir.

Conclusions

Understanding and predicting the major factors that control natural fracture distribution is important in successful exploration and development of hydrocarbon reservoirs. Lithofacies and structure are two main factors that control fracture distribution. Rebound hammer™ results show that wackestone rocks are harder than the mudstone. In our study, the wackestone lithofacies is more prone to fracturing (2.5 times) than mudstone. Additionally, there is a positive linear relationship between fracture intensity and curvature for the mudstone and mud-dominated wackestone lithofacies, and an exponential relation for the wackestone lithofacies.

Four fracture sets, {N-S (340-10^{o}), E-W (81-110^{o}), NW-SE (111-160^{o}), and NE-SW (11-80^{o})}, were observed in the outcrops and borehole images in the Chimneyhill subgroup of the Hunton. NE-SW is the dominant fracture set. Hydraulic fracturing may be conducted in wells drilled in the NW-SE direction to reactivate the NE-striking fracture sets and potentially other sets (N-S, and E-W), providing better connectivity between the artificial hydraulic and natural fracture system resulting in an increased reservoir drainage.

This study will help investigators build generalized predictive models for the dependence of fracture intensity on bed curvature or lithology or both with demonstrated examples from

outcrop and seismic data. The information on fracture intensity may aid geologists and engineers land horizontal wells in areas with high fracture intensity (i.e., wackstone rich or high curvature or both). Also, our 3D fracture intensity modeling method provides quantitative values of fracture abundance, which decreases uncertainty in our understanding of reservoir permeability.

Acknowledgments

The authors thank the Woodford Consortium at the University of Oklahoma for research funding. We would like to thank Herman Burrough for helping to find appropriate locations for measuring fractures. Also, we wish to thank Dr. Tom Rowland for various technical help. Data was provided by the late Jerry Wilson of Pathfinder Energy and Luis Castillo with Paisano Energy. We would like to thank reviewers for their time, suggestions and comments to strengthen the manuscript. A special thanks to Dr. Kurt Marfurt for his great and professional inputs. We also would like to thank Schlumberger Company, AASPI Consortium, and GGG Company for providing Techlog, Petrel and Hampson Russell software for use in research and education.

References

Al-Mudhafar, W., and M. Bondarenko. 2015, Integrating K-means clustering analysis and generalized additive model for efficient reservoir characterization. Paper read at 77th EAGE Conference and Exhibition 2015.

Al-Mudhafar, W. J. 2017, Geostatistical lithofacies modeling of the upper sandstone member/Zubair formation in south Rumaila oil field, Iraq. Arabian Journal of Geosciences, **10**, no. 6,153.

Al-Shaieb, Z., G. Beardall, P. Medlock, K. Lippert, F. Matthews, and F. Manni. 1993, Overview of Hunton facies and reservoirs in the Anadarko Basin. Paper read at Hunton Group core workshop and field trip: Oklahoma Geological Survey Special Publication.

Aliverti, E., M. Biron, A. Francesconi, D. Mattiello, S. Nardon, and C. Peduzzi. 2003, Data analysis, processing and 3D fracture network simulation at wellbore scale for fractured reservoir description. Geological Society, London, Special Publications, **209**, no. 1,27-37.

Amsden, T. W. 1975, Hunton Group, Late Ordovician, Silurian, and Early Devonian in the Anadarko Basin of Oklahoma. Vol. 121: Oklahoma Geological Survey, University of Oklahoma.

Antonellini, M., and P. N. Mollema. 2000, A natural analog for a fractured and faulted reservoir in dolomite: Triassic Sella Group, northern Italy. AAPG bulletin, **84**, no. 3,314-344.

Barbier, M., Y. Hamon, J.-P. Callot, M. Floquet, and J.-M. Daniel. 2012, Sedimentary and diagenetic controls on the multiscale fracturing pattern of a carbonate reservoir: The Madison Formation (Sheep Mountain, Wyoming, USA). Marine and Petroleum Geology, **29**, no. 1,50-67.

Busetti, S. 2009, Fracturing of layered reservoir rocks: The University of Oklahoma.

Chopra, S., and K. J. Marfurt. 2010, Integration of coherence and volumetric curvature images. The Leading Edge, **29**, no. 9,1092-1107.

Coléou, T., M. Poupon, and K. Azbel. 2003, Unsupervised seismic facies classification: A review and comparison of techniques and implementation. The Leading Edge, **22**, no. 10,942-953.

Dershowitz, W. S., and H. H. Herda. 1992, Interpretation of fracture spacing and intensity. Paper read at The 33th US Symposium on Rock Mechanics (USRMS).

Deutsch, C. V. 2006, A sequential indicator simulation program for categorical variables with point and block data: BlockSIS. Computers & Geosciences, **32**, no. 10,1669-1681.

Di Cuia, R., C. Gout, L. Bazalgette, and P. Masse. 2004, Are Fractures, in a Carbonate Sequence, Facies-Controlled?-The Maiella Mountain (Southern Italy), a Key for Complex Reservoir Modeling. Paper read at 66th EAGE Conference & Exhibition.

Dunham, R. J. 1962, Classification of carbonate rocks according to depositional textures, in W. E. Ham, ed. Classification of carbonate rocks—a symposium. AAPG Memoir. 1, p. 108-121.

Ericsson, J., H. McKean, and R. Hooper. 1998, Facies and curvature controlled 3D fracture models in a Cretaceous carbonate reservoir, Arabian Gulf. Geological Society, London, Special Publications, **147**, no. 1,299-312.

Fritz, R. D., and P. L. Medlock. 1994, Sequence stratigraphy of the Hunton Group as defined by core, outcrop, and log data. Bulletin Houston Geological Society,29-58.

Garfield, T. R., N. F. Hurley, and D. A. Budd. 1992, Little Sand Draw Field, Big Horn Basin, Wyoming: A Hybrid Dual-Porosity and Single-Porosity Reservoir in the Phosphoria Formation (1). AAPG Bulletin, **76**, no. 3,371-391.

Gaswirth, S. B., and D. K. Higley. 2013, Petroleum system analysis of the Hunton Group in West Edmond field, Oklahoma. AAPG bulletin, **97**, no. 7,1163-1179.

Gaswirth, S. B., and D. K. Higley. 2014, Petroleum systems and assessment of undiscovered oil and gas in the Anadarko Basin Province, Colorado, Kansas, Oklahoma, and Texas: USGS Province 58. US Geological Survey.

Ghosh, K., and S. Mitra. 2009, Structural controls of fracture orientations, intensity, and connectivity, Teton anticline, Sawtooth Range, Montana. AAPG bulletin, **93**, no. 8,995-1014.

Gringarten, E., and C. Deutsch. 1999, Methodology for variogram interpretation and modeling for improved reservoir characterization. Paper read at SPE Annual Technical Conference and Exhibition.

Hanks, C. L., J. Lorenz, L. Teufel, and A. P. Krumhardt. 1997, Lithologic and structural controls on natural fracture distribution and behavior within the Lisburne Group, northeastern Brooks Range and North Slope subsurface, Alaska. AAPG bulletin, **81**, no. 10,1700-1720.

Ketchen Jr, D. J., and C. L. Shook. 1996, The application of cluster analysis in strategic management research: an analysis and critique. Strategic management journal,441-458.

Kim, Y.-S., D. C. Peacock, and D. J. Sanderson. 2004, Fault damage zones. Journal of structural geology, **26**, no. 3,503-517.

Meissner, F. F., and E. Thomasson. 1999, Exploration Opportunities in the Greater Rocky Mountain Region, Central Western, USA. AAPG Bulletin, **83**, no. 12.

Milad, B., S. Ghosh, and R. M. Slatt. 2018, Comparison of rock and natural fracture attributes in karsted and non-karsted Hunton Group Limestone: Ada and Fittstown area, Oklahoma. Shale Shaker, **69**, no. 2,70-86.

Narr, W. 1991, Fracture density in the deep subsurface: techniques with application to point Arguello oil field (1). AAPG bulletin, **75**, no. 8,1300-1323.

Nelson, R. 2001, Geologic analysis of naturally fractured reservoirs: Gulf Professional Publishing.

Northcutt, R. A. 2002, History of Hunton Oil and Gas Exploration and Development in Oklahoma. Shale Shaker,149-158.

Pyrcz, M. J., and C. V. Deutsch. 2014, Geostatistical reservoir modeling: Oxford University Press.

Rogers, S., D. Elmo, G. Webb, and A. Catalan. 2015, Volumetric fracture intensity measurement for improved rock mass characterisation and fragmentation assessment in block caving operations. Rock Mechanics and Rock Engineering, **48**, no. 2,633-649.

Smith, J. 1951, The Cretaceous Limestone Producing Areas of the Mara and Maracaibo District–Venezuela, Geology. Paper read at 3rd World Petroleum Congress.

Sonntag, R., J. P. Evans, P. La Pointe, M. Deraps, H. Sisley, and D. Richey. 2014, Sedimentological controls on the fracture distribution and network development in Mesaverde Group sandstone lithofacies, Uinta Basin, Utah, USA. Geological Society, London, Special Publications, **374**, no. 1,23-50.

Stanley, T. M. 2013, The Hunton Anticline Quarry. Shale Shaker, **64 no. 3**,228-237.

Stanley, T. M., and K. Rottmann. 2001, Stratigraphy and facies relationships of the Hunton Group, Northern Arbuckle Mountains and Lawrence Uplift, Oklahoma. Vol. 33: Oklahoma Geological Survey, University of Oklahoma.

Staples, E., K. Marfurt, and Z. e. Reches. 2010, Preliminary Analysis of the Fractured Hunton Limestone, Oklahoma. Oklahoma City Geological Society.

Staples, E. R. 2011, Subsurface and Experimental Analyses of Fractures and Curvature, University of Oklahoma.

Terzaghi, R. D. 1965, Sources of error in joint surveys. Geotechnique, **15**, no. 3,287-304.

Thomas, E. 1986, Understanding fractured oil- reservoirs Oil & Gas Journal, **84**, no. 27,75-79.

Wang, G., and T. R. Carr. 2013, Organic-rich Marcellus Shale lithofacies modeling and distribution pattern analysis in the Appalachian BasinOrganic-Rich Shale Lithofacies Modeling, Appalachian Basin. AAPG bulletin, **97**, no. 12,2173-2205.

Watkins, H., R. W. Butler, C. E. Bond, and D. Healy. 2015, Influence of structural position on fracture networks in the Torridon Group, Achnashellach fold and thrust belt, NW Scotland. Journal of Structural Geology, **74**,64-80.

Wennberg, O., T. Svånå, M. Azizzadeh, A. Aqrawi, P. Brockbank, K. Lyslo, and S. Ogilvie. 2006, Fracture intensity vs. mechanical stratigraphy in platform top carbonates: the Aquitanian of the Asmari Formation, Khaviz Anticline, Zagros, SW Iran. Petroleum Geoscience, **12**, no. 3,235-246.

Xu, W., T. Tran, R. Srivastava, and A. G. Journel. 1992, Integrating seismic data in reservoir modeling: the collocated cokriging alternative. Paper read at SPE annual technical conference and exhibition.

Chapter 4: Practical aspects of upscaling geocellular geological models for reservoir fluid flow simulations: A case study in integrating geology, geophysics, and petroleum engineering multiscale data

Benmadi Milad, Sayantan Ghosh, Roger Slatt, Kurt Marfurt, and Mashhad Fahes

This paper will be submitted to **SEG/AAPG Interpretation**

Abstract

Optimal upscaling of a high-resolution static geologic model that reflects the flow performance of the reservoir by honoring reservoir heterogeneity is critical in reducing the time and cost of running reservoir flow simulations. We integrated 3D seismic data, well logs, thin sections, multiscale fracture studies, discrete fracture networks, and geostatistical methods to create a 100x150x1 ft gridded representative geologic model. We calibrated our gridded porosity and permeability parameters, including the evaluation of fractures, by history matching the simulated production rate and cumulative production volumes from a baseline fine-scale model history matching to those measured at five wells. These simulations were then recomputed using a suite of coarser grids to validate our property upscaling workflow.

Compared to our baseline history matching, increasing the horizontal grid cell sizes by factors of 2, 4, 8, and 16 results in cumulative production errors ranging from +0.5% for two time coarser to +74.22% for 16 times coarser. The errors of vertically upscaling was significantly less, i.e., ranging from +0.5% for two times coarser to +10.8% for 16 times coarser. Based on the overall production, a lateral grid cell size of more than the minimum required for successful simulation is not recommended. History matching showed a greater error in modeling the fractures. Fracture apertures 2x and 4x larger resulted in +11% and +169% cumulative production errors. Fracture

lengths 2x and 4x larger resulted in +301% and +1596% errors, indicating that the greater connectivity provided by natural fracture length is more important to production than the aperture. We constructed cumulative production error estimates as a function of the grid cell size (or the number of grid cells) to better define the trade-off between accuracy and run times.

We used 1, 5, 10, and 20 parallel processes for flow simulations. Using larger grid cell sizes and increasing the number of parallel processes both reduce the computation time to acceptable levels; both reductions can be described by simple power law equations. We demonstrate the efficacy of our workflow through the application to a Hunton Carbonate oil field in Oklahoma.

Introduction

Upscaling is the process of reducing a large number of the fine-scale grid blocks of a geological model to a smaller number of coarse-scale grid blocks while retaining the underlying geological properties (King et al., 1998; Stern, 2005; Ezekwe, 2010; Mehmood and Awotunde, 2016). The necessity of the upscaling process arises from the large size of geologic models with respect to the amount of computer processing capability. Although high cell resolution is preferred, such bulky models containing millions of cells are prohibitive for the software/hardware used to simulate a reservoir for purposes such as iterative production history matching, sensitivity analyses, production forecasting, proposing new or infill drilling locations and completion strategy, and risk analysis using a probabilistic approach, (Durlofsky, 2005; Adamson, 1996; Olalotiti-Lawal et al., 2017; Avansi et al., 2019). When a large number of discrete fractures is modeled, the model becomes even more cumbersome (Hui et al., 2017). Upscaling a fine-scale reservoir model must be performed with care. Excessive upscaling will lead to loss of the detailed

heterogeneities in the geologic model that directly affect the accuracy of the results (Mehmood and Awotunde, 2016).

Ma et al. (2013) found a 50% error in the simulated production volumes after upscaling. The flow from thin bed conduits and thin bed baffles is particularly sensitive to inaccurate upscaling. Santacruz et al. (2012) simulated the flow of a leveed-channel system, assigning different permeabilities to the thin slump deposits. They concluded that slump deposits acted as barriers to waterflood penetration into the oil zones, whereby the lower permeability of the slumps significantly reduced the production rate. In many reservoir simulation studies, upscaling is performed only in the vertical direction, as the areal grid cell size of the reservoir model typically approximates the heterogeneity provided by 3D seismic data (Ma et al., 2013).

Meddaugh (2006) examined the impact of vertical and areal upscaling on fluid flow, using multiple geostatically generated porosity model realizations. He concluded that the changes of the cumulative water injection are more sensitive to the number of realizations than to the level of vertical upscaling, and that the recovery factor decreases when the areal upscaling increases. A challenge in upscaling geologic reservoir model parameters is to determine a sufficiently coarse reservoir grid cell size (Stern, 2005; Ezekwe, 2010; Avansi et al., 2019) without sacrificing the detail of the original structures, rock properties, layered nature of the reservoir, and reservoir heterogeneity. Regardless of the upscaling process used, a proper production history match using fluid flow simulation validates the upscaling process.

There are alternative method of upscaling including arithmetic, harmonic, geometric, power law, pressure solver, and weighted averages algorithms, where the choice depends on the rock property (Mehmood and Awotunde, 2016). While in general, arithmetic averaging works well

for low-variability porosity and saturation properties, Deutsch (2017) finds simple arithmetic averages fail to upscale thin layers.

Time is money. Even if a reservoir analysist has unlimited computer resources, he or she may have a larger impact on field performance by history matching dozens of wells using a more economical upscaled model than by history matching a single well using a highly accurate fine-scale model. The purpose of this study is therefore to find the optimal level of upscaling, beyond the production history match grid cell size, at which the most significant geological and petrophysical properties and the simulation accuracy is retained.

We begin our study with a review of the geology of the Hunton carbonate of Oklahoma as it appears in the three study areas. We then describe our methodology, based on the well-established workflow of defining and then history matching a finely gridded, high resolution model. We construct a fine-grid model as our reference and discuss the impact of the simulation on our analysis of the reservoir performance of these Hunton wells. we then use a series of homogenous models to simulate production, thus removing the effect of geologic heterogeneity while divulging the numerical errors associated with each subsequent increase in grid cell sizes. Next, we show the effect of upscaling both the horizontal and vertical property variations on computation run times and accuracy, constructing power law relations that can be used to predict the run times for future models. We conclude with a summary of our results and a recommendation that the reservoir analysis balance the need for accuracy of given well simulation to the value of having less accurate results for multiple wells in the oil field.

Geology

The areas of study are in Pottawatomie, Pontotoc, and Murray Counties, Oklahoma (**Figure 4.1**). We conducted field measurements of the Hunton Anticline exposure as well as the Ada and

Fittstown carbonate outcrops of the Chimneyhill subgroup to build a realistic fracture model for our upscaling and simulation studies. The subsurface data (logs, core, and seismic) comes from a well located in Pottawatomie County.

The Hunton Group is a prolific oil and gas-producing reservoir in the Midcontinent (Gaswirth and Higley 2014). The Hunton Group carbonates were deposited during Late Ordovician-Silurian-Early Devonian time in Oklahoma and is bounded by the underlying conformable Sylvan Shale and the overlying unconformable Woodford Shale (**Figure 4.2**). The Hunton Group, including the Chimneyhill subgroup, is associated with a shallow-warm water carbonate ramp of a gently sloping surface with less than 1^{o} dip (Amsden, 1975; Stanley and Rottmann, 2001). In the area of study (**Figure 4.1**), the stratigraphic thickness ranges from 50 to 120 ft. Three primary lithologies of the Chimneyhill in the study area include wackestone, mudstone, and mud-dominated wackestone (Milad and Slatt, 2018). The Hunton Group facies comprise a series of progradational and aggradational parasequences (shallowing-upward cycles) (Fritz and Medlock, 1994). Fractures in the Hunton Group are considered as one of the key components to enhance the hydrocarbon production (Al-Shaieb et al., 1993).

Ghosh et al. (2018a) and Ghosh et al. (2018b) provide further details on the outcrop and subsurface fractures, current tectonic stress regime, and paleo tectonic stress regimes in the study area and surrounding areas in Oklahoma.

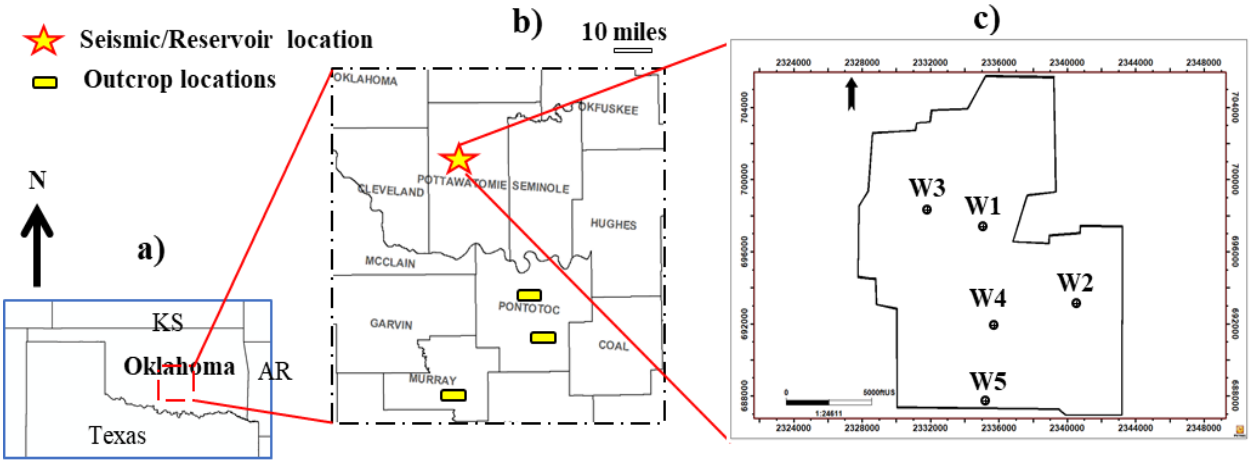

Figure 4.1. Locations of the studied areas. (a) Oklahoma map with adjacent states. (b) Data locations in Pottawatomie, Pontotoc, and Murray Counties. Location of 3D seismic, subsurface log and cores data in Pottawatomie County is indicated by the star. Yellow bars indicate outcrops in Pontotoc and Murray Counties. (c) Limits of the Pottawatomie County survey showing subsurface well locations.

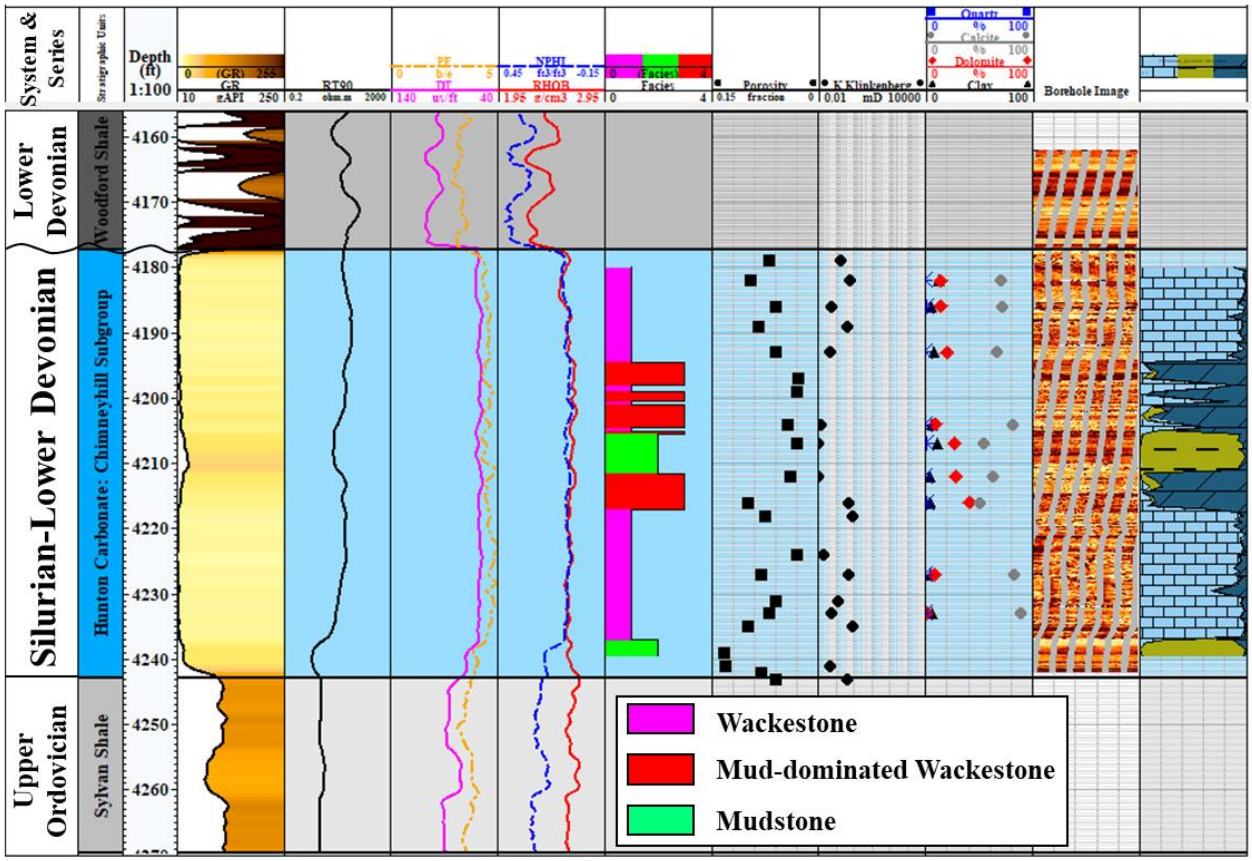

Figure 4.2. Stratigraphic column of the Chimneyhill subgroup of the Hunton Group carbonate in the study area (Pottawatomie County, Oklahoma) from a subsurface well. Tracks from left to right are: geologic time, stratigraphic units (Viola carbonate, Sylvan shale, Hunton Group carbonate, and Woodford shale), true vertical depth (ft), gamma ray, deep resistivity (RT90), photoelectric (PE) and sonic (DT) logs, neutron porosity (NPHI) and bulk density (RHOB), electrofacies, core porosity, core permeability, core mineralogy, borehole image, and lithology.

Methodology

Heterogeneous model

The general workflow includes the following steps:

1. creation of the geologic model including the discrete fracture network (DFN),
2. upscaling the geologic and DFN model for subsequent flow simulation,
3. production history matching of the fine grid baseline model, and

repeated forward modeling of the production rate and volume at increasingly coarser grid sizes and fracture dimensions.

The **Figures 4.3** and **4.4** describe the workflow used to populate the 3D volume, where we:

1) construct the relationship between the acoustic impedance logs, lithology (using thin sections), and porosity logs at well locations,

2) derive core porosity and vertical/horizontal permeability relationships (derived using laboratory experiments,

3) calculate fluid saturation from well logs,

4) invert the seismic data to estimate a P-wave impedance volume,

5) correlate the P-wave impedance to the well log electrofacies and porosity measurements to construct a horizontal variogram to geostatistically construct 3D estimates of lithology and porosity,

6) build DFN models based on the outcrop field measurements, and finally,

7) upscale the fracture and matrix properties together for production simulations.

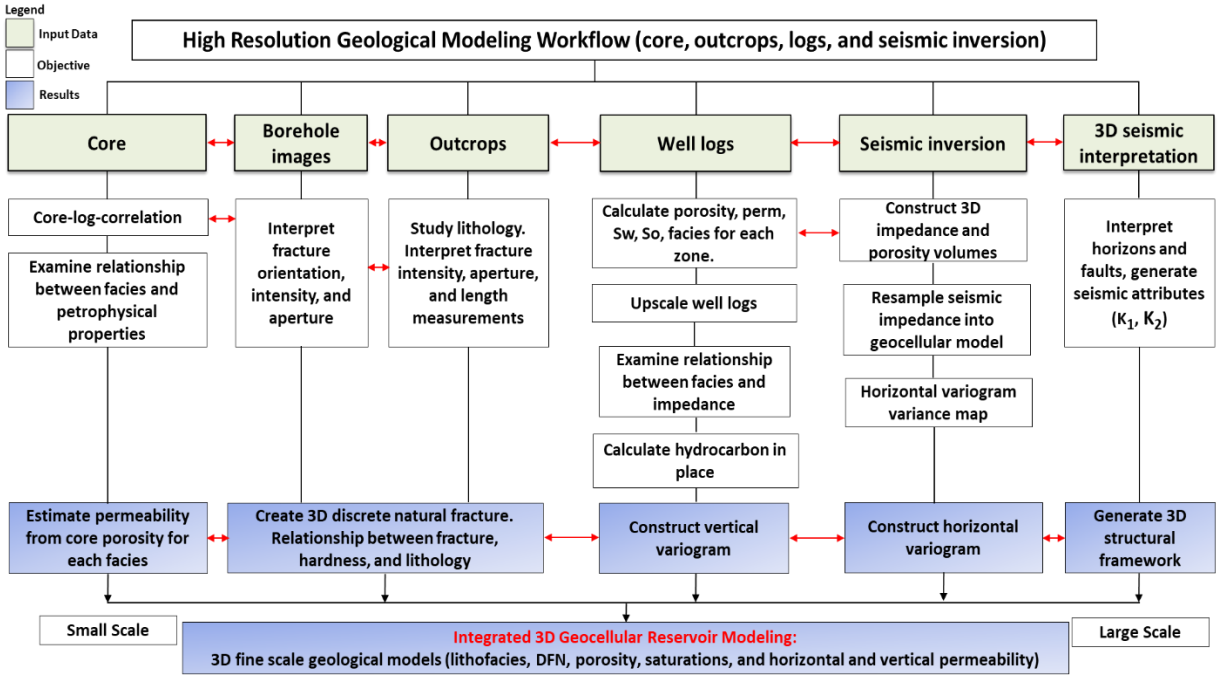

Figure 4.3. Methodology depicting the integration of various sources of data for building the static reservoir model.

The original geologic model using a 20x30x1 ft geologic grid resulted in 13,292,228 cells which exceeded the capabilities of our computer resources. We therefore upscaled the initial grid to 100x150x1 ft to form our baseline model, which was modified to match the production history. This baseline model was then further upscaled to coarser 200x300x1 ft, 400x600x1 ft, 800x1200x1 ft, and 1600x2400x1 ft grid cell sizes with a constant bed thickness of 1 ft for the horizontal upscaling. Doubling the grid cell size in the X and Y directions (constant 1 ft bed thickness in Z direction) reduces the lateral heterogeneity and modifies the production rate and cumulative production. To understand the effect of vertical upscaling on production we coarsened the cell size to 100x150x2 ft, 100x150x4 ft, 100x150x8 ft, and 100x150x16 ft. Finally, to understand the effect of natural fractures on production, we increased the fracture lengths and widths by factors of two and four for the baseline 100x150x1 ft grid used in history matching.

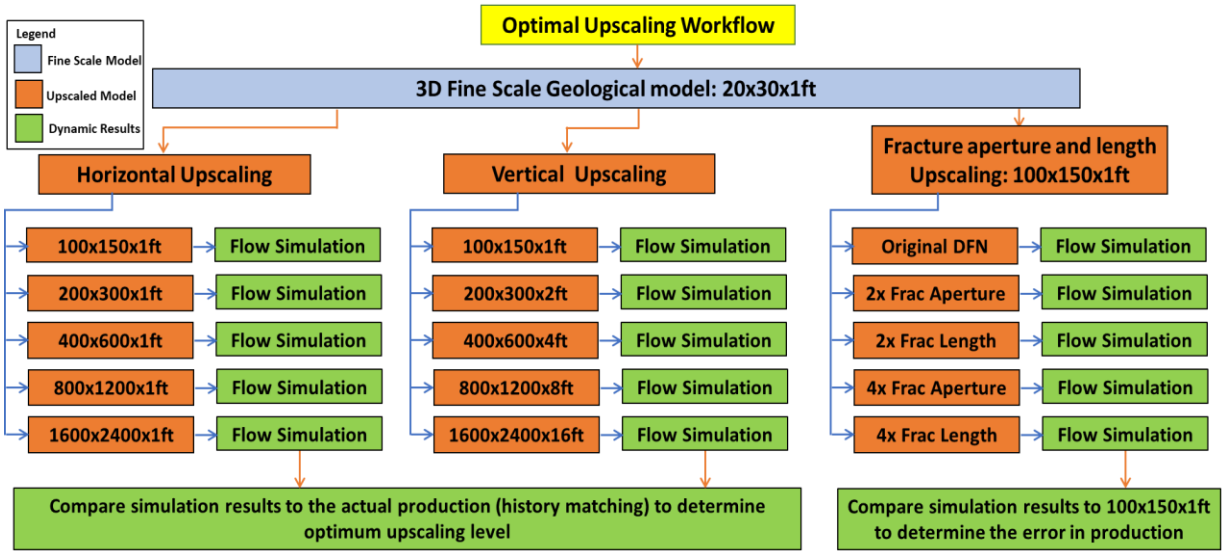

Figure 4.4. Workflow depicting history match. The reference fine grid has cells that measure Δx=20 ft, Δy=30 ft, and Δz=1 ft. Flow was simulated for the coarser horizontally and vertically upscaled models, as well as for the models with upscaled fracture lengths and apertures.

Homogenous model

We constructed homogenous models in order to quantify the production errors, resulting from the upscaling processes, that are associated with reservoir rock heterogeneity. The homogenous models were derived from the already-existing heterogeneous models using average values for the matrix and fracture parameters that were obtained from the fine grid 20 by 30 by 1 model (**Table 4.1).**

The partial differential equations used for the reservoir simulators include the material balance equation, flow equations for three-phase flow of oil, water, and gas, and formation and fluid compressibility equations. The finite difference is a numerical method that is used to solve partial differential equations. However, the numerical method only gives an approximate solution to the discretized grid system of partial differential equations resulting in a truncation error (Lantz, 1971; Fanchi, 1983; Ezekwe, 2010). Therefore, the production errors can be associated with both reservoir heterogeneity and numerical errors.

We quantified the effect of truncation error (numerical error) in the different simulators, first by making a series of homogenous vertical and homogenous horizontal upscaled models with different grid cell sizes (horizontal upscaling: 100x150x1 ft, 200x300x1 ft, 400x600x1 ft, 800x1200x1 ft, and 1600x2400x1 ft; vertical upscaling: 100x150x2 ft, 100x150x4 ft, 100x150x8 ft, and 100x150x16 ft grid cell sizes). We then performed the calculations as shown below. We used the 150x100x4 grid cell size as an example:

$$Horiz\_upsc\_prod\_err\_heterog_{150x100x4} = \frac{heterog_{150x100x4} - heterog_{150x100x1}}{heterog_{150x100x1}} \quad \textbf{(1)}$$

$$Horiz\_upsc\_prod\_err\_homog_{150x100x4} = \frac{homog_{150x100x4} - homog_{150x100x1}}{homog_{150x100x1}} \quad \textbf{(2)}$$

Horizontal upscaling production error due to geologic heterogeneity =

$Horiz\_upsc\_prod\_err\_heterog_{150x100x4}$-$horiz\_upsc\_prod\_err\_homog_{150x100x4}$ **(3)**

Horizontal upscaling production error due to numerical uncertainty=

$Horiz\_upsc\_prod\_err\_homog_{150x100x4}$, i.e., same as **(2)**

Percentage errors for all grid cell sizes are calculated with respect to the history match grid cell size (i.e., 150x100x1 ft). It is noteworthy that history matching was not performed for the homogeneous models. Similar calculations may be performed for the error in vertical upscaling. However, this limitation is overcome by the use of percentage errors instead of actual errors as shown in the equations above.

Table 4.1. Reservoir simulation parameters for the homogenous models used in all vertical and horizontal upscaling and production simulation cases.

Matrix parameters	Average values	Units	Natural fracture parameters	Average values	Units
Φ in XY directions	0.131	mD	Φ	0.00009	fraction
K_V	0.0001	mD	K_I	1	mD
Sw	5	%	K_J	1	mD
Φ	0.07	fraction	K_K	1	mD
			Sigma factor	7.6	

Where:

Φ= porosity

K_V= matrix permeability in vertical direction,

Sw: water saturation,

K_I, K_J, K_K: fracture permeability in x, y, and z directions, and

Sigma factor: link between the matrix and fracture properties that describes fluid flow between the matrix and the dual-porosity/permeability model in a porous medium.

If Sigma factor = 0, no communication between the matrix and natural fractures occurs.

Estimation of reservoir parameters

Electrofacies form one of the key components of the models described in **Figure 4.3**. We begin with Principal Component Analysis (PCA) of the electric logs. These values serve as input to subsequent Self-Organizing Mapping (SOM) to construct electrofacies logs. We corroborate the geologic interpretation of the electrofacies predictions using thin sections and borehole images. We constructed the relationship between the porosity and vertical and horizontal permeabilities from cores. Porosity logs were correlated with core porosity measurements which in turn are linked to the facies distribution (**Figure 4.5e)**. We estimated fluid saturation by applying Archie's law on the well logs. We measured porosities as well as vertical and horizontal permeabilities from core plugs facilitating the construction of porosity-permeability relationships. Following previous work by Milad et al. (2018a), Milad et al. (2018b), Milad and Slatt (2018), we constructed vertical variograms from the well logs to populate the petophysical data spatially.

Seismic data

We used seismic data to delineate formation boundaries, to define major faults, and to provide a volumetric estimation of P- and S-wave impedances. These impedances were crucial in

differentiating fossiliferous wackestone from dolomitized mudstone rocks. The low frequency background model used in impedance inversion used five wells (**Figures 4.1c** and **4.5a**) with P-wave velocity, S-wave velocity, and density logs and ranged from the top of the Woodford surface to the top of the Viola surface (**Figure 4.2**). Six common angle gathers ranging from 0^o to 30^o at 5^o increments were used for prestack inversion. The main purpose of the inversion is to provide horizontal variograms for porosity distribution. Another purpose is to find the major and minor directions of lithologic variation (**Figure 4.5b**), impedance (**Figure 4.5c**), and the facies distribution (**Figure 4.5d**).

DFN Modelling

Figure 4.5f shows a DFN model for one of the four fracture sets. We considered four main parameters in the creation of the fracture network: intensity, geometry, orientation, and aperture. Parameters defining the fracture intensity and dimension can be found in Milad et al. (2018b). The mean dip and mean dip azimuths were assigned for each fracture set based on the borehole measurements. We assigned the statistical distributions of the borehole-measured fracture apertures (calibrated to the maximum aperture value observed in the core) to the model. We used the stochastic technique described by Schlumberger (2014) in © Petrel Software manual to create a DFN volume for the entire seismic cube with a distribution guided by the fracture intensity map (grid cell intensity values) for each set, where the

Fracture porosity = fracture aperture/fracture spacing. **(4)**

Natural fracture permeabilities were calculated using a cubic aperture (y) law

$$Permeabiltiy = \frac{y^3}{12} \quad \textbf{(5)}$$

Upscaling

We follow Oda (1985) to upscale the fracture porosity, the fracture sigma length in the x, y, and z directions (spanned by *J, K,* and *I* grid indices), as well as the fracture permeability. Assuming Darcy's Law for laminar flow through an isotropic porous medium, Oda (1985) shows how to upscale the geometry and properties of the fractures within a given cell to construct the permeabilities of an equivalent grid cell. Projecting the fracture isotropic permeability onto the fracture plane and then scaling it to the ratio between the fracture volume and grid cell volume provides a net permeability tensor for each grid cell. Eigenvectors of the net permeability tensor provide the principal permeabilities.

The simulation software requires two simulation cells to model a dual porosity/dual permeability system where adjacent grid cells communicate through both the fractures and the matrix. This construct allows one to define porosity and permeability where the transmissibilities are connected or coupled to each other using a quantity called the sigma factor (Schlumberger, 2014).

Effective permeability = fracture area/cell volume. **(6)**

Fracture porosity = total fracture area *fracture aperture/cell volume. **(7)**

Geocellular gridding, history matching, and forward modelling

The grid cells are aligned with an orthogonal X, Y, Z Cartesian coordinate system. We used small vertical cell sizes to accommodate the heterogeneities observed in the well logs. The relative grid size is a function of the heterogeneity, where coarser spacing can be used if the reservoir properties are more homogeneous in one direction (**Figure 4.5b**). We used proportional slicing between the top and base correlation surfaces to divide the reservoir into appropriate layers.

Based on P-impedance from seismic inversion, we rotated the computational grid to align with the direction of the depositional trend (30 ft in the major direction of N15E [*x*] direction and 20 ft in the minor [*y*] direction) (**Figure 4.5b**).

Result

Static modelling

Fine scale geologic models

Figure 4.5a shows the trajectories of five wells used in this study. Geologic models in **Figures 4.5b-4.5f** were obtained using the method described in **Figure 4.3**, i.e., by utilization of core, log, outcrop, and seismic data.

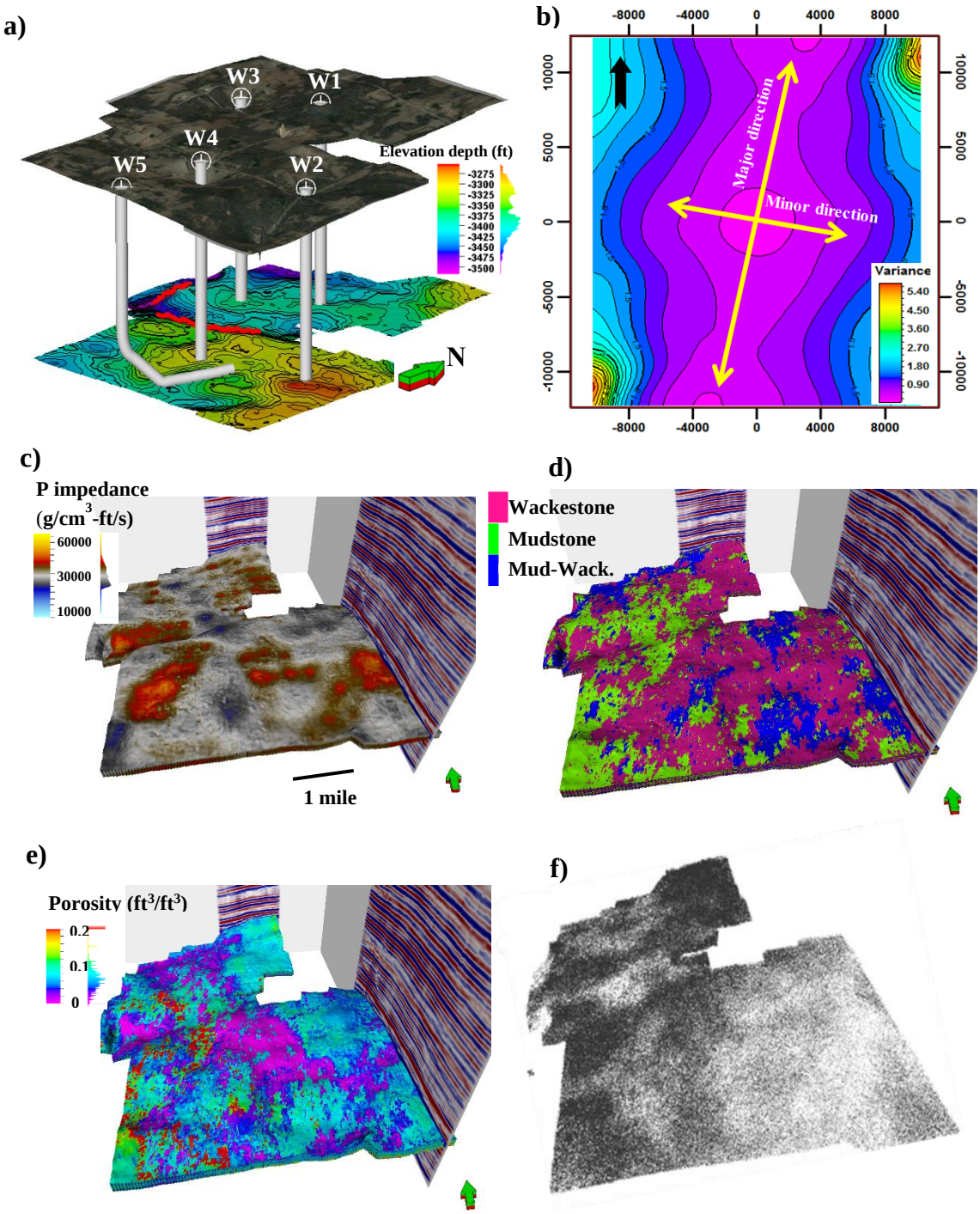

Figure 4.5. Results of fine scale model. (a) Wells showing four vertical and one horizontal well trajectories. (b) Major and minor variogram directions derived from impedance maps of seismic inversion (major direction: N15E, major range: 18840 ft, minor direction: S75E, minor range: 15800 ft). (c) Impedance map from inversion. (d) Lithology derived from seismic impedance map. (e) Porosity maps from the inversion-derived variogram. (f) DFN map of the NE-SW fracture set. All other sets have similar spatial relative density variation.

Coarse scale reservoir simulation models

Figure 4.6a shows a 3-dimensional porosity model that has been upscaled to 150x100x1 ft grid from a 20x30x1 ft (**Figure 4.5e**) grid. **Figure 4.6b** shows the water saturation calculated from the well logs, upscaled onto the 20x30x1 ft grid, and then subsequently upscaled onto the 150x100x1 ft grid. **Figures 4.6c** and **4.6d** show the upscaled combined fracture and matrix permeabilities.

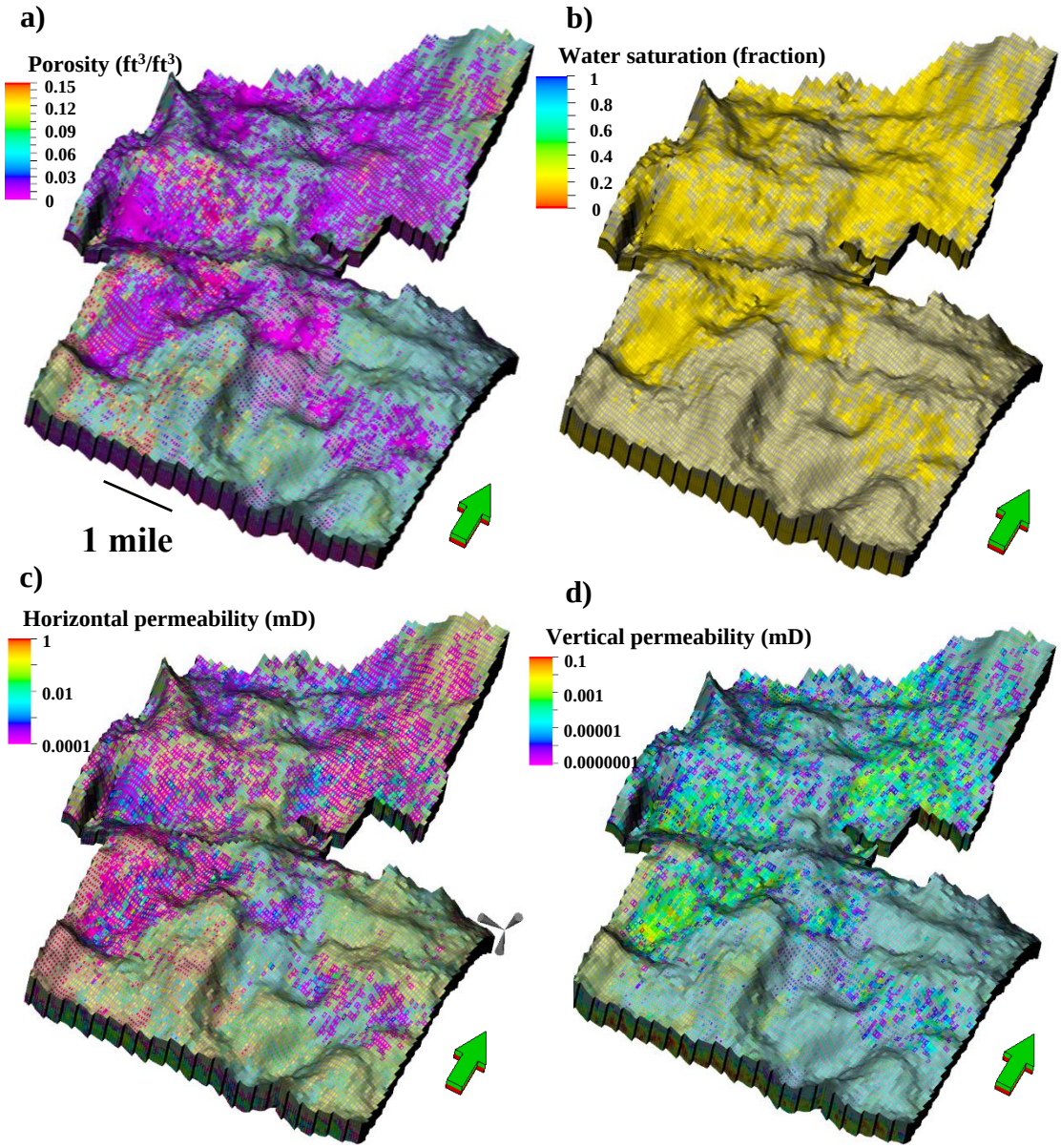

Figure 4.6. Static heterogeneous models upscaled to 100x150x1 ft grid cell size: (a) porosity (b) water saturation, (c) horizontal permeability, and (d) vertical permeability. Vertical exaggeration is 20 times.

Dynamic simulation

Table 4.2 provides detailed information and properties of the reservoir.

Table 4.2. Reservoir simulation parameters and well data constraints. These data are kept the same for all upscaling simulation cases.

Well rate and pressure constraints	
Well No	**Oil rate (STB/d)**
Well 1	50
Well 2	130
Well 3	20
Well 4	40
Well 5	125
Simulation period: 1976-01 to 2016-12	

Fluid Model Parameters	
Phases	Gas, Oil, Water
Min pressure	300 psi
Max pressure	2000 psi
Reference pressure	1860 psi
Temp.	170.33 ^{o}F
Gas Sp.gr	0.815
Oil gravity	45 API
Bubble point pressure	1860 psi
Water salinity	30000 ppm

Effect of horizontal upscaling

Table 4.3 shows total errors resulting from the truncation computation and geologic heterogeneity. **Table 4.4** shows numerical errors due to computation truncation from homogenous models. **Table 4.5** shows the effect of geologic heterogeneity on the effect of production using Equations 1, 2 and 3 as mentioned earlier. The effect of horizontal upscaling on production is highly variable.

For the total (numerical+heterogeneity) error cases, Well 3 (**Figure 4.7c**) shows little variation (-4%) in cumulative production (**Table 4.3**) between the 100x150x1 (history match) green line and the next larger grid (200x300x1 ft). In other wells (**Figures 4.7a**, **4.7b**, **4.7d**, and **7e**), the next larger grid (200x300x1 ft) shows a significant change (total error) in production rate (+22 to + 131%) (**Table 4.3**). The remaining larger grid cell sizes (400x800x1 ft, 800x1600x1 ft, and 1600x2400x1 ft) induced significant differences in cumulative production and production rates with the history-matched grid cell size (i.e., +22% to +537%) [**Figures 4.7a-4.7f**, **Table 4.3**]. Note that progressively larger grid cell sizes do not necessarily result in a progressively larger departure from the history match (green curve) for individual wells. However, such a correlation can be

observed for the cumulative production in all wells combined (**Tables 4.3, 4.4, and 4.5**). For example, the orange (800x1200x1 ft) and black (1600x2400x1ft) curves swap position from one well to the other (**Figures 4.7a-4.7e**).

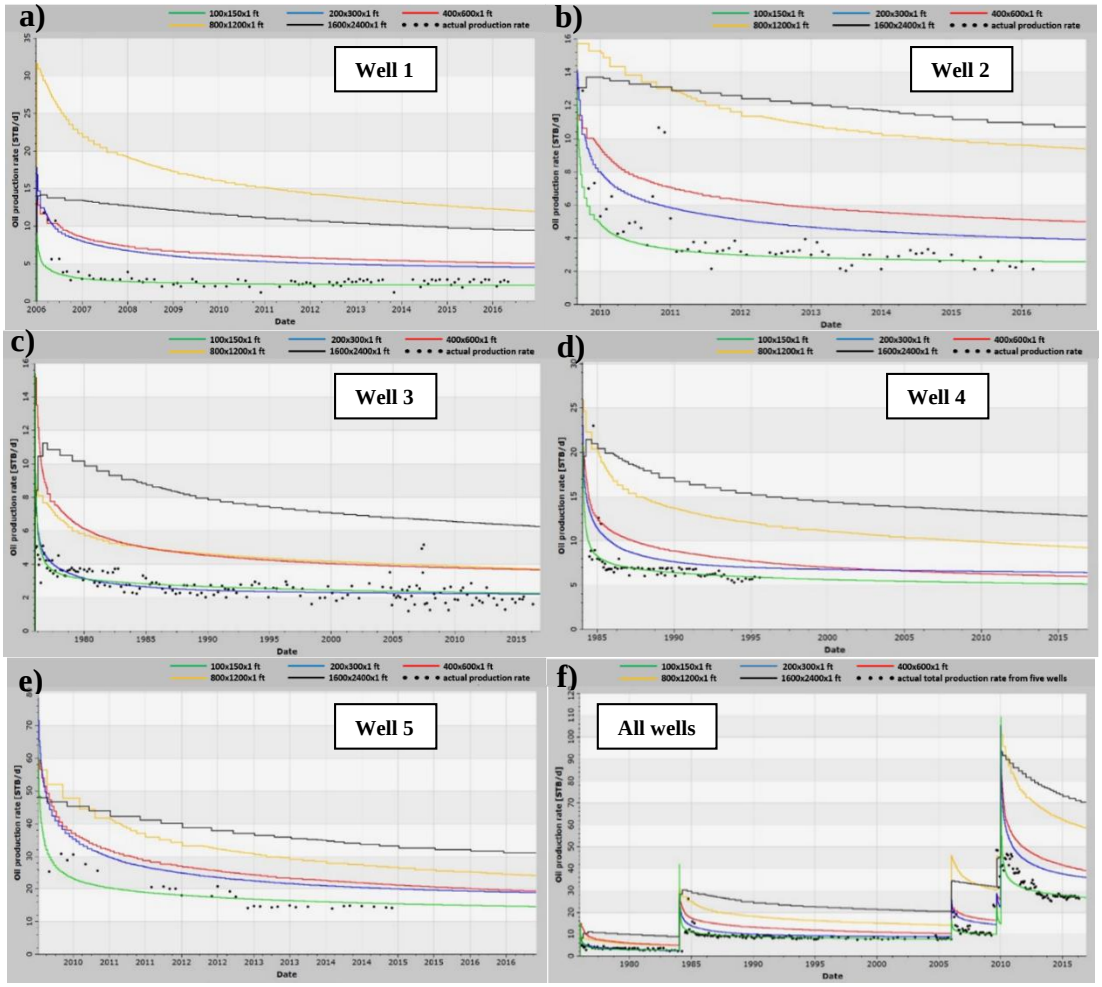

Figure 4.7. Effect of horizontal upscaling on production. (a)-(e) Rate production for wells 1-5 respectively. (f) Production rates for all wells. Dots: actual production rates; Production rates for different grid cell sizes- green curves: 100x150x1 (history match); blue curves: 200x300x1; red curve: 400x600x1; orange curves: 800x1200x1; black curves: 1600x2400x1.

Table 4.3. Cumulative production comparisons in horizontal upscaling cases for the heterogeneous models. Well by well actual cumulative production, history-matched (100x150x1 grid) cumulative production, and comparisons of larger grid cell sizes with history-matched cumulative production are shown. Errors in the history match column are with respect to the actual cumulative production and those in remaining columns are with respect to the history-matched production.

	Actual cumulative production (STB)	100x150x1 (history match) cumulative production error	200x300x1 cumulative production error	400x600x1 cumulative production error	800x1200x1 cumulative production error	1600x2400x1 cumulative production error
Well 1	10,170	9,626 (-5 %)	+131 %	+155 %	+345 %	+537 %
Well 2	10,217	7,542 (-26 %)	+62.6 %	+99 %	+261 %	+285 %
Well 3	37,398	39,634 (6%)	-4 %	+71 %	+72 %	+189 %
Well 4	27,348 @1995	29,333 (7%)	+22 %	+29 %	+100 %	+153 %
Well 5	37,956@2014	34,254 (-10%)	+36 %	+44 %	+80 %	+106 %
All wells combined	175,064	170,015 (0.5%)	+28%	+54%	+120%	+166%

Table 4.4. Cumulative production comparisons in horizontal upscaling cases for the homogenous models. Well by well actual cumulative production and comparisons of larger grid cell sizes with (100x150x1 grid) combined cumulative production are shown.

	100x150x1 cumulative production error	200x300x1 cumulative production error	400x600x1 cumulative production error	800x1200x1 cumulative production error	1600x2400x1 cumulative production error
Well 1	107.99 %	16.57 %	50.48 %	85.95 %	123.84 %
Well 2	69.55 %	19.12 %	54.95 %	91.25 %	121.43 %
Well 3	54.01 %	11.91 %	32.00 %	67.21 %	92.54 %
Well 4	131.78 %	12.78 %	35.50 %	66.05 %	72.97 %
Well 5	-36.87 %	16.56 %	50.30 %	79.46 %	108.21 %
All wells combined	4.77 %	14.02 %	39.90 %	75.22 %	91.78 %

Table 4.5. Cumulative production comparisons in horizontal upscaling cases after subtracting the numerical errors in Table 4.4 from total errors in Table 4.3 for 200x300x1, 400x600x1, 800x1200x1, and 1600x2400x1 cell sizes.

	Actual cumulative production (STB)	100x150x1 (history match) cumulative production error	200x300x1 cumulative production error	400x600x1 cumulative production error	800x1200x1 cumulative production error	1600x2400x1 cumulative production error
Well 1	10,170	9,626 (-5 %)	114.43 %	104.52 %	259.05 %	413.16 %
Well 2	10,217	7,542 (-26 %)	43.48 %	44.05 %	169.75 %	163.57 %
Well 3	37,398	39,634 (6%)	-15.91 %	39.00 %	4.79 %	96.46 %
Well 4	27,348 @1995	29,333 (7%)	9.22 %	-6.50 %	33.95 %	80.03 %
Well 5	37,956@2014	34,254 (-10%)	19.44 %	-6.30 %	0.54 %	-2.21 %
All wells combined	175,064	170,015 (0.5%)	13.98 %	14.10 %	44.78 %	74.22 %

Effect of vertical upscaling

Table 4.6 shows total errors, **Table 4.7** shows numerical errors, and **Table 4.8** shows errors due to geologic heterogeneity for the vertical upscaling cases. **For the total (numerical+heterogeneity) error cases, Figures 4.8a-4.8c** and **4.8e-4.8f** show little difference between the history match (green curves) and larger grid cell curves. In addition, essentially all

vertically upscaled matches may be considered as reasonable history matches to the observed data (**Figures 4.8a-4.8c**, **4.8e-4.8f**). Larger grid cell size always leads to a jump in the cumulative production (**Table 4.6**) and production rate compared to the base history-match grid cell size of 100x150x1 ft. Vertical upscaling makes a noticeable difference in only one well where well 4 (**Figure 4.8d**) has a noticeable 17% deviation in production rate and cumulative production (**Table 4.6**) with the largest vertical grid cell size (i.e., 16 ft).

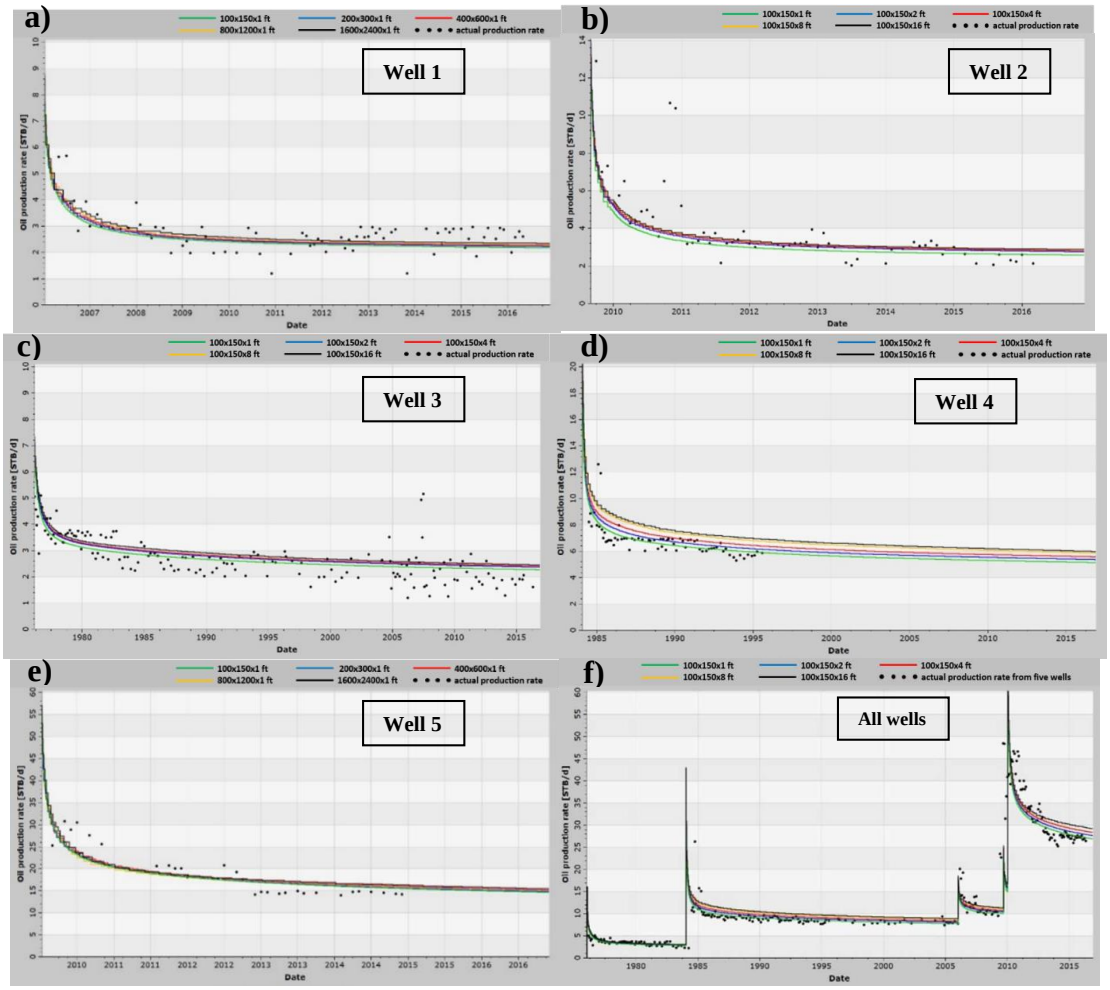

Figure 4.8. Effect of vertical upscaling on production rate. (a)-(e) Production rate for individual wells. (f) Sum of production rates for all wells (field production). The difference in the field production rate is due to different start time of production for these five wells. Dots: actual production rates; Production rates for different grid cell sizes- green curves: 100x150x1 (approximate history match); blue curves: 100x150x2; red curve: 100x150x4; orange curves: 100x150x8; black curves: 100x150x16 of cumulative production for individual wells.

Table 4.6. Cumulative production comparisons in vertical upscaling cases for the heterogeneous models showing total (numerical uncertianty+geologic heterogeneity). Well by well actual cumulative production, history match (100x150x1) cumulative production, and comparisons of larger grid cell size with history match cumulative production are shown. Errors in the history match column are with respect to the actual cumulative production and those in remaining columns are with respect to the history match (i.e., not actual) production case (100x150x1).

	Actual cumulative production (STB)	100x150x1 (history match) cumulative production error	100x150x2 cumulative production error	100x150x4 cumulative production error	100x150x8 cumulative production error	100x150x16 cumulative production error
Well 1	10,170	9,626 (-5 %)	+2.3 %	+3.8 %	+4.9 %	+7.6 %
Well 2	10,217	7,542 (-26 %)	+6.7 %	+8.7 %	+9.4 %	+10.9 %
Well 3	37,398	39,634 (6%)	+4.4 %	+5.7 %	+5.7 %	+8.3 %
Well 4	27,348 @1995	29,333 (7%)	+4.3 %	+8.5 %	+14.6 %	+17.1 %
Well 5	37,956@2014	34,254 (-10%)	+0.5 %	+2.6 %	+0.18 %	+3.6 %
All wells combined	175,064	170,015 (0.5%)	+3.4%	+6.0%	+8.0%	+10.8%

Table 4.7. Cumulative production comparisons in vertical upscaling cases for the homogenous models showing errors due to numerical uncertainty. Well by well actual cumulative production and comparisons of larger grid cell sizes with (100x150x1 grid) cumulative production are shown.

	100x150x1 cumulative production error	100x150x2 cumulative production error	100x150x4 cumulative production error	100x150x8 cumulative production error
Well 1	108.02 %	0.00 %	-0.07 %	0.18 %
Well 2	69.55 %	0.09 %	0.25 %	0.59 %
Well 3	54.01 %	-0.05 %	-0.09 %	0.12 %
Well 4	131.78 %	0.01 %	0.27 %	0.86 %
Well 5	-36.87 %	-0.58 %	-1.96 %	-1.59 %
All wells combined	4.77 %	-0.07 %	-0.17 %	0.21 %

Table 4.8. Cumulative production comparisons in vertical upscaling cases after subtracting the numerical errors in Table 4.7 from total errors in Table 4.6 for 100x150x2, 100x150x4, 100x150x8, and 100x150x16 cell sizes.

	Actual cumulative production (STB)	100x150x1 (history match) cumulative production error	100x150x2 cumulative production error	100x150x4 cumulative production error	100x150x8 cumulative production error	100x150x16 cumulative production error
Well 1	10,170	9,626 (-5 %)	2.30 %	3.87 %	4.72 %	7.60 %
Well 2	10,217	7,542 (-26 %)	6.61 %	8.45 %	8.81 %	10.90 %
Well 3	37,398	39,634 (6%)	4.45 %	5.79 %	5.58 %	8.30 %
Well 4	27,348 @1995	29,333 (7%)	4.29 %	8.23 %	13.74 %	17.10 %
Well 5	37,956@2014	34,254 (-10%)	1.08 %	4.56 %	1.77 %	3.60 %
All wells combined	175,064	170,015 (0.5%)	3.47 %	6.17 %	7.79 %	10.80 %

Comparison

The difference in production rates from vertical upscaling is not nearly as dramatic as that observed from horizontal upscaling (**Figure 4.9a and 4.9b**), though both follow a logarithmic relationship.

a)

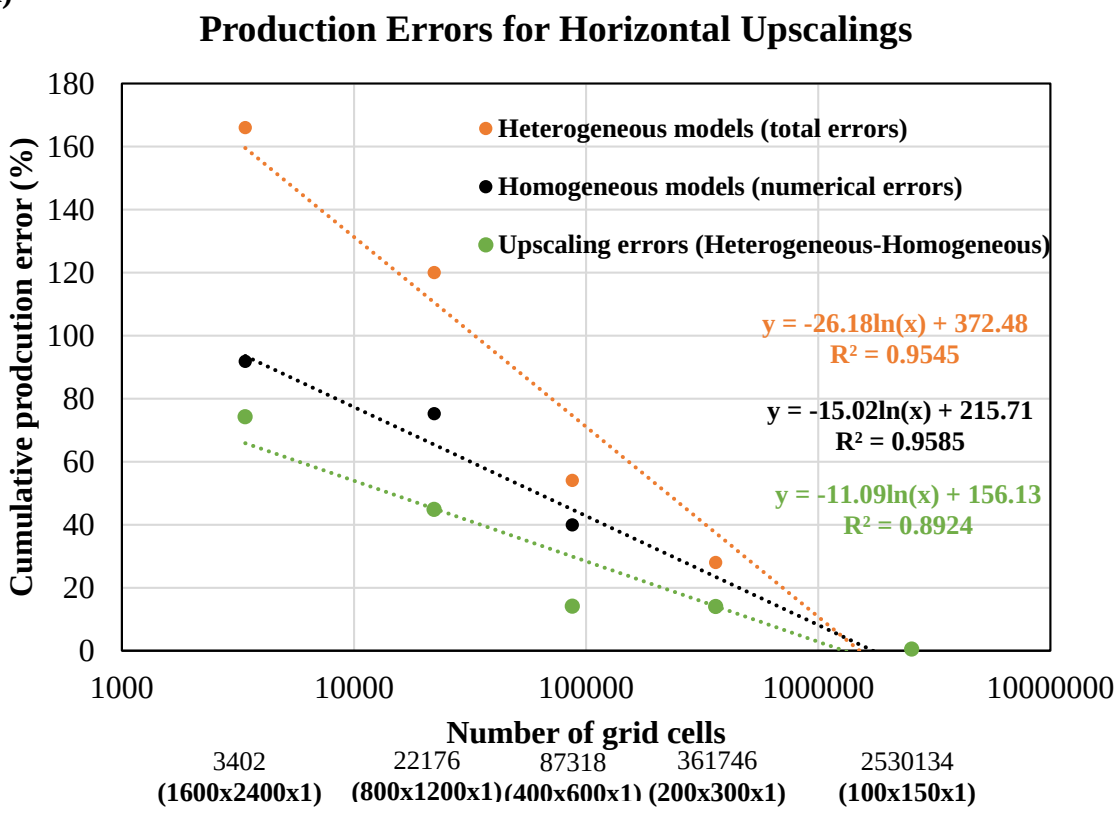
Production Errors for Horizontal Upscalings
Cumulative prodcution error (%)
180
160
140
120
100
80
60
40
20
0
1000
10000
100000
1000000
10000000
Number of grid cells
3402
(1600x2400x1)
22176
(800x1200x1)
87318
(400x600x1)
361746
(200x300x1)
2530134
(100x150x1)
Heterogeneous models (total errors)
Homogeneous models (numerical errors)
Upscaling errors (Heterogeneous-Homogeneous)
y = -26.18ln(x) + 372.48
R² = 0.9545
y = -15.02ln(x) + 215.71
R² = 0.9585
y = -11.09ln(x) + 156.13
R² = 0.8924

b)

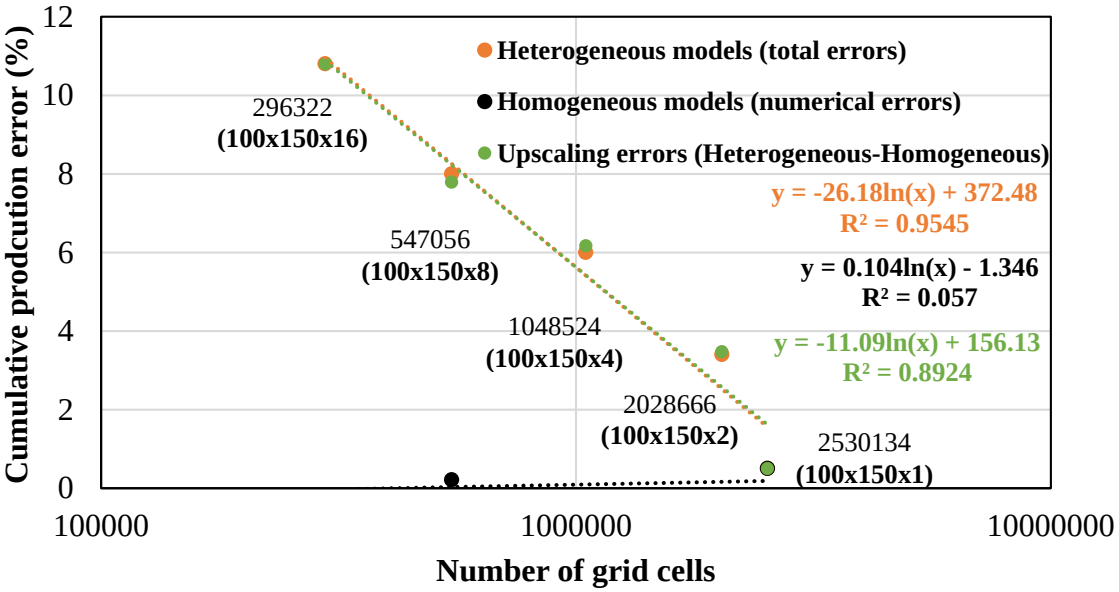
Production Errors for Vertical Upscalings
Cumulative prodcution error (%)
12
10
8
6
4
2
0
100000
1000000
10000000
Number of grid cells
296322
(100x150x16)
547056
(100x150x8)
1048524
(100x150x4)
2028666
(100x150x2)
2530134
(100x150x1)
Heterogeneous models (total errors)
Homogeneous models (numerical errors)
Upscaling errors (Heterogeneous-Homogeneous)
y = -26.18ln(x) + 372.48
R² = 0.9545
y = 0.104ln(x) - 1.346
R² = 0.057
y = -11.09ln(x) + 156.13
R² = 0.8924

Figure 4.9. Comparison between vertical and horizontal upscaling production error. Total errors that are associated with numerical errors and rock heterogeneity due to upscaling (orange), numerical (uncertainty) error resulting from the truncation computational errors (black), and upscaling errors (rock heterogeneity) resulting from changes in grid cell sizes (green). Some orange points are overlapping black points in the upper plot (a) and black points are overlapping each other on the lower plot (b). a) Semilog plot depicting logarithmic best-fit equations (inversely proportional) for the three horizontal upscaling curves (orange, black, and green). Note numerical production errors due to the computational truncation errors (black) are higher than the production errors due to the upscaling of geologic heterogeneity (green) for grid cell sizes. The exact error values for the horizontal upscaling are found in the last columns ("all wells combined") in Tables 4.3, 4.4, and 4.5. b) Semilog plot depicting logarithmic best-fit equations (inversely proportional) for the total errors and numerical errors vertical upscaling. Note numerical upscaling with the vertical upscaling is very low (black). Note much lower numerical errors with vertical upscaling (black) and higher errors with horizontal upscaling (black). The exact error values for the vertical upscaling are found in the last columns ("all wells combined") in Tables 4.6, 4.7, and 4.8.

Effect of fracture size

Table 4.9 and **Figure 4.10a-f** show that increase in aperture has a lesser effect on production than the length. For example, Well 1 shows a difference of 11% in cumulative production compared to the history match using 2x aperture and 301% using 2x length (**Table 4.9**, also see **Figure 4.10a** solid green, solid blue, and solid red curves). Well 1 also shows 190% increase compared to the history match using 4x aperture and 673% increase using 4x length (**Table 4.9**, also see **Figure 4.10a** solid green, broken blue, broken red curves). For Well 2, 2x fracture aperture results in a 63% increase, while 2x fracture length results in 861% increase in production. Similarly, for 4x increase in aperture and length, the increase is 169% and 1595% in production respectively. With 4x aperture and 4x length, the jump in production rate with respect to the respective 2x cases is much higher than the difference between the respective 2x and history match cases. The remainder of the wells show a similar increase for 2x cases. The 4x values indicated by the arrows in **Figure 4.10c-4.10e** (constant values) should be ignored as the model

boundaries were most likely reached. In addition, the cumulative production of the whole field for 4x aperture and length (arrows in **Figure 4.10f**) should be ignored as that includes all five wells.

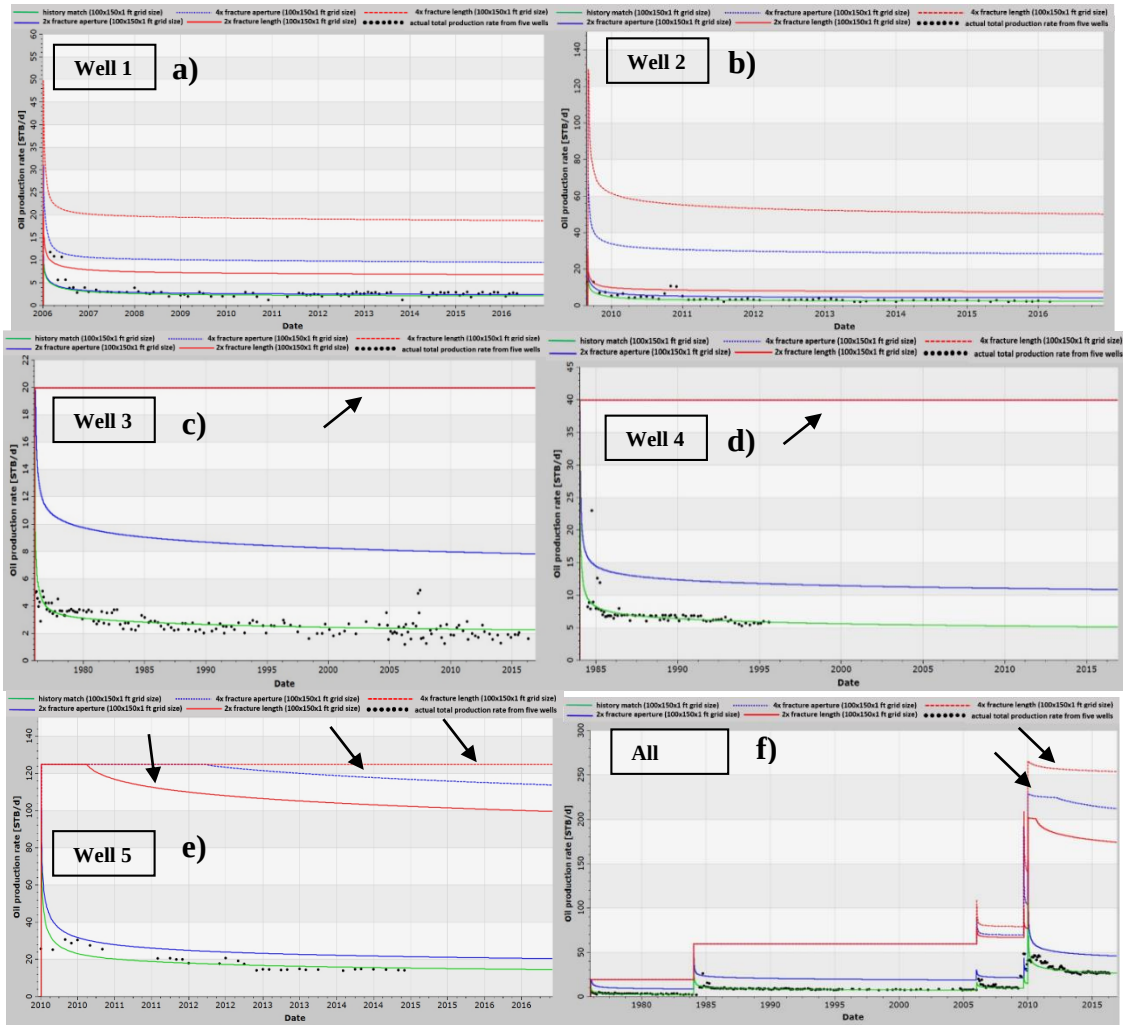

Figure 4.10. Effect of fracture aperture and length on production rate showing history match curves, 2x, and 4x fracture length and aperture. Arrows indicate curves, which may be considered as incorrect due to constant production rates over long periods because model boundaries were probably reached due to high connectivity. (a) and (b) show all curves correctly. (c), (d), and (e) show history match, 2x length, and 2x apertures correctly but not 4x. Dots: actual production rates, Solid green: history match, Solid red: 2x fracture length, Broken red: 4x fracture length; Solid blue: 2x fracture aperture, Broken blue: 4x fracture aperture.

Table 4.9. Cumulative production comparisons for history match, 2x, and 4x fracture aperture and fracture lengths sensitivity analyses. Errors in the history match column are with respect to the actual cumulative production and those in the remaining columns are with respect to the history match (i.e., not actual) production case (100x150x1).

	Actual cumulative production (STB)	**100x150x1** (history match) cumulative production error	**2X** fracture aperture cumulative production error	**4X** fracture aperture cumulative production error	**2X** fracture length cumulative production error	**4X** fracture length cumulative production error
Well 1	10,170	9,626 (-5 %)	+11%	+190%	+301%	+673%
Well 2	10,217	7,542 (-26 %)	+63%	+169%	+861%	+1596%
Well 3	37,398	39,634 (6%)	+224%	642% (?)	+642%	642% (?)
Well 4	27,348 @1995	29,333 (7%)	+86%	470% (?)	+470%	470% (?)
Well 5	37,956@2014	34,254 (-10%)	+37%	480% (?)	+539%	555% (?)

Run time and accuracy

There is a fourth order negative relationship between solution time vs. grid cell size (**Figure 4.11a**), and solution time vs. number of processes (**Figure 4.11b**). In other words, using five parallel processes does not lead to $1/5^{th}$ of the time taken by one processor. For example, for the history match case, five processors consume nearly 13 hours which is $1/3^{rd}$, rather than $1/5^{th}$, the time taken by a single processor. For the 200x300x1 grid cell size, this ratio is different. Similarly, for other cases. The time-gap closes with an increase in the number of processes (**Figure 4.11b**).

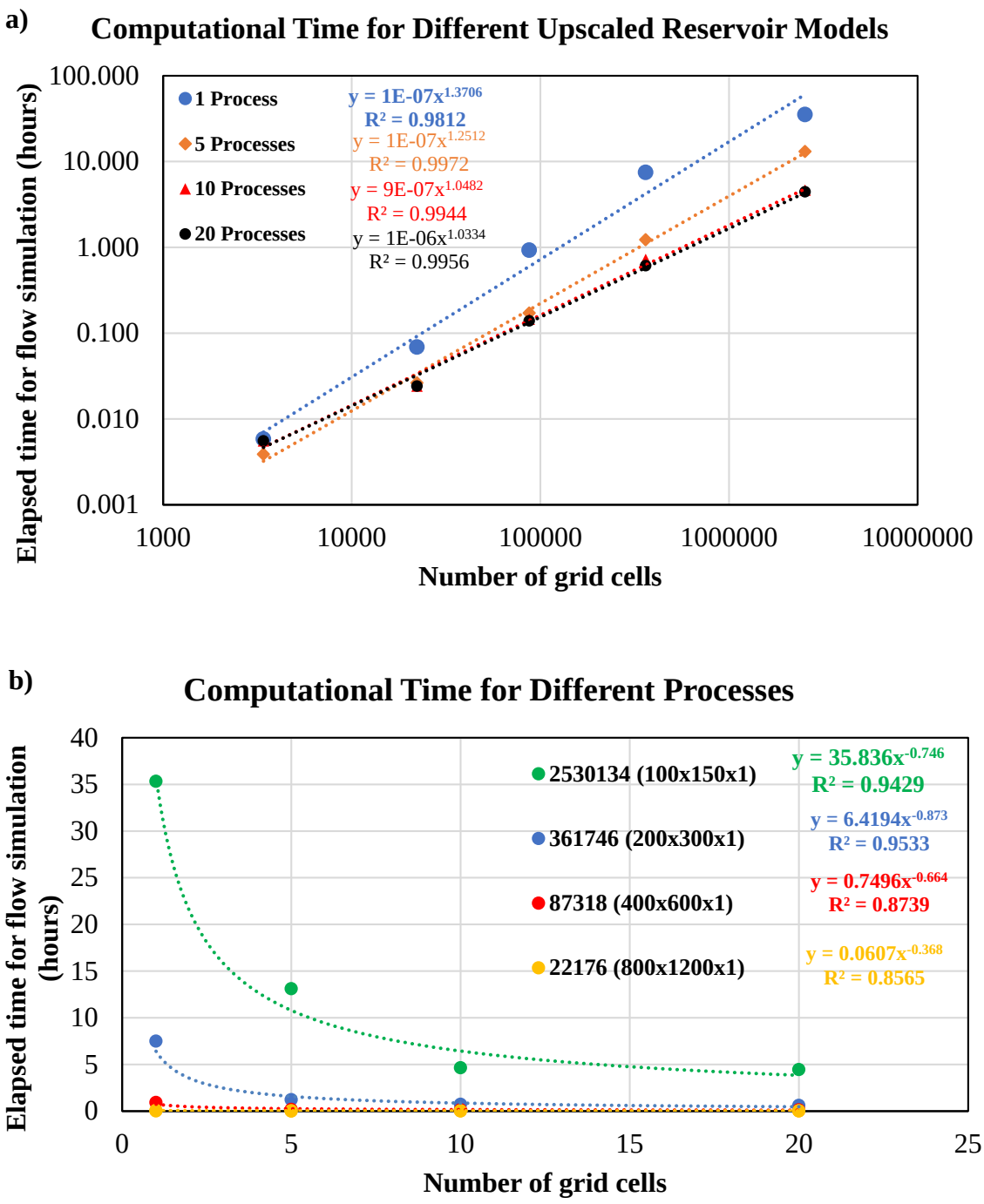

Figure 4.11. Time required time for flow-simulation completion. (a) Log-log plot depicting simulation time required using a different number of grid cells (or grid cell size) while applying a single (blue), five (orange), ten (red), twenty (black) processes. All curves were best fit by a power law. (b) Plot (both x and y-axes are linear) depicting simulation time using different number of processes (curves depicting single grid cell sizes) while using 100x150x1 (green), 200x300x1 (blue), 400x600x1 (red), and 800x1200x1(orange) grid cell sizes. All curves were best fit by negative power law equations.

Discussion

The aforementioned data integration at different scales from core to seismic volume were used to develop a high-resolution stratigraphic framework and complex structures to build detailed fine static geological models consisting of lithofacies, natural fractures, porosities, permeabilities, and saturation. This results in a detailed (20x30x1ft grid cell size) reservoir model which was upscaled to 100x150x1 ft grid cell size for flow (reservoir) simulation. We used a dual porosity/dual permeability model for higher accuracy even though the calculations require higher time for upscaling and flow simulation.

A non-linear relationship between the grid cell size (and consequently the number of grids) and run duration was observed. The runtime gap closes with larger grid cell size as the number of grid cells decreases. Therefore, if the grid cell size is large enough, parallel processes may not be required. However, there will be unacceptably large errors in the simulation results. Therefore, the optimal grid cell size and the time taken based on the number of available processes require optimization. Comparison between vertical and horizontal upscaling shows greater error with horizontal upscaling. In this study, the grid cell size can be reasonably increased to 100x150x2 ft or 100x150x4 ft without incurring more than 6% error compared to the history match (100x150x1 ft). Larger vertical grid cell sizes, i.e., up to 10 ft may be used without incurring more than 11% error. In other words, a reasonable history match and forward modeling can be obtained with 1-10 ft vertical grid cell size, showing that thin beds are not very important in the current study. Increase in lateral grid cell size, however, results in a substantial total error (0.5 to 166%) that includes upscaling processes and numerical errors. The magnitude of numerical truncation (i.e., numerical uncertainty or instability) errors ranges from 4.77 to 91.78% and is inversely proportional to the

number of grid cells, or directly proportional to the grid cell size, in the model. Thus, the effect of numerical errors can be eliminated by decreasing the grid cell sizes in the model. These results agree with Lantz (1971) and Ezekwe (2010) where the numerical errors increase with increases in the areal grid cell sizes. Increase in lateral grid cell size due to upscaling results in errors in the range of 0.5 - 74.2% compared to the vertical grid cell sizes errors in the range of 0.5 -10.8%). This observation is counterintuitive, given more frequent changes in rock properties in the vertical direction, as the heterogeneities are expected to be greater in the vertical direction than the lateral directions. However, it is also noteworthy that the vertical cell size is much smaller compared to horizontal cell size. Also, each step in vertical upscaling increases the grid cell volume by a factor of 2, while each step in horizontal upscaling increases grid cell volume by a factor of 4 (i.e., twice in the x-direction and twice in the y-direction). Based on the overall production, a lateral grid cell size of more than the minimum required for successful simulation is not recommended.

The equation in **Figure 4.9**, i.e., the one defining a monotonous (logarithmic) increase in error with grid cell size (or decrease in the number of grid cells), is presented only for reference and likely to vary in different areas based on geology. The error can also decrease with an increase in grid cell size as observed with individual wells. However, the equation in **Figure 4.5** (grid cell size vs. time), i.e., power law relationship between grid cell size and solution time, is likely to hold true at other places in other geological settings.

Regarding the effect of natural fracture geometry on production, fracture length has a higher impact on the production compared to the aperture. Assuming a constant fracture intensity or surface area, the higher the fracture length, the greater the production even if the total fracture intensity stays constant. This is most likely due to higher reservoir connectivity through natural fractures. However, an increase in aperture does not result in higher natural fracture connectivity

but still increases production. This observation indicates that fracture conductivity is not infinite. Also, constant high production rates with 4x apertures imply a shift from finite conductivity (1x and 2x aperture cases) to infinite conductivity leading to model boundary dominated flow. Since fracture length can affect reservoir production significantly, its accurate estimation is paramount, even though it is very difficult to achieve (Ghosh, 2017).

Conclusions

In this study, we integrated diverse geologic, geophysical, and engineering data to obtain a fine scale geologic model that captures the reservoir heterogeneities of a Hunton carbonate oil field in Oklahoma. We found that we were able to preserve the history matching accuracy of the original fine scale model by upscaling using a dual porosity, dual permeability equivalent model. The instability/numerical errors increased the production errors by more than 60%. Hence, it is essential for modelers to understand the sources of error (i.e., numerical uncertainty vs. rock heterogeneity) and to be able to have an estimate of the relative error magnitudes arising from these sources. In order to balance run time and accuracy, we find that the lateral grid cell size should be kept at the original bin size of the seismic data used in its construction. If the original vertical grid cell size is sufficiently coarse and provides an accurate history match, further vertical upscaling (as opposed to horizontal upscaling) appears to have only a moderate effect on cumulative production. In contrast, upscaling of fracture properties can introduce major errors in the predicted production. Although natural fracture apertures affect fracture permeability and production, natural fracture length has a significantly greater impact on the production response because length controls reservoir connectivity. The overhead of inter-process communication between blocks of grid cells at each computation time step precludes the construction of a linear relationship between the number of parallel processes and the total simulation time. Instead, we

provide power law and lognormal relationships we feel may be useful in prediction computation on simple desktop computers. In conclusion, we recommend the reservoir analyst to balance the need for accuracy and the computer resources and wall clock time available. The construction of our geologic model always has approximations and assumptions. High accuracy modeling of an approximate geologic model provides little additional value. We believe our workflow of using a fine grid and comparing the history match to those of a coarser grid echoes a well-established means of estimating the accuracy of a given simulation. Once an acceptable accuracy has been found, the analyst should balance the desire and cost for increased accuracy for a given well to that of acceptable accuracy in modeling more wells providing a more complete analysis on the performance of the oil field.

Acknowledgments

Thanks to the STACK-MERGE-SCOOP- consortium members at the Institute of Reservoir Characterization at the University of Oklahoma for their generous funding and support. The authors are greatly thankful to Dr. Abeed Awotunde for his critical reviews and comments. We thank Schlumberger for providing Petrel, Techlog, and Eclipse and CGG Geosolutions for providing Hampson-Russell software for use in research and education. We also used software generated by the OU AASPI consortium.

References

Amsden, T.W., 1975, Hunton Group, Late Ordovician, Silurian, and Early Devonian in the Anadarko Basin of Oklahoma: Oklahoma Geological Survey.

Adamson, G., M. Crick, B. Gane, O. Gurpinar, J. Hardiman, and D. Ponting, 1996, Simulation throughout the life of a reservoir: Oilfield Review 2, no. 8, 16-27.

Al-Shaieb, Z., G. Beardall, P. Medlock, K. Lippert, F. Matthews, and F. Manni, 1993. Overview of Hunton facies and reservoirs in the Anadarko Basin: Presented at the Hunton Group Core Workshop and Field Trip, Oklahoma Geological Survey Special Publication.

Avansi, G., V. Rios, and D. J. Schiozer, 2019. Numerical tuning in reservoir simulation: It is worth the effort in practical petroleum applications: Journal of the Brazilian Society of Mechanical Sciences and Engineering, **41**, No. 1, 1-21. Doi: 10.1007/s40430-018-1559-9.

Deutsch, C.V.D, 2017, Geostatistical reservoir modeling: Oxford university press, **91**, 399-404.

Durlofsky, L. J., 2005, Upscaling and gridding of fine-scale geological models for flow simulation: 8th International Forum on Reservoir Simulation Iles Borrmees, Stresa, Italy, **2024**, 1-59.

Ezekwe, N., 2010, Petroleum Reservoir Engineering Practice: Pearson Education, Inc.

Fanchi, J. R., 1983, Multidimensional numerical dispersion: Society of Petroleum Engineering Journal, **23** (1),143-151.

Fritz, R. D., and P. L. Medlock, 1994, Sequence stratigraphy of the Hunton Group as defined by core, outcrop, and log data: Bulletin Houston Geological Society, 29–58.

Gaswirth, S. B., and D. K. Higley, 2014, Petroleum systems and assessment of undiscovered oil and gas in the Anadarko Basin Province, Colorado, Kansas, Oklahoma, and Texas: USGS Province **58**: U.S. Geological Survey.

Ghosh,S., 2017, Integrated studies on Woodford Shale natural fracture attributes, origin, and their relation to hydraulic fracturing: PhD dissertation, The University of Oklahoma.

Ghosh, S., C.P. Bontempi, J.N. Hooker, and R.M. Slatt, 2018a, High-resolution stratigraphic characterization of natural fracture attributes in the Woodford Shale, Arbuckle Wilderness and US-77D Outcrops, Murray County, Oklahoma. Interpretation 6(1): SC29–SC41. https://doi.org/10.1190/int-2017-0056.1

Ghosh, S., H.A. Galvis-Portilla, C.M. Klockow, and R.M. Slatt, 2018b, An application of outcrop analogues to understanding the origin and abundance of natural fractures in the Woodford Shale. Journal of Petroleum Science and Engineering 164 (2018) 623–639. https://doi.org/10.1016/j.petrol.2017.11.073

Hui, M. H. R., M. Karimi-Fard, B. Mallison, and L. J. Durlofsky, 2018, A general modeling framework for simulating complex recovery processes in fractured reservoirs at different resolutions: SPE Journal, **23**, 2, 598-613.

King, M.J., MacDonald, D.G., Todd, S.P., and Leung, H., 1998. Application of Novel Upscaling Approaches to the Magnus and Andrew Reservoirs: European Petroleum Conference, doi:10.2118/50643-MS.

Lantz, R. B., 1971, Quantitative evaluation of numerical diffusion (truncation error): Society of Petroleum Engineering Journal, **11**(3), 315-320.

Ma, E., Ryzhov, S., Wang, Y., Al-houti, R., Dashti, L., Ali, F., and Ibrahim, M., 2013. SPE 164187 Answering the Challenge of Up-scaling a 900 Million-Cells Static Model to a Dynamic Model - Greater Burgan Field, Kuwait: p. 1–11, doi:10.2118/164187-MS

Mehmood, S., and Awotunde, A. A., 2016. Sensitivity-based upscaling for history matching of reservoir models: Petroleum Science, v. 13, no. 3, p. 517–531, doi:10.1007/s12182-016-0107-4

Meddaugh, W. S., 2006, Reservoir modeling for mature fields—Impact of work flow and upscaling on fluid-flow response: SPE Europec/EAGE Annual Conference and Exhibition held in Vienna, Austria 99833, 12–15.

Milad, B., S. Ghosh, and R. Slatt, 2018a, Comparison of rock and natural fracture attributes in karsted and non-karsted Hunton Group Limestone: Ada and Fittstown area, Oklahoma: The Shale Shaker, **69**, no. 2, 70-86.

Milad, B., S. Ghosh, M. Suliman, and R. Slatt, 2018b. Upscaled DFN models to understand the effects of natural fracture properties on fluid flow in the Hunton Group tight Limestone: Unconventional Resource Technology Conference 2903038, 1-16, doi:10.15530/URTEC-2018-2903038.

Milad, B., and R. Slatt, 2018, Impact of lithofacies variations and structural changes on natural fracture distributions: Interpretation, **6**, T873–T887, doi:10.1190/INT-2017-0138.1

Oda, M., 1985, Permeability tensor for discontinuous rock masses: Geotechnique, **35**, 4, 483-495.

Olalotiti-Lawal, F., T. Onishi, A. Datta-Gupta, Y. Fujita, and K. Hagiwara, 2017. Post-combustion CO2 EOR development in a mature oil field: Model calibration using a hierarchical approach: SPE Annual Technical Conference and Exhibition 187116-MS, doi:10.2118/187116-MS.

Schlumberger, 2014, Petrel Fracture Modeling Manual: Houston, TX

Schlumberger, 2018. Petrel 2018 Manual.

Santacruz, C., H. Correa-Correa, and R. M. Slatt, 2012. 3D geological modeling and performance simulation of a leveed-channel outcrop with application to deepwater leveed-channel reservoirs. Search and Discovery Article #50728.

Stanley, T.M., and K. Rottmann, 2001, Stratigraphy and facies relationships of the Hunton Group, Northern Arbuckle Mountains and Lawrence Uplift, Oklahoma: Oklahoma Geological Survey Guidebook Series **33**.

Stern, D., 2005, Practical aspects of scaleup of simulation models: Journal of Petroleum Technology, **57**, no. 09, 74–81, doi:10.2118/89032-JPT.

Chapter 5: Lithology, stratigraphy, and depositional environment of a complete Mississippian Sycamore section of the I-35 outcrop in Southern Oklahoma

Benmadi Milad, Roger Slatt, and Zou Fuge

This paper will be submitted to **Journal of Petroleum Science and Engineering**

Abstract

The Mississippian Sycamore Formation across the SCOOP (South Central Oklahoma Oil Province) area has been a very attractive, emerging unconventional hydrocarbon resource for many operators in the oil industry. However, understanding of the lithology, depositional environment, and reservoir quality of the Sycamore Formation are still not well understood. This paper presents an interpreted depositional environment, and detailed lithofacies identification from a 450ft thick Sycamore outcrop in southern Oklahoma and calibrates the rock properties with wireline log responses to identify the best landing zones within these Mississippian rocks.

Qualitative and quantitative techniques of field, lab, and machine learning studies were conducted. For the field studies, we measured the complete 450 ft of the outcrop stratigraphic section, examined the underlying Woodford Shale and overlying Caney Shale boundary contacts, documented sedimentary structures, constructed an outcrop gamma-ray profile, and developed a preliminary sequence stratigraphic framework. Lab studies included petrographic analyses, detailed X-ray Fluorescence (XRF), Scanning Electron Microscopy (SEM), and X-ray Diffraction (XRD). For machine learning studies, a principal component analysis (PCA), elbow method, and self-organizing map (SOM) were used to analyze the electrofacies and chemofacies from the outcrop and a subsurface uncored well.

The outcrop hand-held gamma ray profile was obtained and correlated with a nearby subsurface well. Five major outcrop lithofacies and chemofacies, within six stratigraphic units of alternating siltstone and shale strata, were identified from the wireline logs with confidence. A Maximum Flooding Surface (MFS), and two major second order Sequence Boundaries (SB) were recognized. Bouma sequences and repetitive cycles of sedimentary structures indicated sediment gravity flow deposition on a marine slope setting.

This study provides geologic insights to better understanding the depositional environment of the Sycamore rocks. The bioturbated siliceous shale and/or the sandy siltstone can be potential target zones due to their reservoir quality, lithology, bed continuity, and brittleness. This information can be of direct benefit to the exploration and development programs of many companies in the Ardmore Basin of South Central Oklahoma.

Introduction

The SCOOP (South Central Oklahoma Oil Province) and STACK (Sooner Trend Anadarko Canadian and Kingfisher) plays of the Anadarko Basin in Oklahoma have continued to impress much of the industry since 2013 due to their large potential oil and gas resources and their high hydrocarbon IP rates (Nojek and Li, 2017). Within the SCOOP and STACK plays, which include the Devonian Woodford, Mississippian Sycamore-Meramec, Caney, and Springer strata pay intervals, drilling activities have significantly increased by more than 50% in 2018 (782 annual well count) compared to the 2016 activity (383 well count) (IHS market, 2018). Of these intervals, the Mississippian Sycamore in the SCOOP area is of economic interest currently for many companies.

The hydrocarbon resource success from the underexplored Mississippian Sycamore in the SCOOP area in southern Oklahoma drives the need to understand the Sycamore strata in detail

with outcrop and subsurface data. Understanding the Sycamore depositional system is critical for effectively developing geological assessment and determining optimal landing zones because it is of current interest to many exploration and production companies in the southern Anadarko and Ardmore basins.

Within the literature there are conflicting and ambiguous interpretations on the lithology and depositional environment of the Sycamore Formation. Previous publications offer different depositional environment interpretations for the Sycamore rocks without clear lithofacies characterization or interpretation. The deposition of the Sycamore rocks was first interpreted as a carbonate limestone deposited in a shallow-water transgressive sea (Bennison, 1956; Prestridge, 1957; Curtis and Chapman,1959; Braun, 1961; Cole, 1988) whereas others interpreted the Sycamore as deposited on a slope/ below storm wave base setting (Schwartzapfel, 1990; Coffey, 2000; Franklin, 2002; Miller and Cullen, 2018). Schwartzapfel (1990) observed partial Bouma sequences in the I-35 outcrop and interpreted the Sycamore to be a deepwater deposit. Franklin (2002) interpreted the Sycamore to be deposited in a deep marine setting as well, but by thermocline bottom currents. On the other side, Coffey (2000) interpreted the Sycamore to be deposited as a carbonate sediment during rising sea-level of a highstand and gravity flows of authochtnonous sediments during a lowstand drop in sea level. The role of glaciation on sedimentation has been suggested (Milad and Slatt 2019), but remains speculative at this time, and a current research program. Lithologically, authors interpreted the hard- calcareous sections either as limestone rock (Taff 1903; Ham, 1965; Fay, 1989; Noble, 1995) or marlstone rock (Donovan, 2001) as a result of lacking fully integrated advanced study.

Due to the discrepancies in the depositional environment, the poor understanding of the lithology and its significance to geological assessments for optimal drilling locations, the objective

of this study was to: 1) present a detailed lithofacies characterization for the Sycamore formation, 2) determine depositional environments, 3) utilize the outcrop studies for subsurface correlation, yielding enhanced subsurface interpretation, 4) develop criteria for predicting rock properties from wireline logs, 5) develop a sequence stratigraphic framework to predict the lateral continuity of a potential target zone, and 6) integrate the aforementioned objectives to propose optimal target zones for the Sycamore formation.

This study provides multiple advanced characterization techniques (petrographic, XRD, SEM, XRF, and machine learning techniques) to provide better understanding of the lithology and depositional environment for the Mississippian Sycamore.

Geological settings and study area

Cambrian rifting formed the southern Oklahoma aulacogen (SOA) through three stages: 1) rifting, 2) subsidence and infilling of the rift, and 3) rock deformation (Hoffman et al., 1974; Suneson, 1996; Allen, 2000). From the Upper Cambrian through the Mississippian period, 17,000 ft of the sediment accumulated in the SOA (Ham et al., 1965).

During Mississippian time, North America was covered by a warm and shallow epeiric sea (Curtis and Champlin, 1959). The wide epeiric sea continued to move throughout the southern Midcontinent (Northcutt, et al., 2001). The climate at this time was considered to be tropical to subtropical with the paleolatitude between 20°-30°S. The surface temperatures of the ocean ranged from 65°-85°F (Buggisch et al., 2008). These conditions affected the eustatic sea level changes, led to changes in accommodation, and affected the sediments that were deposited during Mississippian time.

The whole Mississippian section represents a single 2nd-order (5-50 Ma) transgressive-regressive cycle (Sloss, 1963). The Mississippian was characterized by four stages from oldest to

youngest including, Kinderhookian, Osagean, Meramecian, and Chesterian (Watney et al., 2001). Deposition of siltstone and very fine sandstone separated by shale units comprised the predominant Mississippian Sycamore rocks in Southern Oklahoma.

Later Mississippian-Early Pennsylvanian uplift exposed the entire Paleozoic strata in the Arbuckle Mountains including the Devonian Woodford Shale, Sycamore, and Caney formations. Late Paleozoic Wichita, Ouachita, and Arbuckle orogenies were the main tectonic events that developed the structural setting of the Arbuckle Mountains in south central Oklahoma.

The Mississippian stratigraphic names, nomenclature, and age correlation differ between the outcrops and subsurface. Although the Sycamore limestone was the name used for the Mississippian Sycamore strata (Johnson and Cardott, 1992), no mature limestone facies are present but the Sycamore is alternating intervals of shale and siltstone—very fine sandstone with carbonate cement. Hence, we used different Sycamore lithology nomenclature and modified the Mississippian stratigraphic chart in the Arbuckle Mountains study area (**Figure 5.1**). The modification was based on the detailed analyses we made in this study and observed siltstone-shale sequences that are presented in the I-35 Sycamore outcrop and in the nearby J Little subsurface well (**Figure 5.1**).

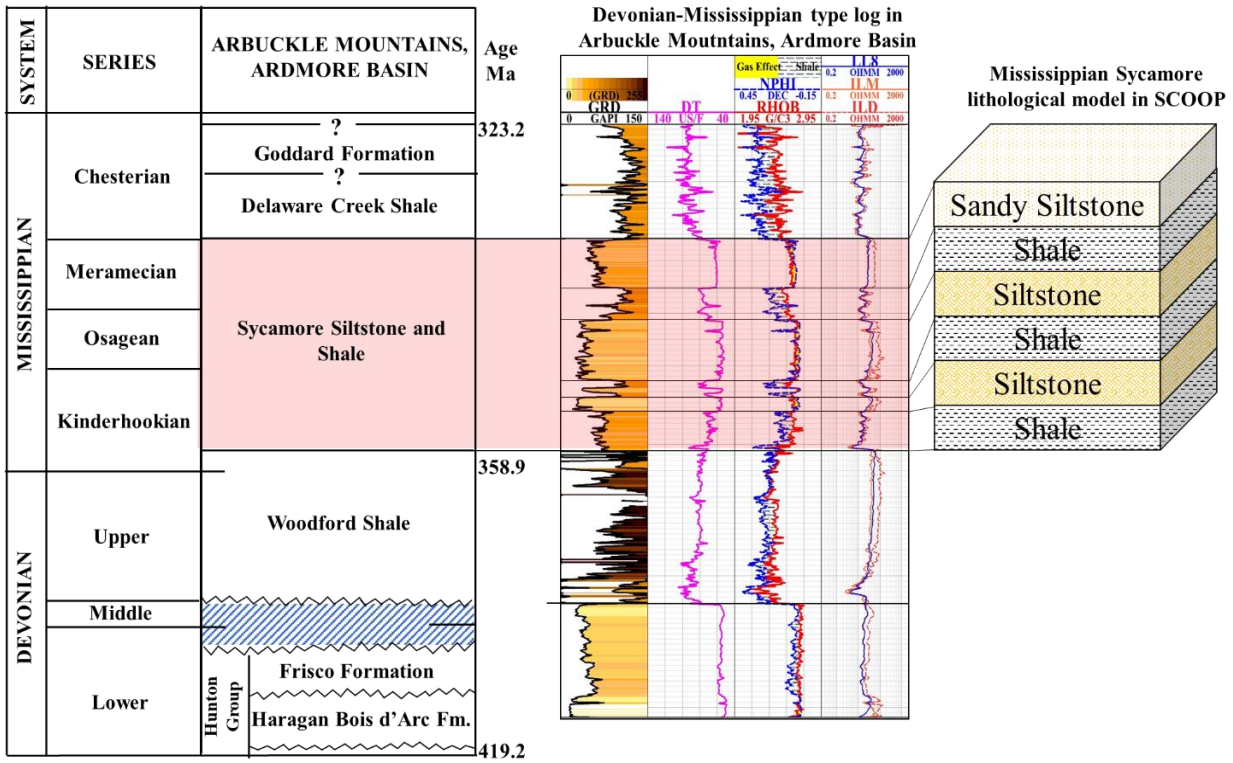

Figure 5.1. Modified Mississippian stratigraphic chart in the Arbuckle Mountains of the study area. We changed the Mississippian stratigraphic column from Sycamore limestone to Sycamore Siltstone and Shale (modified from Johnson and Cardott, 1992). Typical well log near the I-35 Sycamore outcrop in the Arbuckle Mountains (SCOOP area) shows the stratigraphic sequence and rock characteristics on the well logs of Devonian-Mississippian strata.

Regionally, the two Mississippian outcrops are located along the southern limb of the Arbuckle Mountains in Carter and Murray Counties in South Central Oklahoma (**Figure 5.2A**). The geographic coordinates of the I-35 Sycamore are 34°21'3.42"N and 97° 8'54.31"W and the Speake Ranch Outcrop is 34°22′40.36″N and 97°20′17.26″W. The distance between the two locations is 12 miles and the distance between the I-35 Sycamore outcrop and the subsurface well is 3 miles to the east (**Figure 5.2 B**).

Figure 5.2C shows the Sycamore type log in the SCOOP area and the stratigraphic sequence and rock characteristics on the well logs of Silurian- Devonian-Mississippian strata of the Arbuckle Mountains (SCOOP area).

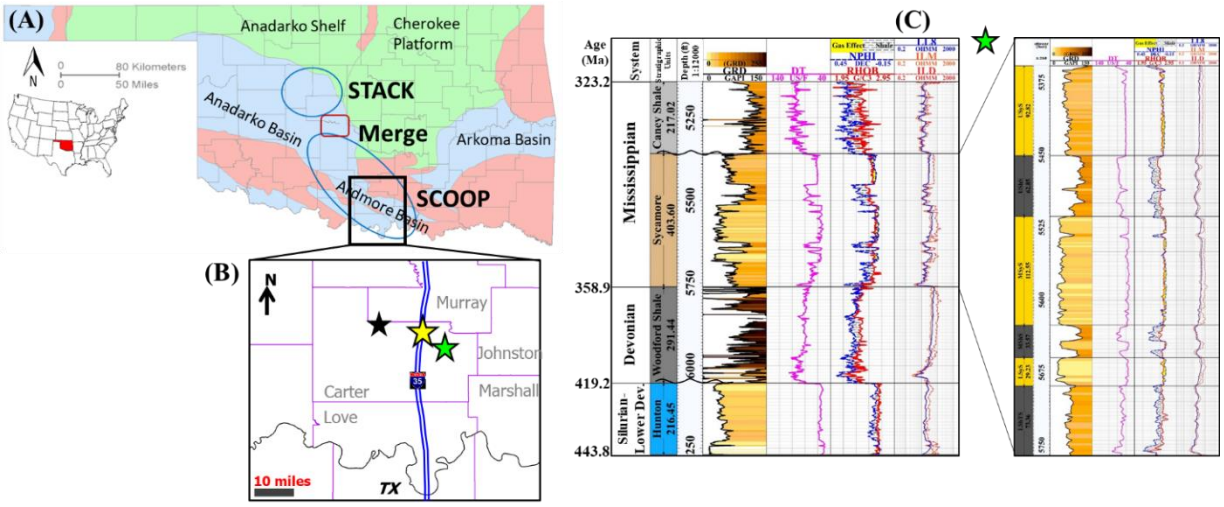

Figure 5.2. Locations of data available. A) Map of Oklahoma showing STACK, Merge, and SCOOP plays. The black box shows the location of outcrop and subsurface data. B) locations of data available within the studied area. Yellow star shows the location of the Sycamore road-cut I-35 outcrop, black star shows the Speake Ranch outcrop location, and the green star shows the subsurface suite log location. C) Typical well log near the I-35 Sycamore outcrop shows the stratigraphic sequence of Silurian- Devonian-Mississippian strata of the Arbuckle Mountains (SCOOP area).

Methods

The objectives of this study where achieved through qualitative and quantitative methods of field work, lab analyses, lithofacies classification, chemofacies, and electrofacies clustering techniques. **Figure 5.3** summarizes the methodology that was used in this study.

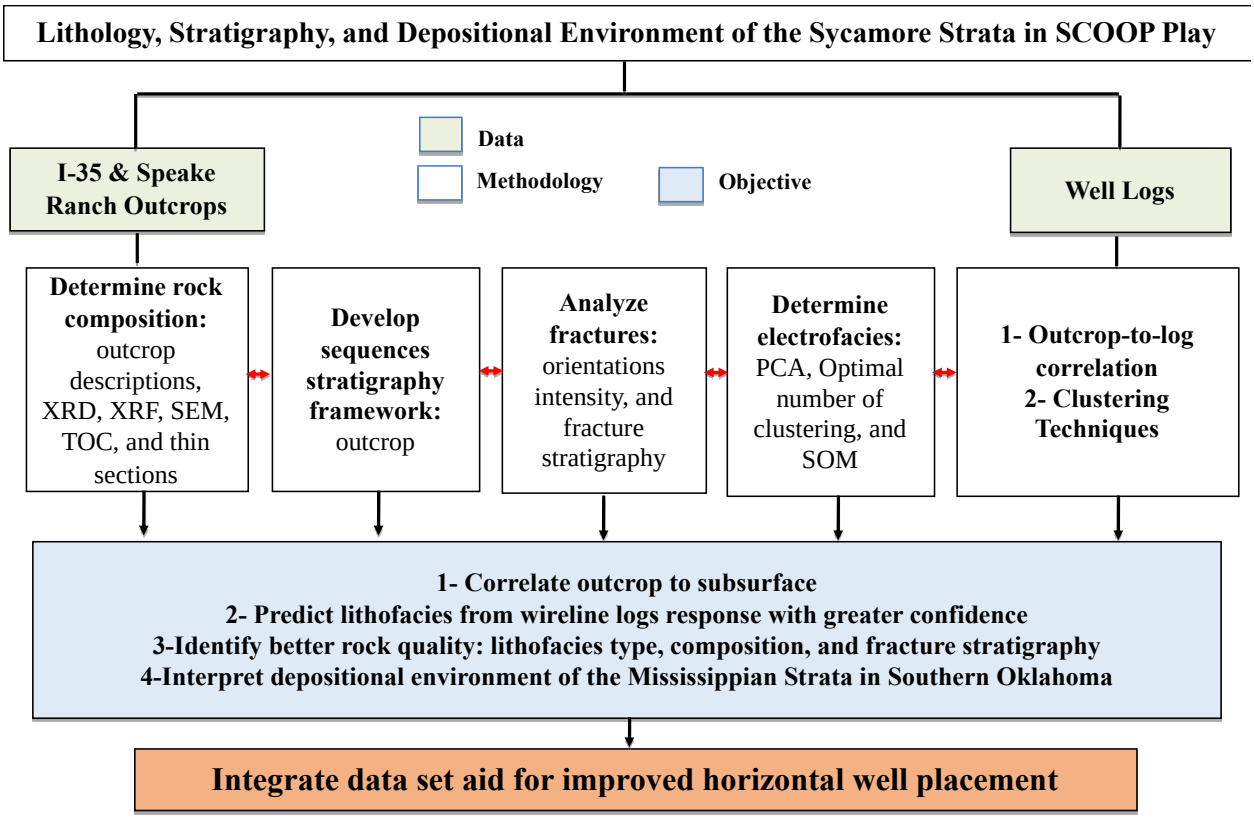

Figure 5.3. Workflow to characterize the lithology, stratigraphy, and depositional environment of the Mississippian Sycamore strata in the SCOOP area.

Field work

First, the true stratigraphic thickness was measured using a Jacob's staff and Brunton compass. Markers were made while measuring the outcrop section after cleaning the covered sections within the I-35 Sycamore outcrop. Detailed descriptions of lithologies, grain sizes, and sedimentary structures were made. Bed thicknesses were documented at the outcrop bed scale to construct accurate stratigraphic columns using EasyCore software for the two outcrops (**Figure 5.4**). Second, at every 1 ft interval or less depending on the bed and lithology changes, five gamma ray (GR) readings were recorded in counts per second (cps) using hand-held scintillometer through the outcrops measured section (Galvis et al., 2018). Then, the five GR readings were averaged into a mean value per one ft interval or less. Outcrop gamma ray measurements (GR) were plotted

vertically to be correlated to subsurface gamma ray profiles, and to relate outcrop facies to the subsurface. Finally, samples were collected every 0.5 ft within the transition sections and 1 ft for the rest of the outcrops' interval for detailed X-ray fluorescence (XRF) analyses. Selective samples based on the lithology changes were collected for further analyses, such as petrographic thin sections, scanning electron microscope (SEM), X-ray diffraction (XRD), and geochemistry Rock Eval Pyrolysis analyses (TOC).

Lab analyses

Fifteen unpolished thin sections were acquired from the I-35 outcrop and eight samples from the Speake Ranch outcrop. The samples were stained with alizarin red S to identify calcite and injected with blue epoxy for porosity identification. Thin sections were observed under Zeiss Axio Imager Z1m microscope in normal transmitted plane-polarized and cross-polarized light.

Seven samples from the I-35 Sycamore outcrop were used to carry out SEM investigations by backscattered electron detector and secondary electron images under high vacuum at 20 KV acceleration voltages using a FEI Quantum 250 with an attached electron dispersive spectrometer. Fifteen samples, seven from the I-35 Sycamore outcrop and eight from the Speake Ranch outcrop, were sent to various labs to be used for XRD, and total organic carbon (TOC) analyses. Detailed XRF measurements were made for the collected outcrop samples.

Four hundred and twenty samples from the two outcrops were smoothed out, washed with water, and dried for the XRF measurements. XRF analyses were conducted on these samples using a Brucker Tracer IV-SD hand-held energy-dispersive XRF analyzer. The samples were scanned two times at the same point. The first scan was for 90 seconds at 15 kV, 35 mA under vacuum, and with no filter for major elements while the second scan was for an additional 60 seconds at 40 kV, 17 mA, under vacuum with Ti-Al filter for the trace elements. Concentrations of 30 major and

trace elements were measured and calibrated to convert them to parts per million (ppm) (Rowe et al., 2012).

Lithofacies classification

Lazar et al. (2015) lithofacies classifications were used to honor the fundamental rock characteristics, such as sedimentary structure, texture and composition aided by petrographic and XRD mineralogical results. The outcrop rocks are composed of clay, silt, and very fine sand-sized sediment grains. **Figure 5.4** shows the seven lithofacies that were identified in the I-35 Sycamore outcrop, including greenish shale, bioturbated siliceous shale, chert, dolomitic mudstone, dolomitic-calcite cemented siltstone, calcite cemented siltstone, and sandy siltstone (non-cemented lithofacies).

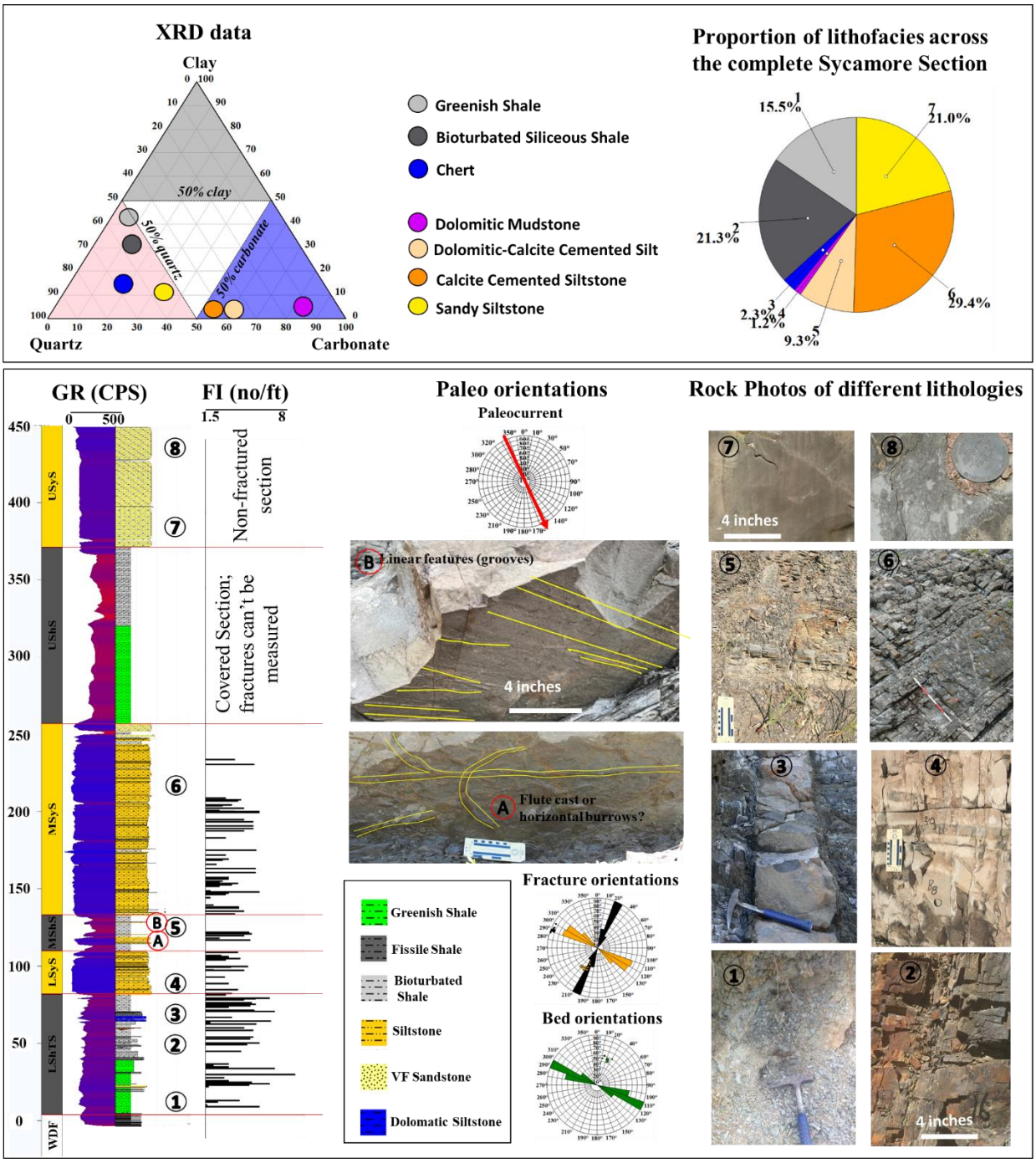

Figure 5.4. Field-based lithofacies classification scheme for the Sycamore Shale and Siltstone rocks. The rock naming and classifications were based on the compositional, textural descriptors, and the XRD data. Seven lithofacies were recognized within the Sycamore section at the I-35 outcrop. The mineral composition of the lithofacies is illustrated in the ternary plot and reveals two groups of rock types; Shale is rich in quartz minerals and siltstone is rich in carbonate minerals mainly calcite cements. The pie chart shows that calcite cemented siltstone, sandy siltstone, siliceous shales, and greenish shales count for more than 80% of the lithofacies present in the I-35 outcrop.

Chemofacies and Electrofacies Clustering Techniques

Chemofacies: Major and trace elements geochemistry were used to characterize and correlate strata based on elemental concentrations (Liborius and slat 2016; Ratcliffe et al., 2010; Zhang 2016a; and Zhang et al., 2016b). Later, they were used to aid depositional environment interpretation. However, due to the large set of major and trace elements as well as to avoid redundancy in the chemofacies clustering, a principal component analysis (PCA) was used to determine which XRF elements are the most variable among the 30 elements analyzed. Then, the elbow method was used to determine the optimal number of clustering for the selected variables (e.g., XRF elements and/or logs) (Milad et al, 2018). Finally, self-organizing maps (SOM), unsupervised statistical clustering technique, was used to obtain the chemofacies and electrofacies clusters. Detailed explanation of these statistical methods are available in Milad and Slatt (2018).

Table 5.1 presents the correlation coefficients of PCA for all geochemical elements that were calculated from the XRF row data. In **Table 5.1**, green cells represent elements with correlation coefficients > 0.49 and the red cells represent elements with correlation coefficients <-0.49. These correlation coefficients were considered to be statistically significant based on total number of samples; thus, they were used for the chemofacies clustering study. Based on the chosen correlation coefficient (cutoff of 0.49), a subset of only 20 elements was used (**Table 5.1**) in this study to characterize Sycamore chemostratigraphy: silicon (Si), calcium (Ca), aluminum (Al), iron (Fe), Manganese (Mn), phosphorus (P), magnesium (Mg), sulfur (S), potassium (K), Barium (Ba), titanium (Ti), Sodium (Na), strontium (Sr), zirconium (Zr), Zinc (Zn), silica aluminum ratio (Si/Al), vanadium (V), silica titanium ratio (Si/Ti), Chromium (Cr), and Nickel (Ni). Those 20 elements represented the first twenty components with the highest variability to be used as primary inputs to classify different clusters of chemofacies. The components of these 20 selected elements

counted for more than 95% of the variance in the XRF data set (**Table 5.1**). **Table 5.2** summarizes the significance of the main XRF elements in chemostratigraphic interpretations. Finally, the unsupervised clustering analysis of self-organizing maps (SOM) was used based on the 20 selected XRF elements, considering the optimal number of 5 clusters (chemofacies) obtained from the elbow method.

Once the chemofacies classifications were identified, a comparison was made with the GR log, thin-sections analyses, and the XRD bulk mineralogy data to identify the geological meaning for these five components (electrofacies).

Table 5.1. Correlation coefficients of PCA for the selected geochemical elements that are statistically significant with a correlation coefficient greater than 0.49 and less than -0.49. Green cells represent the correlation coefficient > 0.94. Red cells represent the correlation coefficient < -0.94.

Considered elements Si. Ca. Al. Fe. Mn. P. Mg. S. K. Ba. Ti. Na. Sr. Zr. Zn. Si/Al V. Si/Ti Cr. Ni.

Std	117913.400	35962.690	12087.330	8739.240	6028.407	4948.314	4170.991	2517.717	1783.436	1435.739	446.739	342.415	108.272	64.741	57.556	40.127	33.598	28.362	26.232	18.414
	PC1	PC2	PC3	PC4	PC5	PC6	PC7	PC8	PC9	PC10	PC11	PC12	PC13	PC14	PC15	PC16	PC17	PC18	PC19	PC20
Na	-0.010	-0.026	-0.025	-0.017	0.039	-0.019	0.019	-0.029	-0.061	0.063	-0.265	0.957	-0.010	0.003	-0.002	-0.008	0.004	0.015	0.005	-0.011
Mg	0.010	0.041	0.079	0.184	-0.038	-0.029	-0.958	-0.194	-0.005	-0.007	0.008	0.023	-0.012	0.004	-0.003	0.001	0.000	-0.001	0.000	0.001
Al	-0.117	-0.021	0.805	-0.449	0.070	0.044	-0.070	0.216	-0.230	0.158	-0.006	-0.010	-0.002	-0.004	0.003	0.001	0.005	-0.002	0.000	0.000
Si	-0.628	0.774	-0.028	0.049	-0.031	-0.005	0.038	-0.016	0.007	-0.014	-0.005	0.014	0.001	0.000	0.000	0.000	-0.001	0.000	0.000	0.000
P	0.001	0.002	-0.019	0.114	0.002	0.990	-0.020	0.051	-0.019	0.043	-0.004	0.018	-0.003	-0.001	0.001	-0.003	0.002	0.000	0.000	0.000
S	-0.007	0.007	0.073	-0.040	0.034	-0.004	-0.120	0.574	0.771	-0.216	-0.031	0.074	-0.001	0.005	0.004	0.000	0.000	-0.001	0.001	-0.001
K	-0.045	-0.050	0.293	-0.173	-0.070	0.089	0.135	-0.726	0.423	-0.357	-0.118	0.000	0.001	0.024	-0.008	-0.001	-0.010	0.003	-0.001	0.001
Ca	0.767	0.622	0.144	0.006	-0.019	0.002	0.052	-0.015	0.003	-0.007	-0.008	0.027	-0.001	0.001	0.000	0.000	0.000	0.000	0.000	0.000
Ba	-0.003	-0.002	0.009	-0.008	-0.185	-0.018	0.036	-0.185	0.399	0.872	0.098	-0.004	0.001	-0.012	0.004	0.000	0.011	0.001	0.002	0.000
Ti	-0.006	-0.006	0.040	-0.029	-0.014	0.012	0.022	-0.054	0.016	-0.129	0.939	0.268	0.046	-0.124	0.038	-0.010	0.018	0.067	0.007	-0.012
V	0.000	0.000	-0.001	0.001	-0.003	-0.001	0.001	-0.010	0.003	-0.016	-0.027	-0.003	0.005	-0.347	0.039	0.061	0.746	-0.512	0.068	-0.033
Cr	0.000	0.000	0.000	0.000	0.001	0.000	0.002	-0.003	0.002	-0.001	0.007	0.019	0.025	-0.013	0.034	0.078	0.134	-0.115	-0.663	0.509
Mn	0.003	-0.031	0.000	-0.083	-0.973	0.007	-0.003	0.129	-0.098	-0.130	-0.036	0.034	0.003	0.003	-0.001	0.000	-0.003	0.001	-0.001	0.001
Fe	-0.043	-0.084	0.480	0.842	-0.063	-0.085	0.196	0.038	-0.002	-0.011	-0.005	0.022	0.001	0.002	0.002	0.000	0.000	0.001	0.000	-0.001
Co	0.000	0.000	0.000	0.000	0.000	0.000	0.000	0.000	-0.001	0.000	0.005	0.000	-0.043	-0.017	0.029	-0.019	-0.117	-0.016	-0.041	0.246
Ni	0.000	0.000	0.001	0.000	0.000	0.000	0.001	0.001	0.001	-0.002	-0.005	0.004	-0.012	-0.088	-0.206	-0.030	0.040	0.027	0.687	0.624
Cu	0.000	0.000	0.000	0.000	0.000	0.000	0.000	0.001	0.001	0.000	0.000	0.003	-0.006	-0.072	-0.129	-0.004	0.032	0.005	-0.041	-0.059
Zn	0.000	0.000	0.003	0.000	0.000	0.000	0.001	0.005	0.003	0.001	0.000	-0.004	-0.053	-0.287	-0.911	-0.039	-0.070	0.043	-0.195	-0.085
As	0.000	0.000	0.000	0.000	0.000	0.000	0.000	0.000	0.000	0.000	0.000	0.000	-0.003	-0.015	-0.042	-0.001	-0.001	0.004	0.003	0.024
Pb	0.000	0.000	0.000	0.000	0.000	0.000	0.000	0.000	0.000	0.000	0.000	0.000	0.001	0.001	-0.004	-0.001	0.004	-0.005	0.007	0.012
Th	0.000	0.000	0.000	0.000	0.000	0.000	0.000	0.000	0.000	0.000	-0.001	0.000	0.002	0.001	-0.002	0.000	0.004	-0.002	0.005	-0.010
Rb	0.000	0.000	0.001	-0.001	0.000	0.000	0.001	-0.005	0.003	-0.002	-0.012	0.001	0.020	0.003	-0.024	0.007	0.074	-0.021	0.059	-0.164
U	0.000	0.000	0.000	0.000	0.000	0.000	0.000	0.000	0.000	0.000	-0.002	0.001	0.002	-0.012	0.001	-0.009	-0.009	-0.003	-0.021	0.023
Sr	0.002	0.001	0.000	0.003	0.004	0.001	-0.014	0.000	0.000	0.007	-0.078	-0.012	0.961	-0.229	0.032	-0.035	-0.069	0.085	-0.009	0.029
Y	0.000	0.000	0.000	0.000	0.000	0.001	0.000	0.000	0.000	0.000	0.005	-0.001	0.022	0.026	-0.021	-0.022	0.028	0.028	0.066	-0.124
Zr	0.000	0.000	0.000	-0.002	0.002	0.001	0.002	0.006	-0.007	0.001	0.110	0.031	0.242	0.835	-0.307	0.116	0.264	-0.132	0.005	0.085
Nb	0.000	0.000	0.000	0.000	0.000	0.000	0.000	0.000	0.000	0.000	0.000	0.000	0.004	0.004	-0.003	-0.005	0.002	0.002	0.009	-0.016
Mo	0.000	0.000	0.000	0.000	0.000	0.000	0.000	0.000	0.000	0.000	0.003	0.003	-0.080	-0.074	0.079	-0.032	-0.186	-0.036	-0.158	0.468
Sn	0.000	0.000	0.000	0.000	0.000	0.000	0.000	0.000	0.000	0.000	0.000	0.000	0.000	0.000	0.000	0.000	-0.001	0.000	-0.001	0.002
Sb	[illegible]	[illegible]	[illegible]	0.000	0.000	0.000	0.000	0.000	0.000	0.000	0.000	-0.002	-0.005	-0.008	0.014	0.000	-0.017	0.004	0.003	0.045
Si/Al		Greater than 0.49		0.000	0.000	0.003	0.001	-0.001	0.001	0.000	-0.004	0.007	0.001	-0.100	-0.009	0.984	-0.127	0.019	0.059	-0.017
Si/Ti		Less than -0.49		0.002	0.000	-0.001	-0.002	0.003	-0.001	0.000	-0.061	-0.032	-0.058	-0.034	0.033	0.051	0.522	0.830	-0.071	0.072

Table 5.2. Summary of XRF elemental proxies and their significance in the interpretations of the chemostratigraphy based on multiple references: (Bhatia and Crook, 1986; Pearce and Jarvis, 1992; Calvert and Pedersen, 1993; Pearce et al., 1999; Sageman and Lyons, 2004; Brumsack, 2006; Algeo and Lyons, 2006; Tribovillard et al., 2006; Algeo and Rowe, 2012; Turner 2016).

Element	Proxy - Significance	Correlation Coefficients
Titanium (Ti)	Continental source and dust input	0.939
Zirconium (Zr)	Continental source / Continentally derived	0.835
Silicon/Aluminum (Si/Al)	Quartz origin (biogenic or detrital)	0.984
Aluminum (Al)	Clay contents and feldspar	0.805
Potassium (K)	Clay contents and feldspar	-0.726
Thorium (Th)	Clay contents and feldspar	0.005
Calcium (Ca)	Carbonate source and phosphates	0.767
Strontium (Sr)	Carbonate source and phosphates	0.961
Magnesium (Mg)	Carbonates, dolomitization	-0.958
Manganese (Mn)	Carbonates, dolomitization	-0.973
Uranium (U)	Organic matter richness, (bitumen)	-0.012
Vanadium (V)	Bottom water anoxia, redox sensitive	0.746
Molybdenum (Mo)	Bottom water euxinia, redox sensitive	0.468
Sulfur (S)	Pyrite, reducing conditions, euxinia	0.771
Phosphorous (P)	Phosphate accumulation	0.002

Electrofacies: Similar techniques to the chemofacies classifications, electrofacies used well logs for clustering purposes. Well logs were examined for their variances, included gamma

ray (GR), photoelectric (PE), bulk density (RHOB), neutron porosity (NPHI), deep resistivity (ILD), medium resistivity (ILM), shallow resistivity (IL8) and acoustic (DT). GR, ILD, IL8, ILM, and DT represented the first five components with the highest variability to be used as primary input to classify different clusters of facies. The components of these five logs counted for more than 95% of the variance in the data set (**Table 3**). Next, the identified well-log variables from PCA were used to determine the optimal number of clusters (electrofacies in groups).

Table 5.3. Correlation coefficients of PCA for the selected well logs that are statistically significant with a correlation coefficient > 0.49 (green cells) and < -0.49 (red cells).

Greater than 0.49
Less than -0.49

Standard	39.129	14.209	4.731	3.830	3.450
	PC1	PC2	PC3	PC4	PC5
DT	-0.195	-0.090	-0.299	0.559	-0.743
GRD	-0.572	-0.796	0.099	-0.138	0.103
ILD	0.714	-0.561	-0.411	0.040	0.076
ILM	0.245	-0.110	0.400	-0.585	-0.653
LI.8	0.256	-0.178	0.756	0.570	0.079
NPHI	-0.002	-0.001	-0.003	0.004	-0.005
RHOB	0.001	0.001	0.002	-0.003	0.005

The elbow method resulted in five chemofacies and five electrofacies for the I-35 Sycamore outcrop to be the optimal number of clusters (**Figure 5.5**). Finally, the unsupervised clustering analysis of self-organizing map (SOM) was used based on the 5 selected logs, considering the optimal number of 5 clusters obtained from the elbow method.

Once the electrofacies classifications were identified, a comparison was done with thin-sections analysis and the XRD bulk mineralogy data to identify the geological meaning of these five electrofacies.

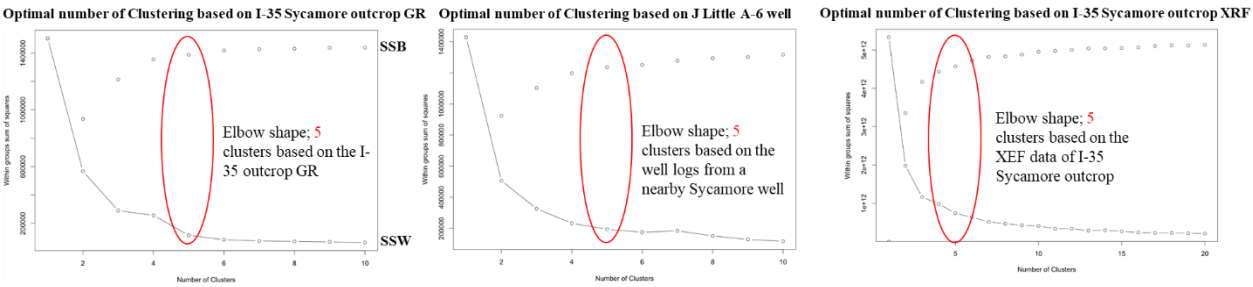

Figure 5.5. Elbow method plots showing the variance vs. the numbers of clustering. Sum of square within clusters (SSW) showed the variance in each cluster. Sum of square between clusters (SSB) shows how each cluster differed from one another. The "elbow" shape indicated by the red oval represented the optimal number of clusters, 5 for GR, and XRF data of I-35 Sycamore outcrop and subsurface well log data, where there was small variance within each cluster (SSW) and large variance between clusters (SSB).

Results

Outcrops characteristics and their stratigraphy

In the studied area, the Mississippian is bounded at its base by upper Woodford unconformity at both outcrops and an overlying unconformity with the top of the Caney Shale at the I-35 Sycamore outcrop (**Figure 5.6**). The boundary between the upper Woodford and Mississippian in both I-35 and Speake Ranch outcrops revealed two immediately distinctive sedimentary lithofacies. The rocks change from chert beds with an abundance of phosphate nodules, organic-rich sediment of the uppermost Woodford Shale to the distinctive softer greenish shale.

Field observations aided by outcrop GR measurements clearly suggested that the I-35 Sycamore outcrop consists of three major hard calcareous siltstone—very fine sandstone intervals separated by another three eroded shale sections (**Figure 5.6)**. Hence, the I-35 Sycamore outcrop was divided into six stratigraphic units/ sections, comprising 1) the Lower Shale “Transition” Section (LShTS) in the lowermost section, followed with 2) Lower Sycamore Section (LSyS), 3) Middle Shale Section (MShS), 4) Middle Sycamore Section (MSyS), 5) Upper Shale Section

(UShS), and the uppermost is the 6) Upper Sycamore Section (USyS). The Speake Ranch outcrop comprised only Lower Shale "Transition" Section (LShTS) above the upper Woodford Shale (**Figure 5.6**). The total vertical stratigraphic thickness of the I-35 Sycamore outcrop is 450 ft, while the Speake Ranch outcrop is 50 ft.

1) **Lower Shale "Transition" Section (LShTS):** the thickness of the LShTS in the I-35 Sycamore outcrop is 78 ft whereas in the Speake Ranch it is 50 ft. Lithologically, in ascending order, LShTS was predominant with siliceous greenish shale (~13 ft) at the base, followed by siliceous brown shale (~16 ft), siliceous chert beds, bioturbated siliceous shale (~22 ft), dolomitic mudstone, and the last 10 ft was mainly bioturbated siliceous, highly radioactive black shale. GR response was high and varied from 173 to 246 cps (average 210 cps; **Figure 5.6**). Clay content is abundant in this section, especially in the greenish shale interval.
2) **Lower Sycamore Section (LSyS):** the stratigraphic thickness of the LSyS is 28 ft. Lithologically, LSyS is predominant with dolomitic calcite cemented siltstone and fine-grained hemipelagic sediment (mud drapes) at the top of most beds (**Figure 5.7**). Ubiquitous characteristics of this section are: scoured surfaces, wavy contacts, irregular beddings and convoluted, repetitive cycles of dolomitic calcite cemented siltstone beds, and Bouma turbidite sequences Ta, Tb, Tc, sometimes Td, and Te (**Figure 5.7**). GR response sharply decreased upward from its underlying LShTS and it was the lowest among the other sections varying from 90 to 160 cps (average 125 cps).
3) **Middle Shale Section (MShS):** the stratigraphic thickness of the MShS is 27 ft. Lithologically, thinly bedded bioturbated fissile shale is the most abundant lithofacies in this section but a few thin (3 to 6 inches) dolomitic beds are present. Radioactive GR response was very high,

decreasing upward, ranging from 119 to 293 cps (average 206 cps; **Figure 5.6**). Clay content is highly abundant throughout this section.

4) **Middle Sycamore Section (MSyS):** the stratigraphic thickness is 120 ft and it is the thickest section among the other sections within the I-35 Sycamore outcrop. The bed thickness of MSyS increases upward in the section. Lithologically, MSyS is largely represented by calcite cemented beds of quartz silt that are capped with fine-grained hemipelagic sediment (mud drapes) on top of most beds (**Figure 5.7**). Observed common features in this section were: scoured surfaces, sharp and wavy basal contact, sediments fining upward with Bouma turbidite sequences Ta, Tb, Tc, sometimes Td, and Te, channels, and thicker beds towards the top of this section (**Figure 5.7**). GR response sharply decreased upward from its underlying MShS, ranging from 108 to 180 cps (average 144 cps). Both calcite and clay contents increased upward in this section.
5) **Upper Shale Section (UShS):** this section was covered but we were able to dig at an interval every 5 ft to measure GR, get samples for thin sections and XRF analyses. It was the thickest shale section in the I-35 Sycamore outcrop, and its stratigraphic thickness is approximately 111 ft. Lithologically, UShS predominantly consists of greenish shale (~50 ft), followed by bioturbated fissile siliceous black shale (~60 ft). Radioactivety, GR response was the highest through the I-35 Sycamore outcrop, ranging from 280 to 320 cps (average 300 cps; **Figure 5.6**) and the GR generally increased upward in the section with a highest peak of GR in the uppermost interval of the section within the fissile black siliceous shale lithofacies.
6) **Upper Sycamore Section (USyS):** the stratigraphic thickness is 82 ft. Lithologically, it is dominated by the sandy siltstone lithofacies. This section was very distinctive by the blocky massive sandy slump beds with little to no fracture occurrences, absence of calcite cement, and

presence of microporosity. GR response sharply decreased upward from its underlying shale unit (UShS), ranging from 180 to 130 cps (average 155 cps), and the GR decreasing upward with an increase of calcite upward in the section.

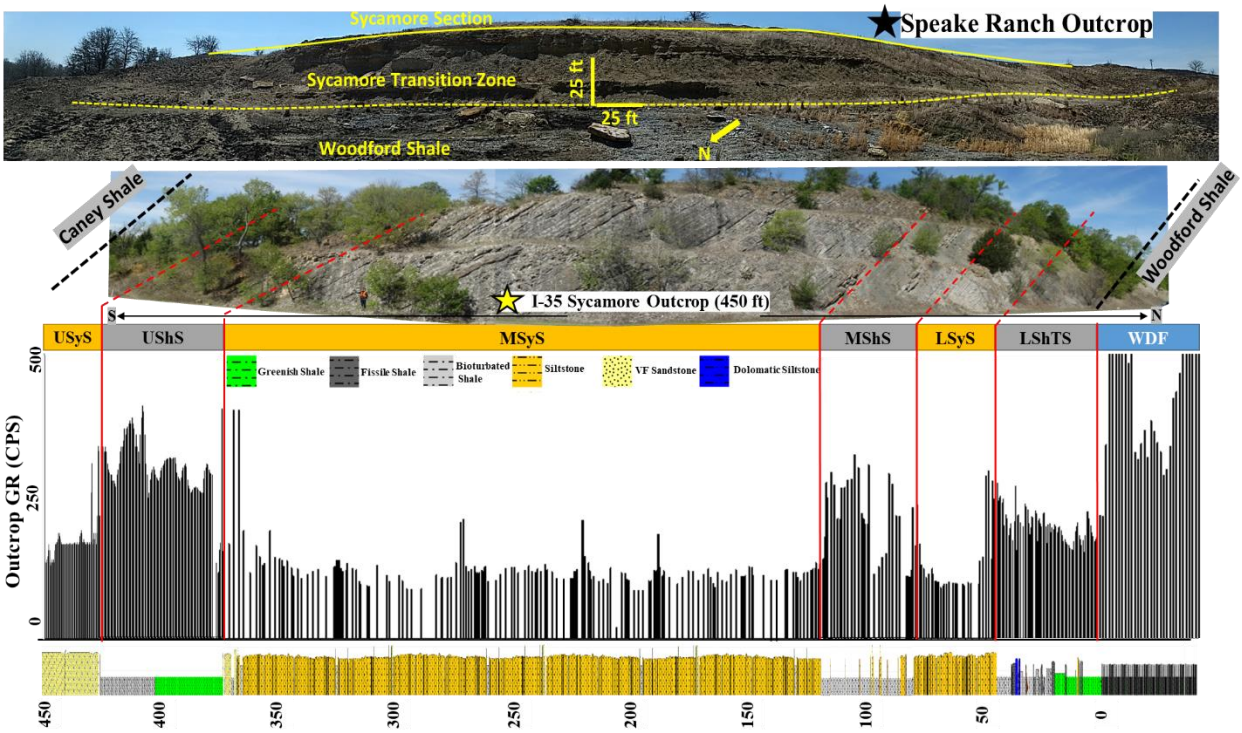

Figure 5.6. Outcrops photomosaic and their stratigraphy. Upper photo is the Speake Ranch outcrop. The lower photo is the I-35 Sycamore outcrop road cut.

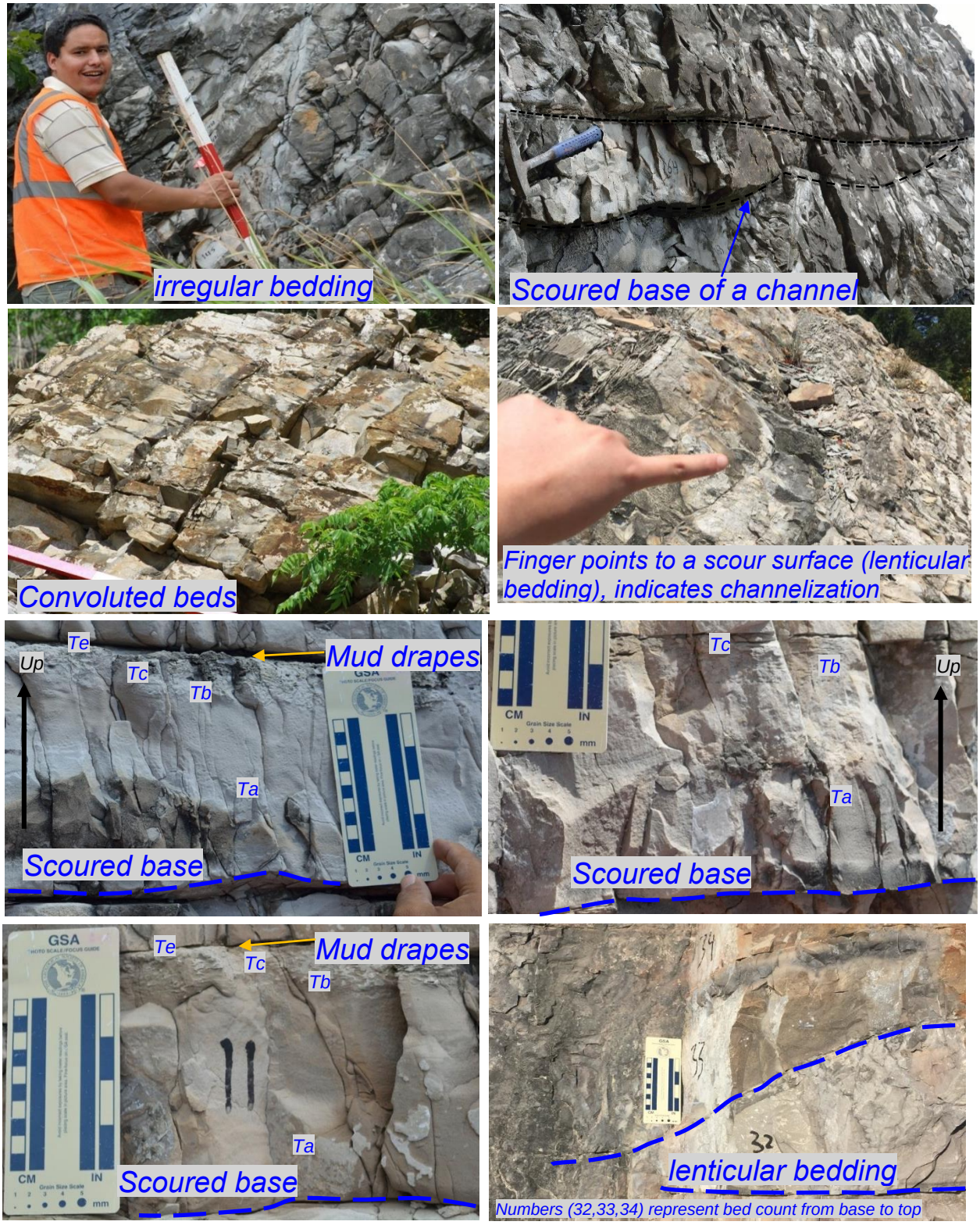

Figure 5.7. I-35 Sycamore outcrop features evidencing the gravity flow (turbidite) deposit, such as Bouma units (Ta, Tb, Tc, Td,Td), scoured surface, lenticular, and irregular beddings.

Outcrop Lithofacies

Within the six stratigraphic sections of the I-35 Sycamore strata, seven lithofacies were identified (**Figure 5.8**). They are listed here in decreasing order of abundance within the outcrop section: 1) calcite cemented siltstone (29.4%), 2) bioturbated siliceous shale (21.3%), 3) sandy siltstone (21%), 4) greenish shale (15.5%), 5) dolomitic-calcite cemented siltstone (9.3%), 6) chert (2.3%), and 7) dolomitic mudstone (1.2%).

1) ***Calcite cemented siltstone***: Average bulk-rock composition is calcite (>40%), quartz (44%), dolomite (5%), and clay (4%) (**Figure 5.8**). This lithofacies is the most abundant of angular with subangular detrital quartz silt size grains (up to 40% visual estimate) and rich with a calcite cement compared to other Mississippian Sycamore lithofacies. Microscopically, the rock also consists of peloidal, minor pyrite framboids, and a little micro porosity (**Figure 5.8**). Very minor concentrations of shell hash (crinoid fragments) were observed under higher magnifications of thin sections, which might indicate reworked sediments. Average total organic carbon (TOC) is 0.36 wt.%. In the outcrops, the calcite cemented siltstone beds are predominantly light- to dark-gray, and aggressively react with hydrochloric acid due to the richness of the calcite cement. The beds commonly present Bouma units (Ta, Tb, Tc, Td, Te), and finer laminated brown to dark material (mud drapes) on the top of beds (**Figure 5.7**). Two sets of natural fractures present: Set 1 (strike N20°E and dip 85°SE) and Set 2 (strike N60°W and dip 40°NE) (**Figure 5.4**).
2) ***Bioturbated siliceous shale***: Average bulk-rock composition is quartz (45%), calcite (8%), dolomite (6%), clay (32%), albite (7%), and pyrite (2%) (**Figure 5.8**). Microscopically, the rock consist of a mixture of minor biogenic quartz, silt size detrital quartz, minor mica, framboidal pyrite, bioturbations, and amorphous organic matter (**Figure 5.8**). TOC is the

highest (1.26 wt.%) among the Sycamore outcrop.

3) ***Sandy siltstone***: Average bulk-rock compositions are quartz (55%), calcite (28%), dolomite (4%), clay (6%), albite (3%), and pyrite (4%) (**Figure 5.8**). Microscopically, the rock consists of calcite grains and detrital subrounded to rounded silt-size with some very fine sand. Abundance of the micro intra-porosity and absence of calcite cement are the most distinctive features of this lithofacies **(Figure 5.8**). In outcrop, this lithofacies is mainly hard, well-indurated, and a bluish-gray color. It is distinctive by the blocky, massive, non-fractured beds with an increase of clay content compared to other siltstone facies. Bouma sequences Ta and Tb were observed in this lithofacies (**Figure 5.7**).

4) ***Greenish shale***: Average bulk-rock composition is quartz (50%), calcite (1%), dolomite (4%), clay (44%), and albite (2%). This lithofacies is the most clay-rich (>40%) among the Sycamore lithofacies, so it may be a frac barrier. Microscopically, the rock consists of biogenic quartz of radiolarian, flattened tasmanites, clay, some pyrite, and intraparticle porosity (**Figure 5.8**). TOC is 0.10 wt.%. In both outcrops, the most outstanding features of this lithofacies are: its pale green color, slightly calcareous to non-calcareous rock, and soft platy appearance.

5) ***Dolomitic-calcite cemented siltstone***: This lithofacies is very similar to the calcite cemented siltstone lithofacies except for the presence of dolomitization. Average bulk-rock composition is quartz (37%), calcite (37%), dolomite (24%), and clay (2%) (**Figure 5.8**). Microscopically, the rock consists of calcite cement (pink color), angular to sub-angular detrital quartz silt, peloidal, dolomite (dolomitizations), minor fossil fragments filled with quartz (crinoids), minor pyrite, and micro-porosity (**Figure 5.7**). The occurrence of silt-sized detrital quartz is less abundant (about 30% visual estimate) compared to the calcite cemented siltstone. Dolomite/ankerite crystals are partially leached or dissolved, revealing a type of intraparticle

porosity within the fossil fragments (crinoids) (**Figure 5.8**). Average TOC is 0.22 wt.%. In the outcrop, they are pale yellowish to light-grey, thick, hard, massive beds with the presence of repetitive finer laminated dark-brown material (mud drapes) on the top of most beds. Bed features such as irregular beddings, lenticular beddings, scoured surface, convoluted beddings, and Bouma sequences (Ta, Tb, Tc, Td, and Te) are commonly observed (**Figure 5.9A**). Two fracture sets were observed: Set 1 (strike N20°E and dip 85°SE) and Set 2 (strike N60°W and dip 40°NE) (**Figure 5.4**).

6) ***Chert***: This lithofacies is the most quartz-rich (quartz >50%) among the Sycamore outcrops. Average bulk-rock composition is quartz (54%), calcite (8%), dolomite (15%), clay (22%), and pyrite (1%). Microscopically, this lithofacies consists of biogenic quartz (radiolarian and flattened tasminites), microcrystalline quartz aggregates arranged in very tight frameworks, minor detrital quartzes, and a few diagenetic pyrite framboid (**Figure 5.8**). Many of the scattered patches of dark-brown organic material, lenticular fabric of organic matter, and amorphous organic matter are present throughout the matrix (**Figure 5.8**). Also, intraparticle porosity, fractures filled with bitumen, and some filled with quartz are present. TOC is 0.43 wt.%. In outcrop, this lithofacies is dark-brown, well-indurated (blocky), and massive.

7) ***Dolomitic mudstone***: This lithofacies is the most dolomite-rich (dolomite >60%) among the Sycamore outcrops. Average bulk-rock composition is quartz (12%), calcite (14%), dolomite (68%), and clay (6%) (**Figure 5.8**). Microscopically, this lithofacies mainly consists of micro-crystalline dolomite (recrystallized matrix), clay, grains of ferroan dolomite (might indicate early diagenesis), some detrital quartz, calcite (~15%), a little pyrite, and fractures filled with bitumen. Fossil fragments are strongly replaced by dolomite. The matrix is made of mosaics of finely crystalline dolomite and clay (**Figure 5.8**). In both outcrops, dolomitic beds are tan-

weathering light- to dark-grey, hard, massive, and crystalline in appearance.

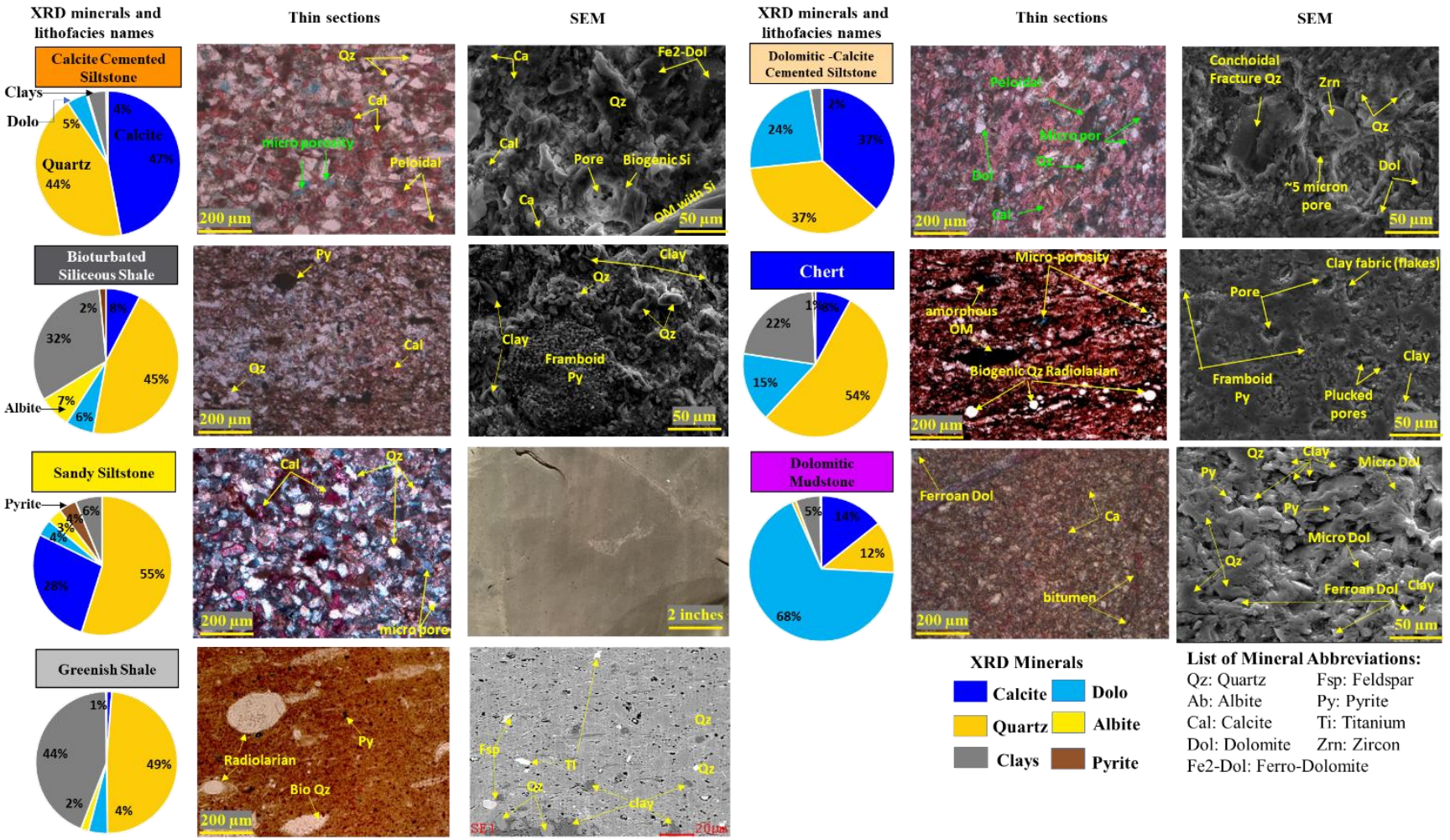

Figure 5.8. Average mineralogical composition, petrographic, and SEM image characteristics of the Mississippian Sycamore lithofacies in the SCOOP area. Color background of each lithofacies' name represents the lithofacies' color in the ternary diagram and pie chart plot in Figure 5.4.

Outcrop chemostratigraphic characterizations

Elemental chemostratigraphy

As mentioned earlier, **Table 5.2** summarizes the significance of the main XRF elements in chemostratigraphic interpretations which could be used as proxies for clay minerals, carbonate minerals, detrital inputs, and elemental proxies for bottom water conditions. This helped to develop a chemostratigraphic framework and infer the variations in the depositional and environmental factors, such as sediment source (detrital vs. biogenic), carbonate, organic paleoproductivity, and redox process. Hence, XRF elements that were used for the chemofacies were grouped into three categories for the Sycamore strata: 1) detrital-sensitive elements (Al, K, Ti, Zr, Th, Si), 2) carbonate-sensitive elements (Ca, Mg, Sr), and 3) redox-sensitive elements (Mo, V, S). **Figure 5.9A** shows the chemostratigraphy profile of the I-35 Sycamore outcrop and exhibits variations within the outcrop sections while **Figure 5.9B** shows the chemostratigraphy profile of the Speake Ranch Sycamore outcrop.

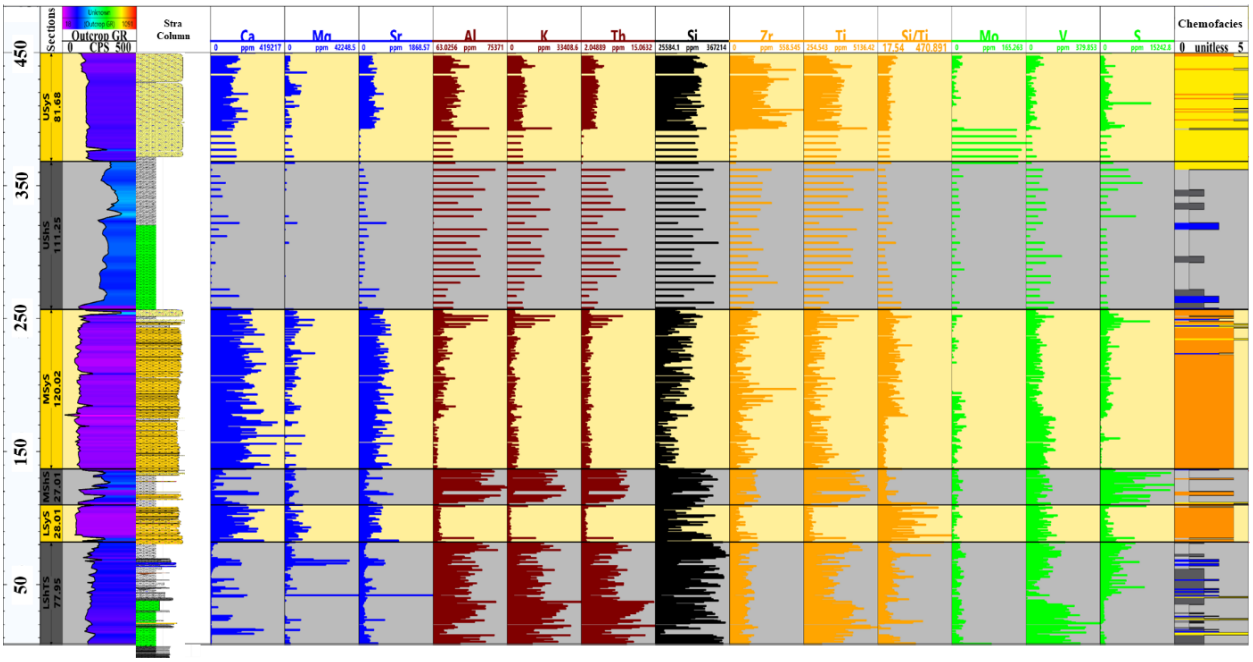

Figure 5.9. Vertical profiles of the XRF data for the I-35 Sycamore outcrop and Speake Ranch outcrop. A) Vertical profile of most common chemostratigraphy proxies across the entire I-35 Mississippian Sycamore section. The subdivision sections are in the column 1, outcrop GR is in column 2, and lithological stratigraphy profile is column 3, and the chemofacies clustering profile is the last column. Carbonate-sensitive elements are colored by blue, clay elements by red, detrital elements by orange, and redox-sensitive elements are colored by green.

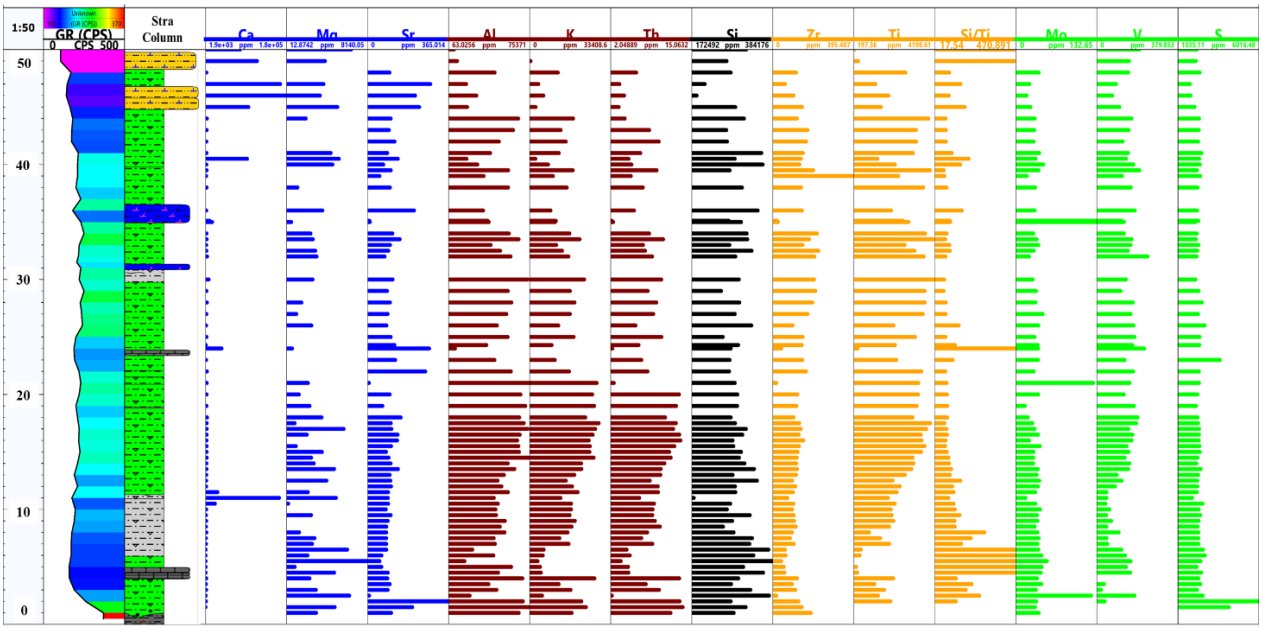

Figure 5.9B. Vertical profile of the most common chemostratigraphy proxies across the entire Speake Ranch Mississippian Sycamore Transition section.

Throughout the entire Mississippian section of the I-35 Sycamore outcrop, certain elements occur similarly, and they are associated with each other (**Figure 5.9A**). Ca and Sr trends are associated, so that when the Ca increases, Sr increases and vice versa. Ti, Th, and K have a strong association with Al, suggesting that these elements are mostly in the clay fraction (**Figure 5.9A**). In general, except for the greenish shale facies in the LShTS, there is a consistency of Si trend with Ti, Al, K, and Th, suggesting most of the silica in the Mississippian system is of detrital origin. The redox proxy of Mo does not exhibit significant changes except in the lowermost 25 ft of the USyS. Sulfur is strongly associated with siliceous shale lithofacies, where S records the highest concentrations for the siliceous shale interval throughout the entire Mississippian section. This might indicate that siliceous shale is deposited deeper into the basin compared to other Mississippian lithofacies.

Carbonate proxies are abundant in the Sycamore siltstone sections (LSyS, MSyS) and the USyS contains medium concentration of carbonate proxies. The shale sections (LShTS, MShS, and UShS) have the lowest carbonate content. Mg is associated with Ca and Sr only in the dolomitic beds. Sr has a strong association with Ca throughout the vertical profile, suggesting that Sr is mostly in the calcite minerals. Additionally, Ca and Mg are mutually associated in some zones (**Figure 5.9A and 5.9B**), indicating the presence of dolomite minerals.

Clay and detrital inputs are abundant through the Mississippian Sycamore section. Zr is associated with clay (aluminosilicate, Al) in the MSyS and USyS sections, whereas Ti, Th, and K are associated with clay (aluminosilicate) (Al) in the shale sections (LShTS, MShS, and UShS).

I-35 Sycamore outcrop shows a Si trend associated with the clay contents, which might suggest that most of the Si content in the outcrop is from extrabasinal deposits.

These previous observations of XRF analyses agree with our petrographic results (**Figure 5.8**) in the Sycamore siltstone units, where the high content of quartz silt-sized grains is non-biogenic in origin (detrital source). Also, within the shale units especially the siliceous shale lithofacies, there are higher contents of detrital silt-sized grains. But the green shale is more a mixture of both biogenic particles (radiolarian) and higher clay content (**Figure 5.8**).

Sulfur element is more sensitive to the lithology variations compared to the Mo and V elements throughout the Mississippian units (**Figure 5.9A**). Hence S is a reliable proxy for redox conditions instead of Mo and V elements. Also, Fe is positively correlated with S (**Figure 5.10**) in the black bioturbated siliceous shale only, indicating S and Fe are mainly in the pyrite phase. The bioturbated siliceous shale intervals might have a relatively higher anoxic-euxinic environment with highest S content and highest organic matter (OM) compared to other Sycamore sections. It is possible they represent condensed section intervals. By looking at the S profile, we may conclude that going from low S to high values indicates a move from anoxia (not oxygen) to euxiniy and/or shallow to deep water system. When the S decreases upward, the oxidation level may increase upward. We observed that S correlates with TOC (**Figure 5.11**).

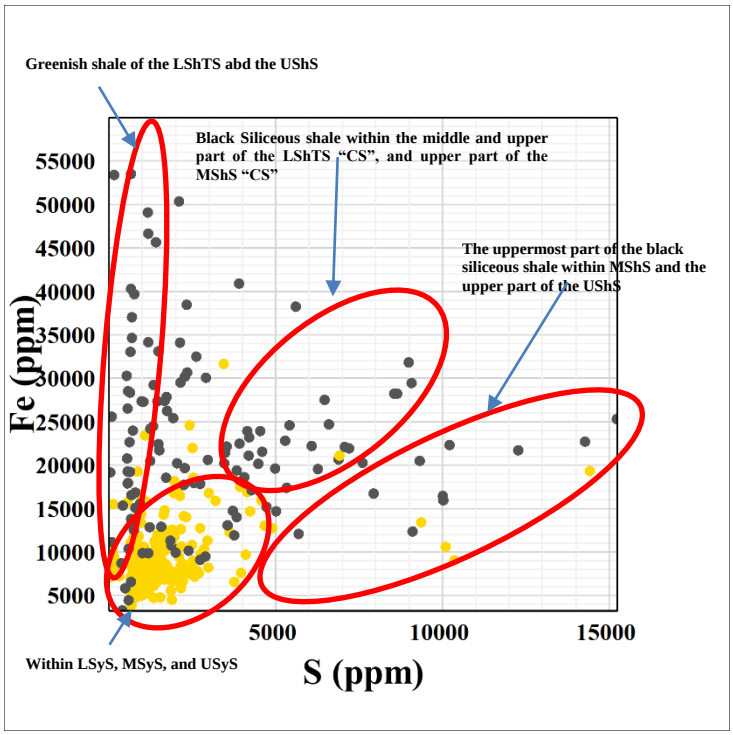

Figure 5.10. Cross plots of redox-sensitive elements vs. sulfur (S) differentiated by Sycamore siltstone (yellow dots) sections and shale (black dots) sections in the I-35 Sycamore outcrop. Sulfur is positively correlated with the Fe, Mo, and V for the bioturbated siliceous shale facies. High levels of sulfur in the bioturbated siliceous shale facies are interpreted to form a relatively more anoxic-euxinic environment.

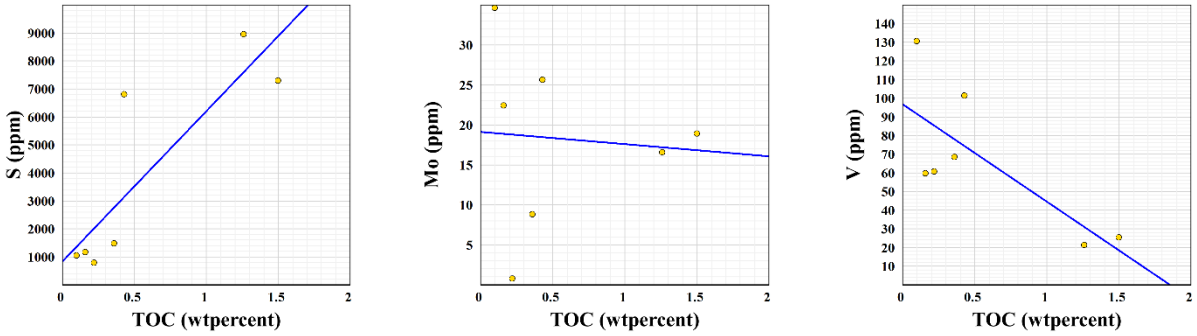

Figure 5.11. TOC vs. S, Mo, and V cross plots based on seven samples from the I-35 Sycamore outcrop. TOC is linearly correlated with TOC and negatively correlated with V. TOC and Mo do not correlate.

The Si vs. S cross plot revealed the highest sulfur content is associated with the siliceous shale and lowest sulfur content is affiliated with the greenish shale. Black siliceous shale (upper

red oval in **Figure 5.12**) has the highest sulfur content, indicating a deep marine environment. Whereas greenish shale samples (lower red oval) have the lowest sulfur content, indicating a shallow marine environment (**Figure 5.12**).

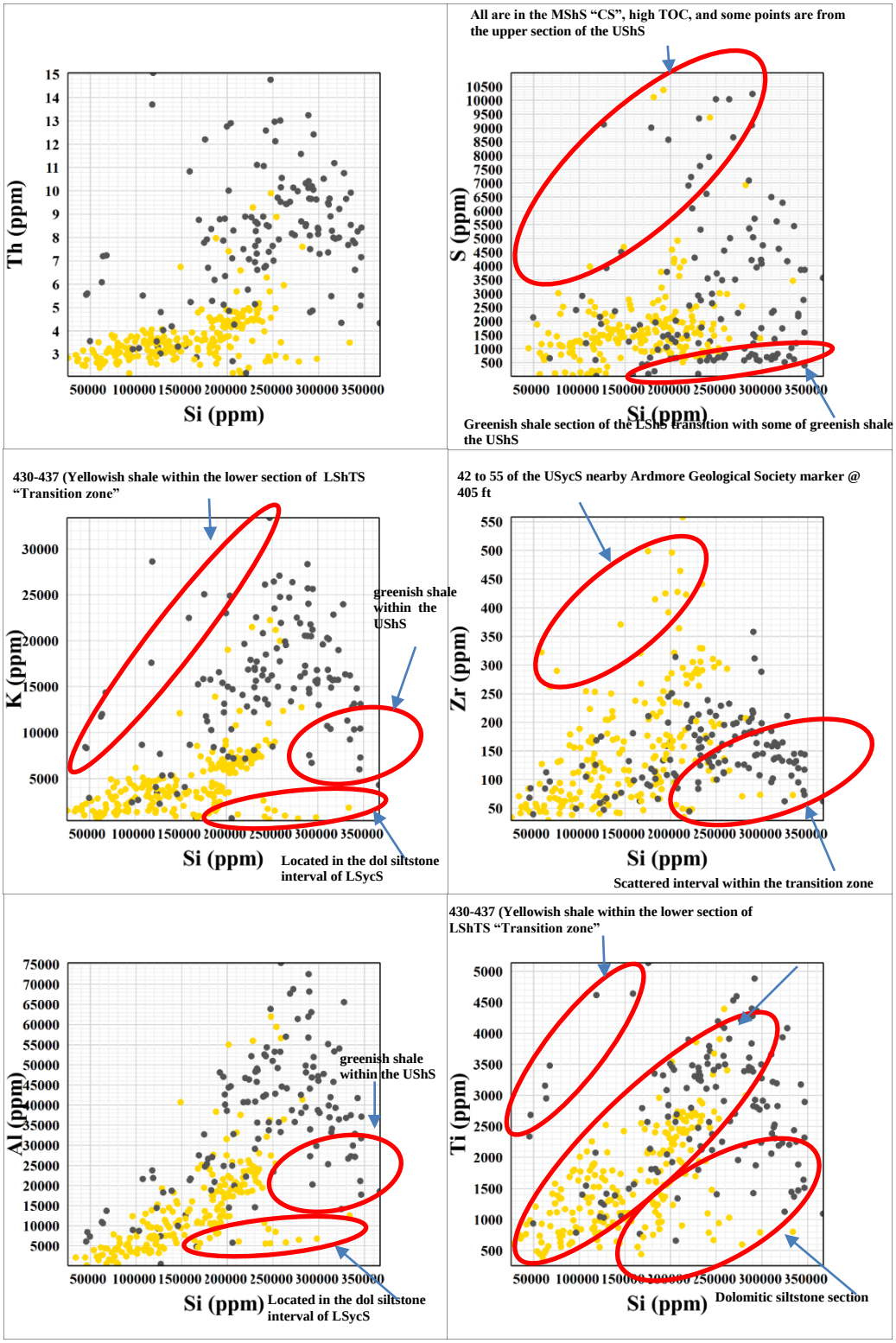

Figure 5.12. Cross plots of detrital-sensitive elements vs. Si differentiated by Sycamore siltstone (yellow dots) sections and shale (black dots) sections in the I-35 Sycamore outcrop.

Th, Al, and K show linearly positive covariance with Si (**Figure 5.12**) in the shale sections (black dots). In this case, Si might be of detrital source that is associated with clay elements (Th, Al, K) rather than biogenic/authigenic Si. On the other hand, Si in the Sycamore siltstone sections is associated with Zr, suggesting Si is from an extrabasinal sediment source.

XRF by facies type

To quantitatively and qualitatively relate the chemo facies to the lithofacies of the I-35 outcrop, **Figure 5.13** and **Table 5.4** show boxplots and summary of elemental proxies for every single lithofacies.

Table 5.4. Summary of XRF elements per lithofacies of the I-35 Sycamore outcrop.

Lithofacies	XRF elemental proxies		
	High	Medium	Low
Greenish shale	K, Th, Ti		Ca, Sr, Mg, S, Zr
Bioturbated siliceous shale	K, Th, Al, Ti, S	Zr	Ca, Sr, Mg
Chert	Si	Al, Th, K, Ti, Zr	Ca, Sr, Mg, S
Dolomitic mudstone	Mg, Sr, S	Ca, Al, Th, K, Ti	Zr
Dolomitic-calcite cemented siltstone	Ca, Sr		Mg, Al, Th, K, Ti, Zr, S, Si
Calcite cemented siltstone	Ca, Sr	Mg	Al, Th, K, Zr, S, Si, Ti
Sandy siltstone	Zr, Ca	Al, Th, K, Ti, Si	S, Sr, Mg

Greenish shale lithofacies: it is characterized by: lowest carbonate content, highest K and Th clay content, high Al clay content, high Si, highest Ti, low Zr, and lowest S (**Table 5.4 and Figure 5.13**). Bulk XRD resulted in the highest clay content (44%), confirming that greenish shale is a clay-rich lithofacies. High content of silica originated from the radiolarian (**Figure 5.8**).

Bioturbated siliceous shale lithofacies: it is characterized by very low carbonate content, the second highest K and Th clay content after greenish shale, the highest Al clay content, very high Si, the second highest Ti, medium Zr detrital content, and the highest sulfur content (**Table 5.4 and Figure 5.13**). XRD resulted in an average of 34% of clay content, and petrographic analyses

revealed that particles of silt-sized detrital quartz were largely within the siliceous shale (**Figure 5.8**). Also, 2% of pyrite was reported from XRD data and also observed in the thin sections. TOC value is the highest (1.26 wt %) for this lithofacies among other Mississippian lithofacies.

Chert lithofacies: it is characterized by: low carbonate content, medium clay content, highest Si, medium Ti, low Zr, highest Mo, medium V, and the second lowest S. Thin sections showed abundance of biogenic silica, mainly Radiolarian and tasminite. Also, bulk XRD revealed 23% of clay mineral and 54% of quartz (the highest amount of quartz compared to other lithofacies) (**Figure 5.8**), suggesting a deeper water environment.

Dolomitic mudstone lithofacies: it is characterized by highest Mg and Sr, the second highest S content, medium Ca, clay, Si, and medium Ti content, and lowest Zr (**Table 5.4 and Figure 5.13**). Corroborating these XRF elemental findings, the highest percentage of dolomite (68 %) revealed the bulk XRD and highest amount of dolomite, especially ferron dolomite observed from both the petrographic and SEM images (**Figure 5.8**). Bitumen filled fractures were also observed in this lithofacies.

Calcite cemented siltstone lithofacies: it is characterized by the second highest Sr, the third highest Ca, low Mg Ti and Zr, second lowest S content, and the lowest Si (**Table 5.4 and Figure 5.13**). The lowest content of Si from XRF is contrary to the 44% of quartz from the XRD results, the abundance of angular to subangular silt-size detrital quartz.

Dolomitic calcite cemented siltstone lithofacies: it has very similar XRF characteristics as calcite cemented siltstone, except the Mg is slightly higher and Ti is the lowest. These findings agree with the petrographic, XRD, and SEM results, except with the low Mg element because dolomite consists of 24% of the total minerals within the lithofacies and was observed in both petrographic

and SEM analyses. Zircon minerals were also observed in the SEM image, supporting the highest Zr XRF element.

Sandy siltstone: it is characterized by highest Zr, high Ca, medium clay and Si, low Ti, low S, low Sr, and the lowest Mg. Although this lithofacies has high Ca element, the intraparticle porosity was clearly the highest compared to the other siltstone lithofacies. This might be because the calcite grains are not a cement as observed by the petrographic analyses (**Figure 5.8**). Also, XRD measured 58% of quartz in this lithofacies.

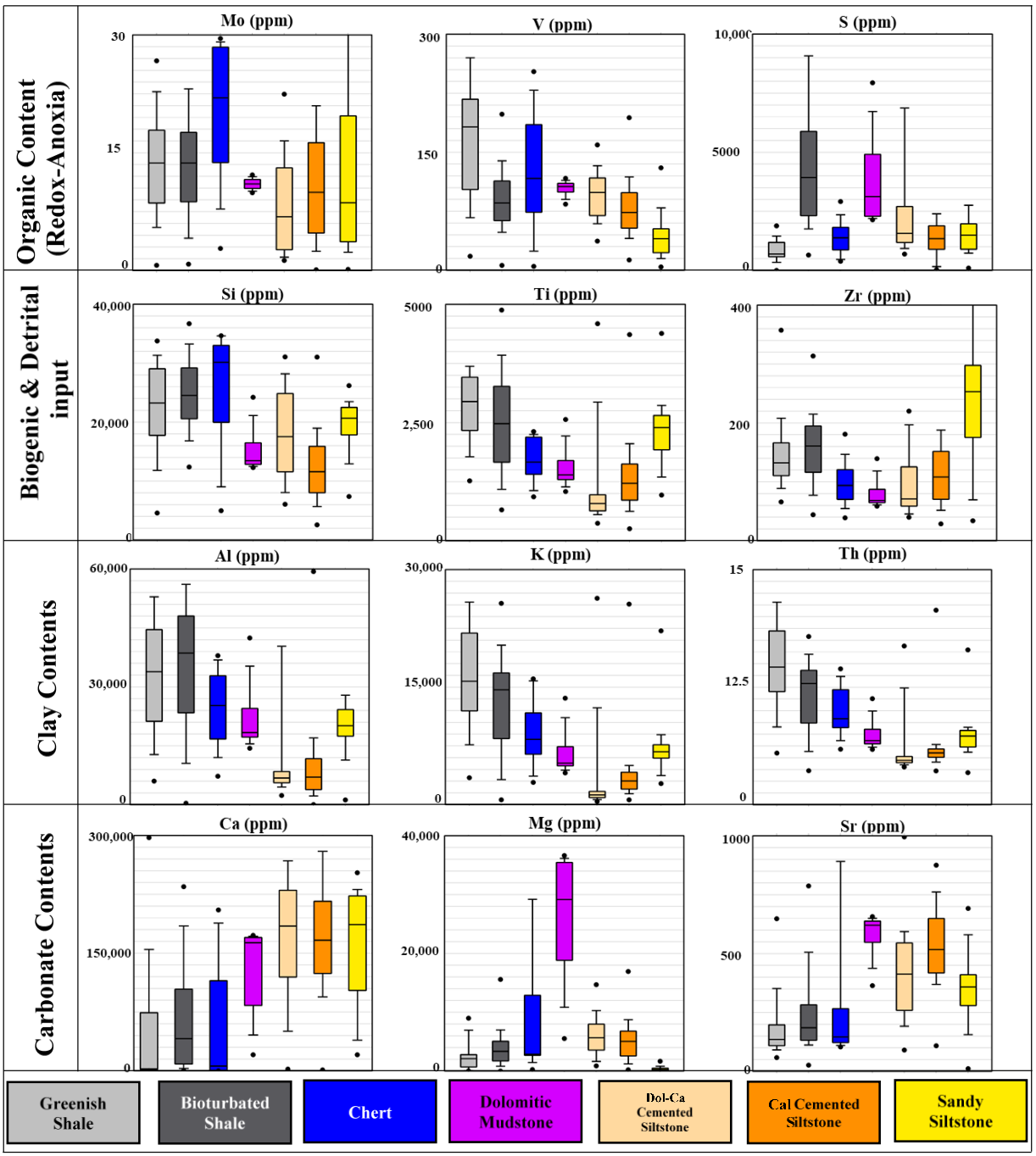

Figure 5.13. Box plots of XRF elemental proxy colored coded by the seven lithofacies of the I-35 Mississippian Sycamore strata outcrop. XRF elements reveal to be changed with the lithofacies types.

Outcrop sequence stratigraphy

The purpose of building a sequence stratigraphy framework was to predict the lateral continuity of the source, seal, and better reservoir quality to predict and drill a lateral well. The general concepts of sequence stratigraphy were based on deposited sediments that were in a cyclical and predictable manner of unconventional shale strata (Slatt and Rodriguez, 2012; Slatt, 2013a). Hence, outcrop GR responses were used to identify high-frequency stratigraphic cycles called Gamma Ray Parasequences (GRP). The interpretation of the Sequence Boundaries (SB) and Maximum Flooding Surfaces (MFS) could be identified based on their laterally continuous deposition (Slatt and Rodriguez, 2012). Between two SBs, a drop in sea level to form the basal SB, and Lowstand Systems Tract (LST), was followed by marine transgression up to FS/MFS to form a Transgressive Systems Tract (TST). Then sea level rose relatively slowly to form the progradational Highstand Systems Tract (HST) and continued to form the upper SB (**Figure 5.14**).

Due to the lack of clear conodont studies, which provide some age control on the Mississippian strata, it is hard to identify the definite order scale of the sequence stratigraphy. However, the general age difference between the Mississippian and Pennsylvanian is 35.7 Ma. Also, assuming each cycle has a similar time deposition, the Mississippian strata was subdivided into a series of 2nd order GRPs. Additionally, high frequency cycles were identified from the outcrop GR without age control.

The depositional sequence was categorized based on: 1) Increasing-upward, 2) Decreasing-upward, and 3) Blocky (no-change upward). Then, the turnaround points of regressive surfaces (rs) and flooding surfaces (fs) were identified as shown in (**Figure 5.14B**).

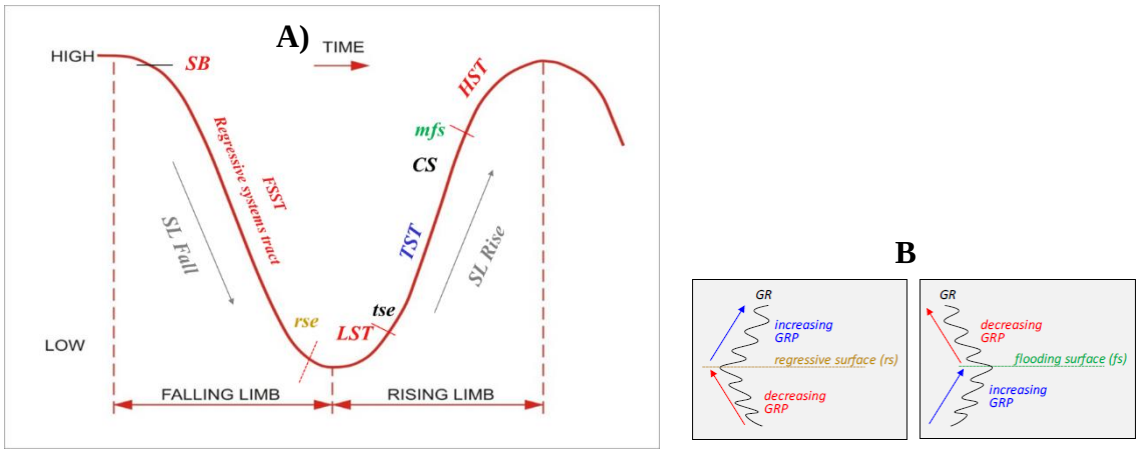

Figure 5.14. A) Sequence stratigraphic model employed in this study. (Slatt and Rodriguez, 2012). B) Criteria for Gamma Ray Parasequences (GRP) high-frequency sequence stratigraphy and the interpretation of their boundary surfaces. Flooding surface (fs) corresponds between the changes from upward increasing GR to upward decreasing GR whereas the regressive surface (rs) is vice versa. (Galvis, 2017).

Figure 5.15 shows the interpreted outcrop sequence stratigraphy framework. This framework was built based on the direct outcrop observations/evidence of rock attributes and outcrop GR measurements.

The lower SB of the Mississippian strata in the I-35 Sycamore outcrop is characterized by a gradual decrease in the GR within the uppermost 5 ft of the Woodford Shale. Then, the GR changed to a blocky and slightly serrated GR pattern within the transition zone.

The upper SB marks the contact between the USyS and the Caney Shale. The upper SB is best identified where the retrogradational trend (increasing upward GR) changes to a high GR pattern of the Caney Shale.

At the middle of the UShS, the MFS was picked at a major turnaround point where the underlying retrogradational trend (TST) changed to progradational (LST). On the GR log, MFS is represented by a peak of GR and a change from upward-increasing to upward-decreasing GR (**Figure 5.15**). The condensed section was just below the MFS which was represented by a long-

time interval in which mud and organics were deposited giving rise to a thin shale interval with high radioactive GR readings.

28 GRPs occurred at high order stratigraphic frequencies on the outcrop location (**Figure 5.15A**). Also, 2nd order sequence stratigraphy framework was interpreted at the outcrop and extended over the nearby subsurface well three miles away to predict the reservoir properties away from the outcrop (**Figure 5.15B**). Lateral changes in the stratigraphic thickness of the second-order packages between the outcrop and the subsurface well is consistent (**Figures 5.15 A & B**). This vertical stratigraphic thickness is reasonable enough for horizontal drilling well placement.

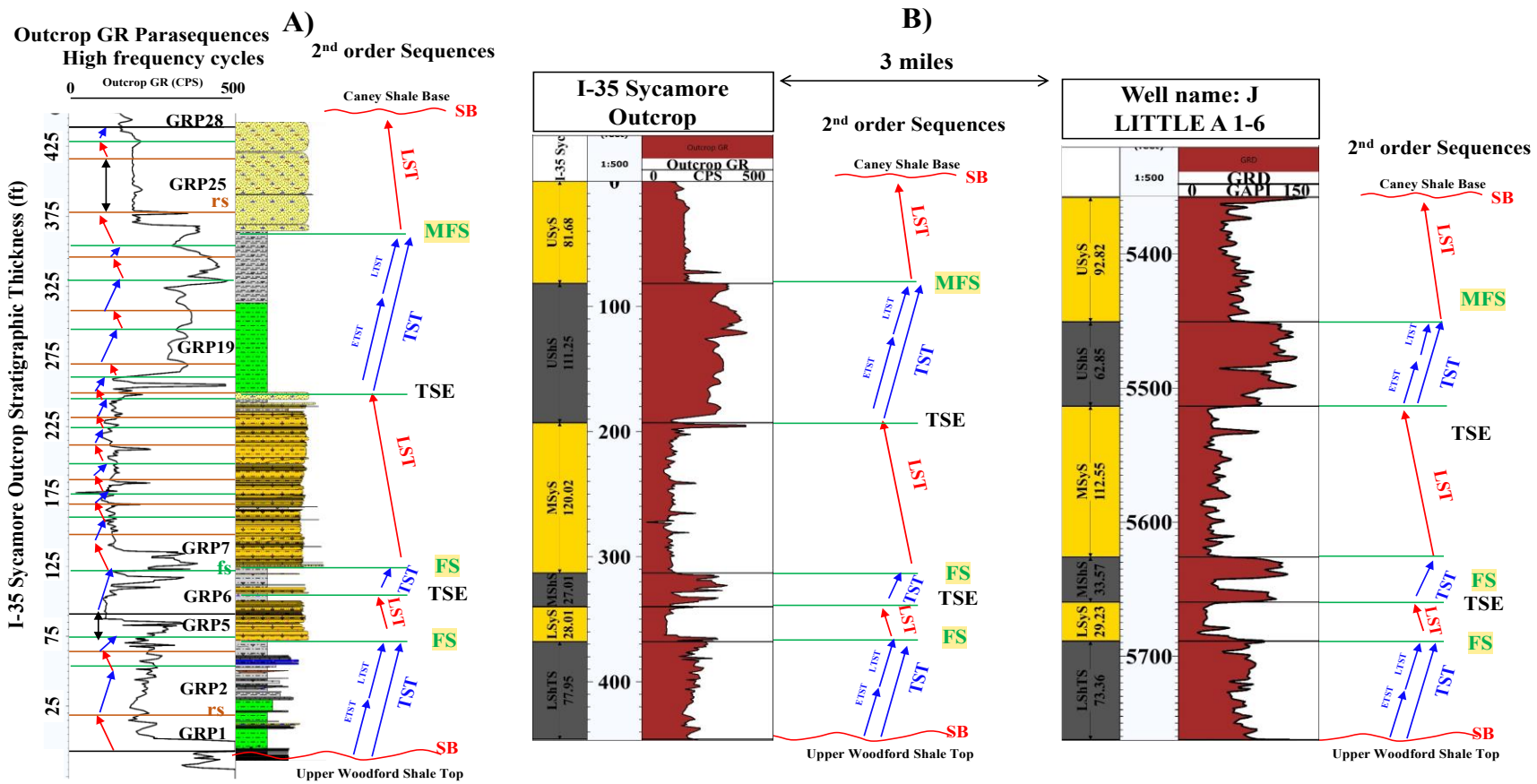

Figure 5.15. Outcrop-based sequence stratigraphic framework of the complete measured section of the Mississippian strata at the I-35 Sycamore outcrop. A) The Sycamore is subdivided into 28 high-frequency stratigraphic GR Parasequences. 2nd order cycles are represented in the last column. B) 2nd order sequence stratigraphy from the I-35 Sycamore outcrop was correlated with the two subsurface wells that are located 3 miles to the south of the outcrop. Blue arrows: increasing-upward GRP. Red arrows: decreasing-upward GRP. Purple arrow: blocky GRP. Sequence Boundary (SB). Transgressive Systems Tract (TST). Early Transgressive Systems Tract (ETST). Late Transgressive Systems Tract (LTST). Lowstand Systems Tract (LST). Transgressive Surface of Erosion (TSE). Condensed Section (CD). Maximum Flooding Surface (MFS) which was between the retrogradational and progradational parasequence sets.

Outcrop-to-subsurface stratigraphic and electrofacies correlation

The vertical stacking of the lithofacies at I-35 Sycamore with its six sections were tied with the hand-held gamma ray profile and correlated well with a nearby subsurface GR logs (3 miles to the south of the outcrop) (**Figure 5.16**). This provided an example of the use of outcrop studies to the subsurface when only uncored wells are available, which is usually the case.

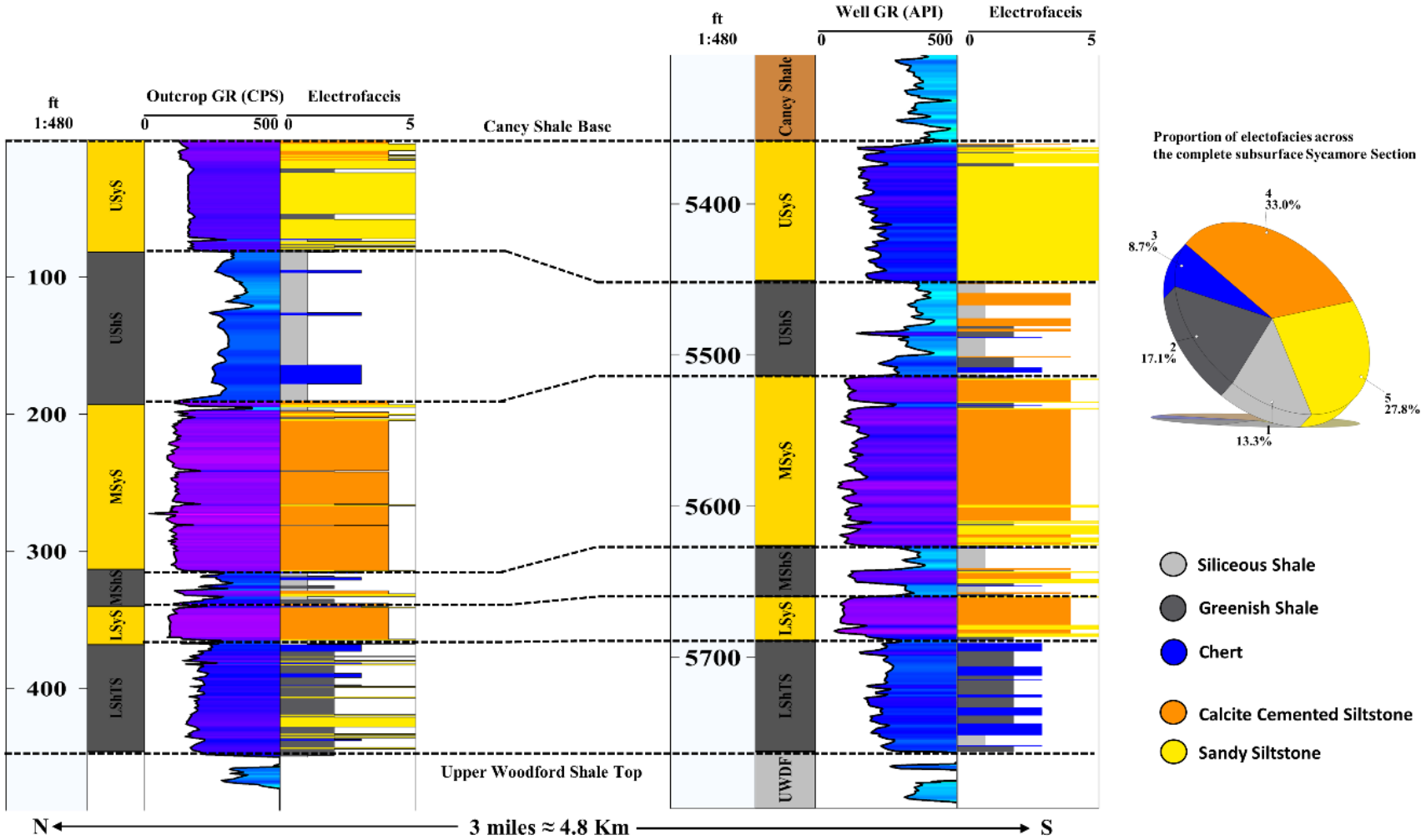

Figure 5.16. Outcrop-to-subsurface gamma ray and electrofacies correlation of the six sections that were subdivided in the I-35 Sycamore outcrop. Stratigraphic thickness and electrofacies variations are relatively symmetric and consistent between the outcrop and the subsurface well. Pie chart shows the proportion of the electrofacies in the subsurface well. True vertical depth (TVD) is the vertical scale for the subsurface well.

The statistical analyses of minimum, maximum, mean, and standard deviation of the I-35 Sycamore outcrop lithofacies types can be obtained from wireline logs with a greater confidence (**Figure5.7 and Table 5.5**).

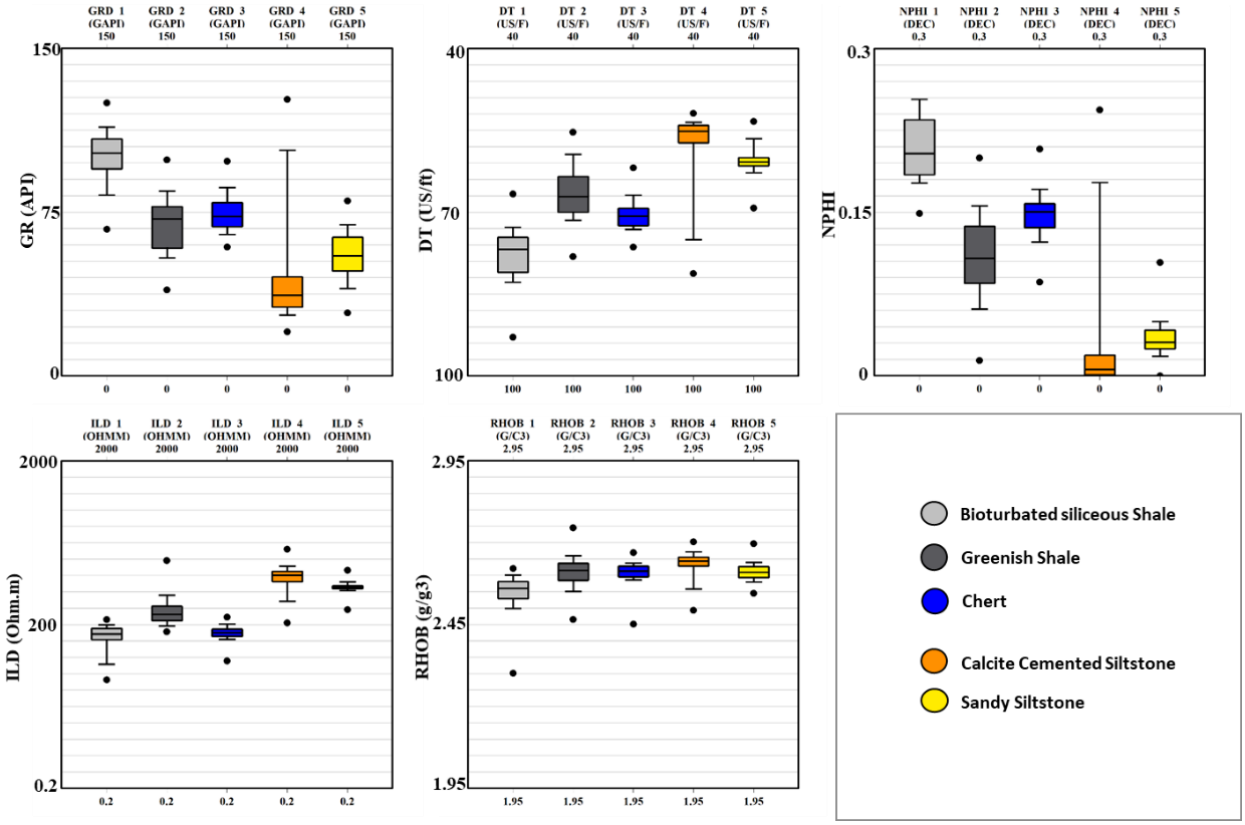

Figure 5.17. Summary of well log characteristics for each lithofacies identified in the Sycamore strata at the I-35 outcrop.

Discussions

The two outcrops and subsurface wells were used to understand the depositional environment, lithology, and to assess drilling locations for the Sycamore formation in the SCOOP area. This was achieved through integrated outcrop descriptions and measurements, lab analyses of petrography, XRD, SEM, chemostratigraphy, and statistical analyses of clustering techniques of chemofacies, electrofacies, and sequence stratigraphy. The findings from this study 1) shed a new light on the deposition environment as deeper water gravity flow/non-carbonates, 2) provide

a detailed lithofacies study to propose a good drilling spot and allow future work to build upon, and 3) bring the surface outcrop studies to a subsurface correlation for a) enhanced subsurface interpretation for the Sycamore formation, b) developing sequence stratigraphy framework, and c) better target zone.

Depositional environment

At the outcrop, bed, and microscopic scales, six sections are recognized in the I-35 Mississippian Sycamore outcrop, consisting of three major hard calcareous siltstone–very fine sandstone intervals separated by another three eroded shale sections. Seven lithofacies are documented.

The stratigraphic thickness of the **shale section** within the I-35 Sycamore outcrop is 39% of the total section. The presence of chert beds, pyrite minerals, and high radioactivity of the bioturbated siliceous shale lithofacies might indicate a deep deposition environment. Additionally, Sulfur measurements from our XRF data record the highest concentrations within the bioturbated siliceous shale interval throughout the entire Mississippian Sycamore outcrop section, indicating the shale facies was deposited in an anoxic environment.

However, **hard siltstone sections** have various structures indicative of sediment gravity flow deposition and possibly turbidite deposition. These include Bouma units (Ta, Tb, Tc, Td, Te), scoured surfaces, contorted beds, lenticular beddings, and irregular beddings. These features may indicate episodic sedimentation with different energy flows. Also, fine-grained hemipelagic sediment (mud drapes) at the top of most beds, especially in the **LSyS & MSyS** show fining upward sediments, an increase in clay content, and horizontal laminations, indicative of episodic sedimentation and decrease of flow energy to yield to decreasing grain sizes. **USyS** is very distinctive by its blocky, slumped massive sandy beds. The siltstone and sandy siltstone rocks

aggressively react with the hydrochloric acid due to calcite cement. The carbonate cement might come from the dissolution of the shell fragments that observed in the thin sections.

The well-sorted silt could be a glacial deposit that might have been transported by wind. The Si trend throughout the I-35 outcrop chemostratigraphy profile reveals association with the clay contents (**Figure 5.9A**). Particularly, Si profile is allied with Al and Zr, within the siltstone sections, suggesting the source of silt-sized quartz that is non-biogenic in origin. This might be similar to the Rocky Mountains paleoloess deposits which are interpreted as eolian glacial weathering products of Precambrian basement uplifts in an icehouse climate across Pangea (Soreghan, et al, 2008).

Although the siltstone sections are apparently featureless beds (Miller and Cullen, 2018), some bottom structures including grooves and flute casts are observed within siltstone beds (**Figure 5.4**). These marks could be indicative of deepwater deposition and might suggest the paleocurrent direction to the north-northwest. Similar features were reported at the northern Sycamore outcrop by Donvon (2001). These observations support our suggestion that the siltstone sections (particularly, **LSyS & MSyS**) were deposited by sediment gravity flow processes. The flows might carry carbonate shell fragments from the carbonate platform North Oklahoma (proximal) into the southern Oklahoma (distal) (STACK- Merge-SCOOP areas), and precipitated. Therefore, the depositional environment is interpreted as a slope setting. This interpretation agrees with previous studies which infer that the Sycamore strata was deposited on a slope or deeper/ below storm wave base (Schwartzapfel, 1990; Coffey, 2000; Franklin, 2002; Miller, 2018; Miller and Cullen, 2018). These interpretations do not agree with the shallow water settings interpreted by Bennison (1956), Prestridge (1957), Curtis and Chapman (1959), Braun (1961), Cole (1988).

At the larger scale, the Sycamore strata downlap onto the underlying Woodford Shale. The

Sycamore strata comprise a second-order transgressive–lowstand systems tracts which downlaps toward an unconformity that caps the underlying transgressive Woodford Shale. On the second order, there is a series of lowstand-highstand cyclic prograding slope systems tracts of dolomitic, calcite-cemented siltstone, and sandy siltstone sitting on either the paleo-basin floor or paleo-slope on shale sections within the entire Sycamore interval. Also, a Maximum Flooding Surface (MFS) is recognized in the middle of the upper shale section (UShS). The lowstand systems tract (LST) is dominated largely by the siltstone facies of turbidite gravity flows (**Figure 5.7**) and high detrital inputs from XRF results (**Figure 5.9**) of the lower and middle Sycamore siltstone sections (LSyS, MSyS & USyS). The lower, middle, and upper shale sections (LShTS, MShS, & UShS) are transgressive systems tracts (TST). The early transgressive systems tract (ETST) is dominated by the greenish shale with mostly biogenic quartz. The late transgressive systems tract (LTST) is dominated by the siliceous shale with mostly detrital quartz.

Greenish shale depositional environment

The greenish shale in the I-35 Sycamore outcrop in southern Oklahoma is clay-rich with high content of silica originated from radiolarian (**Figure 5.8**). The depositional environment of this greenish shale is hard to interpret since quartz is mostly biogenic, and the redox sulfur is the lowest among other lithofacies. This might suggest that the greenish shale is deposited at a relatively shallower depth.

Regionally, in North Oklahoma (STACK area), the greenish shale facies are mostly common with clear preservations of glauconite (Durate, 2018). However, in southern Oklahoma (SCOOP area), the greenish shale facies was deposited locally. The greenish shale lithofacies occurs at the base, followed upwardly by black shale. Our hypothesis for this story is:

1- In situ glauconite is usually deposited in shallow water on the shoreline or beach areas.

2- There are paleo-topographies depocenter and sinkholes derived from regional unconformity karst surface topography of the Hunton carbonate.

3- In Southern Oklahoma, the greenish shale is deposited as follows:

    a. During early transgression, the glauconite was carried from high topography into deeper stagnant waters within a sinkhole or depocenter.

    b. During late transgression, the deeper shale sediments were deposited as found in the I-35 Sycamore Transition zone (LShTS), which comprises chert and bioturbated siliceous shale with high GR.

Optimal drilling locations: Outcrop to subsurface implications

Seven lithofacies (five major and two minor lithofacies) have been identified within the six sections in the I-35 Sycamore outcrop. From subsurface well logs, siltstone lithofacies has low GR ranging from 27 to 70 API whereas the shale lithofacies GR ranges from 70 to 114 API.

For the siltstone facies, cement type strongly controls the porosity of the rock, where the calcite cement healed the porosity of the rock. The porosity in calcareous rocks is dependent on the calcite cements (Durate, 2018). The micro-porosity is very low in the **LShS and MShS** where the cement is calcite with low clay content compared to the **UShS** where the porosity is enhanced.

Since the outcrop stratigraphy and lithofacies are correlated to the subsurface, all the outcrop studies can be applied directly to uncored subsurface wells. More importantly, the I-35 outcrop Sycamore lithofacies can be quantitively predicted on any wireline log suite. Thereby, the outcrop findings are used to develop criteria for predicting rock properties from wireline logs since most companies acquire conventional logs. This ultimately helps predict all Sycamore rock types for exploration and/or development programs. Summarizing these investigations for each lithofacies is essential for further subsurface correlations. **Table 5.5** summarizes rock

characteristics per lithofacies type of the Mississippian Sycamore strata of the I-35 Mississippian outcrop.

Table 5.5. Summary of rock characteristics distributed by lithofacies identified in the Mississippian Sycamore strata at the I-35 Sycamore outcrop. This summary includes field observations, XRD, XRF, fracture data, depositional environment interpretation, and prediction of I-35 Sycamore lithofacies on subsurface wireline logs.

Lithofacies	Weathering Response	Dominant Color	Lithofacies Proportion (%)	XRD Mineralogy (Ave. %)			Fracture intensity (No of frac/ft)		TOC (wt.%)	XRF elemental proxies			Outcrop GR (cps)	Subsurface log characteristics						Depositional Systems
				Carbonate	Quartz	Clays				Ca, Sr, Mg	Ti, Zr, K, Al, Th, Si	S		Statistics	GR (API)	DT (us/ft)	NPHI (dec.)	RHOB (g/cc)	RT (ohm.m)	
Greenish shale	Soft, platy	Pale green	15.5	4	52	44	Min Mean Max Stdv	1.6 3.7 7.3 1.76	0.1	Lowest	Highest (K, Th, Ti) High (A, Si) Low (Zr)	Lowest	Min=185 Avg=192 Max=200	Min Mean Max Stdv	70 75 85 13	58 66 71 5	0.061 0.108 0.156 0.039	2.55 2.61 2.66 0.048	20 29 45 15	**ETST**
Siliceous shale	Soft, thinly fissile, papery-like, slightly indurated	dark brown to black	21.3	14	52	34	Min Mean Max Stdv	3 4.4 6 0.62	1.26	very Low	Highest (K, Th, Al, Ti) High (Si) Medium (Zr)	Highest	Min=215 Avg=267 Max=320	Min Mean Max Stdv	80 100 114 12	70 77 82 4	0.178 0.212 0.254 0.036	2.5 2.55 2.602 0.0527	6.57 14 20 4.5	**LTST**
Chert	Hard, massive	Dark brown	2.3	23	54	23	Min Mean Max Stdv	2 5 7.1 1.4	0.43	Low	Medium clay (Al, Th, K, Ti, Zr) Highest (Si)	Very low	Min=170 Avg=215 Max=260	Min Mean Max Stdv	65 74 74 8	66 70 70.5 3.8	0.123 0.147 0.171 0.021	2.59 2.61 2.637 0.032	13 16 20 3.2	**TST**
Dolomitic mudstone	Hard, massive	Dark grey to black	1.2	82 (68 Dol)	12	6	Min Mean Max Stdv	1.8 4 5.57 1.7	--	Highest (Mg, Sr) Medium (Ca)	Medium (Al, Th, K, Ti) Lowest (Zr)	Very high	Min=150 Avg=175 Max=203	Dolomitic mudstone represents only 1.2% across the completed Sycamore section. Hence, either this lithofacies is not available in the subsurface well or the dolomitic beds are beyond the log sampling rates and its resolutions. As a result, SOM clustering technique does not consider it as a seperate group of facies						**TST**
Dolomitic-calcite cemented siltstone	Hard, massive	Yellowish	9.3	61 (24 Dol)	37	2	Min Mean Max Stdv	2 3.2 4.25 0.62	0.22	High (Ca, Sr) Low (Mg)	Lowest (Si) Low (Al, Th, K, Ti, Zr)	Very low	Min=90 Avg=110 Max=130	Photo electric (PE) log is one of the best logs to recoganize to distinguish dolomitic beds. PE log is not available for this well, making it difficult for the clustering SOM method to group this dolomitic-calcite cemented siltstone facies speperately, instead it grops it with the calcite cemented siltstone facies.						**LST**
Calcite cemented siltstone	Hard, massive	light-dark gray	29.4	52 (47 Cal)	44	4	Min Mean Max Stdv	1.8 3.4 5 0.95	0.36	High (Ca, Sr) Relatively high (Mg)	Lowest (Si) Low (Al, Th, K, Zr) Lowest (Ti)	Very low	Min=80 Avg=102 Max=125	Min Mean Max Stdv	27 47 103 26	53 58 75 7.6	0.0005 0.036 0.178 0.0682	2.56 2.63 2.67 0.045	38 72 107 25	**LST**
Sandy siltstone	Hard, massive	light-dark gray	21	32	58	10	Min Mean Max Stdv	- - - -	--	High (Ca) Low (Sr) Lowest (Mg)	Medium (Al, Th, K, Ti, Si) Highest (Zr)	Low	Min=125 Avg=147 Max=170	Min Mean Max Stdv	40 55 70 11	55 60 62.7 2.5	0.018 0.034 0.05 0.016	2.582 2.61 2.64 0.026	52 57 68 7	**HST**

Reservoir implications

By combining observations from the I-35 Sycamore type section, we may speculate that most favorable target intervals for horizontal drilling and completion are either **1)** the bioturbated siliceous shale lithofacies that is present through the three shale intvervals (LShTS, MShS, and UShS) and/or **2)** the sandy siltstone lithofacies that are present mainly in the USyS (**Figure 5.18**).

The bioturbated siliceous shale is characterized by the highest TOC value (1.26 Wt. %), relatively high fracture abundances (avg. 4.4 fractures/ft), clay content less than 35% with quartz more than 50%, and the highest Si element, which indicates a brittle rock. It represents 21% of lithofacies proportion. This rock can be brittle for good hydraulic fractures and the natural fractures may interact with the hydraulic fractures. More importantly, the average TOC of the upper Woodford shale is about 10 wt. % (Galvis et al., 2018). Hence, the underlying Woodford shale may act as a source rock for the Mississippian sections, especially the ***lower shale transition section (LShTS)*** since Woodford biomarkers were detected in oil samples from Mississippian wells across the Anadarko Basin (Welker et al., 2016). Therefore, ***siliceous shale within the lower shale transition section (LShTS)*** should be targeted for landing a horizontal well when the hydraulic fracture length exceeds 85 ft to interact with the upper Woodford. A horizontal well drilled in the **LShTS**, in the SCOOP area, provided high well productivity as a result of hydraulic fractures penetrating the upper Woodford shale (Personal communications).

The sandy siltstone of upper Sycamore section is characterized by the lack of calcite cement, highest quartz content (58%) (might be a brittle rock), lack of natural fractures, and the highest observed micro-porosity from the petrographic analyses compared to the rest of the Sycamore lithofacies. This rock type represents 21% of lithofacies. It is a non-organic-rich rock, but it might be charged from the siliceous shale from the underlying upper shale section of

Mississippian strata and/or charged from the overlaying Caney shale or the underlying Woodford shale. The Caney Shale is an organic-rich shale that charged some reservoirs within the Anadarko, Ardmore, and Arkoma basins (Kamaan, 2006; Andrews, 2007; Cardott, 2017).

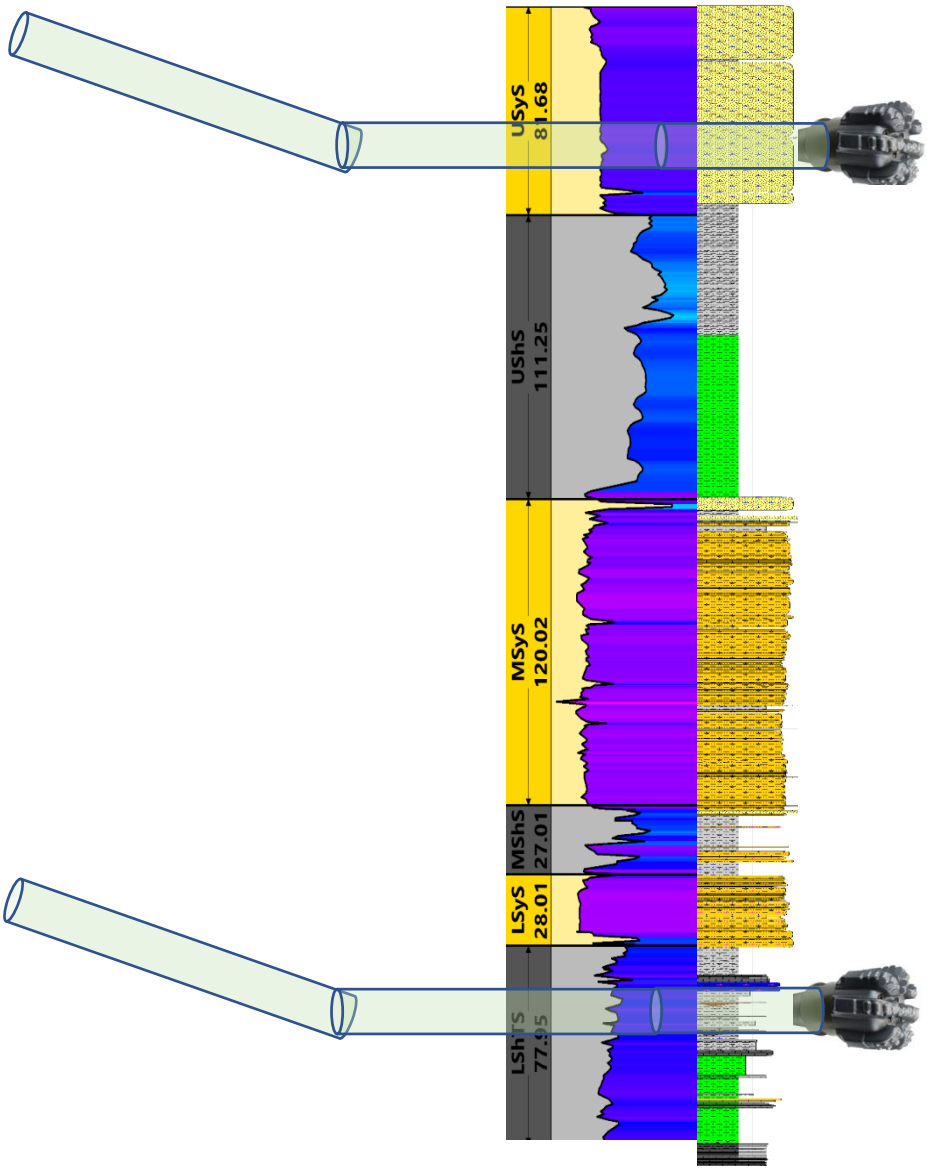

Figure 5.18. Proposed horizontal well within two Mississippian Sycamore sections.

Conclusions

This research evaluates geological assessments through the depositional environment and lithology of the Sycamore in Southern Oklahoma (SCOOP area) for the purpose of highlighting

possible drilling locations. Overall, the Mississippian Sycamore is deposited on a slope or deeper settings by the means of gravity flows.

The bioturbated siliceous shale sections are interpreted to be deposited in a quite deep environment based on the presence of: chert beds, pyrite minerals, high GR readings, and deepwater sedimentary structures (grooves and burrows). XRF data indicate bioturbated siliceous shale has the highest sulfur concentration, and highest TOC (1.26 wt %), thus, indicating that bioturbated siliceous shale could be deposited deeper in the system (indicating deepwater deposition). On the other hand, the greenish shale—which, as opposed to the Siliceous black shale, is interpreted to be deposited in a shallow environment—is a clay and biogenic silica-rich rock, but with the lowest sulfur content, suggesting an early transgression deposit.

The hard siltstone sections form positive relief in the section and highly fractured with limited porosity in the LSyS and MSyS. However, the USyS is a non-fractured and porous section. Turbidites units are the result of different gravity flow energy. The abundant sources of the angular loess quartz (siliciclastic grains) that might be glacial deposits reworked into loess. Finally, the Sycamore was deposited in a quiet, deep marine environment by gravity flow deposits/turbidity currents on a slope setting or deeper.

Below is a summary of major findings:

- The outcrop stratigraphy, lithofacies, electrofacies, and fractures can be directly used to the subsurface well predictions for the enhancement of exploration and/or development programs in southern Oklahoma within the SCOOP area.
- Two fracture sets are found in the outcrop and restored their orientations (N18E and N63W) for the subsurface fracture predictions.

- Fracture intensity varied from 1.5 to 8 fractures per linear ft. Most fractures are filled with calcite.
- Calcite cement is the dominant factor that occlude the rock porosity. Clay could inhibit the formation of calcite by occluding the pore spaces. Clay coats might have prevented the calcite cements within the sandy siltstone facies.
- The pervasive presence of Ta-Te successions and lenticular beddings within the Sycamore siltstone sections strongly imply the product of a slope gravity flow deposits.
- The outcrop lithofacies is tied with both of the outcrop gamma ray and chemofacies and correlated with subsurface well.
- Seven lithofacies (five major and two minor) have been identified by the outcrops within recognized six stratigraphic units of alternating siltstone and shale sections, and five major lithofacies are predicted in the subsurface well from the suite log signatures.
- Sequence stratigraphic framework was developed to predict sediment character and quality; 28 gamma ray parasequence cycles (GRP) were identified on the high frequency order scale.
- Using a uniform statistical methodology of classifying facies resulted in a consistency within the outputs of optimal number of clustering (Chemo and electro facies) outputs.
- Sycamore outcrops contain total organic matter ranges from 0.1 to 1.5 wt. %.
- The bioturbated siliceous shale within the transition section and/or the sandy siltstone within the upper Sycamore section can be a potential target zone for their best reservoir quality.

Future studies

- Biostratigraphy study is important to identify the Mississippian series.
- Understanding the origin of the calcite is important for Mississippian reservoir quality.
- Knowledge of the silt province is crucial to understand the source of the well-sorted silt.
- Regional correlations from STACK-Merge-SCOOP.

Acknowledgments

This work was supported by the Woodford-STACK-Merge-SCOOP Consortium Project at the Institute of Reservoir Characterization. We thank our consortium sponsors for their support of this research. Special thanks go to Dr. Slatt for giving me this project opportunity and his continuous support and guidance. The author is greatly thankful to Henry Galvis, Hannah Morgan, Mahmoud Mohamed Aljabri, Redouane Laaroussi, and Eyad Aljishi for helping on the field work. Also, we would like to thank Dalila De Jesus and Gerhard Heij (Gerry) for helping with the SEM imaging studies. We thank Dr. Zou Fuge for his professional inputs. We also acknowledge the students at the Institute of Reservoir Characterizations for their constructive criticism and the reviewer Austin McGlannan for his critical reviews and comments.

References

Algeo, T. J., and T. W. Lyons, 2006, Mo-total organic carbon covariation in modern anoxic marine environments: Implications for analysis of paleoredox and paleohydrographic conditions. Paleoceanography, **21** (1), 23p.

Algeo, T. J., and H. Rowe, 2012, Paleoceanographic applications of trace-metal concentration data. Chemical Geology, **324**, 6-18.

Allen, R. W., 2000, Stratigraphy, mountain building and complex geological structures of the Ardmore Basin: Shale Shaker, **51**, 10–21.

Andrews, R. D., 2007, Stratigraphy, production, and reservoir characteristics of the Caney Shale in southern Oklahoma: Oklahoma City Geological Society, The Shale Shaker Digest, **58**, (1), 9-25.

Becerra, D., H. Galvis, and R. Slatt, 2018, Characterizing the two principal rock types comprising the Woodford Shale resource play: Application to shale geomechanics: Interpretation, **6** (1), SC67-SC84.

Bennison, A. P., 1956, Springer and related rocks of Oklahoma: Tulsa Geological Society Digest, **24**, 135-143.

Bhatia, M. R., and K. A. Crook, 1986, Trace element characteristics of graywackes and tectonic setting discrimination of sedimentary basins: Contributions to Mineralogy and Petrology, **92**, 181-193.

Braun, J. C., 1961. A stratigraphic study of the Sycamore and related formations in the southeastern Anadarko Basin: Oklahoma City Geological Society, The Shale Shaker Digest III, V IX-XI, 150-164.

Brumsack, H. J., 2006, The trace metal content of recent organic carbon-rich sediments: implications for Cretaceous black shale formation. Palaeogeography, Palaeoclimatology, Palaeoecology, **232** (2-4), 344-361.

Buggisch, W., M. M. Joachimski, G. Sevastopulo, and J. R. Morrow, 2008, Mississippian δ13Ccarb and conodont apatite δ18O records – Their relation to the Late Palaeozoic glaciation: Palaeogeography, Palaeoclimatology, Palaeoecology, **268**, 273-292.

Calvert, S. E., and T. F. Pedersen, 1993, Geochemistry of recent oxic and anoxic marine sediments: implications for the geological record. Marine geology, **113** (1-2), 67-88.

Cardott, B. J., 2017, Oklahoma shale resource plays: Oklahoma Geological Survey, Oklahoma Geology Notes, **76** (2), 21-30.

Coffey, W. S., 2000, The diagentic history and depositional system of the Sycamore Formation (Mississippian), Carter-Knox Field, Grady and Stephens Counties, Oklahoma: Ph.D. dissertation, Oklahoma State University, Stillwater, Oklahoma. 167 p.

Cole, T., 1988, A surface to subsurface study of the Sycamore Limestone (Mississippian) along the North Flank of the Arbuckle Anticline: Master's Thesis, University of Oklahoma, Norman, OK, 140 p.

Curtis, D. M. and S. C. Champlin, 1959, Depositional environments of Mississippian limestones of Oklahoma: Tulsa Geological Society Digest, **27**, 90-103.

Donovan, R. N., 2001, Field study of the Sycamore Formation on interstate highway 35 in the Arbuckle Mountains, Oklahoma: Oklahoma Geological Survey Circular **105**.

Duarte Coronado, D., 2018. Rock characterization and stratigraphy of the Mississippian strata, Meramec/Sycamore. Merge play, Central Oklahoma: Master's thesis, University of Oklahoma.

Fay, R. O., 1989, Geology of the Arbuckle Mountains along Interstate 35, Carter and Murray Counties, Oklahoma: Oklahoma Geological Survey Guidebook **26**, 50 p.

Franklin, K. E., 2002, The depositional history of the Sycamore Limestone: Master's Thesis, Oklahoma State University, Stillwater, OK, 91 p.

Galvis, H., D. Becerra, and R. Slatt, 2018, Lithofacies and stratigraphy of a complete Woodford Shale outcrop section in South Central Oklahoma: Geologic considerations for the evaluation of unconventional shale reservoirs: Interpretation, **6** (1), SC15-SC27.

Ham, W. E., R. E. Denison, and C. A. Merritt, 1965, Basement Rocks and Structural Evolution of Southern Oklahoma--A Summary. AAPG Bulletin, **49** (7), 927-934.

Hoffman, P., J. F. Dewey, and K. Burke,1974, Aulacogens and their genetic relation to geosynclines with a Proterozoic example from Great Slave Lake Canada, in Modern and ancient geosynclinal sedimentation: SEPM Special Publication **19**, 38–55.

IHS market, 2018, Outlook for US Oil and Gas Production 2018-20.

Johnson, K. S., and B.J. Cardott, 1992, Geologic framework and hydrocarbon source rocks of Oklahoma, in K.S. Johnson and B.J. Cardott, eds., Source rocks in the southern Midcontinent, 1990 symposium: OGS Circular **93**, 21-37.

Kamaan, J. K., 2006, Surface-to-subsurface correlation and lithostratigraphic framework of the Caney Shale (including the "Mayes" Formation) in Atoka, Coal, Hughes, Johnston, Pittsburg, and Pontotoc counties, Oklahoma: Master's Thesis, Oklahoma State University, Stillwater, OK, 259 p.

Lazar, O. R., K. M. Bohacs, J. H. S. Macquaker, J. Schieber, and T. M. Demko, 2015, Integrated approach for the nomenclature and description of the spectrum of fine-grained sedimentary rocks. Journal of Sedimentary Research, **85**, 230–246, doi: 10.2110/jsr.2015.11.

Liborius, A., & Slatt, R. 2016. Geological characterization of La Luna Formation as an unconventional resource in Lago de Maracaibo Basin, Venezuela. Unconventional Resources Technology Conference, 25, 3280-3299.

Milad, B., A. Alali, R. Slatt, and K. Marfurt, 2018, Geostatistical Integration of Multiscale Data to Construct the Hunton Group GeocellularModel: Upscaling Logs and Downscaling Seismic Impedance Volumes: AAPG Search and Discovery Article #4225.

Milad, B., and R. Slatt, 2018, Impact of lithofacies variations and structural changes on natural fracture distributions: Interpretation, **6** (4), T873–T887, doi:10.1190/INT-2017-0138.1.

Milad, B., and R. Slatt, 2019, Outcrop to Subsurface Reservoir Characterization of the Mississippian Sycamore/Meramec Play in the SCOOP Area, Arbuckle Mountains, Oklahoma, USA: Unconventional Resource Technology Conference 991-MS, doi:10.15530/urtec-2019-991

Miller, J., 2018. Regional stratigraphy and organic richness of the Mississippian Meramec and associated strata, Anadarko Basin, central Oklahoma: Master's thesis: University of Oklahoma.

Noble, P. J., 1995, Regional sedimentation patterns associated with the passive to active margin transition, Ouachita orogeny, southern Midcontinent, U.S.A. Oklahoma Geological Survey Circular **97**, 99-112.

Nojek, A. and Y. Li, 2017, How central Oklahoma's SCOOP/STACK shale plays are stacking up against the competition: McKinsey Energy Insights.

Northcutt, R. A., K. S. Johnson, and G. C. Hinshaw, 2001, Geology and petroleum reservoirs in Silurian, Devonian, and Mississippian rocks in Oklahoma. In Silurian, Devonian, and Mississippian geology and petroleum in the southern mid-continent: 1999 Symposium Oklahoma Geological Survey Circular, **105**, 1-29.

Pearce, T. H., and I. Jarvis, 1992, Applications of geochemical data to modelling sediment dispersal patterns in distal turbidites: Late Quaternary of the Madeira Abyssal Plain. Journal of Sedimentary Research, **62**, 1112-1129.

Pearce, T. J., B. M. Besly, D. S. Wray, and D. K. Wright, 1999, Chemostratigraphy: a method to improve interwell correlation in barren sequences – a case study using onshore Duckmantian/Stephanian sequences (West Midlands, U.K.). Sedimentary Geology, **124**, 197-220.

Prestridge, J. D., 1957, A subsurface stratigraphic study of the Sycamore Formation in the Ardmore Basin: Master's Thesis, University of Oklahoma, Norman, OK, p. 62.

Ratcliffe, K. T., M. Wright, P. Montgomery, A. Palfrey, A. Vonk, J. Vermeulen, and M. Barrett, 2010. Application of chemostratigraphy to the Mungaroo Formation, the Gorgon field, offshore northwest Australia. Australian Petroleum Production and Exploration Association Journal, **50**, 371-385.

Rowe, H., N. Hughes, and K. Robinson, 2012, The quantification and application of handheld energy-dispersive X-ray fluorescence (ED-XRF) in mudrock chemostratigraphy and geochemistry: Chemical Geology, **324**, 122–131, doi: 10.1016/j.chemgeo.2011.12.023.

Sageman, B. B., and T.W. Lyons, 2004, Geochemistry of fine-grained sediments and sedimentary rocks. In: Mackenzie, F. ed., Sediments, Diagenesis, and Sedimentary Rock. Treatise on Geochemistry, **7**, 115-158.

Schwartzapfel, J. A., 1990, Biostratigraphic investigations of Late Paleozoic (Upper Devonian to Mississippian) radiolaria within the Arbuckle Mountains and Ardmore Basin of south-central Oklahoma: Ph.D. dissertation, University of Texas at Dallas, Dallas, TX, 475 p.

Slatt, R. M., and N. D. Rodriguez, 2012, Comparative sequence stratigraphy and organic geochemistry of gas shales: Commonality or coincidence?. Journal of Natural Gas Science and Engineering, **8**, 68-84.

Slatt, R. M., 2013a, Stratigraphic reservoir characterization for petroleum geologists, geophysicists, and engineers, Elsevier ed. 2nd edition, 688p.

Suneson, N., 1996, The geology of the Ardmore Basin in the Lake Murray Stake Park Area, Oklahoma, an introduction and field-trip guide: Oklahoma Geological Survey, Open File Report, 2–96.

Sloss, L. L., 1963, Sequences in the cratonic interior of North America: Geological Society of America Bulletin, **74** (2), 93-114.

Soreghan, G. S., M. J. Soreghan. and M.A. Hamilton, 2008. Origin and significance of loess in late Paleozoic western Pangaea: A record of tropical cold?. Palaeogeography, Palaeoclimatology, Palaeoecology, **268**, 234- 259.

Taff, J. A., 1903, Geologic atlas of the United States, Tisholningo Folio, Indian Territory, No. 98, p. 5.

Tribovillard, N., T. J. Algeo, T. Lyons, and A. Riboulleau, 2006, Trace metals as paleoredox and paleoproductivity proxies: an update. Chemical Geology, **232**, 12-32.

Turner, B. J., 2016, Utilization of Chemostratigraphic Proxies for Generating and Refining Sequence Stratigraphic Frameworks in Mudrocks and Shales, Ph.D. dissertation, University of Oklahoma, 135 p.

Watney, W. L., W. J. Guy, and A. P. Bynes, 2001, Characterization of the Mississippian chat in south-central Kansas: AAPG Bulletin, **85**, 85-113.

Welker, C., S. Feiner, R. Lishansky, W. Phiukhao, J. C. Chao, R. Moore, and D. Hall, 2016, Trapped fluid analysis of 58 wells from the SCOOP and STACK Plays, Oklahoma: Unconventional Resources Technology Conference, 2922-2933.

Zhang, J., 2016a, Comprehensive Reservoir Characterization of the Woodford Shale in Parts of Garfield and Kingfisher Counties, Oklahoma: Master's thesis, University of Oklahoma, Norman, Oklahoma.

Zhang, J., J. Scott, R. Slatt, and B. Turner, 2016b, Regional Fine-Scale Sequence Stratigraphy of the Woodford Shale and Its Impact on Microseismic Activity and Optimizing Future Hydraulic Fractures: AAPG-SPE Joint Forum Reality-Based Reservoir Development: New Teams, Techniques, Technologies.

Chapter 6: Conclusions

This dissertation presents an example of the integration of multidisciplinary, multi-scalar subsurface and surface data to allow for: idealized reservoir characterization, building 3D geological models, demonstration of optimized upscaling, and simulating of 3D reservoir performance prediction models. Various statistical and machine learning techniques were utilized for the multiscale data. This characterization and modeling was then used in geological and fluid flow assessments in order to: 1) study fractures and build fracture models for fluid flow, 2) construct high heterogeneity fine-scale geological models for upscaling reservoir simulations, and 3) evaluate the stratigraphy, depositional environment, and lithology of the Mississippian Sycamore/Meramec in the SCOOP area.

Natural fracture studies show that grain-supported lithologies and areas with higher curvatures are more prone to fracturing than mud supported lithofacies. The effect of varying fracture aperture and length on hydrocarbon production were examined on the DFN model. Although fracture aperture affects fracture permeability and production, fracture length has greater influence on production response because length controls reservoir connectivity. Successful exploration and development plans for a fractured reservoir should take into account lithology variations, structural changes, and fracture lengths.

Reducing the time and cost of running reservoir flow simulations through the upscaling process is necessary for iterative production history matching, sensitivity analyses, production forecasting, and risk analysis for reservoir management. However, excessive upscaling leads to the loss of detailed geological features and will affect the fluid flow simulation results. The simulation production accuracy decreases by increasing the lateral grid cell size. Hence, horizontal upscaling should be kept at the 100x150x1 ft (or whatever minimum grid size the

system can handle) grid cell size for history matching for the optimal upscaling to be obtained. Power law relationships between grid cell size and computational time were developed.

The Mississippian Sycamore is currently a very active oil play in Oklahoma, but the lithology, stratigraphy, and depositional environment were not well studied before. The Sycamore Formation was interpreted to be composed of three siltstone/sandy siltstones with carbonate cement separated by another three shale units. The depositional environment was characterized as a sediment gravity flow. The shale intervals were interpreted be have been deposited in anoxic-euxinic environment with the highest Sulfur content and organic matter (1.5%) compared to siltstone intervals. Additionally, five major lithofacies were predicted from the wireline logs. The Sycamore study is potentially useful for oil companies in the SCOOP area to target bioturbated siliceous and/or Sandy siltstone.

Chapter 7: Appendix A: Prestack simultaneous inversion of 3D seismic data for attributes to be utilized for geoceullar geological static models

The objective of the prestack seismic inversion was to construct a high resolution fine-scale geologic model to be used for upscaling processes. The generation of an accurate geocellular model requires upscaling of sparse porosity logs followed by their integration with denser seismic impedance volumes. Seismic data provides laterally dense but vertically low resolution, "soft" estimates of lithology and rock properties. In contrast, log data provides corresponding "hard" estimates that are laterally sparse but exhibit high resolution. Upscale well log and downscale seismic impedance results in an integrated gridded reservoir model with reduced uncertainty.

Since I found a relationship between the lithofacies, porosity, and the acoustic impedance at well locations, a 3D acoustic impedance map was generated to assist the population of the 3D lithofacies and porosity models (**Figure A1**). Additionally, a horizontal variogram is essential to design to populate other reservoir rock properties laterally.

To populate the 3D volume, I (1) establish seismic impedance attribute which correlates to the electrofacies and porosity to design the horizontal variograms for the 3D lithology and porosity models, (2) construct the relationship between the acoustic impedance and lithology and porosity logs at well locations, (3) perform a 3D seismic inversion of acoustic impedance volume, (4) downscale (laterally interpolate) the inverted prestack acoustic impedance volume computed at the seismic bin size resolution to geocellular model grid size, (5) create horizontal variogram maps from the downscaled seismic acoustic impedance, and (6) obtain the horizontal variogram parameters and substitute them into lithology horizontal variogram.

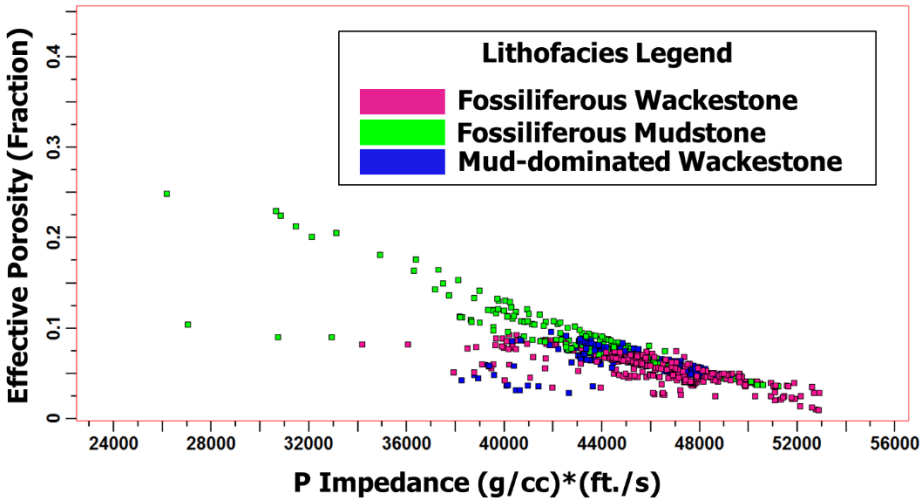

Figure A1. Cross plot between the effective porosity and the acoustic impedance colored with the lithofacies. (Milad et al., 2018).

Inversion steps:

Data set

The available seismic data of this study is shown in **Figure A2**. The 3D volume consists of 172 inlines and 143 crosslines in approximately 7 square miles of pre and post stack volume. The orientations of the inlines are E-W and the crosslines are N-S. The bin size is 100 by 100 ft. The distribution of log data such as GR, Checkshots, DT, RHOB and NPHI are indicated by the legend (**Figure A2**).

Well log data from 6 wells (**Figure A2** and **Table A1**) are available of which one of them has dipole sonic log data to provide S wave velocity (**Well 5**). To determine S wave velocity for the other 5 wells, multilinear regressions were applied. The detrimental type log to be correlated with the shear velocity is crucial. In this case, RHOB and P wave velocity are the two logs that are correlated to the shear velocity and they were used to generate the predicted S wave velocity. The predicted S wave matched with the actual measurement for **Well 5** (**Figure A3**), then an equation

(Shear Velocity = + 2132.73 * Bulk Density - 141.795 * DT + 11481.7) was applied to calculate S wave velocity to various wells.

Table A1. Types of well logs available to study

Well Name	Log type							
	P wave sonic	S wave sonic	Density	Gamma ray	Neutron porosity	Density porosity	Induction deep	SP
Well 5	√	√	√	√	√	√	√	√
Well 11	√	√	√	√	_	_	_	_
Well 12	√	√	√	_	_	_	_	_
Well 14	√	√	√	√	√	√	√	√
Well 18	√	√	√	_	√	√	√	√
Well 21	√	√	√	√	√	√	√	√

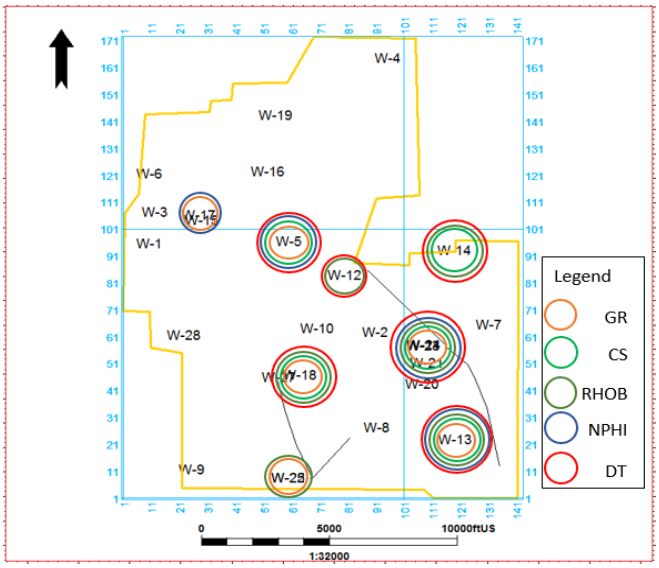

Figure A2. Location of the raster logs inside the seismic polygon. Colored circles are the type of logs at well locations with their respective names.

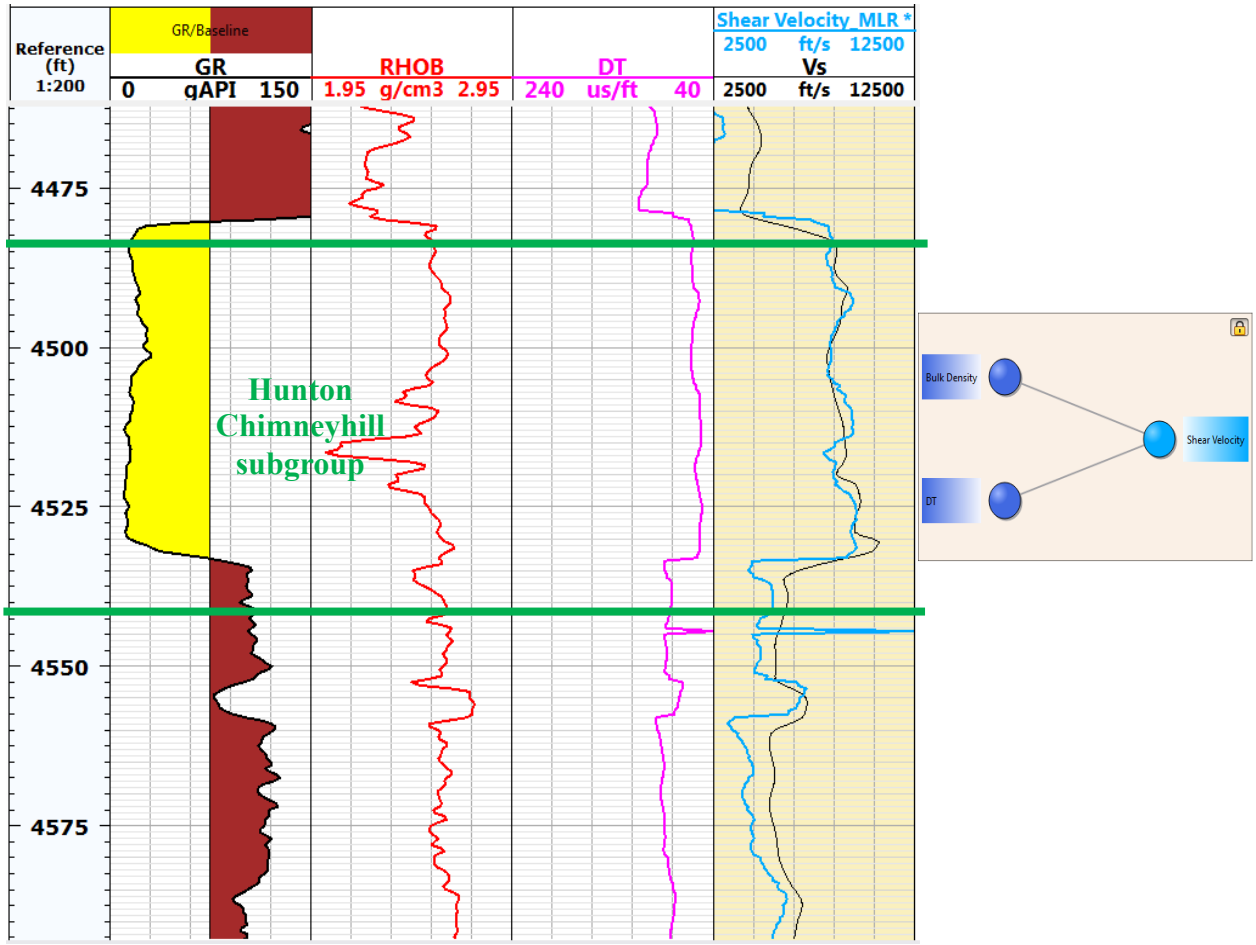

Figure A3. Multilinear regressions for Well-5 in for the Hunton reservoir. Gamma ray is in red, bulk density is in red and P sonic log is in purple. The black curve in the last column is the actual S wave velocity and the blue curve is the calculated S wave velocity.

Data preconditioning

The prestack data has been already trace muted. Before performing the inversion, noise should be removed as it may ruin the inversion result. The noise reduction was done by applying band pass filtering and trim statics.

A. Angle gather

The range of incident angle for the data is from 0 to 30 degrees (**Figure A4**). This range was used for the inversion results.

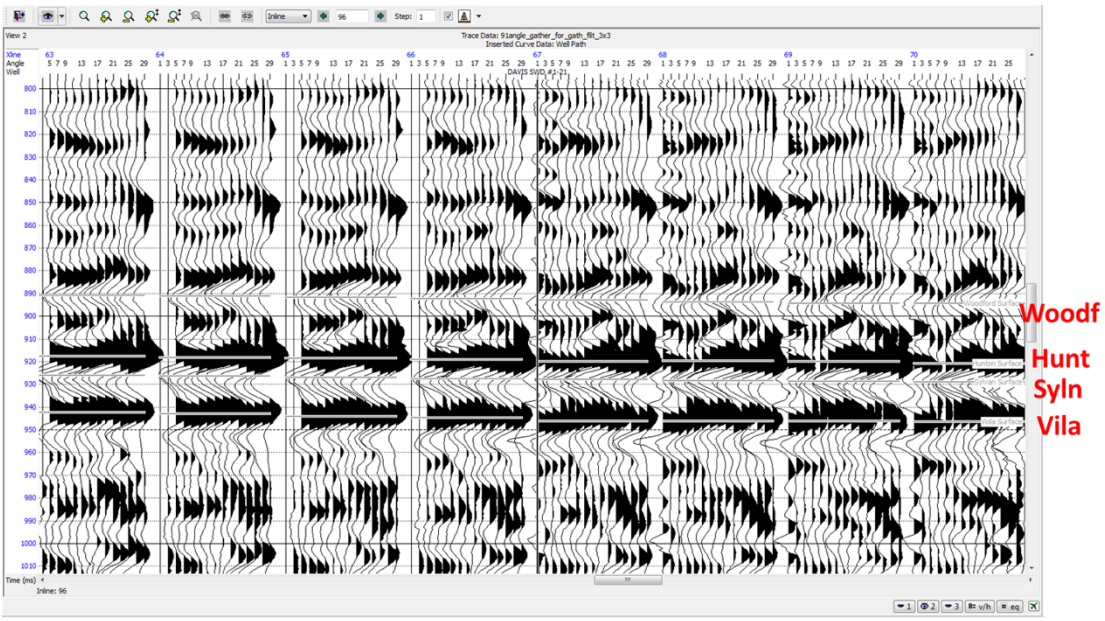

Figure A4. Angle gathers after converted from offset gather. The range of the incident angles for the data is from 0 to 30 degrees.

B. Noise Reduction

Two methods have been adopted for noise reduction in the input angle gather. The first is bandpass filter and the second is trim statics.

Band pass filtering was done to remove frequencies that fluctuate up and down that do not make geological senese, hence the noise frequency of low cut of 5 Hz and high cut of 5 Hz was applied. The max frequency of the data set is 150 Hz as it is shown in the amplitude spectrum (**Figure A5**). By applying the bandpass filter the random noise is slightly removed after applying band pass filter (**Figure A6**).

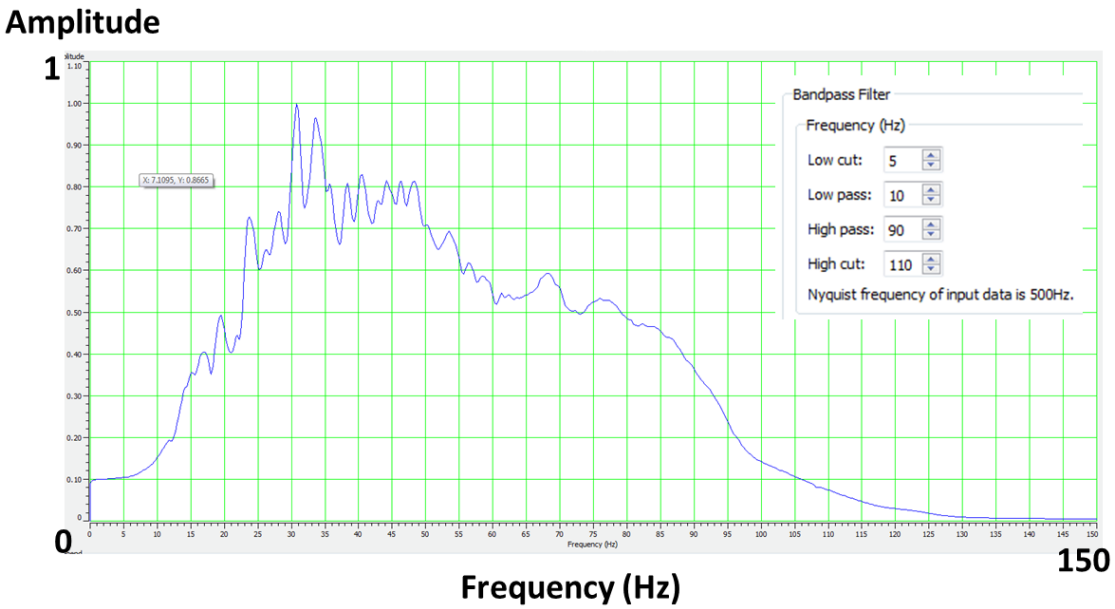

Figure A5. Amplitude spectrum. The frequency ranges from 0 to 150 Hz. noise frequency of low cut of 5 Hz and high cut of 110 Hz is applied.

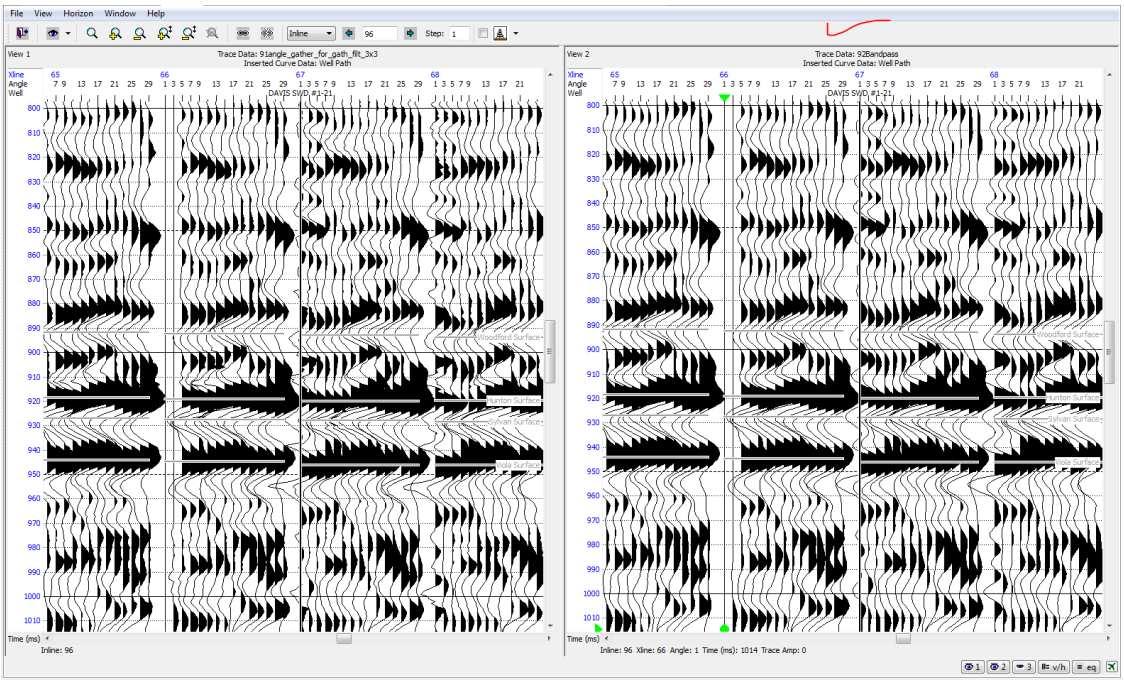

Figure A6. Angle gather after applying band pass filter. Random noises and bending effects at the far offset traces are still present.

After a bandpass filter was applied, it was found that the continuity of the event was slightly improved. But still there are some bending effects at the far offset traces. To remove those, the

second and last method used in this study is trim statics.

Trim statics adjusts the time an event occurs to flattening the far offsets. Trim statics processing has improved the continuity of the events (**Figure A7**).

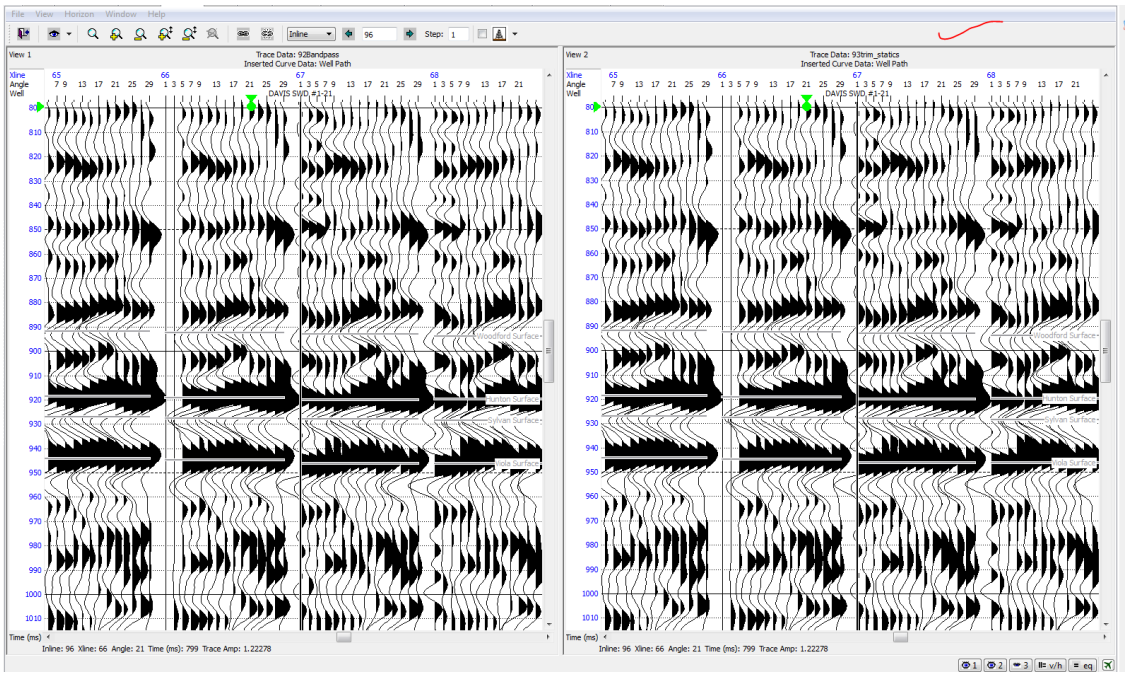

Figure A7: Random noise is removed substantially after applying trim statics.

Pre-stack seismic inversion

Basic preparatory steps, such as well to seismic tie, horizon picking, wavelet extraction based on incident angle, model building, and quality control of the inversion outputs are carried out before running the simultaneous inversion into the pre-stack angle gathers.

A. Incidence angle dependent wavelet extraction

In this part, wavelets are extracted from the seismic data using statistical methods. Three sets of wavelets, which are dependent on the incident angles, are extracted from the seismic model for the well tie and inversion purposes using statistical method (**Figure A8**). One is from 0 to 15 degrees averaged at 7.5 degrees, the second is from 10 to 25 degrees averaged at 17.5 degrees, and the other is from 20 to 29 degrees averaged at 24.5 degrees.

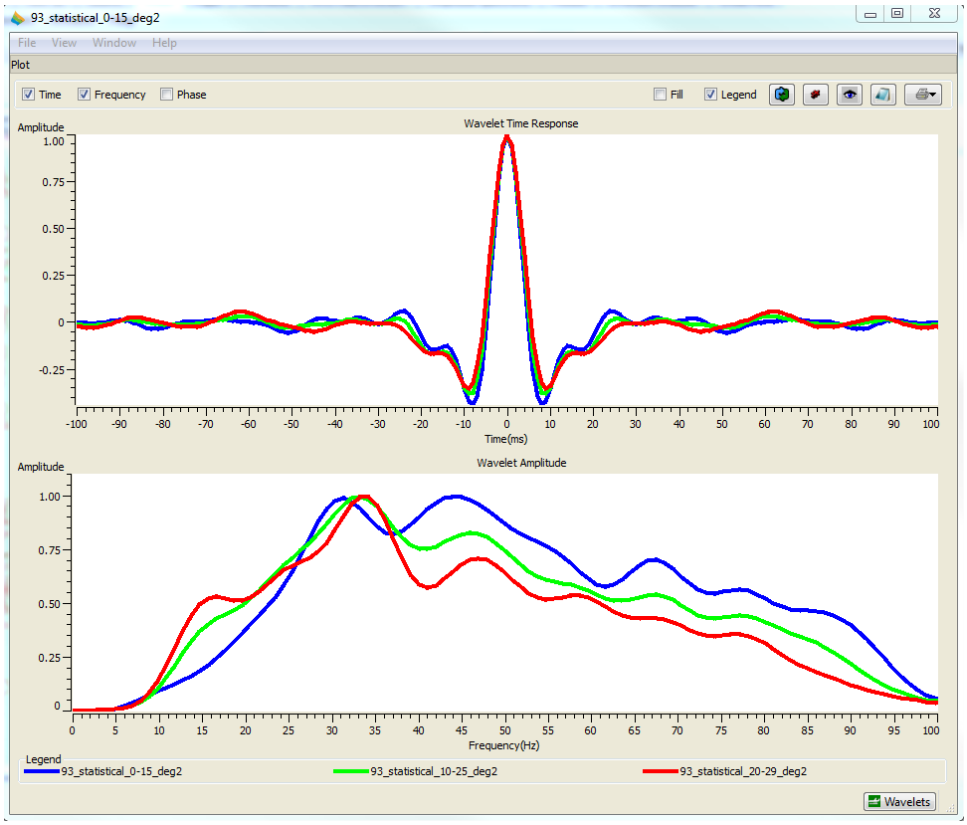

Figure A8. Angle dependent wavelets extracted for well to seismic tie and inversion purposes. Amplitudes at time (top) and frequency (bottom) response are shown.

The optimum parameters to get the desired wavelet are shown in **Table A2**.

Table A2. Parameters taken for wavelet extraction.

Analysis window starts	850 ms
Analysis window ends	960 ms
Wavelet length	280 ms
Taper length	70 ms
Sample rate	1 ms
Phase rotation	0 degree
Phase type	Constant phase

B. Well to seismic tie

Well logs have to be correlated with the seismic data to generate synthetic traces from the convolution between the reflectivity and extracted statistical wavelet at various well locations. The three wavelets are tested to cross correlate them with the synthetic seismic traces to find the best statistical wavelet. The optimum correlation well to seismic tie correlation is obtained at 10

to 25 degrees.

Analysis correlation window is selected from the top of the Woodford to the top of the Viola. Correlation values are found more than 90% for all the wells. **Table A3** shows the correlation values between the synthetic and seismic traces at each well location. **Figure A9** shows well log correlation with the seismic trace at the well location of **Well 11**.

Table A3. Correlation values between synthetic and seismic traces at well locations.

Well name	Log Correlation value (fraction)
Well 5	0.935
Well 11	0.930
Well 12	0.914
Well 14	0.960
Well 18	0.951
Well 21 (Blind Test)	Blind Test

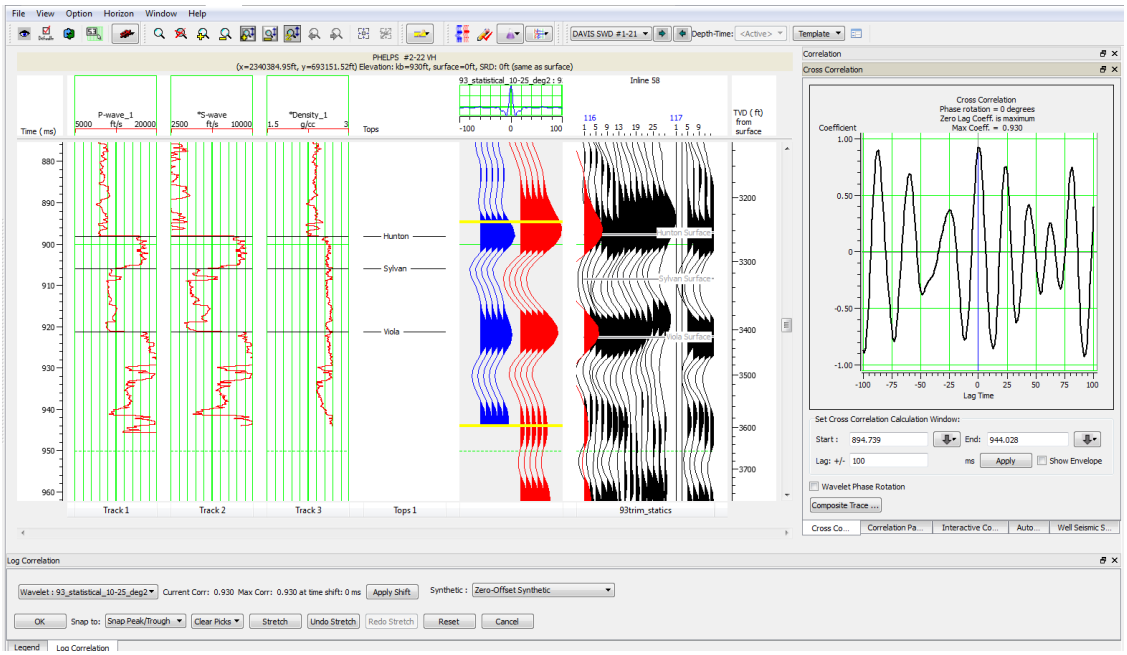

Figure A9. Correlation between synthetic and seismic traces Well 11. Track 1,2 and track 3 show P wave sonic, S wave sonic and density log respectively. Traces in blue represent the synthetic around the borehole and traces in red represent composite trace averaged from the original seismic. Traces in black are original seismic traces. Well location is shown as synthetic trace in red superimposed on the original seismic data. Calculation window is shown in yellow line from the top of Woodford to the top of the Viola. Final correlation coefficient of this well is 0.930.

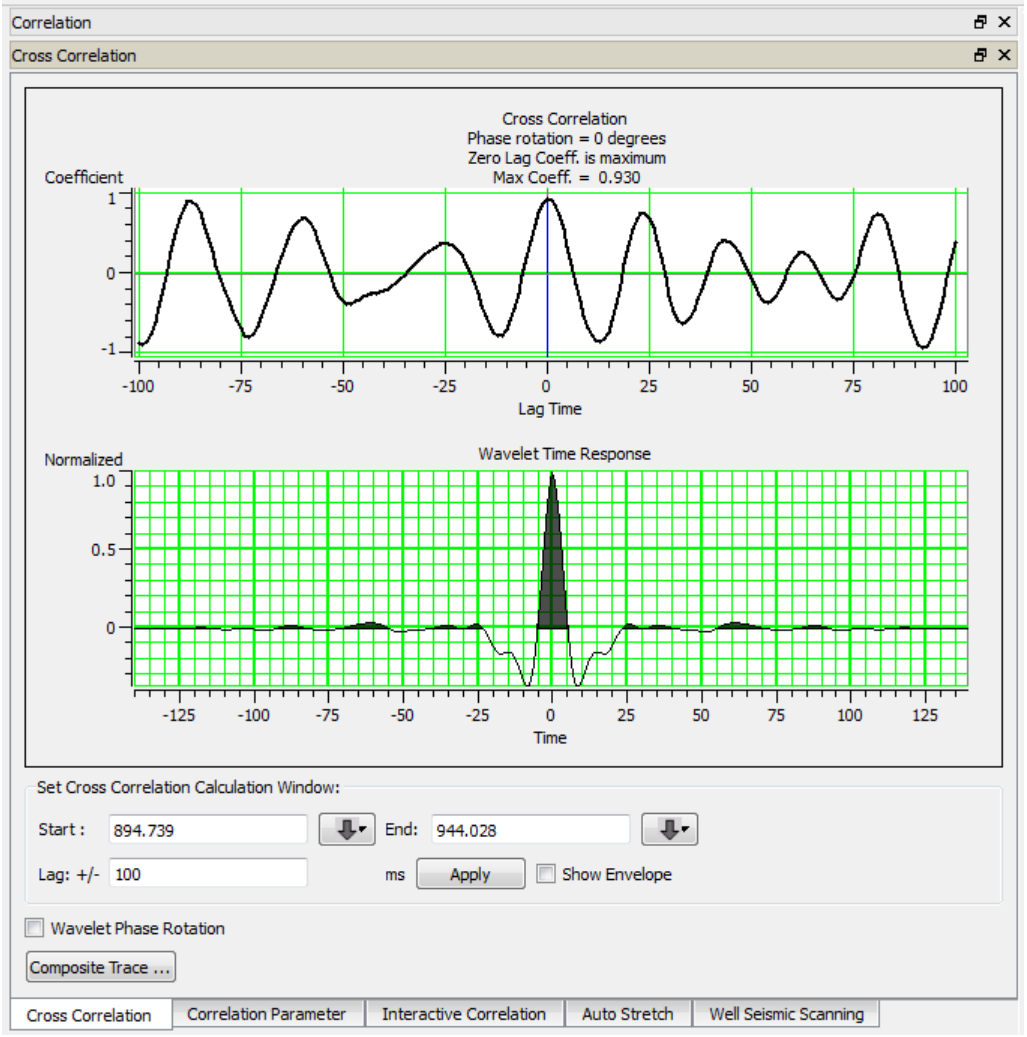

Figure A10. Time response (up) and amplitude and phase response (down) of the extracted wavelet for well to seismic correlation.

C. Model building

The simultaneous inversion model interpolates the values of the logs throughout the seismic volume. The initial model is built with a low frequency geological model with minimum synthetic errors between the model and original seismic volume. The calculation window of the initial model includes the top of the Woodford surface to the top of the Viola surface as this interval is the area of interest and also it is recommended to include intervals with a strong change in impedances (**Chopra and Marfurt, 2013)** (**Figure A11**).

Four smoothed horizons of Woodford, Hunton, Sylvan and Viola are used to guide the inversion interpolation throughout the seismic volume. 5 wells with P wave velocity, S wave velocity and density logs have been used to build the initial P impedance, S impedance and density model (**Figure A12**) to run the inversion process while **Well 21** well has been used as a blind test to quality control the inversion results.

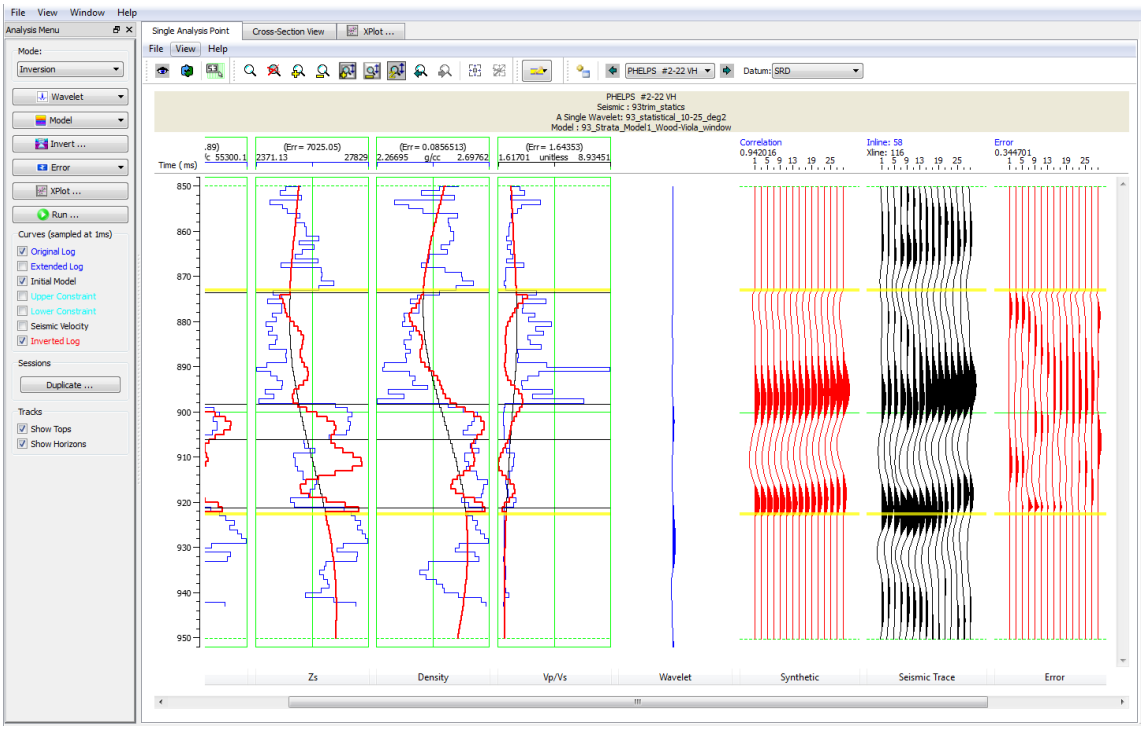

Figure A11. Inversion analysis for Well 11. Calculation window was applied from the Woodford top to Viola top as it is indicated with the yellow lines. A 94% synthetic correlation and 3.4% of relative error are the results of inversion analysis for this well.

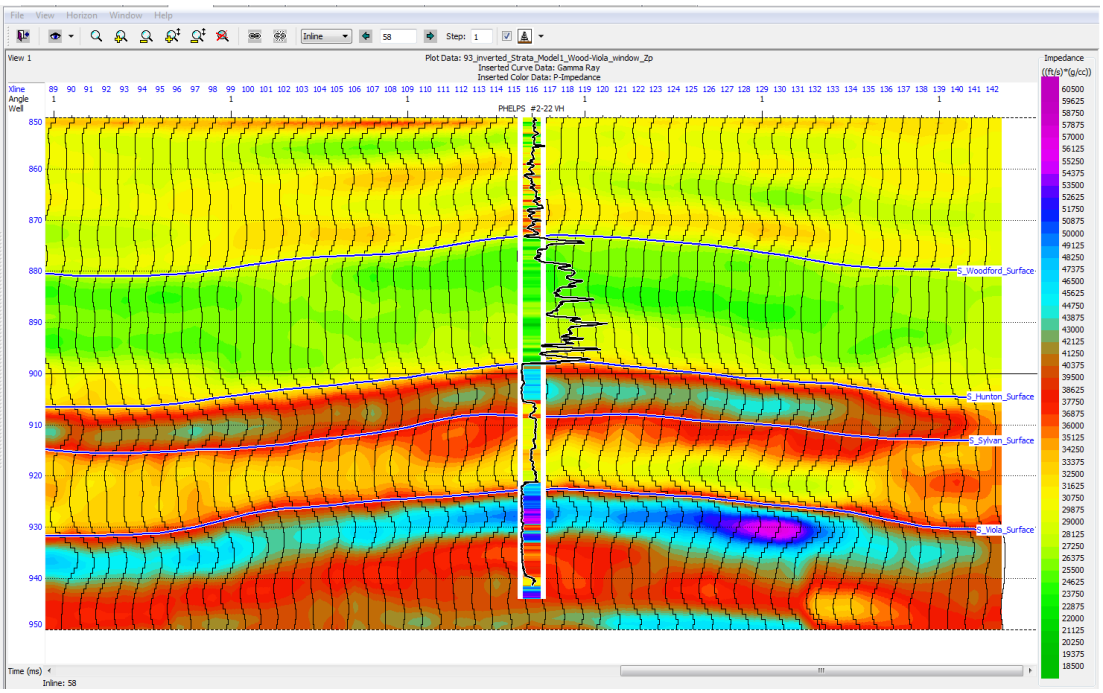

Figure A12. P impedance model used for simultaneous inversion. Black curve shows the density log superimposed on the impedance of the well log from Well 11.

D. Quality Control

To check the quality of the inversion results, the blind test **Well 21** P-impedance at well location matches the P-impedance of the seismic, indicating the inversion was performed well (**Figure A13**).

Correlation values between the inverted and original seismic traces, as well as relative synthetic error at all of the well locations are shown in (**Table A4**). Average values of the synthetic error, inverted correlation and synthetic correlation for P-impedance are shown in (**Table A5**).

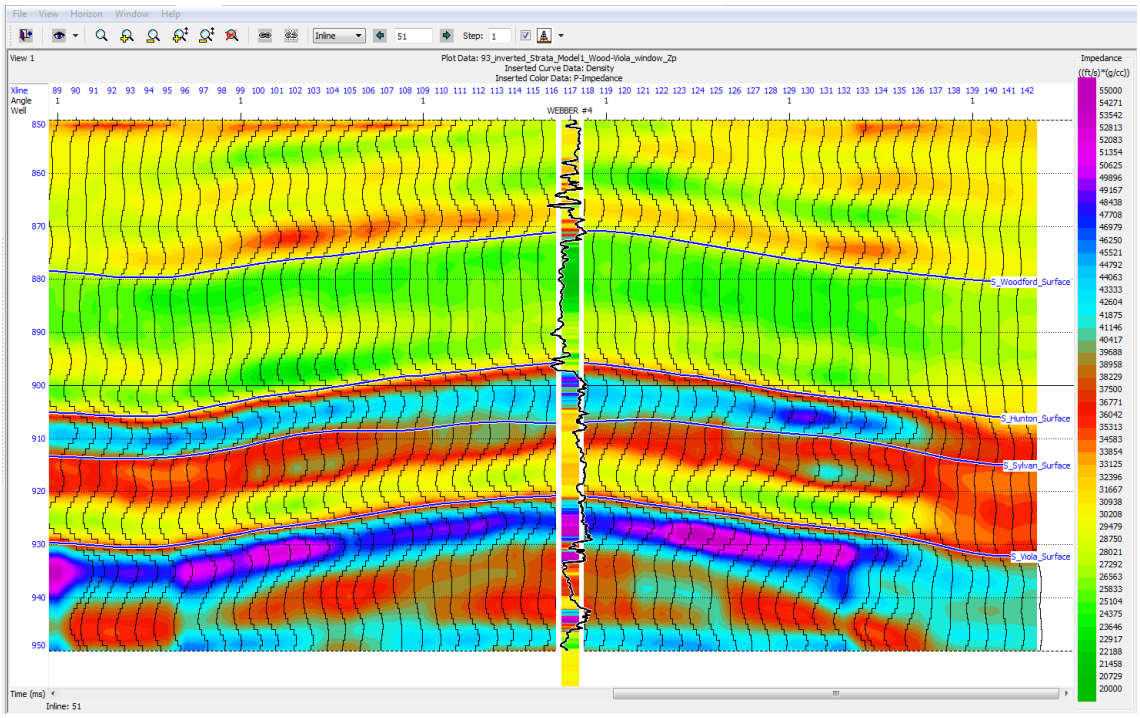

Figure A13. P impedance model used for simultaneous inversion. The black curve shows the density log superimposed on the impedance of the well log from the blind test Well 21. There is a good trend match between the P-impedance from the log and the seismic at well location.

Table A4. Correlation values between the inverted and original seismic trace and errors calculated from the inverted and original seismic trace at all of well locations.

Well name	Synthetic Correlation	Relative Synthetic Error
Well 5	0.895	0.450
Well 11	0.942	0.344
Well 12	0.922	0.385
Well 14	0.961	0.278
Well 18	0.948	0.324
Well 21	Blind Test	

Table A5. Average correlation value for all wells.

Parameter	Correlation Value
Total synthetic error	0.365
Total Inverted synthetic correlation	0.933
Total synthetic correlation for Zp	0.932

E. Inversion Results

The window has been chosen from the Woodford top to the Viola top as the target zone.

The angle dependent wavelet, from 10 to 25 averaged at 17.5 degrees, is used and the sampling rate was taken as 1 ms. An E-W cross section (**Figure A14**) of the final inversion results of P-impedance, S-impedance and density volumes are shown in **Figures A15, A16, and A17**.

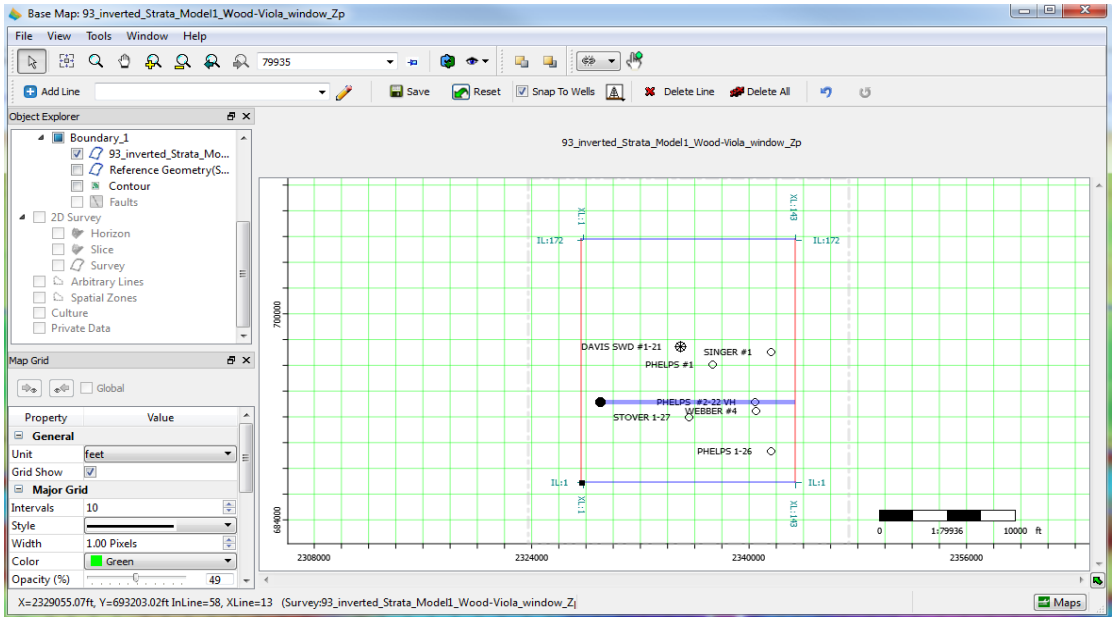

Figure A14. E-W cross section location.

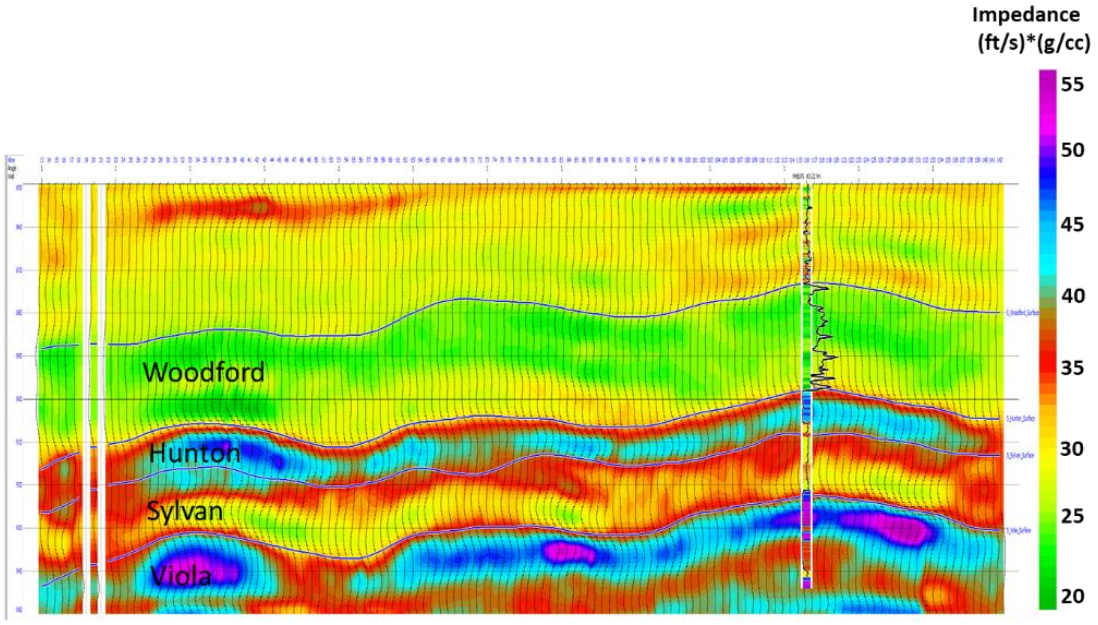

Figure A15. Inverted P impedance of E-W cross section at the location of Well 11. The black curve is gamma ray. Note that the trend of P-impedance from logs matches with the inverted P-impedance from the seismic.

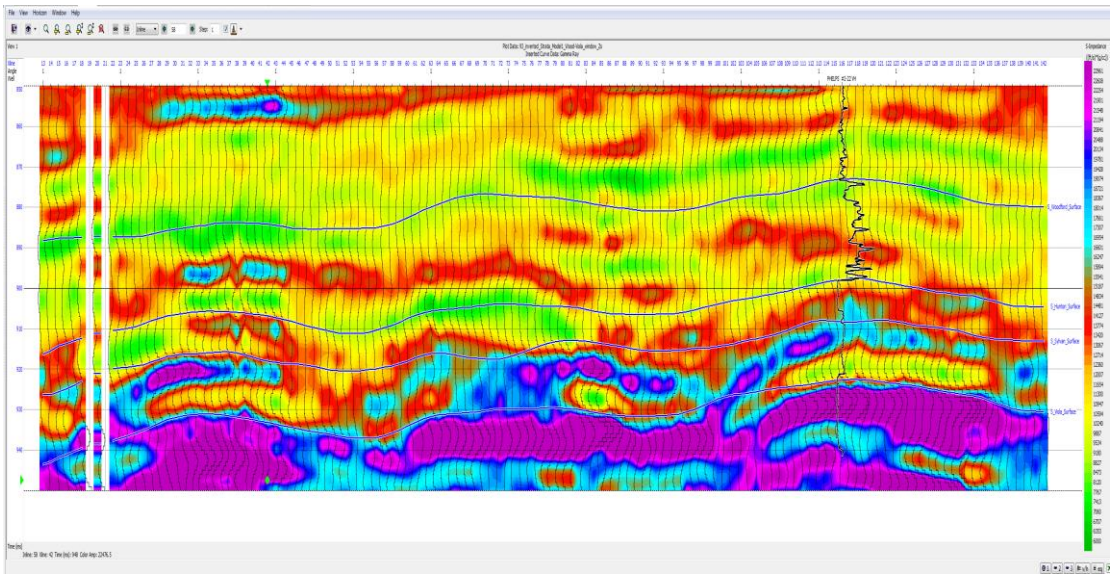

Figure A16. Inverted S impedance of E-W cross section at the location of Well 11. The black curve is gamma ray.

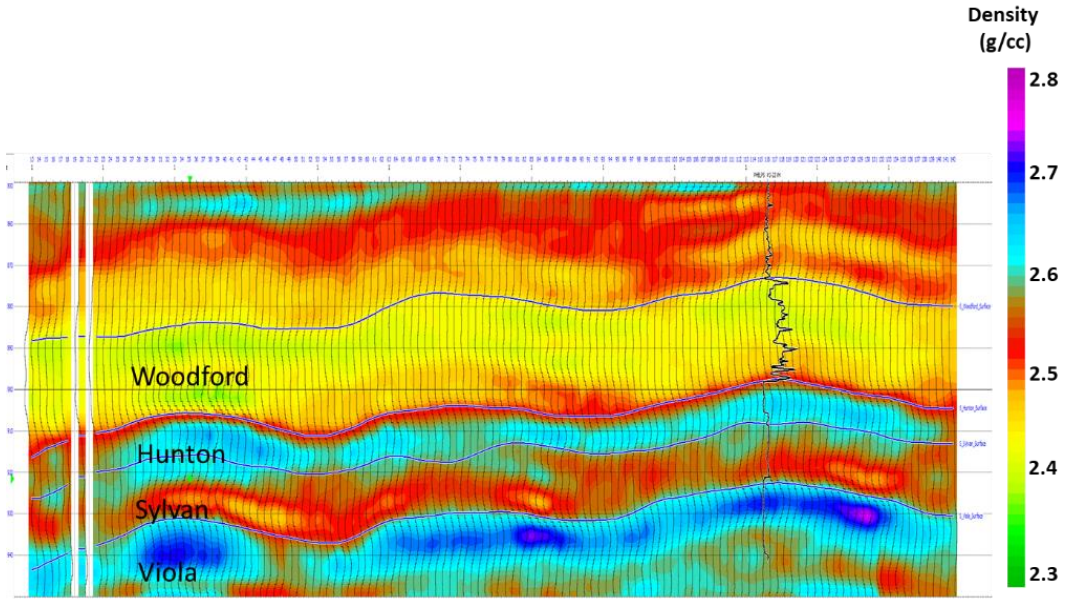

Figure A17. Inverted Density of E-W cross section at the location of Well 11. The black curve is gamma ray.

References

Chopra, S., and K. J. Marfurt, 2013, Preconditioning seismic data with 5D interpolation for computing geometric attributes: The Leading Edge, 32, 1456-1460.

Milad, B., A. Alali, R. Slatt, and K. Marfurt, 2018, Geostatistical Integration of Multiscale Data to Construct the Hunton Group GeocellularModel: Upscaling Logs and Downscaling Seismic Impedance Volumes: AAPG Search and Discovery Article #4225.